While k-ϵ solutions for both of these adverse pressure gradient cases are nearly as close to measurements as k-ω solutions, similar results should not be expected for higher Mach numbers. Many compressible-flow experiments have been conducted for Mach numbers of 3 and less. Far fewer experiments have been done at higher Mach numbers. Hence, these results show how a turbulence model calibrated for the best data available may not apply at higher Mach numbers. The k-ϵ model's near-wall behavior has a significant impact on model predictions, and Chien's model happens to be optimum for these two flows. The Jones-Launder (1972) and Launder-Sharma (1974) models, for example, predict skin friction values more than twice the measured values for both flows.

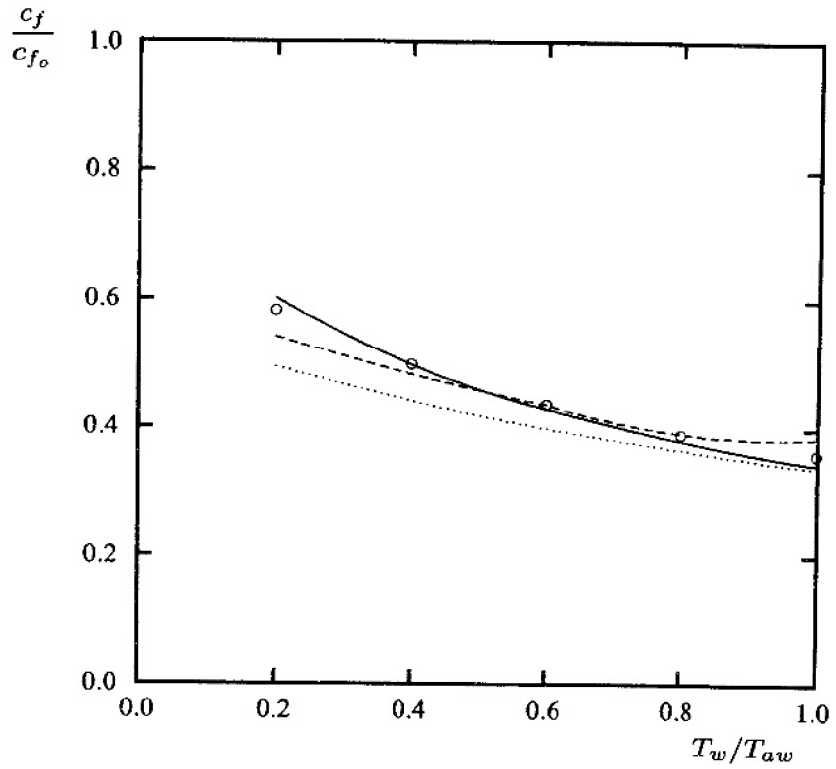

Figure 5.6: *Computed and measured effects of surface cooling on skin friction for a Mach 5 flat-plate boundary layer:* — *k-ω model, $\xi^* = 0$;* · · · *k-ω model, $\xi^* = 2$;* - - - *Zhang et al. k-ϵ model;* ○ *Van Driest correlation.*

Focusing now on effects of surface heat transfer, Figure 5.6 compares computed skin friction with a correlation of measured values [see Kline et al. (1981) — Flow 8201]. The Wilcox (2006) k-ω model is within 4% of the Van Driest correlation in the absence of compressibility modifications. Using the Wilcox compressibility modification, Equation (5.83), reduces predicted c_f/c_{f_o} by up to 15%. The k-ϵ model predictions of Zhang et al. (1993) show a similar trend, with differences from measured values of less than 10%.

As the final application, we consider compressible flow over roughened flat plates. Note that this provides a test of the Wilcox (2006) k-ω model rough-surface boundary condition on flows for which it has not been calibrated. Figure 5.7 compares computed skin friction with the data summarized by Reda, Ketter and Fan (1974). Computations have been done for Mach numbers of 0, 2 and 5 and dimensionless roughness height, k_s^+, ranging from 0 to 100. For each Mach number, the values of c_f and the reference smooth-wall skin friction coefficient, c_{f_o}, correspond to a momentum-thickness Reynolds number, Re_θ, of 10^4. As shown, computed skin friction falls within experimental data scatter for the entire range of roughness heights considered in the computations.

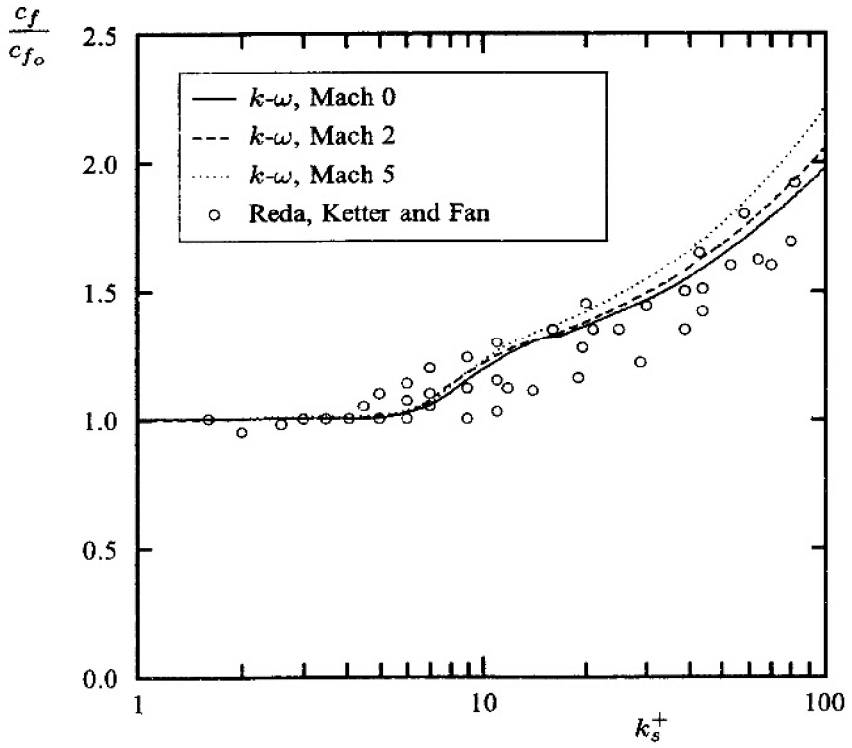

Figure 5.7: *Computed and measured effects of surface roughness on skin friction for compressible flat-plate boundary layers.*

The computations also demonstrate consistency with the observation originally made by Goddard (1959) that "the effect of surface roughness on skin-friction drag is localized deep within the boundary layer at the surface itself and is independent of the external flow, i.e., Mach number, per se, is eliminated as a variable." Consistent with Goddard's observation, Mach number has little effect on predicted c_f/c_{f_o}. Additionally, consistent with Reda's findings, computed skin friction departs noticeably from the smooth-wall value for k_s^+ values near 4 to 5 as opposed to Goddard's correlation which indicates no effect for $k_s^+ < 10$.

5.8 Shock-Induced Boundary-Layer Separation

One of the most interesting and challenging CFD problems is the interaction of a turbulent boundary layer with a shock wave. In this section, we examine some of the earliest applications, illustrate the profound effect a stress limiter has on k-ω model solutions for shock-separated flows, and discuss a series of applications ranging from transonic to hypersonic speeds.

5.8.1 The Earliest Applications

The earliest efforts were confined to algebraic models, largely because of the long computing times required to solve the full Favre-averaged continuity, Navier-Stokes and energy-conservation equations. The fastest computer of the late 1960's and early 1970's was the CDC 7600, a machine that executed at about $1/40^{\text{th}}$ the speed of a 3-GHz Pentium-D microcomputer. Additionally, the best compressible-flow numerical algorithms of that era were explicit time-marching methods that required many thousands of timesteps to achieve a solution.

Wilcox (1974) obtained the first solutions to the Favre-averaged Navier-Stokes equation, using an advanced turbulence model, for shock-induced separation of a turbulent boundary layer. This early CFD study included six computations, three for reflection of an oblique shock from a flat plate and three for flow into a compression corner. The study showed that a two-equation turbulence model could provide a reasonably accurate description of the flowfield for reflection of an oblique shock from a flat plate. Figure 5.8 compares computed and measured pitot-pressure, p_p, profiles throughout the interaction region. The quantity p_{t_∞} is freestream total pressure, x is streamwise distance along the plate, x_s denotes separation-point location and δ is incident boundary-layer thickness.

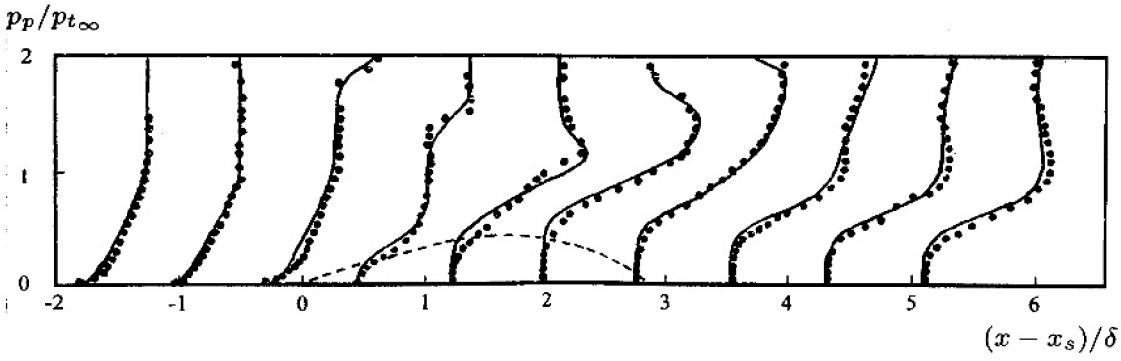

Figure 5.8: *Computed and measured Pitot-pressure profiles for a Mach 3 shock-wave/boundary-layer interaction;* —— *Saffman-Wilcox k-ω^2 model;* - - - *computed separation-bubble dividing streamline;* • *Reda-Murphy (1972). [From Wilcox (1974) — Copyright © AIAA 1974 — Used with permission.]*

However, the numerical flowfields for the three compression corners [Law (1973)] differ significantly from the experimentally observed flowfields, even though Mach and Reynolds numbers and shock strength are identical to those of the flat-plate shock/boundary-layer interaction cases. This is particularly evident from the surface-pressure variation. Figure 5.9 compares the computed and measured surface-pressure distributions for two of the shock-wave/boundary-layer interactions and two of the compression-corner flows.

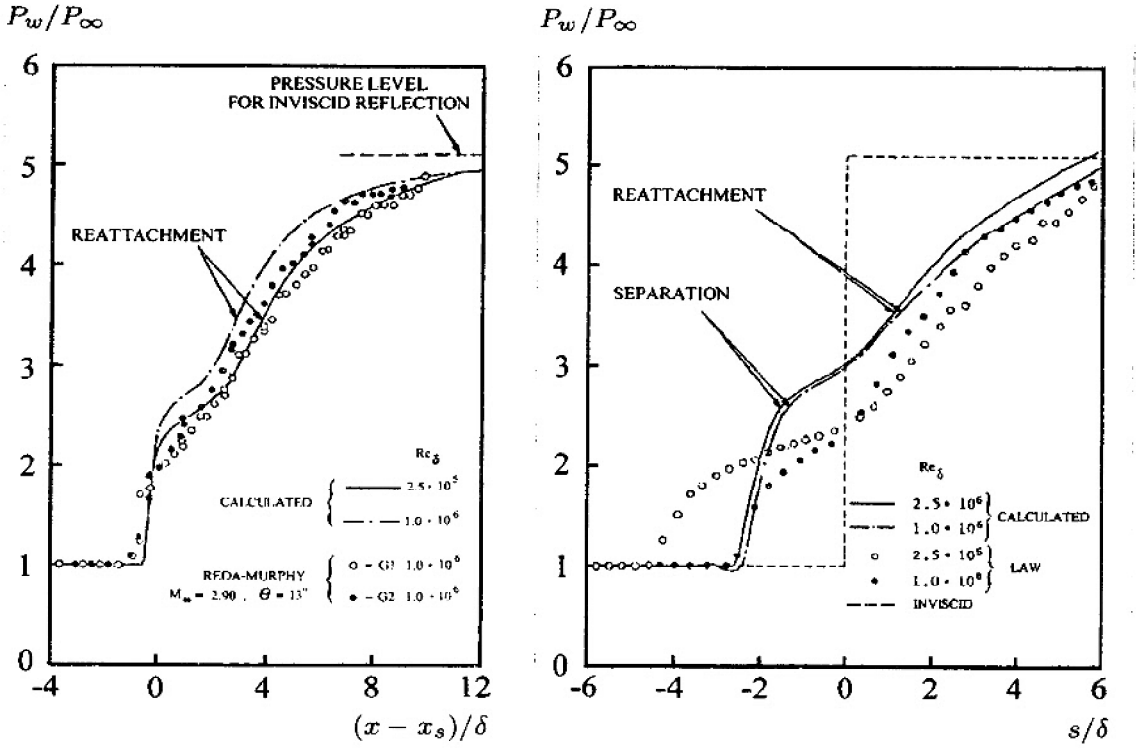

Figure 5.9: *Computed and measured surface-pressure for Mach 3 shock-wave/boundary-layer interactions and 26° compression-corner flows computed with the Saffman-Wilcox k-ω^2 model. [From Wilcox (1974) — Copyright © AIAA 1974 — Used with permission.]*

To put these computations in proper perspective, note that the turbulence model used was the Saffman-Wilcox (1974) k-ω^2 model with surface boundary conditions given by matching to the law of the wall. The numerical algorithm used was a first-order accurate explicit time-marching procedure. The computations, which were done on 4000-point finite-difference grids and required about 10000 timesteps to achieve steady-state conditions, took 40 to 50 hours of UNIVAC 1108 computer time — a commonly-used computer of that era that executed at about $1/200^{\text{th}}$ the speed of a 3-GHz Pentium-D microcomputer.

Since that time, computational methods have improved dramatically thanks to the innovative work of many researchers such as Beam and Warming (1976),

Steger and Warming (1979), Roe (1981), Van Leer (1982), MacCormack (1985), and Roache and Salari (1990), to name just a few. As a result of their innovations, converged solutions for separated flows can often be obtained in a few hundreds of timesteps or iterations. A two-equation turbulence model computation for a shock-separated flow using a 50000-point grid and 500 timesteps now takes about 15 minutes of 3-GHz Pentium-D microcomputer CPU time.

While great advances have been made in developing accurate and efficient finite-difference algorithms, until recently, far less improvement was made with turbulence models for such flows. A veritable plethora of CFD researchers including Shang, Hankey and Law (1976), Viegas and Horstman (1979), Viegas, Rubesin and Horstman (1985), Champney (1989), Horstman (1992), Huang and Liou (1994), Liou and Huang (1996), Knight (1997) and Forsythe (2000) provides clear substantiation of this claim. They have applied many turbulence models to shock-separated flows with almost universal results, viz.:

1. too little upstream influence, as shown by pressure starting to rise well downstream of the measured start of adverse pressure gradient;
2. surface pressure in excess of measured values in the separation bubble;
3. skin friction and heat transfer higher than measured downstream of reattachment;
4. velocity profiles downstream of reattachment that indicate flow deceleration within the boundary layer in excess of corresponding measurements.

On the one hand, using wall functions and the k-ϵ model, Viegas, Horstman and Rubesin (1985) are able to remove Item 3 from this list. On the other hand, they achieve only modest improvements in the other items. As we will see in this section, with the aid of a stress limiter, the k-ω model removes Items 1, 2 and half of Item 3 (the skin friction) from the list. While its predictions are closer to measurements than most other models, it nevertheless displays the symptoms cited in Item 4, as well as excessive heat transfer downstream of reattachment. This slow track record of success on the compression-corner problem, which has persisted for more than three decades, is excellent testimony to the oft quoted statement that...

Turbulence modeling is the pacing item in CFD.

5.8.2 The Use of Wall Functions for Shock-Separated Flows

Most modern shock-separated computations are done without introducing wall functions. There is no evidence that the law of the wall holds in separated regions, and its use via wall functions is therefore a questionable approximation.

The primary motivation for using wall functions in large scale computations that require substantial computer resources is in reducing CPU time.

Viegas, Horstman and Rubesin (1985), in effect, create a two-layer turbulence model where their wall functions apply in the sublayer, and the Standard k-ϵ model applies above the sublayer. While their procedure yields significant reduction in computing time, numerical results are sensitive to the location of the grid point closest to the surface, y_2^+. In fact, there is no obvious convergence to a well defined limiting value as $y_2^+ \to 0$. Consequently, the value of y_2^+ is effectively an adjustable parameter in their model equations, to be selected by the user. In practice, it is typical for the user to fix y_2 at each location, rather than modify it locally as the solution develops, which would be required to achieve a constant value of y_2^+. Thus, in practice, y_2^+ actually varies throughout the flow in a manner that cannot be determined a priori, so that the sensitivity to its value is a computational liability.

The sensitivity can be removed by using perturbation methods to devise suitable wall functions. Following Wilcox (1989), for example, we can deduce the following compressible-flow wall functions for the k-ω model as given in Equations (4.36) through (4.42):

$$\left.\begin{aligned} u^* &= u_\tau \left[\frac{1}{\kappa} \ell n \left(\frac{u_\tau y}{\nu_w} \right) + C - 1.13 \frac{u_\tau y}{\nu_w} P^+ + O(P^+)^2 \right] \\ k &= \frac{\bar{\rho}_w}{\bar{\rho}} \frac{u_\tau^2}{\sqrt{\beta^*}} \left[1 + 1.16 \frac{u_\tau y}{\nu_w} P^+ + O(P^+)^2 \right] \\ \omega &= \sqrt{\frac{\bar{\rho}_w}{\bar{\rho}}} \frac{u_\tau}{\sqrt{\beta^*} \kappa y} \left[1 - 0.30 \frac{u_\tau y}{\nu_w} P^+ + O(P^+)^2 \right] \end{aligned}\right\} \qquad (5.126)$$

where P^+ is the dimensionless pressure-gradient parameter defined by

$$P^+ = \frac{\nu_w}{\rho u_\tau^3} \frac{dP}{dx} \qquad (5.127)$$

As with the incompressible wall functions deduced for the k-ω model (see Subsection 4.7.1), the expansions in Equation (5.126) have been derived assuming P^+ is a small parameter. Using these wall functions, numerical solutions show very little sensitivity to placement of the grid point closest to the surface, provided it lies below $y^+ = 100$.

Shih et al. (1999) and Nichols and Nelson (2004) have developed wall functions with attention focused on eliminating sensitivity to the location of y_2^+. Consequently, they appear to provide satisfactory results. Nevertheless, keep in mind that there is virtually no evidence that the law of the wall, upon which wall functions are based, applies in separated regions.

5.8.3 The Next Two Decades of "Progress"

Efforts following the early work of Wilcox (1974) yielded little progress in reducing discrepancies between theory and experiment. Figure 5.10 compares computed and measured [Settles, Vas and Bogdonoff (1976)] surface pressure for Mach 3 flow into a 24° compression corner using algebraic models, a one-equation model and several two-equation models. None of the algebraic, one-equation or two-equation models provides a satisfactory solution. In more recent computations, Huang and Liou (1994) show that the RNG k-ϵ model [Yakhot and Orszag (1986)] consistently predicts separation bubbles that are: (a) nearly double the length of those predicted by the standard version; and (b) much longer than measured. Also, Forsythe (2000) has shown that Menter's (1992c) hybrid k-ω/k-ϵ model and the Spalart-Allmaras (1992) one-equation model, both of which have proven to be reliable for incompressible and transonic applications, predict a separation bubble nearly double the measured size for this flow.

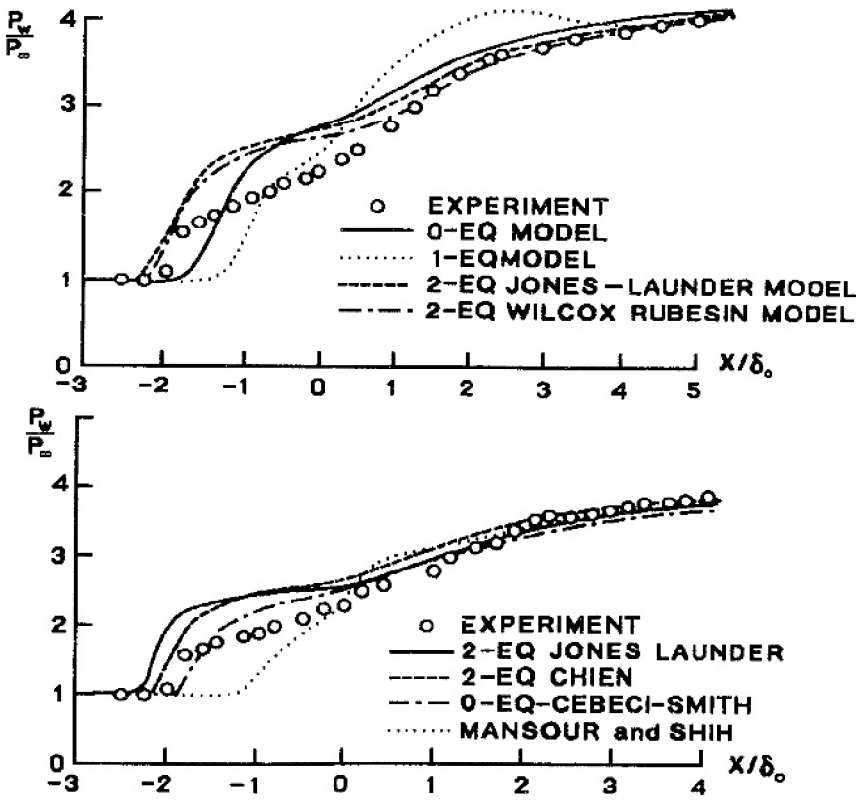

Figure 5.10: *Comparison of computed and measured surface pressure for Mach 3 flow into a 24° compression corner for several turbulence models. [From Marshall and Dolling (1992) — Copyright © AIAA 1992 — Used with permission.]*

5.8.4 Effect of the Stress Limiter on Shock-Separated Flows

Coakley (1983) was the first to suggest that shock-separated flows can be more accurately simulated with the k-ω model by simply limiting the magnitude of the Reynolds shear stress when production of turbulence kinetic energy exceeds its dissipation. He developed a stress limiter that showed some promise for improving k-ω model predictions. Menter (1992c), Kandula and Wilcox (1995), Durbin (1996), and Huang (1999) for example, have subsequently confirmed the effectiveness of a stress limiter for flow speeds up to the transonic range.

Durbin (1996) and Moore and Moore (1999) have assessed the **realizability** of turbulence-energy production predicted using the Boussinesq approximation. They observe that for flows such as impinging jets and the inviscid, highly-strained flow approaching a stagnation point, without the assistance of a stress limiter, the Boussinesq approximation leads to unrealistically high turbulence-energy levels — levels that are not realized in nature. Moore and Moore propose the following general relation for limiting the Reynolds stress.

$$\mu_T = \frac{\bar{\rho}k}{\tilde{\omega}}, \qquad \tilde{\omega} = \max\left\{\omega, \quad C_0\omega + C_{lim}\sqrt{\frac{2\lambda_1\bar{S}_{ij}\bar{S}_{ij} + 2\lambda_2\Omega_{ij}\Omega_{ij}}{(\lambda_1+\lambda_2)\beta^*}}\right\} \tag{5.128}$$

Recall that $\bar{S}_{ij} = S_{ij} - \frac{1}{3}S_{kk}\delta_{ij}$. Table 5.4 lists the values of the constants C_0, C_{lim}, λ_1 and λ_2 proposed by several researchers.

Table 5.4: *Stress-Limiter Coefficients.*

Reference	C_0	C_{lim}	λ_1	λ_2
Coakley (1983)	0	1.00	1	0
Durbin (1996)	0	1.03	1	0
Menter (1992c)	0	1.00	0	1
Moore and Moore (1999)	2.85	0.75	1	1
Wilcox (2006)	0	0.88	1	0

To understand the way in which the stress limiter suppresses the magnitude of the Reynolds shear stress, we first simplify Equation (5.128) for the most-commonly used version that has $C_0 = 0$, $\lambda_1 = 1$ and $\lambda_2 = 0$, viz.,

$$\mu_T = \frac{\bar{\rho}k}{\tilde{\omega}}, \qquad \tilde{\omega} = \max\left\{\omega, \quad C_{lim}\sqrt{\frac{2\bar{S}_{ij}\bar{S}_{ij}}{\beta^*}}\right\} \tag{5.129}$$

In a shear layer, we know that $2\bar{S}_{ij}\bar{S}_{ij} \approx (\partial\tilde{u}/\partial y)^2$. So, Equation (5.129) tells us that

$$\bar{\rho}\tau_{xy} = \mu_T\frac{\partial\tilde{u}}{\partial y} = \min\left\{\frac{\bar{\rho}k}{\omega}\frac{\partial\tilde{u}}{\partial y}, \quad C_{lim}^{-1}\sqrt{\beta^*}\,\bar{\rho}k\right\} \tag{5.130}$$

Also, observe that, in the absence of a stress limiter, the ratio of production, P_k, to dissipation, D_k, in the turbulence kinetic energy equation is

$$\frac{P_k}{D_k} = \frac{(\bar{\rho}k/\omega)\partial\tilde{u}/\partial y}{\beta^*\bar{\rho}k\omega} = \left(\frac{\partial\tilde{u}/\partial y}{\sqrt{\beta^*}\,\omega}\right)^2 \tag{5.131}$$

Thus, the stress-limiter modification is such that

$$\bar{\rho}\tau_{xy} = C_{lim}^{-1}\sqrt{\beta^*}\,\bar{\rho}k \quad \text{for} \quad \frac{P_k}{D_k} \geq C_{lim}^{-2} \tag{5.132}$$

Consequently, the stress limiter drives the Reynolds shear stress toward the form Bradshaw implemented in his one-equation turbulence model (see Section 4.2). When $C_{lim} = 1$, the coefficient $C_{lim}^{-1}\sqrt{\beta^*} = 0.30$, which matches the value of Bradshaw's constant, β_r. For the Wilcox (2006) k-ω model, we find that $C_{lim}^{-1}\sqrt{\beta^*} = 0.34$.

Interestingly, in a shear layer the turbulence kinetic energy production term in the Saffman-Wilcox (1974) k-ω^2 model is $P_k = 0.30\bar{\rho}k\,|\partial\tilde{u}/\partial y|$. Hence, production of k is constrained although the eddy viscosity is not. This is the reason Wilcox and Traci (1974) were able to accurately compute the increase in turbulence kinetic energy approaching a stagnation point. This is not possible with a two-equation turbulence model that does not implement a stress limiter [Durbin (1996)] because the strain-rate field is such that P_k/D_k is typically in excess of 100. Although experimental data are not shown in Figure 5.11, the computed amplification is consistent with the measurements of Bearman (1972).

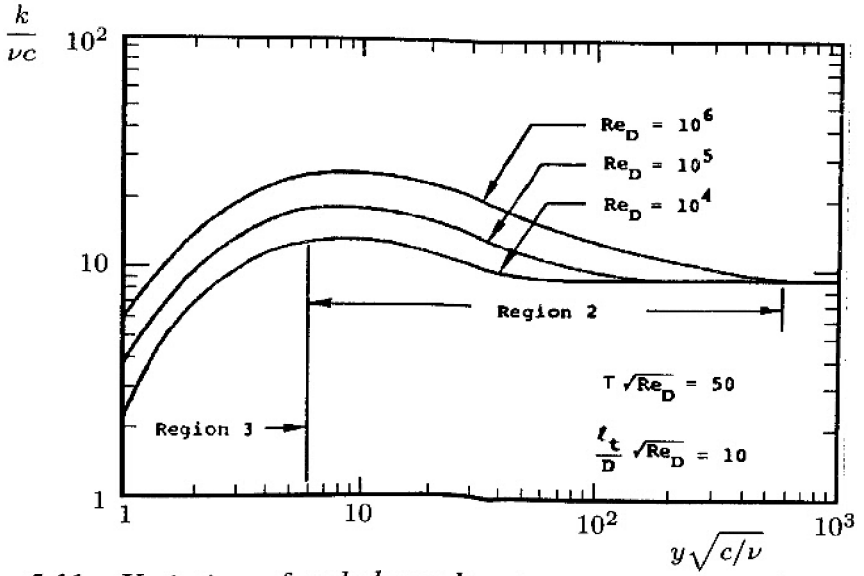

Figure 5.11: *Variation of turbulence kinetic energy approaching a stagnation point; —— Saffman-Wilcox k-ω^2 model. [From Wilcox and Traci (1974) — Copyright © AIAA 1974 — Used with permission.]*

Figure 5.12 shows the dramatic improvement for Mach 0.8 flow past an NACA 0012 airfoil at 2.26° angle of attack. The solid curves identified as "original" correspond to the Wilcox (1988a) k-ω model, which does not use a stress limiter. The dashed curves identified as "SST" correspond to the same model with a stress limiter applied with $C_{lim} = 1$. The most dramatic difference is the location of the shock. Without the stress-limiter, the predicted shock location is farther downstream than the measured location. Adding the stress limiter increases the size of the separation bubble on the upper surface of the airfoil, causing the computed shock location to lie much closer to the experimentally-observed location.

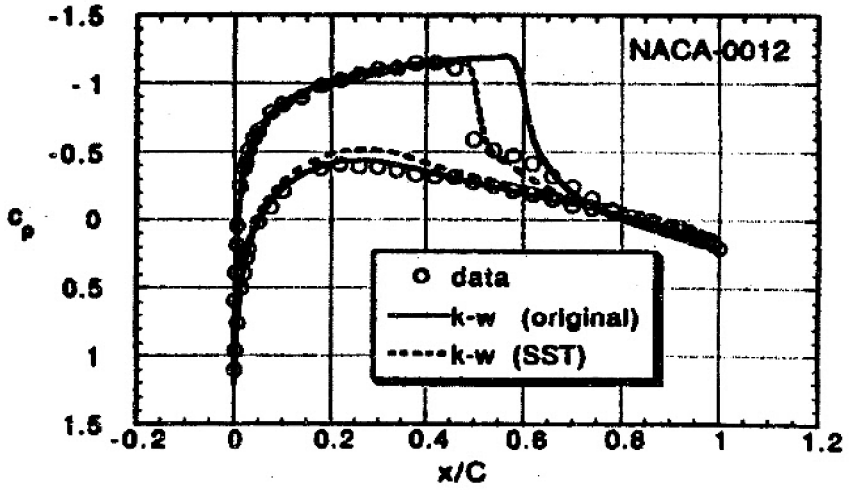

Figure 5.12: *Comparison of computed and measured surface pressure for transonic flow past an NACA 0012 airfoil at 2.26° angle of attack. [From Kandula and Wilcox (1995) — Copyright © AIAA 1995 — Used with permission.]*

We saw in Chapter 4.10 that the stress limiter has a relatively small effect on most incompressible attached and separated flows. The most noteworthy counter example occurs for flow past a backward-facing step. Figure 4.49 shows that using $C_{lim} = 1$ yields a reattachment length that is 25% longer than measured. By contrast, using $C_{lim} = 7/8$ reduces the discrepancy to 13%. In Subsections 5.8.6 and 5.8.7, we will discover that C_{lim} has a similar effect on supersonic backsteps and flow into compression corners.

We will also see that Menter's model predicts separation bubbles that are far larger than measured for Mach numbers in excess of 2. This occurs because the model uses $C_{lim} = 1$. We can reasonably conclude that $C_{lim} = 1$ may be optimum for the transonic-flow regime, yields a somewhat stronger than desired stress-limiting effect for incompressible flows and yields much too strong an effect for supersonic flows.

5.8.5 Transonic Flow Over an Axisymmetric Bump

The transonic-bump experiment of Bachalo and Johnson (1979) is a particularly challenging separated-flow application. In the experiment, a long slender bump is fared onto the surface of a cylinder. Freestream Mach number is $M_\infty = 0.875$ and unit Reynolds number is $Re_\infty = 4 \cdot 10^6$ ft^{-1}. A shock wave develops over the bump, which separates the boundary layer. The flow reattaches in the wake of the bump, giving rise to a reattachment shock. This flow is very difficult to predict because the bump surface pressure is extremely sensitive to the size of the separation bubble, which is strongly coupled to the precise shock locations.

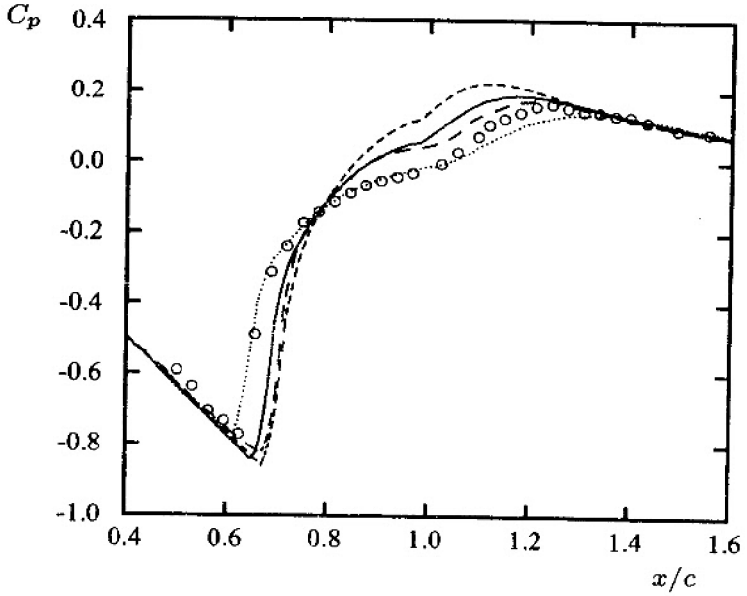

Figure 5.13: *Application of several turbulence models to transonic flow past an axisymmetric bump:* — *Wilcox (2006) k-ω;* - - - *Wilcox (1988a) k-ω;* · · · *Menter (1992c) k-ω/k-ϵ;* – – *Spalart-Allmaras (1992);* ○ *Bachalo and Johnson.*

Figure 5.13 compares computed and measured C_p for four turbulence models. The short-dashed curve corresponds to the Wilcox (1988a) k-ω model, which does not have a stress limiter. Although the predicted separation-shock location differs from the measured location by only 6% of the bump's chord length, c, computed and measured C_p differ significantly. The solid curve corresponds to the Wilcox (2006) k-ω model, which includes a stress limiter. Differences between computed and measured C_p are generally less than 7%. The long-dashed curve corresponds to the Spalart-Allmaras model. Although separation-shock location and separation are about the same as for the Wilcox (1988a) model, computed C_p is closer to measured C_p near reattachment. The dotted curve corresponds to Menter's (1992c) k-ω/k-ϵ model with a stress limiter. Computed and measured shock locations and C_p are quite close [see, e.g., Forsythe (2000)].

Using $C_{lim} = 1$ with the Wilcox (2006) k-ω model yields C_p nearly identical to the Menter prediction. Unfortunately, the improvement in predictive accuracy for this flow comes at the expense of much greater discrepancies between theory and experiment for both smaller and larger Mach numbers. This explains why Menter's model fares well for Mach numbers from incompressible up to transonic speeds, but very poorly for supersonic and hypersonic flows.[3] Menter's model, in fact, appears to be fine tuned for the transonic regime. By accepting 7% discrepancies between predicted and measured properties for this flow, which are comparable to those obtained with the Spalart-Allmaras (1992) model, the Wilcox (2006) k-ω model reproduces measurements quite closely all the way from incompressible speeds to the hypersonic regime.

The Wilcox (1988a) and (2006) model computations were done using Programs **EDDYBL** and **EDDY2C** (see Appendix C). Starting from the leading edge of the cylinder ($x/c = -3.5$), **EDDYBL** was used to solve from laminar flow through transition and results were saved at $x/c = -3$. Reynolds number based on momentum thickness, Re_θ, at this point is 2450. Output from **EDDYBL** was used to define upstream boundary conditions for a full Navier-Stokes solution using **EDDY2C** on a 201 x 101 finite-difference mesh. All of the **EDDY2C** computations in the following sections have been done in this manner.

5.8.6 Mach 2 Flow Past a Backward-Facing Step

We turn now to compressible flow past a backward-facing step. The case we will discuss has a freestream Mach number of 2.07 and the incident boundary layer has a momentum-thickness Reynolds number of $Re_\theta = 1.2 \cdot 10^4$. This flow was investigated experimentally by Samimy, Petrie and Addy (1985). The computation was done with Program **EDDY2C** using the Wilcox (2006) k-ω model with and without the stress limiter. The finite-difference grid consists of 401 streamwise points and 201 points normal to the freestream flow direction.

As shown in Figure 5.14, with $C_{lim} = 7/8$, the stress limiter has a barely noticeable effect on the computed surface-pressure coefficient. Computed and measured values of C_p differ by less than 7% for the entire flowfield. Predicted reattachment length with the limiter is $x_r = 2.67H$. The length decreases to $x_r = 2.55H$ without the limiter. Both values are within a few percent of the value measured by Samimy et al., which is $x_r = 2.76H$. Using $C_{lim} = 1$ for this flow increases x_r to $2.78H$, which is also quite close to the measured reattachment length. Clearly, the effect is less pronounced than for an incompressible backstep. However, as we will see in the next subsection, with $C_{lim} = 1$ the stress-limiter effect is a far too strong at Mach 3.

[3] The primary culprit is not so much the stress-limiter strength, as reflected by the value of C_{lim}, as it is the Boussinesq approximation. We will explore this point in greater depth in Chapter 6.

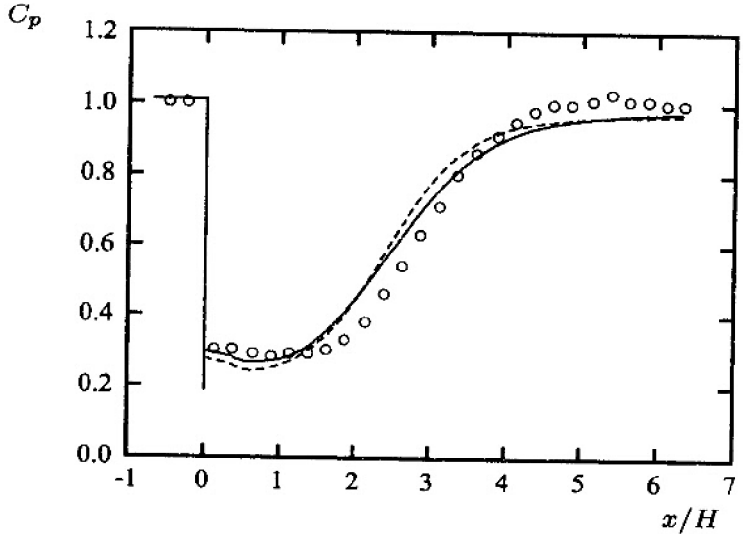

Figure 5.14: *Effect of the stress limiter on the k-ω model for Mach 2 flow past a backward-facing step:* —— *with limiter;* - - - *without limiter;* o *Samimy et al.*

5.8.7 Mach 3 Compression Corners and Reflecting Shocks

As discussed in Subsections 5.8.1 and 5.8.3, supersonic flow into a compression corner and reflection of an oblique shock from a flat surface have proven to be the most challenging of all two-dimensional separated-flow applications. Figure 5.15 sketches these two geometries, including some of the main features of flow structure for each. While the geometries are fundamentally different, these flows are nevertheless very similar. Through extensive experimental investigations, Petrov et al. (1952) and Chapman et al. (1957) developed the **free-interaction concept**. They found that flow details in the vicinity of separation are local and depend almost entirely on Mach number and static-pressure ratio across the separation shock. Thus, if we test a turbulence model for compression-corner flows, we should simultaneously test the model for reflecting shocks to check consistency with the free-interaction concept.

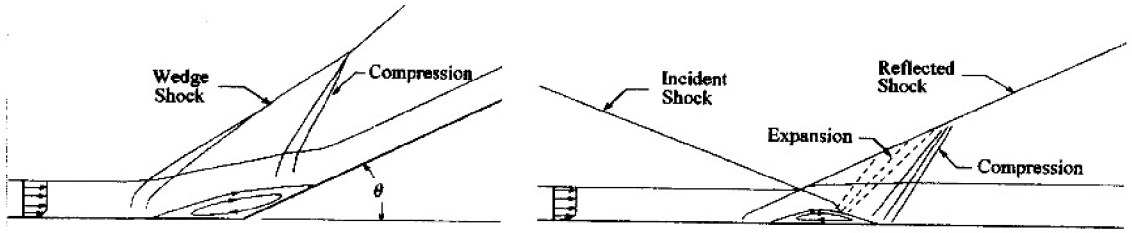

(a) Compression Corner Flow (b) Shock-Wave/Boundary-Layer Interaction

Figure 5.15: *Schematics of supersonic flow into a compression corner and shock-wave/boundary-layer interaction (reflecting shock).*

Figure 5.16 compares computed and measured surface pressure and skin friction for two compression-corner flows and a reflecting-shock case. All three flows have a freestream Mach number close to three and have separation bubbles of different sizes. The two compression-corner flows have wedge angles of 20° and 24°, corresponding to experiments conducted by Settles, Vas and Bogdonoff (1976) and by Dolling and Murphy (1983). The reflecting-shock case was investigated experimentally by Reda and Murphy (1972) and by Murthy and Rose (1978). The incident shock makes an angle of 31° with the horizontal and turns the flow by 13°. All three computations were done with Program **EDDY2C** (see Appendix C) on finite-different grids with 401 streamwise points and 201 points normal to the surface.

The graphs include results for the k-ω model with and without the stress limiter. In all three cases, with the stress-limiter implemented, computed and measured surface pressures are very close. Most important, the initial pressure rise in the computed flowfields matches the measured rise. This means the separation shock is in the same location in the numerical and experimental flowfields. The predicted pressure plateau in the separation bubble and skin friction downstream of reattachment are much closer to measurements than any of the results shown in Figure 5.10. Discrepancies between computed and measured c_f downstream of reattachment indicates the rate of recovery from separation and the return to equilibrium conditions is a bit different.

Without the stress limiter, the computed separation-shock location is clearly further downstream than measured, which distorts the entire flowfield.

The similarity between the shapes of the computed surface-pressure and skin-friction curves for the shock-wave/boundary-layer interaction and the 24° compression-corner flow is striking. Because the overall pressure rise is nearly the same for the two flows, this similarity confirms that the k-ω model's predictions are consistent with the free-interaction concept.

The numerical separation points for these flows are further upstream than indicated by oil-flow measurements. Marshall and Dolling (1992) indicate that the flow includes a low-frequency oscillation of the separation shock. Adams (2000) has found this oscillation in a Direct Numerical Simulation of a Mach 3 compression-corner flow. This phenomenon is also observed in three-dimensional shock-separated flows [Brusniak and Dolling (1996)]. The time-mean pressure distribution upstream of the corner is affected by these oscillations, whose frequency content includes substantial energy at time scales of the mean motion. This unsteadiness is responsible for the apparent mismatch between the beginning of the pressure rise and the separation point. Since computations with the k-ω model are so close to measured properties, yet display no low-frequency oscillation of the shock, we can reasonably conclude that the computations effectively incorporate the slow oscillation into the Favre-averaged flow variables.

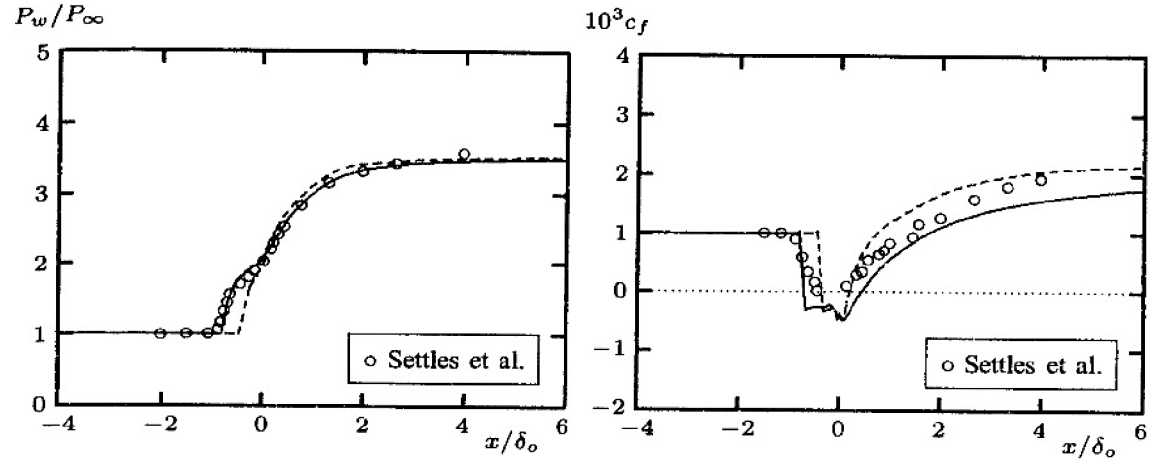

(a) 20° Compression Corner, $M_\infty = 2.79$

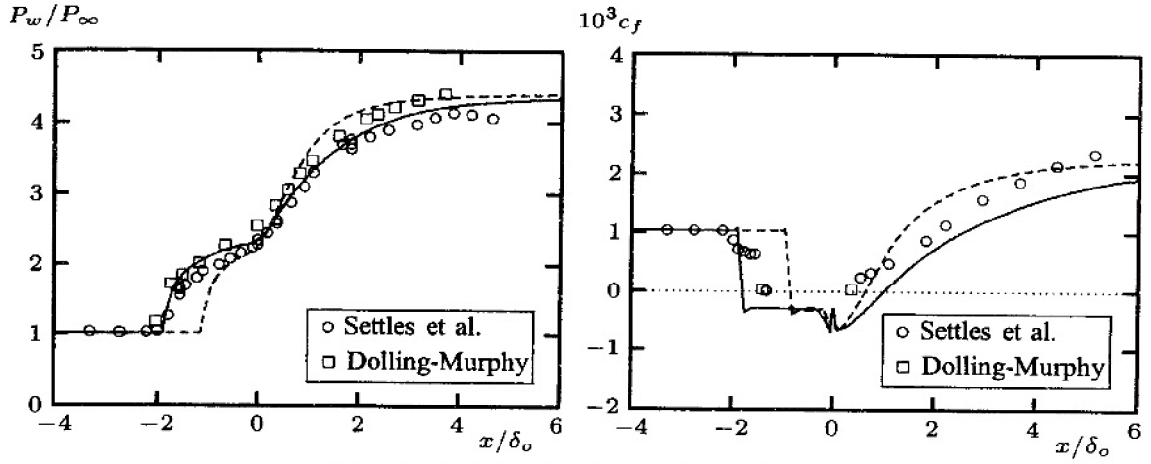

(b) 24° Compression Corner, $M_\infty = 2.84$

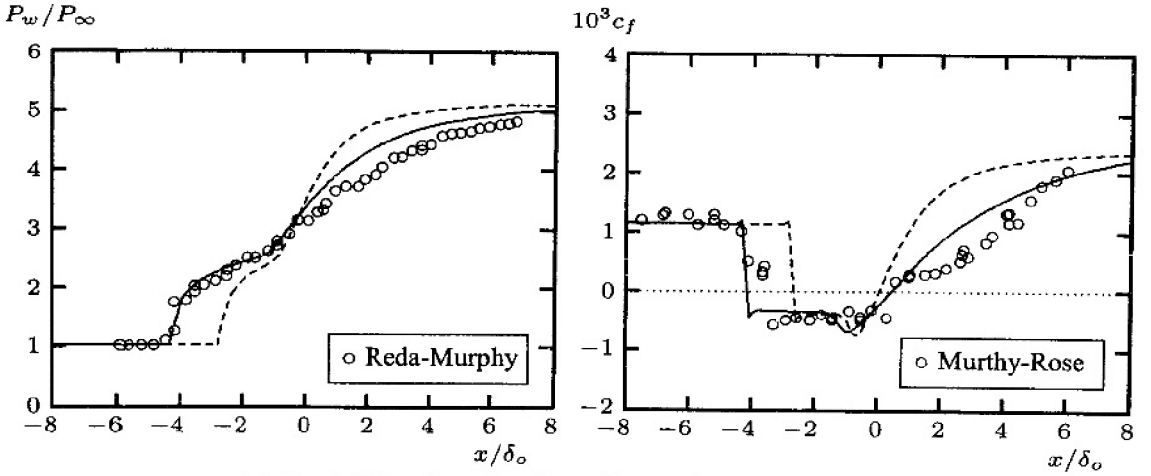

(c) Shock-Wave/Boundary-Layer Interaction, $M_\infty = 2.90$

Figure 5.16: *Comparison of computed and measured surface pressure and skin friction for Mach 3 shock-separated flows using the Wilcox (2006) k-ω model: —— with limiter; - - - without limiter.*

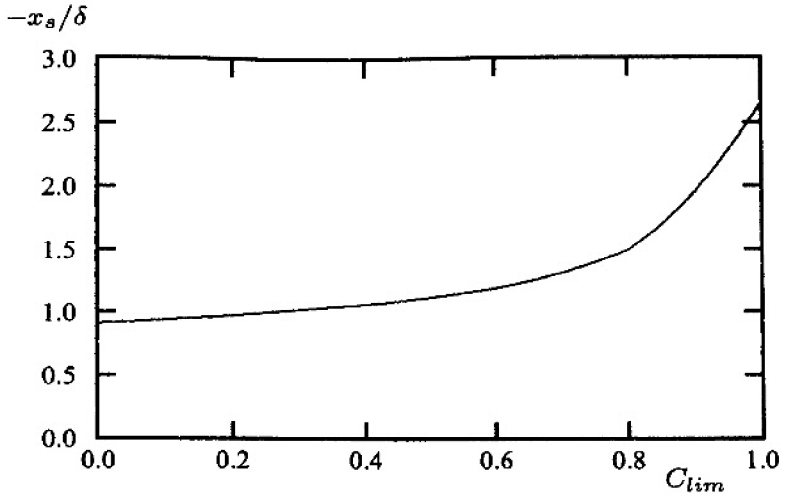

Figure 5.17: *Effect of the stress-limiter coefficient, C_{lim}, on computed separation-point location for Mach 3 flow into a 24° compression corner.*

Figure 5.17 indicates how separation-point location, x_s, for the 24° compression corner flow varies with C_{lim}. As shown, similar to the effect for an incompressible backward-facing step (see Figure 4.49), $-x_s$ increases monotonically as C_{lim} increases. Selecting $C_{lim} = 7/8$ yields a value of $x_s = -1.82\delta$, which provides a very close match to most details of this flowfield. Figure 5.18 shows that using $C_{lim} = 1$ produces a separation bubble roughly twice the measured size. This explains why Menter's model fares so poorly for this flow [Forsythe (2000)].

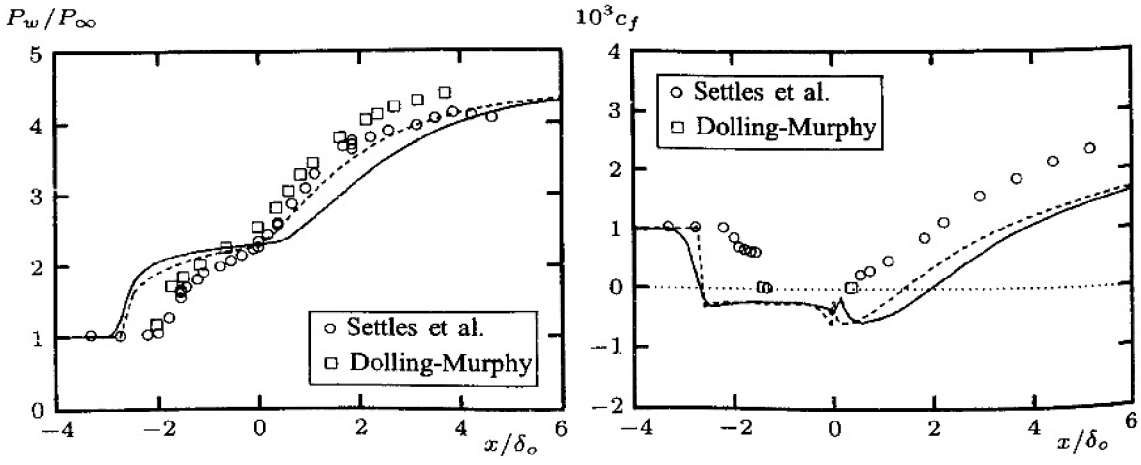

Figure 5.18: *Comparison of computed and measured surface pressure and skin friction for Mach 3 flow into a 24° compression corner: —— Menter (1992c) k-ω/k-ϵ model; - - - Wilcox (2006) k-ω model with $C_{lim} = 1$.*

5.8.8 Mach 11 Reflecting-Shock

We turn now to a hypersonic flow, viz., the Mach 11 shock-wave/boundary-layer interaction investigated by Holden (1978). The incident shock makes a 17.6° angle with the surface and increases the static pressure by a factor of 70. The surface is highly cooled with a wall to adiabatic-wall temperature ratio of $T_w/T_{aw} = 0.2$. All computations discussed below were done with Program **EDDY2C** on a 501 x 301 point finite-difference mesh.

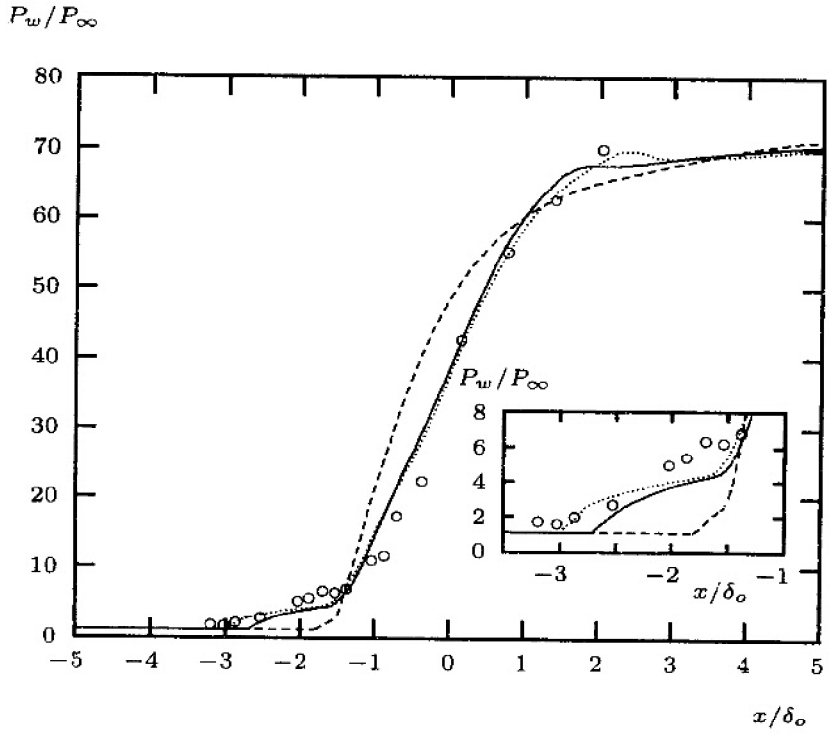

Figure 5.19: *Effect of the stress limiter and viscous modifications on the k-ω model for a Mach 11 shock-wave/boundary-layer interaction:* —— *with limiter;* - - - *without limiter;* · · · *with viscous modifications;* o *Holden (1978)*

Figure 5.19 compares computed and measured surface pressure for three versions of the Wilcox (2006) k-ω model, viz., with the stress limiter, without the stress limiter and with low-Reynolds-number viscous modifications. As shown, the limiter increases separation bubble length from $0.34\delta_o$ to $1.53\delta_o$. The computed surface pressure rise is much closer to the measured rise when the limiter is used. As with the Mach 3 applications of the preceding subsection, this indicates that the predicted shock pattern closely matches the experimental pattern. Holden estimated the size of the separation bubble to be about $1.00\delta_o$. The surface-pressure data suggest a separation bubble about twice that size.

The third computation shows the effect of the k-ω model's viscous modifications (Subsection 4.9.2). The low-Reynolds-number modifications make very

little difference for all of the shock-separated flows considered thus far. For this flow, the effect is more pronounced. The low-Reynolds-number model predicts a separation bubble with a length of $1.81\delta_o$, an increase in length of 18%. As shown in the inset figure, this yields even closer agreement between theory and experiment throughout the region of reversed flow.

5.8.9 The Reattachment Point Heat-Transfer Anomaly

While significant progress has finally been made in predicting surface pressure, skin friction and velocity profiles in shock-separated flows, one problem continues to defy accurate prediction. Specifically, surface heat transfer in the vicinity of reattachment predicted by all turbulence models is much higher than measured. To illustrate the problem, Figure 5.20 compares computed and measured surface pressure and heat transfer for Mach 7.05 flow into a 35° axisymmetric compression corner [Kussoy and Horstman (1989)]. The surface is cooled and has a wall to adiabatic-wall temperature ratio of $T_w/T_{aw} = 0.4$. Computed results shown are for the Wilcox (2006) k-ω model with and without the stress limiter. The computation was done with Program **EDDY2C** on a 301 x 151 mesh.

The graph to the right shows the ratio of surface heat transfer rate, q_w, to its value far upstream of the interaction, q_{w_∞}. Without the stress limiter, the peak heat transfer rate to the surface is double the measured value. Even with the stress limiter included, the peak heating rate is 50% higher than measured. Interestingly, increasing the strength of the stress limiter by using a larger value of C_{lim} does two things. First, it increases the size of the separation bubble. Second, it

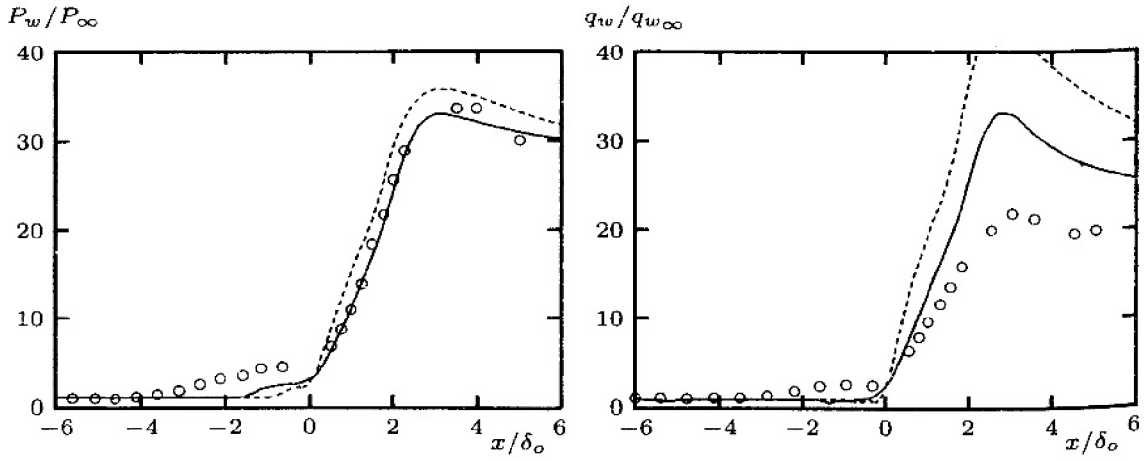

Figure 5.20: *Computed and measured surface pressure and heat transfer for Mach 7 flow into a 35° axisymmetric compression corner (cylinder-flare geometry) using the Wilcox (2006) k-ω model: —— with limiter; - - - without limiter; ○ Kussoy-Horstman (1989)*

causes the ratio q_w/q_{w_∞} to *increase* slightly. In fact, a series of computations varying C_{lim} from 0 to 1 shows that the maximum value of q_w/q_{w_∞} occurs when $C_{lim} = 0$, decreases to a minimum value of 1.51 when $C_{lim} = 0.8$ and increases to 1.57 when $C_{lim} = 1$.

This is consistent with the fact that turbulent transfer of heat and momentum are fundamentally different processes. On the one hand, the largest eddies determine the nature of the Reynolds stresses, which are responsible for the turbulent transport of momentum throughout a given flow. On the other hand, heat transfer occurs at much smaller scales and is less directly related to the large eddies. The stress-limiter primarily effects the Reynolds stresses well above the sublayer, i.e., it affects the larger eddies in a boundary layer. So, it is sensible that the stress limiter would increase the length of the separation bubble and simultaneously have a less pronounced effect on surface heat transfer.

Coakley and Huang (1992) propose and test numerous compressibility modifications, one of which is very effective in reducing predicted heating rates at the reattachment point for shock-separated flows. Specifically, they first define the so-called **von Kármán length scale**, ℓ_μ, as follows.

$$\ell_\mu = \begin{cases} \min\left(2.5y, k^{1/2}/\omega\right), & k-\omega \text{ model} \\ \min\left(2.5y, k^{3/2}/\epsilon\right), & k-\epsilon \text{ model} \end{cases} \tag{5.133}$$

where y is distance normal to the surface. Then, the value of ω or ϵ is recomputed according to

$$\omega = k^{1/2}/\ell_\mu, \qquad \epsilon = k^{3/2}/\ell_\mu \tag{5.134}$$

This compressibility correction is very effective and yields realistic heating rates at reattachment for both k-ω and k-ϵ models. Figure 5.21 illustrates how well the modification works for the Kussoy-Horstman Mach 7 cylinder-flare experiment.

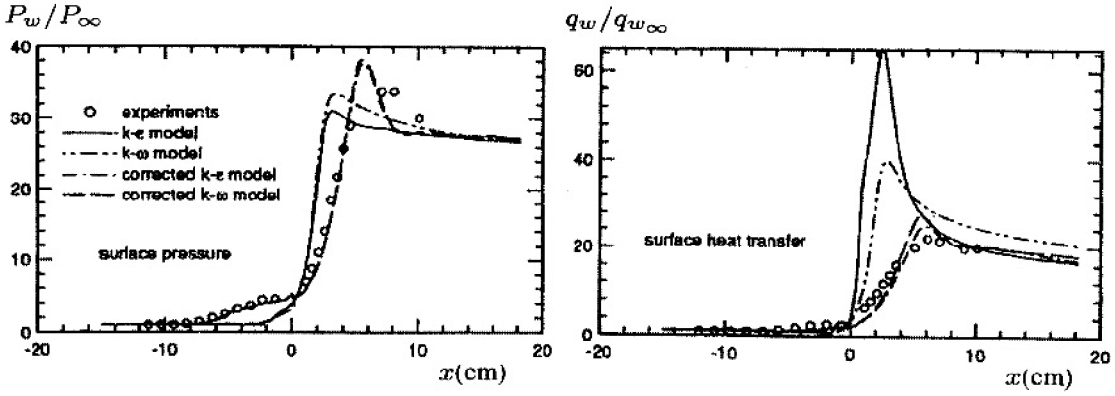

Figure 5.21: *Computed and measured surface pressure and heat transfer for Mach 7 flow into a 35° axisymmetric compression corner. [From Huang and Coakley (1993) — Copyright © AIAA 1993 — Used with permission.]*

Results are shown for the Launder-Sharma (1974) k-ϵ model and the Wilcox (1988a) k-ω model. Without a heat-transfer correction, the Launder-Sharma model surface heat transfer, q_w, is triple the measured value, while the k-ω model is high by a factor of about two. The Coakley-Huang modification brings the computed heat transfer into much closer agreement with measurements. Note that the computed results in Figure 5.21 also include a compressibility modification that increases the length of the separation bubble. Like the stress-limiter, the same modification produces much too strong an effect for Mach 3 shock-separated flows [Coakley and Huang (1992)].

5.8.10 Three-Dimensional Applications

There has been substantial progress in the capability for prediction of three-dimensional shock wave, turbulent boundary layer interactions. Recent reviews by Knight (1993, 1997, 2003) describe the status of research for five basic geometries. Figure 5.22(a) illustrates the three-dimensional single fin, arguably the most extensively studied such interaction. The deflection of the fin surface by an angle α generates an oblique shock that interacts with the boundary layer on the flat plate. This interaction is of some practical interest, as it represents a geometric abstraction of a fin-body juncture for a high-speed aircraft. Figure 5.22(b) compares computed and measured surface pressure for $M_\infty = 2.9$, $\alpha = 20°$, and $Re_{\delta_o} = 9 \cdot 10^5$, where δ_o is boundary-layer thickness upstream of the interaction. The comparison has been made at a spanwise distance, $z = 6.8\delta_o$ from the plane of symmetry. Computations using the Baldwin-Lomax (1978) model (labeled "Knight") and Rodi's (1991) k-ϵ model (labeled "Horstman") are in close

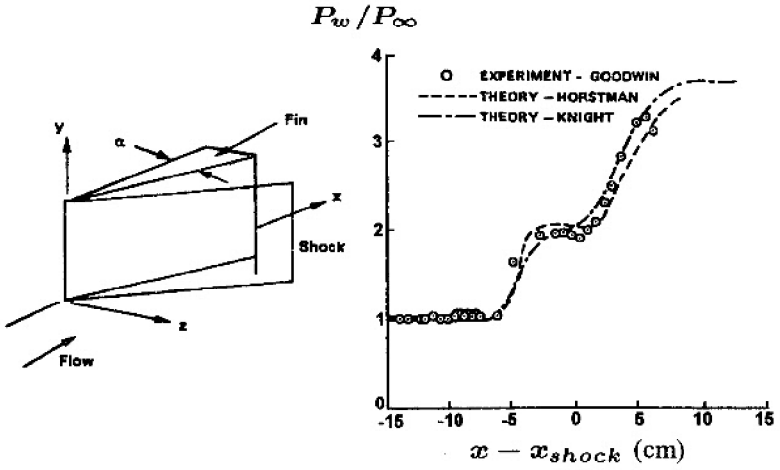

(a) Flow Geometry (b) Surface pressure, $z = 6.8\delta_o$

Figure 5.22: *Single-fin shock-wave/boundary-layer interaction at Mach 2.9 with $\alpha = 20°$. [Figure provided by D. D. Knight.]*

agreement with measurements. Similar close agreement has been obtained with experimental data for pitot pressure and yaw angle [Knight et al. (1987)]. These results imply that the flowfield is predominantly rotational and inviscid, except within a thin region adjacent to the solid boundaries. This result is similar to the triple-deck theory developed for interacting boundary layers [e.g., Stewartson (1981)] and extended to non-separated three-dimensional shock wave, turbulent boundary layer interactions by Inger (1986). Consequently, the choice of turbulence model is unimportant for comparison with all but the inner (lower deck) provided the upstream boundary layer is correct. However, predicted skin friction and surface heat transfer are very sensitive to the turbulence model chosen, and can exhibit significant disagreement with experiment [Knight (1993)].

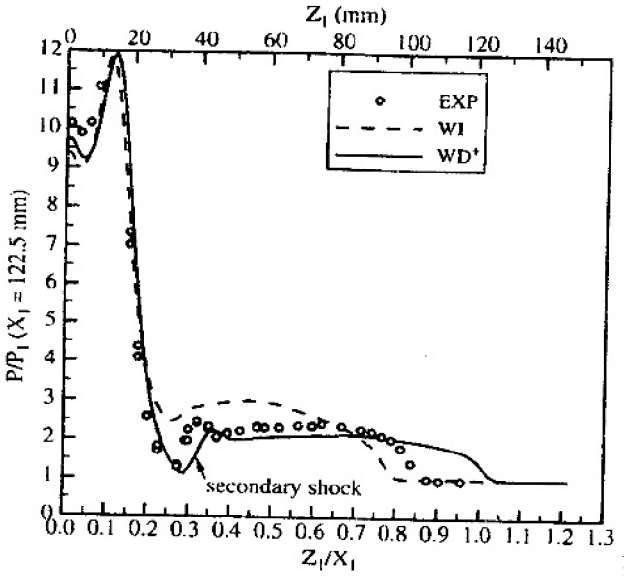

Figure 5.23: *Single-fin shock wave/boundary layer interaction at Mach 4 with* $\alpha = 30.6°$*:* — *Durbin (1996)* k-ω *model;* - - - *Wilcox (1988a)* k-ω *model;* ○ *Experiment. [Figure provided by D. D. Knight.]*

Figure 5.23 shows how the stress limiter affects k-ω model predictions for a single-fin shock-wave/boundary-layer interaction. The Mach number is 4, the fin angle is 30.6° and Reynolds number just upstream of the interaction is $Re_{\delta_o} = 1.6 \cdot 10^5$. The dashed curve labeled "WI" corresponds to the Wilcox (1988a) k-ω model, which has no stress limiter. Computed surface pressure is typically 40% higher than measured over the interaction region. The length of the region is about 10% shorter than measured. By contrast, using the Durbin (1996) k-ω model (the solid curve labeled WD$^+$), which is essentially the Wilcox (1988a) model with a $C_{lim} = 1.03$ stress limiter, differences between computed and measured surface pressures are reduced to a few percent. However, the

length of the interaction region is nearly 20% longer than measured. This is similar to the effect of C_{lim} on two-dimensional flows observed throughout Section 5.8. Using a smaller value such as $C_{lim} = 7/8$ would be likely to reduce discrepancies between computed and measured properties for this flow.

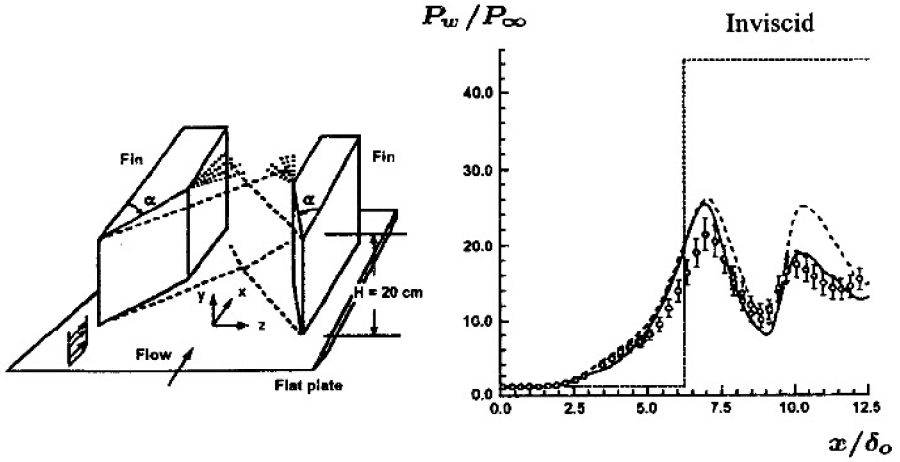

(a) Flow Geometry (b) Peak surface pressure

Figure 5.24: *Double-fin shock wave/boundary layer interaction at Mach 8.3 with* $\alpha = 15°$*:* —— *Baldwin-Lomax model;* - - - *Rodi* k-ϵ *model;* ○ *Experiment. [Figure provided by D. D. Knight.]*

Figure 5.24(a) shows the double-fin geometry. This geometry is of practical interest as it represents a geometric simplification of a hypersonic inlet using sidewall compression, or a sidewall interaction for a supersonic mixed compression inlet. The two fins generate opposing shocks that intersect on the centerline, and interact with the boundary layers on the flat plate and fin. Figure 5.24(b) compares computed [Narayanswami, Horstman and Knight (1993)] and measured peak surface pressure (on the centerline) for $M_\infty = 8.3$, $\alpha = 15°$, and $Re_{\delta_o} = 1.7 \cdot 10^5$. The turbulence models are the Baldwin-Lomax (1978) model and the Rodi (1991) version of the k-ϵ model. The predictions are reasonably close except at the peak near $x/\delta_o = 10$. Baldwin-Lomax predictions are within about 20% of measurements, while k-ϵ predictions differ by as much as 45%. It is interesting to note that the peak pressure is approximately half the theoretical inviscid level because of the viscous-inviscid interaction. Reasonable agreement is obtained between computed and measured pitot pressure and yaw-angle profiles. Comparison of computed eddy viscosity shows significant differences, however. As a result, Knight concludes that, similar to the single-fin case, the flow is predominantly rotational and inviscid, except within a thin region near the surface.

As with two-dimensional shock-wave/boundary-layer interactions, the turbulence model has a very significant effect on computed heat transfer. Figure 5.25

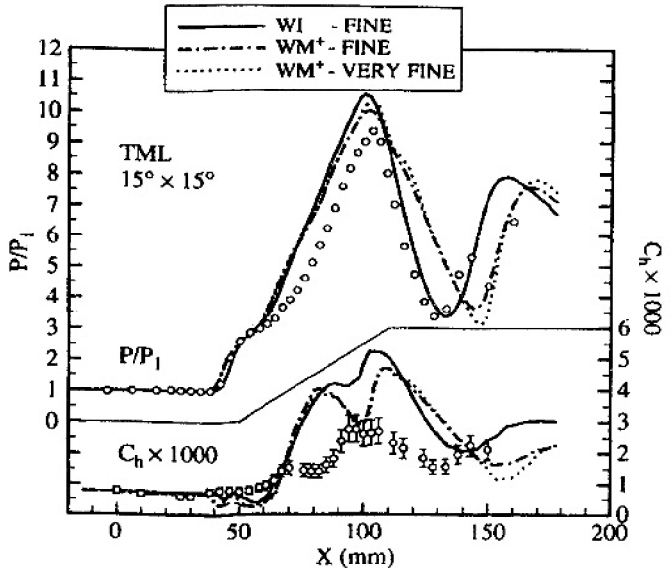

Figure 5.25: *Surface pressure and heat transfer on the throat middle line for a double-fin shock wave/boundary layer interaction at Mach 4. [Figure provided by D. D. Knight.]*

compares computed and measured surface pressure and heat transfer along the centerline for a Mach 4 double-fin flow with $\alpha = 15°$. The solid curve identified as "WI" is the Wilcox (1988a) k-ω model. While the computed pressure is arguably the best of the three curves shown, the surface heat transfer lies farthest from measurements. The maximum heat-transfer rate is double the measured value. The curves identified as "WM$^+$" correspond to the Moore and Moore (1999) version of the k-ω model with a stress limiter. As shown, the computed and measured surface heat-transfer differs significantly.

5.9 Summary

This chapter underscores the correctness of **Morkovin's hypothesis** that the effect of density fluctuations on the turbulence is small provided they remain small relative to the mean density. This is especially obvious given the close agreement between computed and measured flow properties for shock-separated flows with the Wilcox (2006) k-ω model using no special compressibility modifications.

Favre averaging simplifies the basic conservation equations and helps avoid the need to model most of the correlations involving density fluctuations. The terms that require modeling, viz., dilatation dissipation, pressure diffusion, pressure dilatation and pressure work, have been modeled based on DNS studies.

Research has shown that these DNS studies feature Reynolds numbers that are small compared to those realized in practical engineering applications. All of these terms appear to be negligible for Reynolds numbers of practical interest.

The dilatation-dissipation compressibility correction has proven useful in describing the reduced growth of a mixing layer as Mach number increases. However, the term has an adverse effect on most other flows and cannot be used for general applications.

Perturbation analysis demonstrates that the k-ϵ model does not faithfully reproduce the compressible law of the wall, even for a constant-pressure boundary layer. This failure of the model means any compressible-flow computations based on k-ϵ are highly suspect. By contrast, the k-ω model faithfully reproduces the compressible law of the wall.

Thanks to the stress-limiter concept, the Wilcox (2006) k-ω model predicts reasonably close agreement with measured properties of shock-separated flows for transonic, supersonic and hypersonic regimes. While discrepancies can be reduced even further by increasing the strength of the limiter in specific cases (i.e., by increasing C_{lim}), choosing a limiter strength of $C_{lim} = 7/8$ appears to be the optimum choice for covering the entire range of flow speeds from incompressible to hypersonic. The stress-limiter concept is generally ineffective for the k-ϵ model.

As originally formulated, the popular Spalart-Allmaras (1992) one-equation model and the Menter (1992c) k-ω/k-ϵ hybrid two-equation model are very inaccurate for supersonic and hypersonic flows. In the latter case, computations in this chapter show that the model fails for such flows because its stress limiter is too strong.

Finally, all models predict much larger than measured heat-transfer rates at a reattachment point. While the model correction introduced by Coakley and Huang (1992) appears to be effective for two-dimensional and axisymmetric flows, it does not fare as well for three-dimensional applications.

Problems

5.1 Derive the Reynolds-averaged momentum-conservation equation for compressible flow.

5.2 Derive the Favre-averaged Reynolds-stress equation [Equation (5.43)].

5.3 Verify that Equations (5.58) and (5.59) are equivalent.

5.4 The classical Crocco temperature-velocity relationship for an adiabatic-wall boundary layer is

$$\frac{\tilde{T}}{\tilde{T}_w} = 1 - A^2 \left(\frac{\tilde{u}}{U_\infty}\right)^2$$

where A is a constant. Use this approximation to evaluate the following integral.

$$u^* = \int_0^{\tilde{u}} \sqrt{\frac{\rho}{\rho_w}}\, du$$

Compare your result with Equation (5.125).

5.5 To use the WKB method in solving an equation such as

$$\frac{d^2\omega}{dv^2} + \xi \frac{f'(v)}{f(v)} \frac{d\omega}{dv} - \frac{\lambda^2}{f(v)}\omega = 0, \qquad \lambda \to \infty$$

we assume a solution of the form

$$\omega(v) \sim \exp\left[\lambda \sum_{n=0}^{\infty} S_n(v)\lambda^{-n}\right] \sim \exp\left[\lambda S_0(v) + S_1(v) + O(\lambda^{-1})\right]$$

(a) Verify that $S_0(v)$ and $S_1(v)$ are given by

$$S_0(v) = \pm \int \frac{dv}{\sqrt{f(v)}} + \text{constant}$$

$$S_1(v) = \ell n\, |f(v)|^{(1-2\xi)/4} + \text{constant}$$

(b) Use the result of Part (a) to show that the leading-order solution to Equation (5.102) is given by Equations (5.104) and (5.105).

(c) Now, complete the derivation of Equation (5.107).

5.6 Derive the compressible law of the wall implied by the Cebeci-Smith model.

5.7 Using the compressible log-layer solution, show that the turbulence length scale for the k-ω model defined by $\ell = k^{1/2}/\omega$ varies linearly with distance from the surface in the compressible log layer.

5.8 Using the compressible log-layer solution, show that the turbulence length scale for the k-ϵ model defined by $\ell = k^{3/2}/\epsilon$ varies linearly with distance from the surface in the compressible log layer.

5.9 Coakley and Huang (1992) have developed a compressibility modification for two-equation turbulence models by observing that, under rapid distortion due to sudden flow compression or expansion, the equations for k and ϵ assume the form

$$\frac{dk}{dt} \approx -\frac{2}{3}\frac{\partial \tilde{u}_i}{\partial x_i}k \qquad \text{and} \qquad \frac{d\epsilon}{dt} \approx -c\frac{\partial \tilde{u}_i}{\partial x_i}\epsilon$$

where c is a constant. If the turbulence length scale, $\ell = k^{3/2}/\epsilon$, is such that $\rho\ell$ remains constant under a sudden compression or expansion, what is the value of c?

5.10 For incompressible flow, Pope's vortex-stretching parameter is

$$\chi_P = \frac{\Omega_{ij}\Omega_{jk}S_{ki}}{(\beta^*\omega)^3}$$

For incompressible flows, this parameter vanishes in two-dimensional geometries. Verify that $\chi_P \neq 0$ in a compressible, two-dimensional flow.

5.11 The object of this problem is to deduce the jump condition on turbulence kinetic energy across a normal shock wave. For flow through a normal shock far from solid boundaries, the k-ω model's equation for k is

$$\bar{\rho}\tilde{u}\frac{dk}{dx} = \bar{\rho}\nu_T\left(\frac{d\tilde{u}}{dx}\right)^2 - \beta^*\bar{\rho}\omega k + \frac{d}{dx}\left[\left(\mu + \sigma^*\frac{\bar{\rho}k}{\omega}\right)\frac{dk}{dx}\right]$$

(a) Noting that the velocity has a step discontinuity and flow is uniform just ahead of and just behind the shock, explain why this equation simplifies to

$$\bar{\rho}\tilde{u}\frac{dk}{dx} \approx \bar{\rho}\nu_T\left(\frac{d\tilde{u}}{dx}\right)^2$$

(b) Show that, with a stress limiter, the jump condition for k across a normal shock is

$$\frac{k_2}{k_1} \approx \left(\frac{\bar{\rho}_2}{\bar{\rho}_1}\right)^{\sqrt{\beta^*}/C_{lim}}$$

(c) What is the maximum value of k_2/k_1 possible if the gas is air and $C_{lim} = 7/8$?

5.12 Using Program **MIXER** and its menu-driven setup utility, Program **MIXER_DATA** (see Appendix C), compute δ'/δ'_o at Mach 5 for the k-ω, k-ϵ and RNG k-ϵ models. That is, let the Mach number of the upper stream be $M_1 = 5$, and let the lower stream be at rest. Do your computations using 101 grid points, and exercise the program for the Sarkar, Zeman and Wilcox compressibility corrections defined in Equations (5.81) through (5.83).

5.13 The object of this problem is to compare predictions of modern turbulence models with measured properties of a Mach 2.65 turbulent boundary layer with adverse pressure gradient and surface heat transfer. The experiment to be simulated was conducted

by Fernando and Smits. Use Program **EDDYBL**, its menu-driven setup utility, Program **EDDYBL_DATA**, and the input data provided on the companion CD (see Appendix C). Do 3 computations using the k-ω model, the Launder-Sharma k-ϵ model and the Spalart-Allmaras one-equation model. Compare computed skin friction with the following measured values.

s (m)	c_f	s (m)	c_f	s (m)	c_f
1.151	$9.92 \cdot 10^{-4}$	1.248	$9.46 \cdot 10^{-4}$	1.349	$1.08 \cdot 10^{-3}$
1.172	$9.96 \cdot 10^{-4}$	1.273	$9.41 \cdot 10^{-4}$	1.361	$1.04 \cdot 10^{-3}$
1.197	$9.67 \cdot 10^{-4}$	1.299	$1.01 \cdot 10^{-3}$		
1.222	$9.43 \cdot 10^{-4}$	1.324	$1.07 \cdot 10^{-3}$		

5.14 The object of this problem is to compare predictions of modern turbulence models with measured properties of a Mach 2.2 flat-plate turbulent boundary layer. The experiment to be simulated was conducted by Shutts. Use Program **EDDYBL**, its menu-driven setup utility, **EDDYBL_DATA**, and the input data provided on the companion CD (see Appendix C). Do 3 computations using the k-ω model, the Launder-Sharma k-ϵ model and the Spalart-Allmaras model. Compare computed velocity profiles with the following measured values. Also, compare to the measured skin friction at $s = 3.02$ ft, which is $c_f = 0.00162$.

y^+	$u^*/u\tau$	y^+	$u^*/u\tau$	y^+	$u^*/u\tau$
$6.1100 \cdot 10^1$	16.056	$3.3197 \cdot 10^2$	19.064	$1.5200 \cdot 10^3$	24.527
$7.4670 \cdot 10^1$	16.069	$4.0052 \cdot 10^2$	19.838	$1.8607 \cdot 10^3$	25.544
$8.7570 \cdot 10^1$	16.030	$4.6841 \cdot 10^2$	20.580	$2.1995 \cdot 10^3$	26.445
$1.1540 \cdot 10^2$	16.030	$5.7090 \cdot 10^2$	20.962	$2.8776 \cdot 10^3$	27.749
$1.4420 \cdot 10^2$	16.030	$6.7206 \cdot 10^2$	21.360	$3.5573 \cdot 10^3$	28.056
$1.8261 \cdot 10^2$	16.961	$8.4178 \cdot 10^2$	22.098	$4.2367 \cdot 10^3$	28.081
$2.2402 \cdot 10^2$	17.894	$1.0115 \cdot 10^3$	22.764	$4.9150 \cdot 10^3$	28.105
$2.7900 \cdot 10^2$	19.218	$1.1812 \cdot 10^3$	23.423		

5.15 The object of this problem is to compare predictions of modern turbulence models with measured properties of a Mach 4.5 flat-plate turbulent boundary layer. The experiment to be simulated was conducted by Coles. Use Program **EDDYBL**, its menu-driven setup utility, **EDDYBL_DATA**, and the input data provided on the companion CD (see Appendix C). Do 3 computations using the k-ω model, the Spalart-Allmaras model and the Baldwin-Lomax algebraic model. Compare computed velocity profiles with the following measured values. Also, compare to the measured skin friction at $s = 1.90$ ft, which is $c_f = 0.00126$.

y^+	$u^*/u\tau$	y^+	$u^*/u\tau$	y^+	$u^*/u\tau$
$1.4420 \cdot 10^1$	10.295	$5.1570 \cdot 10^1$	14.990	$1.9650 \cdot 10^2$	19.893
$1.7100 \cdot 10^1$	10.972	$6.2450 \cdot 10^1$	15.472	$2.3909 \cdot 10^3$	20.951
$2.0380 \cdot 10^1$	11.713	$7.5510 \cdot 10^1$	15.968	$2.8953 \cdot 10^3$	21.951
$2.4440 \cdot 10^1$	12.456	$9.1470 \cdot 10^1$	16.559	$3.5196 \cdot 10^3$	22.523
$2.6230 \cdot 10^1$	13.182	$1.1099 \cdot 10^2$	17.258	$4.2800 \cdot 10^3$	22.540
$3.5590 \cdot 10^1$	13.848	$1.3466 \cdot 10^2$	18.052		
$4.2930 \cdot 10^1$	14.465	$1.6282 \cdot 10^2$	18.943		

5.16 Compute Samimy's Mach 2.07 flow past a backward-facing step using the Baldwin-Lomax algebraic model. Use Program **EDDY2C**, its menu-driven setup utility, Program **EDDY2C_DATA**, and the input data provided on the companion CD (see Appendix C).

(a) You must first run Program **EDDYBL** to establish flow properties at the upstream boundary. Modify the supplied input-data file *eddybl.dat*, using trial and error to adjust the "Maximum Arclength" (SSTOP) so that the Reynolds number based on momentum thickness is $1.20 \cdot 10^4$.

(b) Modify the supplied input-data file *eddy2c.dat* for Program **EDDY2C** to run the computation 500 timesteps (NEND).

(c) Make graphs of the "residual" and the value of the reattachment length, x_r/H, as functions of timestep number.

(d) Compare the value of x_r/H predicted by the Baldwin-Lomax model relative to the measured value and the value predicted by the k-ω model (see Subsection 5.8.6). Examine the surface-pressure graph provided by **EDDY2C_DATA** and comment on the quality of the solution relative to that of the k-ω model.

NOTE: This computation will take about 20 minutes of CPU time on a 3-GHz Pentium-D microcomputer.

5.17 Compute Settles' Mach 2.79 flow into a 20° compression corner using the k-ω model with viscous modifications. Use Program **EDDY2C**, its menu-driven setup utility, Program **EDDY2C_DATA**, and the input data provided on the companion CD (see Appendix C).

(a) You must first run Program **EDDYBL** to establish flow properties at the upstream boundary. After selecting the k-ω model with viscous modifications, modify the supplied input-data file *eddybl.dat*, using trial and error to adjust the "Maximum Arclength" (SSTOP) so that the Reynolds number based on momentum thickness is $9.38 \cdot 10^4$.

(b) Run **EDDY2C** and make graphs of the "residual" and the length of the separation bubble, $(x_r - x_s)/\delta_o$, as functions of timestep number.

(c) Compare the value of $(x_r - x_s)/\delta_o$ predicted by the k-ω model relative to the value predicted without viscous modifications, viz., $(x_r - x_s)/\delta_o = 1.16$.

NOTE: This computation will take about 45 minutes of CPU time on a 3-GHz Pentium-D microcomputer.

5.18 Compute Settles' Mach 2.79 flow into a 20° compression corner using the k-ω model with the Wilcox compressibility term. Use Program **EDDY2C**, its menu-driven setup utility, Program **EDDY2C_DATA**, and the input data provided on the companion CD (see Appendix C).

(a) You must first run Program **EDDYBL** to establish flow properties at the upstream boundary. After selecting the Wilcox compressibility term, modify the supplied input-data file *eddybl.dat*, using trial and error to adjust the "Maximum Arclength" (SSTOP) so that the Reynolds number based on momentum thickness is $9.38 \cdot 10^4$.

(b) Run Program **EDDY2C_DATA** and, in the "Numerics" menu, change the maximum number of timesteps (NEND) to 2000. Run **EDDY2C** with the Wilcox compressibility term and make graphs of the "residual" and the length of the separation bubble, $(x_r - x_s)/\delta_o$, as functions of timestep number.

(c) Compare the value of $(x_r - x_s)/\delta_o$ predicted by the k-ω model with the Wilcox compressibility term relative to the value predicted without the compressibility term, viz., $(x_r - x_s)/\delta_o = 1.16$. Examine the skin-friction and surface-pressure graphs provided by **EDDY2C_DATA** and comment on the quality of the solution relative to that of the k-ω model without the compressibility term.

NOTE: This computation will take about 90 minutes of CPU time on a 3-GHz Pentium-D microcomputer.

Chapter 6

Beyond the Boussinesq Approximation

The Boussinesq eddy-viscosity approximation assumes that the principal axes of the Reynolds-stress tensor, τ_{ij}, are coincident with those of the mean strain-rate tensor, S_{ij}, at all points in a turbulent flow. This is the analog of Stokes' postulate for laminar flows. The coefficient of proportionality between τ_{ij} and S_{ij} is the eddy viscosity, ν_T. Unlike the molecular viscosity which is a property of the fluid, the eddy viscosity depends upon many details of the flow under consideration. It is affected by the shape and nature (e.g., roughness height) of any solid boundaries, freestream turbulence intensity, and, perhaps most significantly, flow-history effects. Flow-history effects on τ_{ij} often persist for long distances in a turbulent flow, thus casting doubt on the validity of a simple linear relationship between τ_{ij} and S_{ij}, even for the primary shear stress. In this chapter, we examine several flows for which the Boussinesq approximation yields a completely unsatisfactory description. We then examine some of the remedies that have been proposed to provide more accurate predictions for such flows. Although our excursion into the realm beyond the Boussinesq approximation is brief, we will see how useful the analytical tools developed in preceding chapters are for even the most complicated turbulence models.

6.1 Boussinesq-Approximation Deficiencies

While models based on the Boussinesq eddy-viscosity approximation provide excellent predictions for many flows of engineering interest, there are some applications for which predicted flow properties differ greatly from corresponding measurements. Generally speaking, such models are inaccurate for flows with

sudden changes in mean strain rate and for flows with what Bradshaw (1973a) refers to as **extra rates of strain**. It is not surprising that flows with sudden changes in mean strain rate pose a problem. The Reynolds stresses adjust to such changes at a rate unrelated to mean-flow processes and time scales, so that the Boussinesq approximation must fail. Similarly, when a flow experiences extra rates of strain caused by rapid dilatation, out of plane straining, or significant streamline curvature, all of which give rise to unequal normal Reynolds stresses, the approximation again becomes suspect. Some of the most noteworthy types of applications for which models based on the Boussinesq approximation fail are:

1. flows with sudden changes in mean strain rate;
2. flow over curved surfaces;
3. flow in ducts with secondary motions;
4. flow in rotating fluids;
5. three-dimensional flows.

As an example of a flow with a sudden change in strain rate, consider the experiment of Tucker and Reynolds (1968). In this experiment, a nearly isotropic turbulent flow is subjected to uniform mean normal strain rate produced by the following mean velocity field:

$$U = \text{constant}, \qquad V = -ay, \qquad W = az \tag{6.1}$$

The coefficient a is the constant strain rate. The strain rate is maintained for a finite distance in the x direction in the experiment and then removed. The turbulence becomes anisotropic as a result of the uniform straining, and gradually approaches isotropy downstream of the point where the straining ceases. Wilcox and Rubesin (1980) have applied their k-ω^2 eddy-viscosity model to this flow to demonstrate the deficiency of the Boussinesq approximation for flows in which mean strain rate abruptly changes. Figure 6.1 compares the computed and measured distortion parameter, K, defined by

$$K \equiv \frac{\overline{v'^2} - \overline{w'^2}}{\overline{v'^2} + \overline{w'^2}} \tag{6.2}$$

As shown, when the strain rate is suddenly removed at $x \approx 2.3$ m, the model predicts an instantaneous return to isotropy, i.e., all normal Reynolds stresses become equal. By contrast, the turbulence approaches isotropy at a finite rate. Note also that the model predicts a discontinuous jump in K when the straining begins at $x = 0$. Interestingly, if the computation is extended downstream of $x = 2.3$ m without removing the strain rate, the model-predicted asymptotic

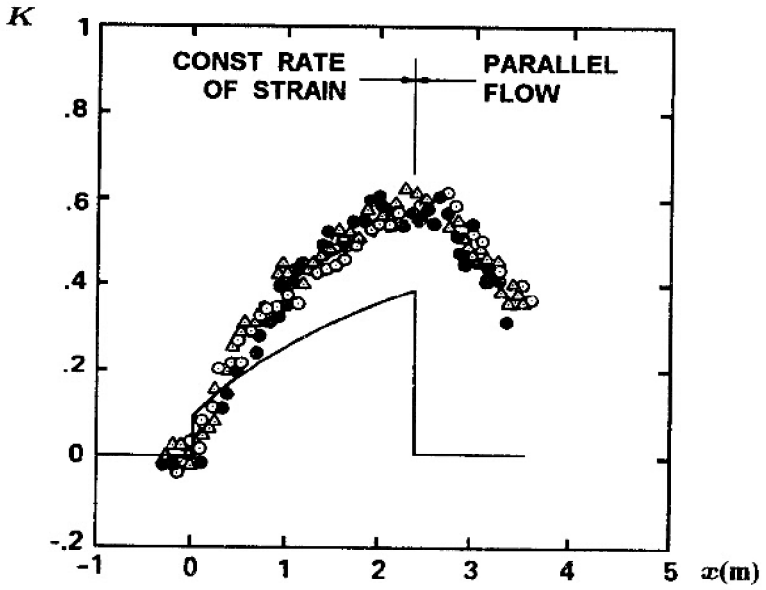

Figure 6.1: *Computed and measured distortion parameter for the Tucker-Reynolds plane-strain flow:* — *k-ω^2 model;* ○ ● △ *Tucker-Reynolds. [From Wilcox and Rubesin (1980).]*

value of K matches the measured value at $x = 2.3$ m, but approaches this value at a slower-than-measured rate.

As an example of a flow with significant streamline curvature, consider flow over a curved surface. Meroney and Bradshaw (1975), and later investigators, find that for both convex and concave walls, when the radius of curvature, $\mathcal{R}$, is 100 times the local boundary-layer thickness, δ, skin friction differs from its corresponding plane-wall value by as much as 10%. By contrast, laminar skin friction changes by about 1% for $\delta/\mathcal{R} = 0.01$. Similar results have been obtained by Thomann (1968) for supersonic boundary layers; for constant-pressure flow over surfaces with $\delta/\mathcal{R} \sim 0.02$, heat transfer changes by nearly 20%. Clearly, many practical aerodynamic surfaces are sufficiently curved to produce significant curvature effects. For such flows, a reliable turbulence model must be capable of predicting effects of curvature on the turbulence.

Standard two-equation turbulence models fail to predict any significant effect of streamline curvature. For an incompressible boundary layer on a surface with radius of curvature $\mathcal{R}$, the k equation is

$$U\frac{\partial k}{\partial x} + V\frac{\partial k}{\partial y} = \nu_T \left(\frac{\partial U}{\partial y} - \frac{U}{\mathcal{R}}\right)^2 - \epsilon + \frac{\partial}{\partial y}\left[(\nu + \sigma^* \nu_T)\frac{\partial k}{\partial y}\right] \qquad (6.3)$$

The effects of curvature appear only in the production term, and have a negligible impact on model predictions, since $(U/\mathcal{R})/(\partial U/\partial y)$ is somewhat less than $\delta/\mathcal{R}$ over most of the boundary layer.

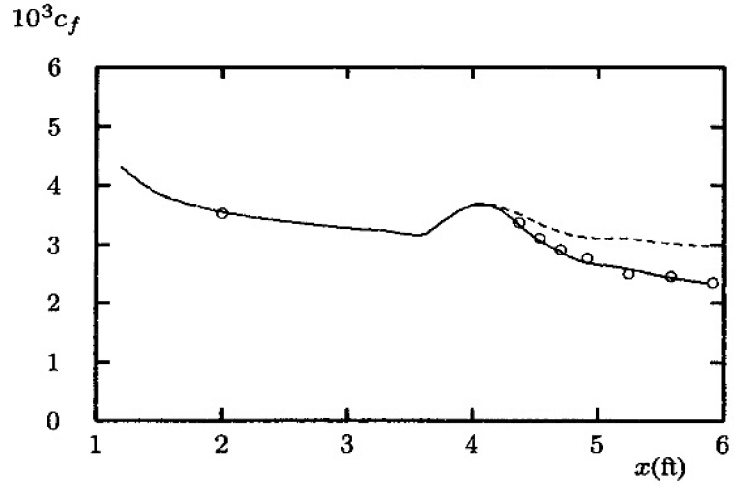

Figure 6.2: *Computed and measured skin friction for flow over a convex surface with constant pressure, Wilcox (2006) k-ω model : —— without curvature correction; - - - with curvature correction; ○ So and Mellor.*

For example, Figure 6.2 compares computed and measured skin friction for flow over a convex wall. The flow, experimentally investigated by So and Mellor (1972), has nearly constant pressure. The wall is planar up to $x = 4.375$ ft and has $\delta/\mathcal{R} \sim 0.075$ beyond that location. As shown, computed skin friction for the k-ω model (the dashed curve) is as much as 40% higher than measured.

Wilcox and Chambers (1977) propose a curvature correction to the turbulence kinetic energy equation that provides an accurate prediction for flow over curved surfaces. Appealing to the classical stability arguments for flow over a curved wall advanced by von Kármán (1934), they postulate that the equation for k should more appropriately be thought of as the equation for $\overline{v'^2}$. For flow over a curved surface, again with radius of curvature $\mathcal{R}$, the equation for $\overline{v'^2}$ is

$$U\frac{\partial \overline{v'^2}}{\partial x} + V\frac{\partial \overline{v'^2}}{\partial y} - 2\frac{U}{\mathcal{R}}\overline{u'v'} = \cdots \tag{6.4}$$

The last term on the left-hand side of Equation (6.4) results from transforming to surface-aligned coordinates.[1] Approximating $\overline{v'^2} \approx \frac{4}{9}k$ and $-\overline{u'v'} \approx \nu_T \partial U/\partial y$, Wilcox and Chambers model this effect by adding a term to the k-ω model's k equation. The boundary-layer form of the equations for flow over a curved surface is as follows.

$$U\frac{\partial U}{\partial x} + V\frac{\partial U}{\partial y} = -\frac{1}{\rho}\frac{dP}{dx} + \frac{\partial}{\partial y}\left[(\nu + \nu_T)\left(\frac{\partial U}{\partial y} - \frac{U}{\mathcal{R}}\right)\right] \tag{6.5}$$

[1]The equation for $\overline{u'^2}$ has the same term with the opposite sign and the $\overline{w'^2}$ equation has no additional curvature-related term. Thus, when we contract the Reynolds-stress equation to form the k equation, no curvature-related term appears.

$$U\frac{\partial k}{\partial x}+V\frac{\partial k}{\partial y}+\frac{9}{2}\nu_T\frac{U}{\mathcal{R}}\frac{\partial U}{\partial y}=\nu_T\left(\frac{\partial U}{\partial y}-\frac{U}{\mathcal{R}}\right)^2-\beta^*\omega k+\frac{\partial}{\partial y}\left[\left(\nu+\sigma^*\frac{k}{\omega}\right)\frac{\partial k}{\partial y}\right] \tag{6.6}$$

$$U\frac{\partial \omega}{\partial x}+V\frac{\partial \omega}{\partial y}=\alpha\left(\frac{\partial U}{\partial y}-\frac{U}{\mathcal{R}}\right)^2-\beta\omega^2+\frac{\sigma_d}{\omega}\frac{\partial k}{\partial y}\frac{\partial \omega}{\partial y}+\frac{\partial}{\partial y}\left[\left(\nu+\sigma\frac{k}{\omega}\right)\frac{\partial \omega}{\partial y}\right] \tag{6.7}$$

The last term on the left-hand side of Equation (6.6) is the Wilcox-Chambers curvature-correction term. As shown in Figure 6.2, including the curvature term brings model predictions into much closer agreement with measurements. A perturbation analysis of Equations (6.5) to (6.7) for the log layer (see problems section) shows that the model predicts a modified law of the wall given by

$$\left[1-\beta_R\frac{y}{\mathcal{R}}\right]\frac{U}{u_\tau}=\frac{1}{\kappa}\ell n\left(\frac{u_\tau y}{\nu}\right)+\text{constant} \tag{6.8}$$

with $\beta_R \approx 8.9$. This is very similar to the modified law of the wall deduced by Meroney and Bradshaw (1975), who conclude from correlation of measurements that $\beta_R \approx 12.0$.

Other curvature corrections have been proposed for two-equation models. Lakshminarayana (1986) and Patel and Sotiropoulos (1997) present comprehensive overviews. Often, in the context of the k-ϵ model, a correction term is added to the ϵ equation. Launder, Priddin and Sharma (1977), for example, replace the coefficient $C_{\epsilon 2}$ [see Equation (4.48)] by

$$C_{\epsilon 2} \rightarrow C_{\epsilon 2}\left(1-0.2Ri_T\right) \tag{6.9}$$

where Ri_T is the turbulence Richardson number defined by

$$Ri_T=\frac{2U}{\mathcal{R}\partial U/\partial y} \tag{6.10}$$

This type of correction yields improved accuracy comparable to that obtained with the Wilcox-Chambers curvature correction.

While two-equation model curvature-correction terms greatly improve predictive accuracy for flow over curved walls, they are *ad hoc* modifications that cannot be generalized for arbitrary flows. The Wilcox-Chambers curvature term is introduced by making analogy to the full Reynolds-stress equation and by assuming that k behaves more like $\overline{v'^2}$ than the turbulence kinetic energy for such flows. This implicitly assumes that a stress-transport model will naturally predict effects of streamline curvature. We will see in Section 6.3 that this can indeed be the case, at least for convex curvature.

These two applications alone are sufficient to serve as a warning that models based on the Boussinesq approximation will fail under some frequently encountered flow conditions. Such models also fail to predict secondary motions that commonly occur in straight, non-circular ducts, and in the absence of ad hoc corrections, fail to predict salient features of rotating and stratified flows. While these are more subtle and specialized applications, each failure underscores the fact that models based on the Boussinesq approximation are not universal. The following sections explore some of the proposals made to remove many of these deficiencies in a less ad hoc fashion.

6.2 Nonlinear Constitutive Relations

One approach to achieving a more appropriate description of the Reynolds-stress tensor without introducing any additional differential equations is to assume the Boussinesq approximation is simply the leading term in a series expansion of functionals. Proceeding with this premise, numerous researchers have developed such relations with varying degrees of complexity. This section sketches some of the most important progress in developing nonlinear constitutive relations.

6.2.1 The Earliest Formulations

Lumley (1970) and Saffman (1976) show that for incompressible flow the expansion must proceed through second order according to

$$\tau_{ij} = -\frac{2}{3}k\delta_{ij} + 2\nu_T S_{ij} - B\frac{k}{\omega^2}S_{mn}S_{mn}\delta_{ij} - C\frac{k}{\omega^2}S_{ik}S_{kj}$$
$$-D\frac{k}{\omega^2}\left(S_{ik}\Omega_{kj} + S_{jk}\Omega_{ki}\right) - F\frac{k}{\omega^2}\Omega_{mn}\Omega_{mn}\delta_{ij} - G\frac{k}{\omega^2}\Omega_{ik}\Omega_{kj} \qquad (6.11)$$

where B, C, D, F and G are closure coefficients, and k/ω^2 may be equivalently written as k^3/ϵ^2. Also, S_{ij} and Ω_{ij} are the mean strain-rate and rotation tensors, viz.,

$$S_{ij} = \frac{1}{2}\left(\frac{\partial U_i}{\partial x_j} + \frac{\partial U_j}{\partial x_i}\right) \quad \text{and} \quad \Omega_{ij} = \frac{1}{2}\left(\frac{\partial U_i}{\partial x_j} - \frac{\partial U_j}{\partial x_i}\right) \qquad (6.12)$$

In order to guarantee that the trace of τ_{ij} is $-2k$, we must have $B = -C/3$ and $F = -G/3$. Equation (6.11) can be simplified by requiring it to conform with certain fundamental experimental observations. In the experiment of Tucker and Reynolds (1968), for example, the normal Reynolds stresses are related approximately by

$$\tau_{xx} \approx \frac{1}{2}(\tau_{yy} + \tau_{zz}) \qquad (6.13)$$

Substituting Equations (6.1) and (6.13) into Equation (6.11) shows that necessarily $C = 0$. In addition, Ibbetson and Tritton (1975) show that homogeneous turbulence in rigid body rotation decays without developing anisotropy. This observation requires $G = 0$. Finally, if Equation (6.11) with $C = G = 0$ is applied to a classical shear layer where the only significant velocity gradient is $\partial U/\partial y$, Equation (6.13) again applies with τ_{xx} and τ_{zz} interchanged, independent of the value of D. Thus, Saffman's general expansion simplifies to:

$$\tau_{ij} = -\frac{2}{3}k\delta_{ij} + 2\nu_T S_{ij} - D\frac{k}{\omega^2}\left(S_{ik}\Omega_{kj} + S_{jk}\Omega_{ki}\right) \tag{6.14}$$

In analogy to this result, Wilcox and Rubesin (1980) propose the following simplified **nonlinear constitutive relation** for their k-ω^2 model.

$$\tau_{ij} = -\frac{2}{3}k\delta_{ij} + 2\nu_T\left(S_{ij} - \frac{1}{3}\frac{\partial U_k}{\partial x_k}\delta_{ij}\right) + \frac{8}{9}\frac{k(S_{ik}\Omega_{kj} + S_{jk}\Omega_{ki})}{(\beta^*\omega^2 + 2S_{mn}S_{mn})} \tag{6.15}$$

The term $2S_{mn}S_{mn}$ in the denominator of the last term is needed to guarantee that $\overline{u'^2}$, $\overline{v'^2}$ and $\overline{w'^2}$ are always positive. The primary usefulness of this prescription for the Reynolds-stress tensor is in predicting the normal stresses. The coefficient 8/9 is selected to guarantee

$$\overline{u'^2} : \overline{v'^2} : \overline{w'^2} = 4 : 2 : 3 \tag{6.16}$$

for the flat-plate boundary layer. Equation (6.16) is a good approximation throughout the log layer and much of the defect layer. The model faithfully predicts the ratio of the normal Reynolds stresses for boundary layers with adverse pressure gradient where the ratios are quite different from those given in Equation (6.16). Bardina, Ferziger and Reynolds (1983) have used an analog of this stress/strain-rate relationship in their Large Eddy Simulation studies.

However, the model provides no improvement for flows over curved surfaces. Also, because the nonlinear term has no effect on τ_{xy} in a classical shear layer, it would require a stress-limiter correction [cf. Equation (4.36)] to provide accurate solutions for separated flows.

Speziale (1987b) proposes a nonlinear constitutive relation for the k-ϵ model as follows (for incompressible flow):

$$\begin{aligned}\tau_{ij} = -\frac{2}{3}k\delta_{ij} + 2\nu_T S_{ij} + 4C_D C_\mu^2\frac{k^3}{\epsilon^2}\left(S_{ik}S_{kj} - \frac{1}{3}S_{mn}S_{mn}\delta_{ij}\right) \\ +4C_E C_\mu^2\frac{k^3}{\epsilon^2}\left(\mathring{S}_{ij} - \frac{1}{3}\mathring{S}_{mm}\,\delta_{ij}\right)\end{aligned} \tag{6.17}$$

where $\mathring{S}_{ij}$ is the frame-indifferent Oldroyd derivative of S_{ij} defined by

$$\mathring{S}_{ij} = \frac{\partial S_{ij}}{\partial t} + U_k\frac{\partial S_{ij}}{\partial x_k} - \frac{\partial U_i}{\partial x_k}S_{kj} - \frac{\partial U_j}{\partial x_k}S_{ki} \tag{6.18}$$

The closure coefficients C_D and C_E are given by

$$C_D = C_E = 1.68 \tag{6.19}$$

Speziale's nonlinear constitutive relation satisfies three key criteria that assure consistency with properties of the exact Navier-Stokes equation.

1. Like the Saffman and Wilcox-Rubesin models, it satisfies general coordinate and dimensional invariance.
2. It satisfies a limited form of the Lumley (1978) realizability constraints (i.e., positiveness of $k \equiv -\frac{1}{2}\tau_{ii}$).
3. It satisfies material-frame indifference in the limit of two-dimensional turbulence. The latter consideration leads to introduction of the Oldroyd derivative of S_{ij}.

The appearance of the rate of change of S_{ij} in the constitutive relation is appropriate for a viscoelastic-like medium. While, to some degree, the Speziale constitutive relation includes rate effects, it still fails to describe the gradual adjustment of the Reynolds stresses following a sudden change in strain rate. For example, consider the Tucker-Reynolds flow discussed above. The Oldroyd derivative of S_{ij} is given by

$$\overset{\circ}{S}_{yy} = \overset{\circ}{S}_{zz} = -2a^2; \qquad \text{all other } \overset{\circ}{S}_{ij} = 0 \tag{6.20}$$

When the strain rate is abruptly removed, $a = 0$ and the Speziale model predicts that the normal Reynolds stresses instantaneously return to isotropy. Hence, the model is no more realistic than other eddy-viscosity models for such flows.

For flow over a curved surface, the contribution of the nonlinear terms in the Speziale model to the shear stress is negligible. Consequently, this model, like the Wilcox-Rubesin model, offers no improvement over the Boussinesq approximation for curved-wall flows.

While the Speziale model fails to improve model predictions for flows with sudden changes in strain rate and flows with curved streamlines, it does make a dramatic difference for flow through a rectangular duct [see Figure 6.3(a)]. For such a flow, the difference between τ_{zz} and τ_{yy} according to Speziale's relation is, to leading order,

$$\tau_{zz} - \tau_{yy} = C_D C_\mu^2 \frac{k^3}{\epsilon^2} \left[\left(\frac{\partial U}{\partial z} \right)^2 - \left(\frac{\partial U}{\partial y} \right)^2 \right] \tag{6.21}$$

while, to the same order, the shear stresses are

$$\tau_{xy} = \nu_T \frac{\partial U}{\partial y}, \qquad \tau_{xz} = \nu_T \frac{\partial U}{\partial z}, \qquad \tau_{yz} = C_D C_\mu^2 \frac{k^3}{\epsilon^2} \frac{\partial U}{\partial y} \frac{\partial U}{\partial z} \tag{6.22}$$

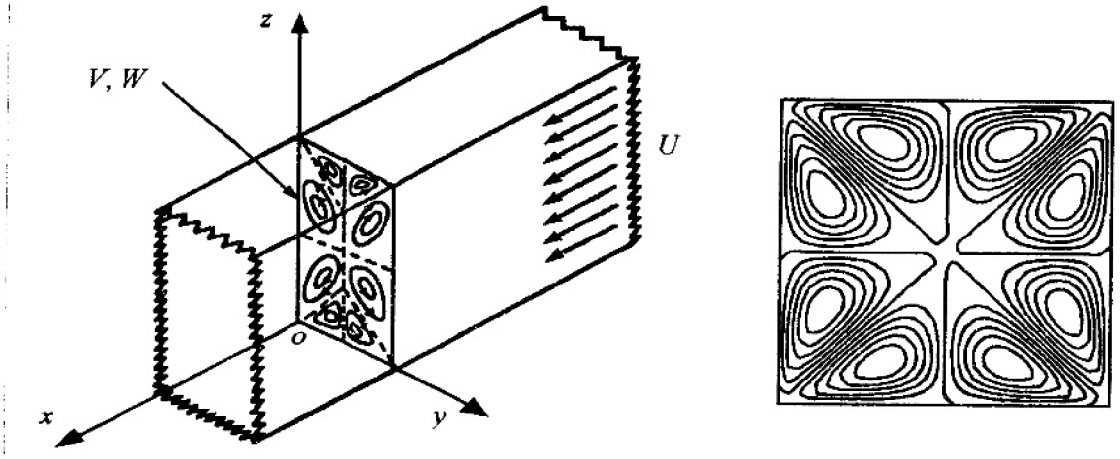

(a) Flow geometry (b) Secondary-flow streamlines

Figure 6.3: *Fully developed turbulent flow in a rectangular duct. [From Speziale (1991) — Published with the author's permission.]*

Having a difference between τ_{zz} and τ_{yy} is critical in accurately simulating secondary motions of the second kind, i.e., stress-induced motions.[2] Using his model, Speziale (1987b) has computed flow through a rectangular duct. Figure 6.3(b) shows computed secondary-flow streamlines, which clearly illustrates that there is an eight-vortex secondary-flow structure as seen in experiments. Using the Boussinesq approximation, no secondary flow develops, so that the Speziale model obviously does a better job of capturing this missing feature. Although Speziale presents no comparison of computed and measured results, the net effect of the nonlinear terms is very dramatic.

Speziale's nonlinear constitutive relation also improves k-ϵ model predictions for the backward-facing step. Focusing on the experiment of Kim, Kline and Johnston (1980), Thangam and Speziale (1992) have shown that using the nonlinear model with a low-Reynolds-number k-ϵ model increases predicted reattachment length for this flow from 6.3 step heights to 6.9 step heights. The measured length is 7.0 step heights.

6.2.2 Algebraic Stress Models

Rodi (1976) deduces a nonlinear constitutive equation by working with a model for the full Reynolds-stress equation [Equation (2.34)]. Rodi begins by approximating the convective and turbulent transport terms for incompressible flow as

[2] By contrast, secondary motions of the first kind, by definition, are pressure driven, and can be predicted by eddy-viscosity models.

proportional to the Reynolds-stress component considered, i.e.,

$$\frac{\partial \tau_{ij}}{\partial t} + U_k \frac{\partial \tau_{ij}}{\partial x_k} - \frac{\partial}{\partial x_k}\left(\nu \frac{\partial \tau_{ij}}{\partial x_k} + C_{ijk}\right) \approx \frac{\tau_{ij}}{k}\left[\frac{\partial k}{\partial t} + U_k \frac{\partial k}{\partial x_k} - \frac{\partial}{\partial x_k}\left(\nu \frac{\partial k}{\partial x_k} + \frac{1}{2} C_{jjk}\right)\right] \quad (6.23)$$

This approximation yields a nonlinear algebraic equation that can be used to determine the Reynolds-stress tensor, viz.,

$$\frac{\tau_{ij}}{k}\left\{\tau_{mn}\frac{\partial U_m}{\partial x_n} - \epsilon\right\} = -\tau_{ik}\frac{\partial U_j}{\partial x_k} - \tau_{jk}\frac{\partial U_i}{\partial x_k} + \epsilon_{ij} - \Pi_{ij} \quad (6.24)$$

With suitable closure approximations for the dissipation tensor, ϵ_{ij}, and the pressure-strain correlation tensor, Π_{ij}, Equation (6.24) defines a nonlinear constitutive relation. A model derived in this manner is known as an **Algebraic Stress Model** or, in abbreviated form, as an **ASM**.

One of the most inconvenient features of the traditional ASM is the fact that it provides **implicit** equations for the several Reynolds stresses. Also, experience has shown that such models have unpleasant mathematical behavior. Speziale (1997) explains how such models can have either multiple solutions or singularities, defects that can wreak havoc with any numerical solver.

Gatski and Speziale (1992) regard such models as strain-dependent generalizations of nonlinear constitutive relations, which can be solved explicitly to yield anisotropic eddy-viscosity models. That is, an ASM can be written in a form similar to Saffman's expansion [Equation (6.11)]. The various closure coefficients then become functions of certain Reynolds-stress tensor invariants. Such explicit algebraic stress models bear the acronym **EASM** — some authors prefer **EARSM**. The complexity of the constitutive relation depends on the closure approximations, and alternative approximations have been tried by many researchers [see Lakshminarayana (1986) or Speziale (1997)]. Gatski and Speziale describe the methodology that can be used to deduce algebraic stress models. Building on the procedures pioneered by Pope (1975), Gatski and Speziale argue that the Reynolds-stress tensor can be approximated by

$$\tau_{ij} = -\frac{2}{3}k\delta_{ij} + \frac{3}{3 - 2\eta^2 + 6\xi^2}\left[\alpha_1 \frac{k^2}{\epsilon} S_{ij} + \alpha_2 \frac{k^3}{\epsilon^2}\left(S_{ik}\Omega_{kj} + S_{jk}\Omega_{ki}\right) - \alpha_3 \frac{k^3}{\epsilon^2}\left(S_{ik}S_{kj} - \frac{1}{3}S_{mn}S_{mn}\delta_{ij}\right)\right] \quad (6.25)$$

where α_1, α_2 and α_3 are constants that depend upon the stress-transport model used. The quantities ξ and η are

$$\xi^2 = C_\xi \frac{k}{\epsilon}\sqrt{\Omega_{ij}\Omega_{ij}} \qquad \eta = C_\eta \frac{k}{\epsilon}\sqrt{S_{ij}S_{ij}} \quad (6.26)$$

with the coefficients C_ξ and C_η depending upon the ratio of production to dissipation. As it turns out, this *explicit* model, like *implicit* models, can exhibit singular behavior. Specifically, the Reynolds stresses can become infinite when

$$3 - 2\eta^2 + 6\xi^2 \to 0 \tag{6.27}$$

To remove this shortcoming, Gatski and Speziale (1992) **regularize** the relationship by using a Padé approximation [cf. Bender and Orszag (1978)] whereby

$$\frac{3}{3 - 2\eta^2 + 6\xi^2} \approx \frac{3\left(1 + \eta^2\right)}{3 + \eta^2 + 6\xi^2\eta^2 + 6\xi^2} \tag{6.28}$$

These two algebraic relations are nearly identical for turbulent flows that are close to equilibrium, i.e., for ξ and η less than 1. However, the right-hand side of Equation (6.28) remains finite for all values of ξ and η, which correspond to strongly nonequilibrium flows. Subsequently, Speziale and Xu (1996) regularize the relationship for consistency with *Rapid Distortion Theory*.[3]

When an ASM is used for a flow with zero mean strain rate, Equation (6.24) simplifies to

$$\tau_{ij} = \frac{k}{\epsilon}\left(\Pi_{ij} - \epsilon_{ij}\right) \tag{6.29}$$

As we will discuss in Subsection 6.3.1, in the limit of vanishing mean strain rate, the most common closure approximations for ϵ_{ij} and Π_{ij} simplify to

$$\Pi_{ij} \to C_1 \frac{\epsilon}{k}\left(\tau_{ij} + \frac{2}{3}k\delta_{ij}\right) \qquad \text{and} \qquad \epsilon_{ij} \to \frac{2}{3}\epsilon\delta_{ij} \tag{6.30}$$

where C_1 is a closure coefficient. Hence, when the mean strain rate vanishes, the algebraic stress model simplifies to

$$\tau_{ij} = -\frac{2}{3}k\delta_{ij} \tag{6.31}$$

This shows that algebraic stress models predict an instantaneous return to isotropy in the Tucker-Reynolds flow discussed above. Hence, like the Wilcox-Rubesin and Speziale nonlinear constitutive relations, an ASM fails to properly account for sudden changes in the mean strain rate.

Regarding secondary motions, the track record of algebraic stress models has been a bit erratic. On the one hand, So and Mellor (1978) develop an ASM that predicts most qualitative features and provides fair quantitative agreement for flows with secondary motions as shown, for example, by Demuren (1991). On the other hand, a recent study by Rung et al. (2000) cites shortcomings of

[3] The usefulness of Equation (6.28) is questionable since, as ξ and η become large, the denominator dominates and forces the Reynolds stress to zero, which will usually destabilize a computation.

ASM predictions for secondary motions. The primary difficulty originates in a closure-coefficient constraint that is not satisfied by many algebraic stress models.

One of the most successful applications of the ASM has been to flows in which streamline curvature plays a significant role. So and Mellor (1978) and Shur et al. (2000) show that excellent agreement between computed and measured flow properties is possible using an ASM for boundary layers on curved surfaces and for rotating channel flow. Jongen et al. (1998) have obtained reasonably good agreement between computed and measured properties for flow through a three-dimensional "S-duct," which is a duct with a curved-wall section.

Another successful — and particularly impressive — application is for a multi-element wing section. Figure 6.4 shows the NHLP 2D airfoil, which has been analyzed by Hellsten (2005) using a k-ω model and an EASM. Hellsten's computations were done for an angle of attack $\alpha = 20.18°$, a Mach number of 0.197 and Reynolds number based on chord length of $3.52 \cdot 10^6$.

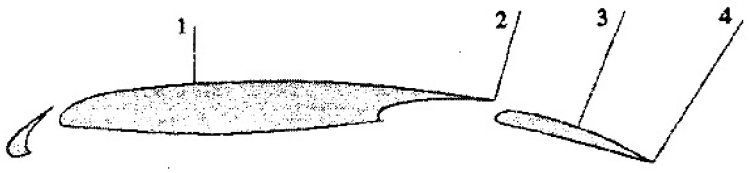

Figure 6.4: *Geometry of the NHLP 2D airfoil with lines indicating the stations where total-pressure distributions have been measured. [From Hellsten (2005) — Copyright © AIAA 2005 — Used with permission.]*

Table 6.1 summarizes computed lift and drag coefficients as tabulated by Hellsten (2005) for three k-ω models enhanced with an EASM. The table also includes results for the Wilcox (1988a) k-ω model without an EASM. Interestingly, while the three models that use an EASM predict a lift coefficient within 1% of the measured value, the Wilcox (1988a) model — without the aid of an EASM — predicts a value of C_L that is within 2% of the measured value. In two cases, this 1% reduction in difference between theory and experiment has been accomplished with a significant increase in the difference between computed and measured drag coefficient, C_D. While the k-ω model without an

Table 6.1: *Lift and Drag Coefficients for the NHLP 2D Airfoil.*

Model	EASM	C_L	Difference	C_D	Difference
Hellsten (2005) k-ω	Yes	4.06	-1.2%	0.057	-16.2%
Menter (1992c) k-ω/k-ϵ	Yes	4.09	-0.5%	0.055	-19.1%
Rumsey (1998) k-ω	Yes	4.08	-0.7%	0.068	0.0%
Wilcox (1988a) k-ω	No	4.01	-2.4%	0.071	4.4%
Measured	—	4.11	—	0.068	—

EASM predicts a drag coefficient just 4% higher than measured, the values for the Hellsten (2005) and Menter (1992c) models is 16% and 19% lower than measured, respectively. The computation by Rumsey et al. (1998) does not trade a 1% improvement in C_L for a double-digit-percent deterioration in C_D.

Figure 6.5 compares computed and measured total-pressure coefficient distributions at the four points indicated in Figure 6.4. The solid curves labeled "New k-ω + EARSM" correspond to the Hellsten (2005) model, while the dotted curves labeled "SST k-ω" are for the Menter (1992c) k-ω/k-ϵ model. Also, the dashed curves labeled "BSL k-ω + EARSM" correspond to a variant of the original Menter hybrid model. The most significant point to be gleaned from these graphs is how well the turbulence models reflect the complexity of the flow.

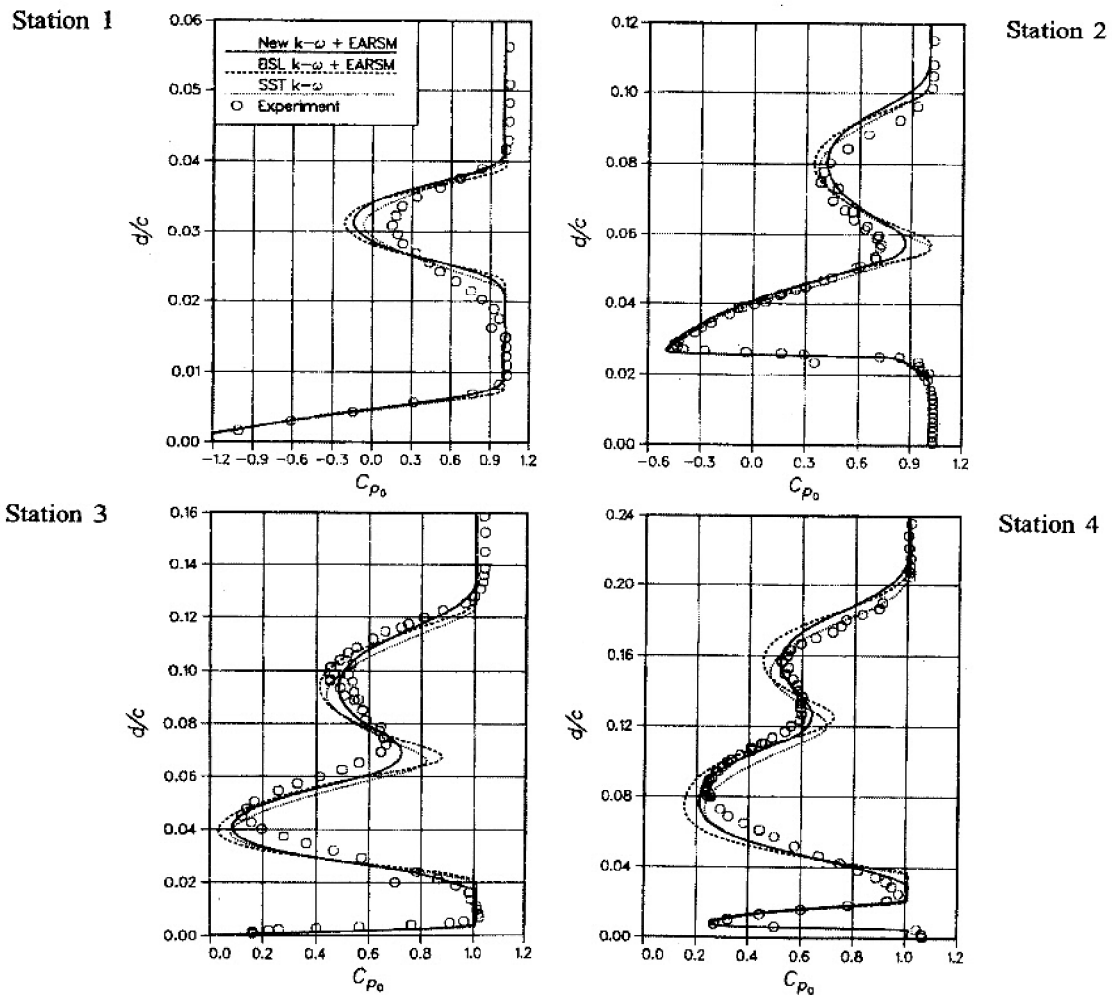

Figure 6.5: *Computed and measured total-pressure coefficients at the four stations on the NHLP 2D airfoil depicted in Figure 6.4. [From Hellsten (2005) — Copyright © AIAA 2005 — Used with permission.]*

Increasing the Mach number to 3, we find that algebraic stress model predictions are just as unreliable as the Menter (1992c) hybrid k-ω/k-ϵ model (cf. Figure 5.18) with a stress limiter. To demonstrate this point, Rizzetta (1998) has performed computations with models using an ASM for two flows. The first is the Reda-Murphy (1972) Mach 2.90 shock-wave/boundary-layer interaction. The second is the Kuntz et al. (1987) Mach 2.94 flow into a 24° compression corner. Table 6.2 summarizes the six models tested by Rizzetta, three of which use an ASM and three that do not.

Table 6.2: *Designation of Turbulence Models in Rizzetta's Computations.*

Model	ASM	Designation
Baldwin-Lomax (1978) Algebraic	No	BL
Jones-Launder (1972) k-ϵ	No	JL
Speziale-Abid (1995) k-ϵ	No	SA
Gatski-Speziale (1996) k-ϵ	Yes	GS-ARS
Shih-Zhu-Lumley (1995) k-ϵ	Yes	SZL-ARS
Craft-Launder-Suga (1996) k-ϵ	Yes	CLS-ARS

Figure 6.6 compares computed and measured surface-pressure distributions for the two flows. Clearly, all three ASM models fail to yield a satisfactory solution for either flow. To some extent, this is a reflection of the models having the k-ϵ model as their foundation. As shown in Section 5.6, this model features a distorted law of the wall for compressible flows even for the simplest of all compressible, wall-bounded flows, viz., the constant-pressure boundary layer.

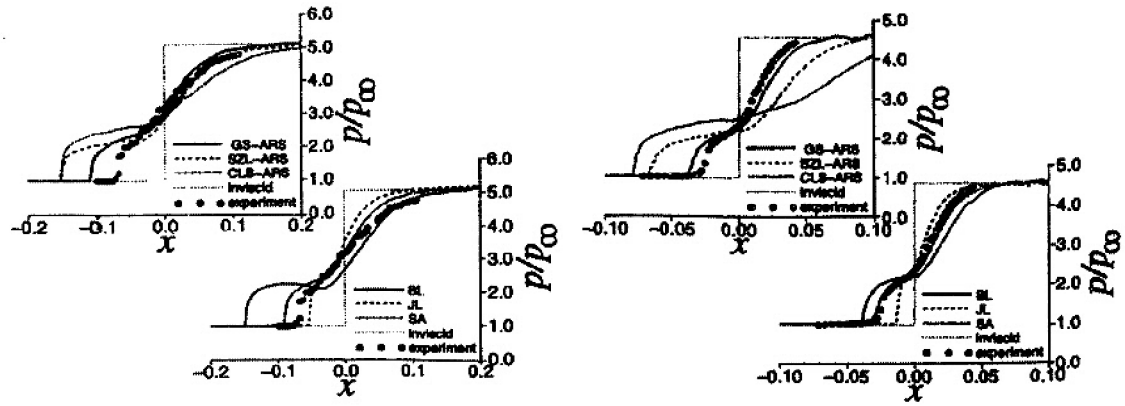

(a) Shock-Wave/Boundary-Layer Interaction (b) 24° Compression Corner

Figure 6.6: *Computed and measured surface pressure for several k-ϵ model based turbulence models. [From Rizzetta (1998) — Copyright © AIAA 1998 — Used with permission.]*

Just as a stress limiter does nothing to help correct the model's fundamental flaws for compressible flows, so whatever advantages the ASM offers are obscured by the shaky foundation provided by the k-ϵ model. As we will see in the next subsection, with the possible exception of the Craft-Launder-Suga ASM, these models should be expected to produce reasonable separation-bubble size when a k-ω model is used.

In summary, the primary advantage of nonlinear constitutive relations appears to be for flows with nontrivial streamline curvature and for predicting the anisotropy of the normal Reynolds stresses. Algebraic stress models yield greatly-improved prediction of flows with curved streamlines, both qualitatively and quantitatively. Although quantitative agreement with measurements is somewhat less satisfactory, algebraic stress models are certainly applicable to flow in ducts with secondary motions of the second kind, which models based on the Boussinesq approximation are not.

The nonlinear stress models discussed in this section have potential for improving computed results for separating and reattaching flows. However, while the improvements attending use of a nonlinear constitutive relation with two-equation models may be nontrivial, such relations cannot eliminate fundamental flaws in the model with which they are implemented. For example, in the case of an incompressible backward-facing step, while the k-ϵ model's predicted reattachment length is closer to the measured length when the Speziale, or any other, nonlinear model is used, it is not clear that a better description of the physics of this flow has been provided. After all, using the Boussinesq approximation, the k-ω model [see Section 4.10] gives an excellent backstep solution. Rizzetta's study of shock-separated flows further reinforces the fact that the k-ϵ model provides a greatly distorted mathematical representation of basic physical properties of turbulent flows that cannot be corrected with an ASM. By contrast, the excellent shock-separated flow predictions [see Section 5.8] obtained with the k-ω model assisted only with a stress limiter strongly suggest that the k-ϵ model's inaccuracy for such flows has nothing to do with the basic eddy-viscosity assumption.

6.2.3 Relation to the Stress Limiter

The shock-induced separation computations discussed in the preceding subsection reveal an interesting feature of algebraic stress models. In such flows, the dominant effect of the ASM is to limit the magnitude of the Reynolds shear stress. Huang (1999) supplies the primary evidence supporting this claim. If we write the eddy viscosity in terms of k-ϵ model variables, we have

$$\mu_T = C_\mu \frac{\rho k^2}{\epsilon} \tag{6.32}$$

Also, recall that the ratio of turbulence-energy production, P_k, to dissipation, D_k, in a thin shear layer is

$$\frac{P_k}{D_k} = \frac{\mu_T(\partial U/\partial y)^2}{\rho\epsilon} = \left[C_\mu \frac{(\partial U/\partial y)k}{\epsilon}\right]^2 \tag{6.33}$$

Huang has examined the three algebraic stress models tested by Rizzetta, viz., the models developed by Gatski and Speziale (1996), Shih, Zhu and Lumley (1995) and Craft, Launder and Suga (1996). Figure 6.7 shows the implied variation of C_μ with $C_\mu^{-1/2}\sqrt{P_k/D_k} = (\partial U/\partial y)k/\epsilon$ for these three models [UMIST corresponds to the Craft-Launder-Suga model] along with the variation of C_μ given by Menter's version of the stress limiter [denoted by SST]. Huang's observations are consistent with the notion that the leading-order effect of an ASM is to limit the Reynolds shear stress in a manner similar to what the stress limiter does.

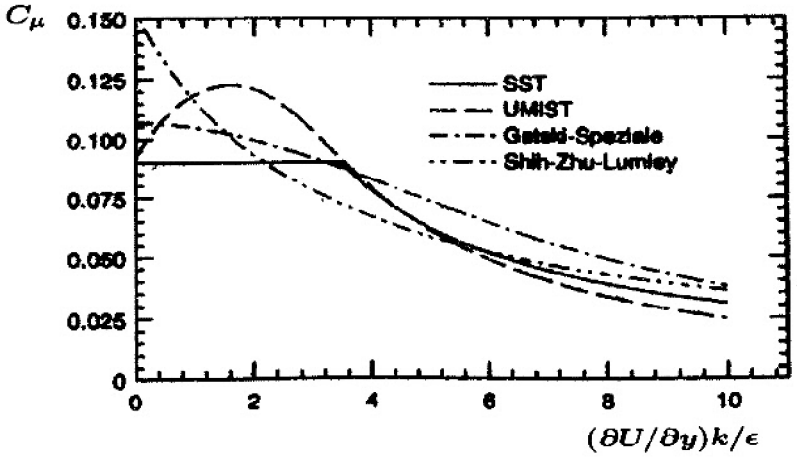

Figure 6.7: *Effective variation of C_μ with the ratio of turbulence-energy production to dissipation ratio. [From Huang (1999) — Published with the author's permission.]*

The stress limiter, in its essence, is an empirical correction to the Boussinesq approximation that greatly improves separated-flow predictions for the k-ω model.[4] Ideally, an ASM would add sufficient additional physics to improve upon the stress limiter. To get a glimpse into whether or not this is possible, it is convenient to recast our discussion in terms of k-ω model variables. In a thin shear layer, the stress limiter is [see Equation (5.73)]

$$\mu_T = \frac{\rho k}{\tilde{\omega}}, \qquad \tilde{\omega} = \max\left\{\omega, \ \frac{C_{lim}}{\sqrt{\beta^*}}\frac{\partial U}{\partial y}\right\} \tag{6.34}$$

[4] As discussed in the previous subsection, it is ineffective for the k-ϵ model.

We can compute the effective value of C_{lim} as a function of C_μ and $(\partial U/\partial y)k/\epsilon$ by noting that when the stress limiter is active,

$$\mu_T = \frac{\rho k}{\tilde{\omega}} = \frac{\rho k}{C_{lim}(\partial U/\partial y)/\sqrt{\beta^*}} = \frac{\sqrt{\beta^*}}{C_{lim}} \frac{\rho k^2}{(\partial U/\partial y)k} \tag{6.35}$$

Then, using Equation (6.32), we can solve for C_{lim}, viz.,

$$C_\mu \frac{\rho k^2}{\epsilon} = \frac{\sqrt{\beta^*}}{C_{lim}} \frac{\rho k^2}{(\partial U/\partial y)k} \quad \Longrightarrow \quad C_{lim} = \frac{\sqrt{\beta^*}}{C_\mu (\partial U/\partial y)k/\epsilon} \tag{6.36}$$

Figure 6.8 shows the implied variation of C_{lim} with $\sqrt{P_k/D_k}$ for the four models included in Figure 6.7 and for the Wilcox (2006) k-ω model. The implied C_{lim} values suggest the following regarding the three algebraic stress models.

- Since C_{lim} almost always exceeds 1.0 for the Craft-Launder-Suga ASM, it will normally yield separation bubbles at least as large as those of the Menter k-ω/k-ϵ model. Rizzetta's computations confirm this since — like Menter's model — this ASM yields separation bubbles that are about double the measured size for Mach 3 shock-separated flows.
- Since the asymptotic value of C_{lim} for large P_k/D_k is smallest for the Gatski-Speziale ASM, its separation bubbles should be the smallest of the three for shock-separated flows. Rizzetta's computations confirm this also.

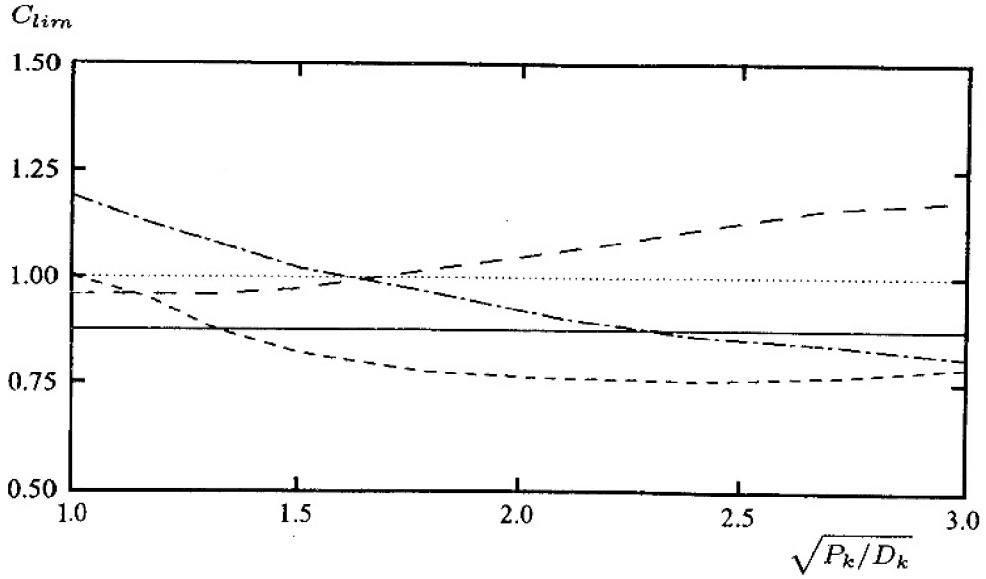

Figure 6.8: *Inferred stress-limiter strength, C_{lim}:* —— *Wilcox (2006) k-ω;* · · · *Menter;* – – *Craft-Launder-Suga;* - - - *Gatski-Speziale;* – · – *Shih-Zhu-Lumley.*

We saw in Chapters 4 and 5 that selecting a value for the stress-limiter strength, C_{lim}, equal to 1 works reasonably well for incompressible and transonic flows, but yields separation bubbles that are typically twice the measured length for supersonic and hypersonic flows. By contrast, selecting $C_{lim} = 7/8$ is a satisfactory compromise that yields acceptable separated-flow predictions from incompressible through hypersonic flow regimes. Nevertheless, numerical experimentation with the Wilcox (2006) k-ω model reveals the following.

- Using $C_{lim} = 1$ reduces discrepancies between computed and measured flow properties for axisymmetric flows, e.g., Figures 4.45, 5.13 and 5.20.
- Using $C_{lim} \approx 0.95$ reduces discrepancies between computed and measured flow properties for hypersonic flows.

By design, the Wilcox (2006) k-ω model can immediately accommodate an ASM in place of the stress limiter. This is true because its stress limiter has no impact on anything other than the Reynolds-stress tensor. For the same reason, it can serve, without modification as the foundation of a stress-transport model (Subsection 6.3.3). More research is needed to establish an algebraic stress model with sufficient generality to remove the limitations attending the otherwise successful stress limiter.

6.2.4 Lag Model

Olsen and Coakley (2001) have developed an interesting model that is reminiscent of the Shang and Hankey (1975) and Hung (1976) relaxation eddy viscosity models [see Equations (3.146) and (3.147)]. They postulate the following first-order equation for the kinematic eddy viscosity.

$$\frac{\partial \nu_T}{\partial t} + U_j \frac{\partial \nu_T}{\partial x_j} = a\omega \left(\frac{k}{\omega} - \nu_T \right), \qquad a = 0.35 \tag{6.37}$$

While this equation can be used in conjunction with any turbulence model, Olsen and Coakley have confined their applications to the Wilcox (1988a) k-ω model.[5] By introducing a lag between the "equilibrium" eddy viscosity, k/ω, and the "non-equilibrium" value, ν_T, the lag model permits adjustments to flow conditions following a fluid particle. It is thus capable of accurately describing flows with sudden changes in mean strain rate, which an ASM cannot. Model applications show that, similar to the stress limiter, it limits the magnitude of the Reynolds shear stress in strong adverse-pressure-gradient flows.

[5] To improve model predictions near a turbulent/nonturbulent interface, the lag model increases the turbulence kinetic energy diffusion coefficient σ^* from 0.5 to 1.5. The model is otherwise identical to the version presented by Wilcox (1988a).

Figure 6.9 compares computed and measured surface-pressure distributions for the Bachalo-Johnson (1979) transonic-bump experiments. The figure includes results for three freestream Mach numbers and four turbulence models, viz., the Lag model, the Wilcox (1988a) k-ω model, the Menter (1992c) k-ω/k-ϵ model and the Spalart-Allmaras one-equation model. For all three Mach numbers, the Lag model accurately predicts the location of the shock waves, and arguably provides the best overall agreement with measurements of the four models.

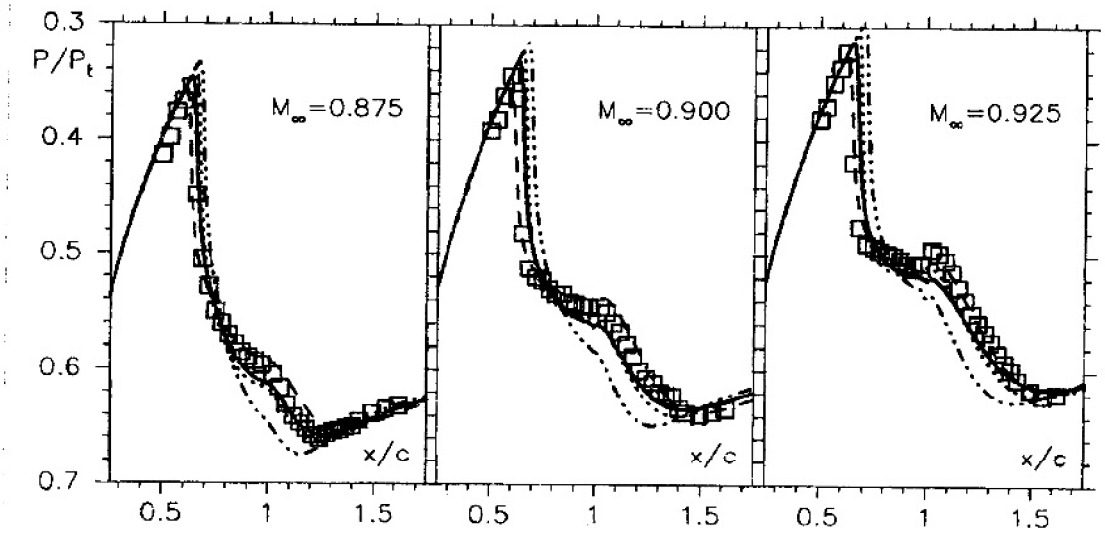

Figure 6.9: *Computed and measured surface pressure for transonic flow over a bump:* —— *Olsen-Coakley (2002) Lag model;* – · · · *Wilcox (1988a) k-ω model;* – – – *Menter (1992c) k-ω/k-ϵ model;* · · · · · *Spalart-Allmaras (1992) one-equation model. [From Olsen and Coakley (2001) — Published with the authors' permission.]*

Olsen, Lillard and Coakley (2005) have tested the lag model for several high-speed flows including the Mach 7 cylinder-flare experiment of Kussoy and Horstman (1989), an overexpanded nozzle and Mach 6 flow past the Space Shuttle Orbiter at a 40° angle of attack. In general, the lag model reduces discrepancies between predictions based on the Wilcox (1988a) k-ω model and predicts separation bubbles that are much closer to measured size than the Menter (1992c) k-ω/k-ϵ model. Most important, the surface heating rates are reasonably close to measured rates both for the Kussoy-Horstman application and for the Space Shuttle Orbiter.

While the results obtained to date are encouraging, soon-to-be-published applications to shock-separated flows at Mach 3 indicate that the model's predicted separation bubbles are significantly larger than measured. This indicates that further development and refinement of this promising approach are needed.

6.3 Stress-Transport Models

Although posing a more formidable task with regard to establishing suitable closure approximations, there are potential gains in universality that can be realized by devising a stress-transport model. In general turbulence-modeling literature, such models are often referred to as *second-order closure* or *second-moment closure* models. As we will see, stress-transport models naturally include effects of streamline curvature, sudden changes in strain rate, secondary motions, etc. We will also see that there is a significant price to be paid in complexity and computational difficulty for these gains.

Virtually all researchers use the same starting point for developing such a model, viz., the exact differential "transport" equation describing the behavior of the specific Reynolds-stress tensor, $\tau_{ij} \equiv -\overline{u_i' u_j'}$. Note that, as we have done throughout this book and consistent with common practice, we usually drop the term "specific" in referring to τ_{ij}. As shown in Chapter 2, the incompressible form of the exact equation is

$$\frac{\partial \tau_{ij}}{\partial t} + U_k \frac{\partial \tau_{ij}}{\partial x_k} = -\tau_{ik}\frac{\partial U_j}{\partial x_k} - \tau_{jk}\frac{\partial U_i}{\partial x_k} + \epsilon_{ij} - \Pi_{ij} + \frac{\partial}{\partial x_k}\left[\nu \frac{\partial \tau_{ij}}{\partial x_k} + C_{ijk}\right] \tag{6.38}$$

where

$$\Pi_{ij} = \overline{\frac{p'}{\rho}\left(\frac{\partial u_i'}{\partial x_j} + \frac{\partial u_j'}{\partial x_i}\right)} \tag{6.39}$$

$$\epsilon_{ij} = 2\nu \overline{\frac{\partial u_i'}{\partial x_k}\frac{\partial u_j'}{\partial x_k}} \tag{6.40}$$

$$\rho C_{ijk} = \rho \overline{u_i' u_j' u_k'} + \overline{p' u_i'}\delta_{jk} + \overline{p' u_j'}\delta_{ik} \tag{6.41}$$

Inspection of Equation (6.38) shows why we can expect a stress-transport model to correct some of the Boussinesq approximation's shortcomings. **First,** since the equation automatically accounts for the convection and diffusion of τ_{ij}, a stress-transport model will include effects of flow history. The dissipation and turbulent-transport terms indicate the presence of time scales unrelated to mean-flow time scales, so history effects should be more realistically represented than with a two-equation model. **Second,** Equation (6.38) contains convection, production and (optionally) body-force terms that respond automatically to effects such as streamline curvature, system rotation and stratification, at least qualitatively. Thus, there is potential for naturally representing such effects with a well-formulated stress-transport model. **Third,** Equation (6.38) gives no a priori reason for the normal stresses to be equal even when the mean strain rate vanishes. Rather, their values will depend upon initial conditions and other flow processes, so that the model should behave properly for flows with sudden changes in strain rate.

Chou (1945) and Rotta (1951) were the first to accomplish closure of the Reynolds-stress equation, although they did not carry out numerical computations. Many researchers have made important contributions since their pioneering efforts. Two of the most important conceptual contributions have been made by Donaldson and Lumley. Donaldson [cf. Donaldson and Rosenbaum (1968)] was the first to advocate the concept of **invariant modeling**, i.e., establishing closure approximations that rigorously satisfy coordinate invariance. Lumley (1978) has tried to develop a systematic procedure for representing closure approximations that guarantees **realizability**, i.e., that all physically positive-definite turbulence properties be computationally positive definite and that all computed correlation coefficients lie between ± 1. However, while being generally supportive of the concepts involved, Speziale, Abid and Durbin (1994) have cast doubt on some aspects of the Lumley approach.

6.3.1 Closure Approximations

To close Equation (6.38), we must model the dissipation tensor, ϵ_{ij}, the turbulent-transport tensor, C_{ijk}, and the pressure-strain correlation tensor, Π_{ij}. Because each of these terms is a tensor, the approximations required for closure may be much more elaborate than the approximations used for the simpler scalar and vector terms in the k equation. In this subsection, we will discuss some of the most commonly used closure approximations.

Dissipation: Because dissipation occurs at the smallest scales, most modelers use the Kolmogorov (1941) hypothesis of local isotropy, which implies

$$\epsilon_{ij} = \frac{2}{3}\epsilon\delta_{ij} \tag{6.42}$$

where

$$\epsilon = \nu\overline{\frac{\partial u_i'}{\partial x_k}\frac{\partial u_i'}{\partial x_k}} \tag{6.43}$$

The scalar quantity ϵ is the dissipation rate appearing in the turbulence kinetic energy equation of standard two-equation models. This becomes evident upon contracting Equation (6.38) to form an equation for $k = -\frac{1}{2}\tau_{ii}$. As with simpler models, we must establish a procedure for determining ϵ. In most of his work, for example, Donaldson specified ϵ algebraically, similar to what is done with a one-equation model.

As a final observation, most researchers use the ϵ equation as formulated for the k-ϵ model. Wilcox and Rubesin (1980), Wilcox (1988b) and Wilcox (1998) compute ϵ by using an equation for the specific dissipation rate, ω.

Since dissipation is in reality anisotropic, particularly close to solid boundaries, efforts have been made to model this effect. Generalizing a low-Reynolds-number proposal of Rotta (1951), Hanjalić and Launder (1976) write[6]

$$\epsilon_{ij} = \frac{2}{3}\epsilon\delta_{ij} + 2f_s\epsilon b_{ij} \tag{6.44}$$

where b_{ij} is the dimensionless **Reynolds-stress anisotropy tensor**, viz.,

$$b_{ij} = \frac{\overline{u_i'u_j'} - \frac{2}{3}k\delta_{ij}}{2k} \tag{6.45}$$

Also, f_s is a low-Reynolds-number damping function, which they choose empirically to vary with turbulence Reynolds number, $Re_T \equiv k^2/(\epsilon\nu)$, as

$$f_s = \left(1 + \frac{1}{10}Re_T\right)^{-1} \tag{6.46}$$

Turbulent Transport: As with the turbulence kinetic energy equation, pressure fluctuations, as well as triple products of velocity fluctuations, appear in the tensor C_{ijk}. Pressure fluctuations within the fluid cannot be measured with any assurance of accuracy, so there are no experimental data to provide any guidance for modeling the pressure-correlation terms. Currently-available DNS data seem to support neglecting pressure fluctuations. Traditionally, they are effectively ignored. The most common approach used in modeling C_{ijk} is to assume a gradient-transport process. Daly and Harlow (1970), argue that the simplest tensor of rank three that can be obtained from the second-order correlation τ_{ij} is $\partial\tau_{ij}/\partial x_k$, and make the following approximation.

$$C_{ijk} \propto \frac{\partial\tau_{ij}}{\partial x_k} \tag{6.47}$$

This form, although mathematically simple, is inconsistent with the fact that C_{ijk} is symmetric in all three of its indices, i.e., it is **rotationally invariant** [provided pressure fluctuations are neglected – see Equation (6.41)].

To properly reproduce the symmetry of C_{ijk}, Donaldson (1972) postulates

$$C_{ijk} \propto \frac{\partial\tau_{jk}}{\partial x_i} + \frac{\partial\tau_{ik}}{\partial x_j} + \frac{\partial\tau_{ij}}{\partial x_k} \tag{6.48}$$

This tensor has the proper symmetry, but is not dimensionally correct. We require a factor whose dimensions are length^2/time — a gradient diffusivity — and the ratio of k^2/ϵ has been employed by Mellor and Herring (1973) and Launder,

[6]Note that $b_{ii} = 0$ and $\delta_{ii} = 3$ so that Equation (6.44), like Equation (6.42), gives $\epsilon_{ii} = 2\epsilon$.

Reece and Rodi (1975). Using the notation of Launder et al., the final form of the closure approximation is

$$C_{ijk} = \frac{2}{3} C_s \frac{k^2}{\epsilon} \left[\frac{\partial \tau_{jk}}{\partial x_i} + \frac{\partial \tau_{ik}}{\partial x_j} + \frac{\partial \tau_{ij}}{\partial x_k} \right] \tag{6.49}$$

where $C_s \approx 0.11$ is a scalar closure coefficient.

Launder, Reece and Rodi also postulate a more general form based on analysis of the transport equation for C_{ijk}. Through a series of heuristic arguments, they infer the following alternative closure approximation:

$$C_{ijk} = -C_s' \frac{k}{\epsilon} \left[\tau_{im} \frac{\partial \tau_{jk}}{\partial x_m} + \tau_{jm} \frac{\partial \tau_{ik}}{\partial x_m} + \tau_{km} \frac{\partial \tau_{ij}}{\partial x_m} \right] \tag{6.50}$$

where $C_s' \approx 0.25$ is also a scalar closure coefficient. Note that optimizing C_s and C_s' implies that any pressure diffusion is combined with triple-product diffusion.

Pressure-Strain Correlation: The tensor Π_{ij} defined in Equation (6.39), which is often referred to as the **pressure-strain redistribution** term, has received the greatest amount of attention from turbulence modelers. The reason for this interest is twofold. First, being of the same order as production, the term plays a critical role in most flows of engineering interest. Second, because it involves essentially unmeasurable correlations, a great degree of ingenuity is required to establish a rational closure approximation.

To determine pressure fluctuations in an incompressible flow we must, in principle, solve the following Poisson equation for p'.

$$\frac{1}{\rho} \nabla^2 p' = -2 \frac{\partial U_i}{\partial x_j} \frac{\partial u_j'}{\partial x_i} - \frac{\partial^2}{\partial x_i \partial x_j} \left(u_i' u_j' - \overline{u_i' u_j'} \right) \tag{6.51}$$

This equation follows from taking the divergence of the Navier-Stokes equation, using the continuity equation and subtracting the time-averaged equation from the instantaneous equation.

As an aside, note that in a compressible flow, these operations lead to a transport equation for the divergence of u_i', viz., $\partial u_i'/\partial x_i$. Equation (6.51), depending upon $\partial u_i'/\partial x_i = 0$, is a degenerate case. This is consistent with the fact that pressure signals travel through a fluid at the speed of sound, which is infinite for Mach number approaching zero. Hence, we should expect the fluctuating pressure to be governed by an elliptic equation such as Equation (6.51) for incompressible flow. By contrast, pressure signals travel at finite speed in a compressible flow. Thus, we should expect the pressure fluctuations to satisfy a transport equation, which is typically hyperbolic in nature, for compressible flows.

The classical approach to solving Equation (6.51) is to write p' as the sum of two contributions, viz.,

$$p' = p'_{slow} + p'_{rapid} \tag{6.52}$$

By construction, the **slow** and **rapid** pressure fluctuations satisfy the following equations.

$$\frac{1}{\rho}\nabla^2 p'_{slow} = -\frac{\partial^2}{\partial x_i \partial x_j}\left(u'_i u'_j - \overline{u'_i u'_j}\right) \tag{6.53}$$

$$\frac{1}{\rho}\nabla^2 p'_{rapid} = -2\frac{\partial U_i}{\partial x_j}\frac{\partial u'_j}{\partial x_i} \tag{6.54}$$

The general notion implied by the nomenclature is that changes in the mean strain rate contribute immediately to p'_{rapid} because the mean velocity gradient appears explicitly in Equation (6.54). By contrast, such effects are implicitly represented in Equation (6.53). The terminology **slow** and **rapid** should not be taken too literally, however, since in real-life flows the mean strain rate does not necessarily change more rapidly than $u'_i u'_j$.

For homogeneous turbulence, these equations can be solved in terms of appropriate Green's functions, and the resulting form of Π_{ij} is

$$\Pi_{ij} = A_{ij} + M_{ijkl}\frac{\partial U_k}{\partial x_l} \tag{6.55}$$

where A_{ij} is the **slow pressure strain** and the tensor $M_{ijkl}\partial U_k/\partial x_l$ is the **rapid pressure strain**. The tensors A_{ij} and M_{ijkl} are given by the following.

$$A_{ij} = \frac{1}{4\pi}\iiint_V \overline{\left(\frac{\partial u'_i}{\partial x_j} + \frac{\partial u'_j}{\partial x_i}\right)\frac{\partial^2 (u'_k u'_l)}{\partial y_k \partial y_l}}\frac{d^3 y}{|\mathbf{x} - \mathbf{y}|} \tag{6.56}$$

$$M_{ijkl} = \frac{1}{2\pi}\iiint_V \overline{\left(\frac{\partial u'_i}{\partial x_j} + \frac{\partial u'_j}{\partial x_i}\right)\frac{\partial u'_l}{\partial y_k}}\frac{d^3 y}{|\mathbf{x} - \mathbf{y}|} \tag{6.57}$$

The integration range for Equations (6.56) and (6.57) is the entire flowfield. For inhomogeneous turbulence, the second term in Equation (6.55) becomes an integral with the mean velocity gradient inside the integrand. This emphasizes a shortcoming of single-point closure schemes that has not been as obvious in any of the closure approximations we have discussed thus far. That is, we are postulating that we can accomplish closure based on correlations of fluctuating quantities at the same physical location. The pressure-strain correlation very clearly is not a localized process, but rather, involves contributions from every point in the flow. This would suggest that two-point correlations, i.e., products of fluctuating properties at two separate physical locations, are more appropriate.

Nevertheless, we expect contributions from more than one or two large eddy sizes away to be negligible, and this would effectively define what is usually referred to as the **locally-homogeneous approximation**. Virtually all modelers assume that turbulent flows behave as though they are locally homogeneous, and use Equation (6.55).

The forms of the tensors A_{ij} and M_{ijkl} must adhere to a variety of constraints resulting from the symmetry of indices, mass conservation and other kinematic constraints. We know, for example, that the trace of Π_{ij} must vanish and this is true for the slow and rapid parts individually. Rotta (1951) postulates that the **slow pressure-strain** term, often referred to as the **return-to-isotropy** term, is given by

$$A_{ij} = C_1 \frac{\epsilon}{k} \left(\tau_{ij} + \frac{2}{3} k \delta_{ij} \right) \tag{6.58}$$

where C_1 is a closure coefficient whose value can be inferred from measurements [Uberoi (1956)] to lie in the range

$$1.4 < C_1 < 1.8 \tag{6.59}$$

Turning now to the **rapid pressure strain**, early research efforts of Donaldson [Donaldson and Rosenbaum (1968)], Daly and Harlow (1970), and Lumley (1972) assume that the rapid pressure strain is negligible compared to the slow pressure strain. However, Crow (1968) and Reynolds (1970) provide simple examples of turbulent flows for which the effect of the rapid pressure strain far outweighs the slow pressure strain.

Launder, Reece and Rodi (1975) have devised a particularly elegant closure approximation based almost entirely on kinematical considerations. Building upon the analysis of Rotta (1951), they write M_{ijkl} in terms of a tensor a_{ijkl} as follows.

$$M_{ijkl} = a_{ijkl} + a_{jikl} \tag{6.60}$$

This relation is strictly valid only for homogeneous turbulence. Rotta demonstrated that the tensor a_{ijkl} must satisfy the following *symmetry* and *normalization* constraints:

$$a_{ijkl} = a_{ljki} = a_{lkji} \qquad \text{(symmetry)} \tag{6.61}$$

$$a_{iikl} = 0, \qquad a_{ijjl} = -2\tau_{il} \qquad \text{(normalization)} \tag{6.62}$$

Launder et al. propose that the fourth-rank tensor a_{ijkl} can be expressed as a linear function of the Reynolds-stress tensor. The most general tensor, linear in τ_{ij}, satisfying the symmetry constraints of Equation (6.61) is

$$\begin{aligned} a_{ijkl} = &-\alpha \delta_{kj} \tau_{li} - \beta(\delta_{lk}\tau_{ij} + \delta_{lj}\tau_{ik} + \delta_{ik}\tau_{lj} + \delta_{ij}\tau_{lk}) \\ &-C_2 \delta_{li}\tau_{kj} + [\eta \delta_{li}\delta_{kj} + \upsilon(\delta_{lk}\delta_{ij} + \delta_{lj}\delta_{ik})]k \end{aligned} \tag{6.63}$$

where α, β, C_2, η and υ are closure coefficients. Invoking the conditions of Equation (6.62), all of the coefficients can be expressed in terms of C_2, viz.,

$$\alpha = \frac{4C_2 + 10}{11}, \quad \beta = -\frac{3C_2 + 2}{11}, \quad \eta = -\frac{50C_2 + 4}{55}, \quad \upsilon = \frac{20C_2 + 6}{55} \tag{6.64}$$

Finally, combining Equations (6.60) through (6.64), we arrive at the well-known LRR model for the rapid pressure strain.

LRR Rapid Pressure-Strain Model:

$$M_{ijkl}\frac{\partial U_k}{\partial x_l} = -\hat{\alpha}\left(P_{ij} - \frac{1}{3}P_{kk}\delta_{ij}\right) - \hat{\beta}\left(D_{ij} - \frac{1}{3}D_{kk}\delta_{ij}\right) - \hat{\gamma}kS_{ij} \tag{6.65}$$

$$P_{ij} = \tau_{im}\frac{\partial U_j}{\partial x_m} + \tau_{jm}\frac{\partial U_i}{\partial x_m} \quad \text{and} \quad D_{ij} = \tau_{im}\frac{\partial U_m}{\partial x_j} + \tau_{jm}\frac{\partial U_m}{\partial x_i} \tag{6.66}$$

$$\hat{\alpha} = \frac{8 + C_2}{11}, \quad \hat{\beta} = \frac{8C_2 - 2}{11}, \quad \hat{\gamma} = \frac{60C_2 - 4}{55}, \quad 0.4 < C_2 < 0.6 \tag{6.67}$$

Note that for compressible flows, the mean strain-rate tensor, S_{ij}, is usually replaced by $S_{ij} - \frac{1}{3}S_{kk}\delta_{ij}$ in Equation (6.65).

One of the most remarkable features of this closure approximation is the presence of just one undetermined closure coefficient, namely, C_2. The value of C_2 has been established by comparison of model predictions with measured properties of homogeneous turbulent flows. Launder, Reece and Rodi (1975) suggested using $C_2 = 0.40$. Morris (1984) revised its value upward to $C_2 = 0.50$, while Launder (1992) recommends $C_2 = 0.60$. Section 6.4 discusses the kind of flows used to calibrate this model.

Bradshaw (1973b) has shown that there is an additional contribution to Equations (6.56) and (6.57) that has a nontrivial effect close to a solid boundary. It is attributed to a surface integral that appears in the Green's function for Equation (6.51), equivalent to a volume integral over an identical "image" flowfield below the solid surface. This has come to be known as the **pressure-echo effect** or **wall-reflection effect**. Launder, Reece and Rodi (1975), and most others until recently, propose a near-wall correction to their model for Π_{ij} that explicitly involves distance from the surface. Gibson and Launder (1978), Craft and Launder (1992) and Launder and Li (1994) propose alternative models to account for the pressure-echo effect. For example, the LRR wall-reflection term, $\Pi_{ij}^{(w)}$, is

$$\Pi_{ij}^{(w)} = \left[0.125\frac{\epsilon}{k}(\tau_{ij} + \frac{2}{3}k\delta_{ij}) - 0.015(P_{ij} - D_{ij})\right]\frac{k^{3/2}}{\epsilon n} \tag{6.68}$$

where n is distance normal to the surface.

More recent efforts at devising a suitable closure approximation for Π_{ij} have focused on developing a nonlinear expansion in terms of the anisotropy tensor,

b_{ij}, defined in Equation (6.45). Lumley (1978) has systematically developed a general representation for Π_{ij} based on Equations (6.51) through (6.57). In addition to insisting upon coordinate invariance and other required symmetries, Lumley insists upon **realizability**. As noted earlier, this means that all quantities known to be strictly positive must be guaranteed to be positive by the closure model. Additionally, all computed correlation coefficients must lie between ± 1. This limits the possible form of the functional expansion for Π_{ij}. Lumley shows that the most general form of the complete tensor Π_{ij} for incompressible flow is as follows.

Lumley Pressure-Strain Model:

$$\begin{aligned}\Pi_{ij} = a_0\epsilon b_{ij} + a_1\epsilon\left(b_{ik}b_{jk} - \frac{1}{3}II\delta_{ij}\right) + a_2 k S_{ij} \\ +k\left(a_3 b_{kl}S_{lk} + a_4 b_{kl}b_{lm}S_{mk}\right)b_{ij} \\ +k\left(a_5 b_{kl}S_{lk} + a_6 b_{kl}b_{lm}S_{mk}\right)\left(b_{ik}b_{kj} - \frac{1}{3}II\delta_{ij}\right) \\ +a_7 k\left(b_{ik}S_{jk} + b_{jk}S_{ik} - \frac{2}{3}b_{kl}S_{lk}\delta_{ij}\right) \\ +a_8 k\left(b_{ik}b_{kl}S_{jl} + b_{jk}b_{kl}S_{il} - \frac{2}{3}b_{kl}b_{lm}S_{mk}\delta_{ij}\right) \\ +a_9 k\left(b_{ik}\Omega_{jk} + b_{jk}\Omega_{ik}\right) + a_{10}k\left(b_{ik}b_{kl}\Omega_{jl} + b_{jk}b_{kl}\Omega_{il}\right)\end{aligned} \tag{6.69}$$

The eleven closure coefficients are assumed to be functions of the **tensor invariants** II and III, i.e.,

$$a_i = a_i(II, III), \qquad II = b_{ij}b_{ij}, \qquad III = b_{ik}b_{kl}b_{li} \tag{6.70}$$

The tensor Ω_{ij} is the mean rotation tensor defined in Equation (6.12). The LRR model can be shown to follow from Lumley's general expression when nonlinear terms in b_{ij} are neglected, i.e., when all coefficients except a_0, a_2, a_7 and a_9 are zero.

A similar, but simpler, nonlinear model has been postulated by Speziale, Sarkar and Gatski (1991). For incompressible flows, this model, known as the **SSG** model, is as follows.

SSG Pressure-Strain Model:

$$\begin{aligned}\Pi_{ij} = -\left(C_1\epsilon + C_1^*\tau_{mn}\frac{\partial U_m}{\partial x_n}\right)b_{ij} + C_2\epsilon\left(b_{ik}b_{kj} - \frac{1}{3}b_{mn}b_{mn}\delta_{ij}\right) \\ + \left(C_3 - C_3^*\sqrt{II}\right)kS_{ij} + C_4 k\left(b_{ik}S_{jk} + b_{jk}S_{ik} - \frac{2}{3}b_{mn}S_{mn}\delta_{ij}\right) \\ +C_5 k(b_{ik}\Omega_{jk} + b_{jk}\Omega_{ik})\end{aligned} \tag{6.71}$$

$$\left.\begin{array}{llll} C_1 = 3.4, & C_1^* = 1.8, & C_2 = 4.2, & C_3 = 0.8 \\ C_3^* = 1.3, & C_4 = 1.25, & C_5 = 0.4 & \end{array}\right\} \tag{6.72}$$

Interestingly, the SSG model does not appear to require a correction for the pressure-echo effect in order to obtain a satisfactory log-layer solution.

Many other proposals have been made for closing the Reynolds-stress equation, with most of the attention on Π_{ij}. Weinstock (1981), Shih and Lumley (1985), Haworth and Pope (1986), Reynolds (1987), Shih, Mansour and Chen (1987), Fu, Launder and Tselepidakis (1987) and Craft et al. (1989) have formulated nonlinear pressure-strain correlation models.

As with the k-ϵ model, low-Reynolds-number damping functions are needed to integrate through the sublayer when the ϵ equation is used. Damping functions appear in the pressure-strain correlation tensor as well as in the dissipation. So et al. (1991) give an excellent review of stress-transport models including low-Reynolds-number corrections. Compressibility, of course, introduces an extra complication, and a variety of new proposals are being developed.

While the discussion in this subsection is by design brief, it illustrates the nature of the closure problem for stress-transport models. Although dimensional analysis combined with physical insight still plays a role, there is a greater dependence upon the formalism of tensor calculus. To some extent, this approach focuses more on the differential equations than on the physics of turbulence. This is necessary because the increased complexity mandated by having to model second and higher rank tensors makes it difficult to intuit the proper forms solely on the strength of physical reasoning. Fortunately, the arguments developed during the past decade have a stronger degree of rigor than the drastic surgery approach discussed in Subsection 4.3.2.

Increasingly, stress-transport models are being tested for nontrivial flows. The paper by Schwarz and Bradshaw (1994), for example, illustrates the actual performance of some of these models in three-dimensional boundary layers. So and Yuan (1998) test 8 two-equation models and 3 stress-transport models for flow past a backward-facing step. The studies by Parneix et al. (1998) and Gerolymos et al. (2004a, 2004b) also provide useful assessments of modern stress-transport models.

6.3.2 Launder-Reece-Rodi Model

The model devised by Launder, Reece and Rodi (1975) is the best known and most thoroughly tested stress-transport model based on the ϵ equation. Many stress-transport models are based on the LRR model and differ primarily in the closure approximation chosen for Π_{ij}. Combining the closure approximations discussed in the preceding subsection, we have the following high-Reynolds-number, compressible form of the model.

Reynolds-Stress Tensor:

$$\bar{\rho}\frac{\partial \tau_{ij}}{\partial t} + \bar{\rho}\tilde{u}_k\frac{\partial \tau_{ij}}{\partial x_k} = -\bar{\rho}P_{ij} + \frac{2}{3}\bar{\rho}\epsilon\delta_{ij} - \bar{\rho}\Pi_{ij} - C_s\frac{\partial}{\partial x_k}\left[\frac{\bar{\rho}k}{\epsilon}\left(\tau_{im}\frac{\partial \tau_{jk}}{\partial x_m} + \tau_{jm}\frac{\partial \tau_{ik}}{\partial x_m} + \tau_{km}\frac{\partial \tau_{ij}}{\partial x_m}\right)\right] \quad (6.73)$$

Dissipation Rate:

$$\bar{\rho}\frac{\partial \epsilon}{\partial t} + \bar{\rho}\tilde{u}_j\frac{\partial \epsilon}{\partial x_j} = C_{\epsilon 1}\frac{\bar{\rho}\epsilon}{k}\tau_{ij}\frac{\partial \tilde{u}_i}{\partial x_j} - C_{\epsilon 2}\frac{\bar{\rho}\epsilon^2}{k} - C_\epsilon\frac{\partial}{\partial x_k}\left[\frac{\bar{\rho}k}{\epsilon}\tau_{km}\frac{\partial \epsilon}{\partial x_m}\right] \quad (6.74)$$

Pressure-Strain Correlation:

$$\begin{aligned}\Pi_{ij} = {} & C_1\frac{\epsilon}{k}\left(\tau_{ij} + \frac{2}{3}k\delta_{ij}\right) - \hat{\alpha}\left(P_{ij} - \frac{2}{3}P\delta_{ij}\right) \\ & -\hat{\beta}\left(D_{ij} - \frac{2}{3}P\delta_{ij}\right) - \hat{\gamma}k\left(S_{ij} - \frac{1}{3}S_{kk}\delta_{ij}\right) \\ & + \left[0.125\frac{\epsilon}{k}(\tau_{ij} + \frac{2}{3}k\delta_{ij}) - 0.015(P_{ij} - D_{ij})\right]\frac{k^{3/2}}{\epsilon n}\end{aligned} \quad (6.75)$$

Auxiliary Relations:

$$P_{ij} = \tau_{im}\frac{\partial \tilde{u}_j}{\partial x_m} + \tau_{jm}\frac{\partial \tilde{u}_i}{\partial x_m}, \quad D_{ij} = \tau_{im}\frac{\partial \tilde{u}_m}{\partial x_j} + \tau_{jm}\frac{\partial \tilde{u}_m}{\partial x_i}, \quad P = \frac{1}{2}P_{kk} \quad (6.76)$$

Closure Coefficients [Launder (1992)]:

$$\left.\begin{array}{lll} \hat{\alpha} = (8 + C_2)/11, & \hat{\beta} = (8C_2 - 2)/11, & \hat{\gamma} = (60C_2 - 4)/55 \\ C_1 = 1.8, & C_2 = 0.60, & C_s = 0.11 \\ C_\epsilon = 0.18, & C_{\epsilon 1} = 1.44, & C_{\epsilon 2} = 1.92 \end{array}\right\} \quad (6.77)$$

Note that Equation (6.74) differs from the ϵ equation used with the Standard k-ϵ model [Equation (4.48)] in the form of the diffusion term. Rather than introduce an isotropic eddy viscosity, Launder, Reece and Rodi opt to use the analog of the turbulent transport term, C_{ijk}. The values of the closure coefficients in Equation (6.77) are specific to the LRR model of course, and their values are influenced by the specific form assumed for Π_{ij}. In their original paper, Launder, Reece and Rodi recommend $C_1 = 1.5$, $C_2 = 0.4$, $C_s = 0.11$, $C_\epsilon = 0.15$, $C_{\epsilon 1} = 1.44$ and $C_{\epsilon 2} = 1.90$. The values quoted in Equation (6.77) are those recommended by Launder (1992).

6.3.3 Wilcox Stress-ω Model

Not all stress-transport models use the ϵ equation to compute the dissipation. Wilcox and Rubesin (1980) postulate a stress-transport model based on their ω^2 equation and the LRR model for Π_{ij}, with $\epsilon = \beta^* \omega k$. Although the model showed some promise for flows over curved surfaces and for swirling flows, its applications were very limited. More recently, Wilcox (1988b) proposed a stress-transport model, known as the **multiscale model**, that has had a wider range of application. While the multiscale model proved to be as accurate as the k-ω model for wall-bounded flows, including separation, its equations are ill conditioned for free shear flows. Subsequently, Wilcox (1998) introduced the **Stress-ω model**, which removed the multiscale model's deficiencies.

This section introduces a revised version of the Stress-ω model. The high-Reynolds-number, compressible version of the model is as follows. Note that, by design, aside from the equation for the Reynolds-stress tensor replacing the stress-limiter, the underlying equations for k and ω are identical to those of the Wilcox (2006) k-ω model.

Reynolds-Stress Tensor:

$$\bar{\rho}\frac{\partial \tau_{ij}}{\partial t} + \bar{\rho}\tilde{u}_k \frac{\partial \tau_{ij}}{\partial x_k} = -\bar{\rho}P_{ij} + \frac{2}{3}\beta^* \bar{\rho}\omega k \delta_{ij} - \bar{\rho}\Pi_{ij} + \frac{\partial}{\partial x_k}\left[(\mu + \sigma^* \mu_T)\frac{\partial \tau_{ij}}{\partial x_k}\right] \tag{6.78}$$

Specific Dissipation Rate:

$$\bar{\rho}\frac{\partial \omega}{\partial t} + \bar{\rho}\tilde{u}_j \frac{\partial \omega}{\partial x_j} = \alpha \frac{\bar{\rho}\omega}{k}\tau_{ij}\frac{\partial \tilde{u}_i}{\partial x_j} - \beta \bar{\rho}\omega^2 + \sigma_d \frac{\bar{\rho}}{\omega}\frac{\partial k}{\partial x_j}\frac{\partial \omega}{\partial x_j} + \frac{\partial}{\partial x_k}\left[(\mu + \sigma \mu_T)\frac{\partial \omega}{\partial x_k}\right] \tag{6.79}$$

Pressure-Strain Correlation:

$$\Pi_{ij} = \beta^* C_1 \omega \left(\tau_{ij} + \frac{2}{3}k\delta_{ij}\right) - \hat{\alpha}\left(P_{ij} - \frac{2}{3}P\delta_{ij}\right) - \hat{\beta}\left(D_{ij} - \frac{2}{3}P\delta_{ij}\right) - \hat{\gamma}k\left(S_{ij} - \frac{1}{3}S_{kk}\delta_{ij}\right) \tag{6.80}$$

Auxiliary Relations:

$$\mu_T = \bar{\rho}k/\omega \tag{6.81}$$

$$P_{ij} = \tau_{im}\frac{\partial \tilde{u}_j}{\partial x_m} + \tau_{jm}\frac{\partial \tilde{u}_i}{\partial x_m}, \quad D_{ij} = \tau_{im}\frac{\partial \tilde{u}_m}{\partial x_j} + \tau_{jm}\frac{\partial \tilde{u}_m}{\partial x_i}, \quad P = \frac{1}{2}P_{kk} \tag{6.82}$$

Closure Coefficients:

$$\hat{\alpha} = (8 + C_2)/11, \quad \hat{\beta} = (8C_2 - 2)/11, \quad \hat{\gamma} = (60C_2 - 4)/55 \tag{6.83}$$

$$C_1 = \frac{9}{5}, \qquad C_2 = \frac{10}{19} \tag{6.84}$$

$$\alpha = \frac{13}{25}, \quad \beta = \beta_o f_\beta, \quad \beta^* = \frac{9}{100}, \quad \sigma = \frac{1}{2}, \quad \sigma^* = \frac{3}{5}, \quad \sigma_{do} = \frac{1}{8} \tag{6.85}$$

$$\beta_o = 0.0708, \quad \sigma_d = \begin{cases} 0, & \dfrac{\partial k}{\partial x_j}\dfrac{\partial \omega}{\partial x_j} \le 0 \\ \sigma_{do}, & \dfrac{\partial k}{\partial x_j}\dfrac{\partial \omega}{\partial x_j} > 0 \end{cases} \tag{6.86}$$

$$f_\beta = \frac{1+85\chi_\omega}{1+100\chi_\omega}, \quad \chi_\omega \equiv \left|\frac{\Omega_{ij}\Omega_{jk}\hat{S}_{ki}}{(\beta^*\omega)^3}\right|, \quad \hat{S}_{ki} = S_{ki} - \frac{1}{2}\frac{\partial \tilde{u}_m}{\partial x_m}\delta_{ki} \tag{6.87}$$

All closure coefficients shared by the k-ω and Stress-ω models have the same values. The values chosen for $\hat{\alpha}$, $\hat{\beta}$ and $\hat{\gamma}$ are those used in the original Launder, Reece and Rodi (1975) pressure-strain correlation model. This means there are two new closure coefficients to be determined, namely, C_1 and C_2.

In analyzing the Stress-ω model's sublayer predictions (see Subsection 6.6.1), we find that the constant in the law of the wall, C, depends on the values of σ and C_2. Retaining $\sigma = 1/2$ from the k-ω model, selecting $C_2 = 10/19$ yields $C \approx 5.5$ with no viscous damping functions. The traditional procedure for determining C_1 and C_2 is to appeal to measurements of homogeneous turbulent flows, which we do in the next section. Because we have selected C_2 to optimize sublayer predictions, in addressing homogeneous turbulence, we effectively seek the optimum value of C_1 that is compatible with $C_2 = 10/19$.

Unlike the LRR model, the Stress-ω model does not require a wall-reflection term such as $\Pi_{ij}^{(w)}$ defined in Equation (6.68). By design, the most significant difference between the LRR and Stress-ω models is in the scale-determining equation. The LRR model uses the ϵ equation while the Stress-ω model uses the ω equation. All other differences are minor by comparison. This strongly suggests that the end accomplished by the LRR wall-reflection term may be to mitigate a shortcoming of the model equation for ϵ rather than to correctly represent the physics of the pressure-echo process [see Parneix et al. (1998)].

Before proceeding to applications, it is worthwhile to pause and discuss two guidelines followed in formulating the Stress-ω model. **First**, a key objective is to create as simple and elegant a stress-transport model as possible. This dictates use of the LRR model for Π_{ij}, for example, but certainly does not preclude the use of a nonlinear model such as that developed by Speziale, Sarkar and Gatski (1991). Similarly, the Daly-Harlow (1970) approximation for C_{ijk} could be replaced by a rotationally-invariant form with little additional effort. **Second**, because of the k-ω model's good predictions for a wide range of turbulent flows, the Stress-ω model is designed to resemble the k-ω model to as great an extent as possible

for the flows to which both models apply. As we will see in the following sections, its predictions for free shear flows and attached boundary layers are usually within less than 5% of k-ω model predictions. Also, low-Reynolds-number modifications and surface boundary conditions for rough surfaces and for mass injection are very similar to those used with the k-ω model.

6.4 Application to Homogeneous Turbulent Flows

Homogeneous turbulent flows are useful for establishing the new closure coefficients introduced in modeling the pressure-strain correlation tensor, Π_{ij}. This is the primary type of flow normally used to calibrate a stress-transport model. Recall that homogeneous turbulence is defined as a turbulent flow that is statistically uniform in all directions. This means that the diffusion terms in all of the equations of motion are identically zero, as is the pressure-echo correction. Hence, the only difference between the ϵ-based LRR model and the ω-based Stress-ω model when applied to homogeneous turbulent flows is in the scale-determining equation. That is, both models use the LRR pressure-strain model and the Kolmogorov isotropy hypothesis for ϵ_{ij}, so that the equations for the Reynolds stresses are nearly identical, with C_2 lying within the range of values recommended for the LRR model, viz., between 0.4 and 0.6.

Additionally, since the diffusion terms vanish, the equations simplify to first-order, ordinary differential equations, which can sometimes be solved in closed form. At most, a simple Runge-Kutta integration is required. Such flows are ideal for helping establish values of closure coefficients such as C_1 and C_2 in the LRR model, provided of course that we believe the same values apply to all turbulent flows. As noted in the preceding section, we have already selected $C_2 = 10/19$ for the Stress-ω model. Hence, we seek the optimum value for C_1 compatible with this value of C_2.

The simplest of all homogeneous flows is the decay of isotropic turbulence, which we discussed in Section 4.4 and used to set the ratio of β^* to β_o for the k-ω model. The Stress-ω model equations for k and ω simplify to

$$\frac{dk}{dt} = -\beta^* \omega k \qquad \text{and} \qquad \frac{d\omega}{dt} = -\beta_o \omega^2 \tag{6.88}$$

For large time, the asymptotic solution for k according to the Stress-ω and LRR models is given by

$$k \sim t^{-\beta^*/\beta_o} \qquad \text{and} \qquad k \sim t^{-1/(C_{\epsilon 2}-1)} \tag{6.89}$$

Experimental observations summarized by Townsend (1976) indicate that turbulence energy varies according to $k \sim t^{-n}$ where $n = 1.25 \pm 0.06$ for decaying

homogeneous, isotropic turbulence. Hence, we can conclude that our closure coefficients must lie in the following ranges.

$$1.19 < \beta^*/\beta_o < 1.31, \qquad 1.76 < C_{\epsilon 2} < 1.84 \tag{6.90}$$

The Stress-ω model's chosen values for β_o and β^* [Equations (6.85) and (6.86)] give $\beta^*/\beta_o = 1.27$, which satisfies Equation (6.90). However, the value chosen for $C_{\epsilon 2}$ in the LRR model is 1.92, which lies outside the range indicated in Equation (6.90).

Figures 6.10(a) and (b) compare computed and measured k for decaying homogeneous, isotropic turbulence as predicted by the Stress-ω model. The experimental data in (a) and (b) are those of Comte-Bellot and Corrsin (1971) and Wigeland and Nagib (1978), respectively.

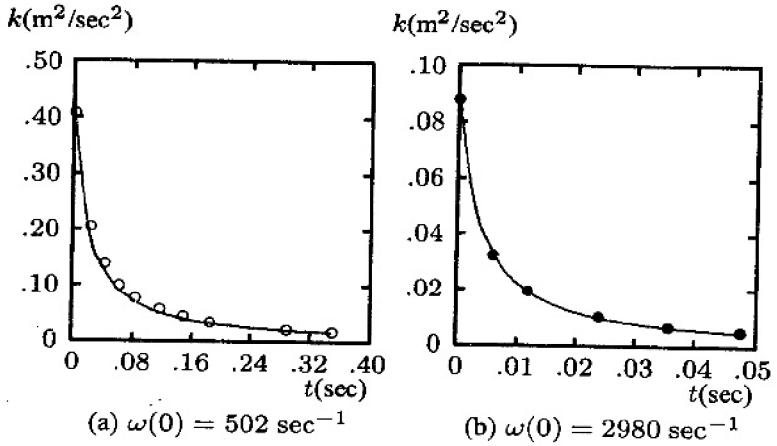

Figure 6.10: *Computed and measured decay of turbulence energy for homogeneous, isotropic turbulence: — Wilcox (2006) Stress-omega model; ○ Comte-Bellot and Corrsin (1971); • Wigeland and Nagib (1978).*

Because the equations we solve for homogeneous shear flows are initial-value problems, the entire solution is affected by the assumed initial conditions, especially the initial value of ϵ or ω. Estimates of the initial dissipation rate, ϵ_o, are often quoted for homogeneous turbulence experiments. However, any errors in these estimates can have a large effect on the solution at all subsequent times. An alternative method for setting initial conditions is to estimate ϵ_o from the differential equation for k at the initial station. In the case of homogenous isotropic turbulence, this means

$$\epsilon_o = -\left(\frac{dk}{dt}\right)_o \qquad \text{or} \qquad \omega_o = -\frac{1}{\beta^*}\left(\frac{1}{k}\frac{dk}{dt}\right)_o \tag{6.91}$$

The initial value of ω has been selected to match the initial shape of the measured curves for the two cases, and the inferred values are quoted in Figure 6.10. Computed and measured values of k are within 5% for both cases.

The second type of homogeneous turbulent flow that is useful for establishing the value of pressure-strain correlation closure coefficients is decaying, anisotropic turbulence. Such flows are created in the laboratory, for example, by subjecting turbulence to uniform strain-rate, which yields unequal normal Reynolds stresses. The turbulence then enters a region free of strain, and gradually returns to isotropy. The Tucker-Reynolds (1968) experiment that we discussed in Section 6.1 is an example of this type of flow (see Figure 6.1).

Because the mean strain rate is zero, the rapid pressure-strain term vanishes. Then, assuming dissipation follows the Kolmogorov (1941) isotropy hypothesis [Equation (6.42)], and using Rotta's (1951) slow pressure-strain term [Equation (6.58)], the Reynolds-stress equation written in terms of ϵ is

$$\frac{d\tau_{ij}}{dt} = \frac{2}{3}\epsilon\delta_{ij} - C_1\frac{\epsilon}{k}\left(\tau_{ij} + \frac{2}{3}k\delta_{ij}\right) \tag{6.92}$$

If the scale-determining equation is for ω rather than for ϵ, we simply replace $C_1\epsilon/k$ by $C_1\beta^*\omega$. The solutions according to the LRR and Stress-ω models are

$$\frac{\tau_{ij} + \frac{2}{3}\rho k\delta_{ij}}{\left(\tau_{ij} + \frac{2}{3}\rho k\delta_{ij}\right)_o} = \left(\frac{k_o\epsilon}{k\epsilon_o}\right)^{C_1/(C_{\epsilon 2}-1)} = \left(\frac{\omega}{\omega_o}\right)^{C_1\beta^*/\beta_o} \tag{6.93}$$

where subscript o denotes initial value. Measurements of decaying anisotropic turbulence have been used to determine the closure coefficient C_1. The data of Uberoi (1956), for example, indicate that C_1 lies between 1.4 and 1.8 [see Equation (6.59)]. More recent experiments such as those of Le Penven et al. (1984) further confirm that C_1 lies in this range.

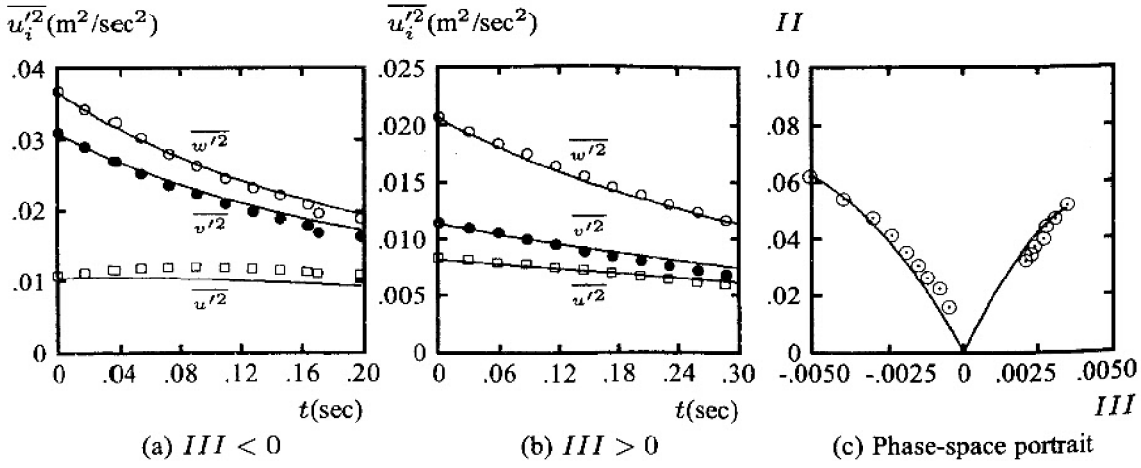

Figure 6.11: *Comparison of computed and measured decay of Reynolds stresses for homogeneous, anisotropic turbulence:* — *Wilcox (2006) Stress-omega model;* ▫, ●, ○, ⊙ *Le Penven et al. ($\overline{u'^2}$, $\overline{v'^2}$, $\overline{w'^2}$, II).*

Figure 6.11 compares computed normal Reynolds stresses with the measurements of Le Penven et al. for decaying homogeneous, anisotropic turbulence as predicted by the Stress-ω model. The figure presents results in terms of the Reynolds-stress anisotropy second and third tensor invariants, II and III, defined by [see Equations (6.45) and (6.70)]

$$II = b_{ij}b_{ij} \quad \text{and} \quad III = b_{ik}b_{kl}b_{li} \qquad \text{where} \qquad b_{ij} \equiv \frac{\overline{u_i'u_j'} - \frac{2}{3}k\delta_{ij}}{2k} \tag{6.94}$$

Parts (a) and (b) of the figure correspond to III assuming negative and positive values, respectively. Part (c) displays II as a function of III, which is generally referred to as the **phase-space portrait** for this type of flow. As shown, differences between theory and experiment are small, indicating that $C_1 = 1.8$ is optimum for the Stress-ω model.

Figure 6.12(a) compares computed and measured [Choi and Lumley (1984)] normal components of the Reynolds-stress anisotropy tensor, b_{ij}. This experiment is similar to that of Tucker and Reynolds, with turbulence initially subjected to plain strain and then returning to isotropy after the strain is removed. Figure 6.12(b) shows the phase-space portrait of the return-to-isotropy problem, plotted as $II^{1/2}$ versus $III^{1/3}$. As shown, $II^{1/2}$ is essentially a linear function of $III^{1/3}$ for this flow according to the LRR model. This computation has been done with the original LRR coefficients, i.e., those corresponding to $C_1 = 1.5$.

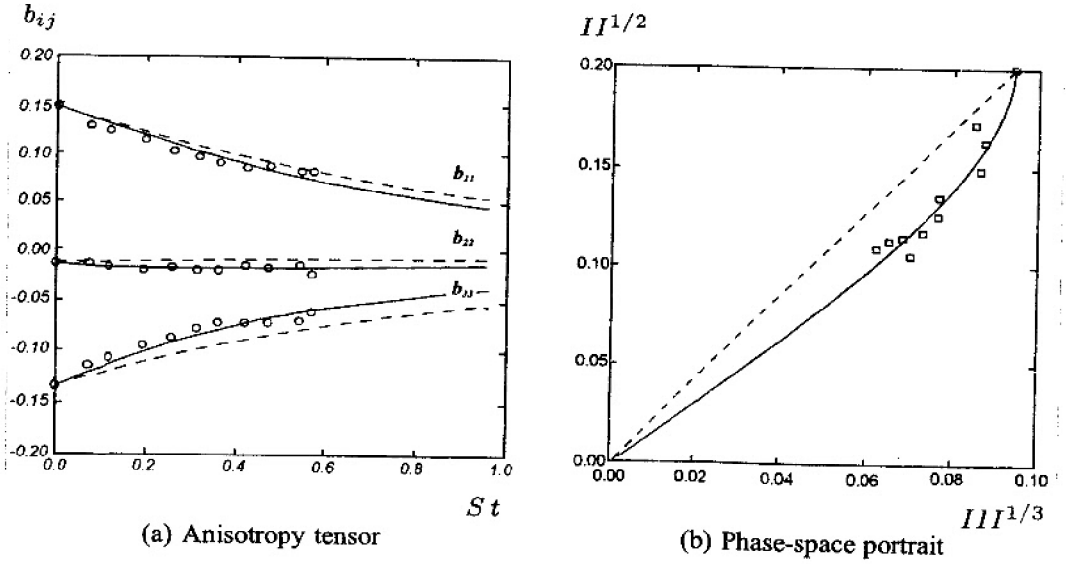

(a) Anisotropy tensor (b) Phase-space portrait

Figure 6.12: *Comparison of computed and measured anisotropy tensor and phase-space portrait for homogeneous, anisotropic turbulence: - - - LRR model; —— Sarkar-Speziale model; ○, □ Choi and Lumley. [From Speziale and So (1996) — Published with the authors' permission.]*

While discrepancies between computed and measured stresses are satisfactory, even closer agreement between theory and experiment can be obtained with a nonlinear model for the slow pressure-strain model. Sarkar and Speziale (1990), for example, propose a simple quadratic model for the slow pressure-strain, i.e.,

$$A_{ij} = -C_1 \epsilon b_{ij} + C_2 \epsilon \left(b_{ik} b_{kj} - \frac{1}{3} b_{mn} b_{mn} \delta_{ij} \right) \tag{6.95}$$

where $C_1 = 3.4$ and $C_2 = 4.2$ [see Equation (6.71)]. Figures 6.12(a) and (b) compare computed and measured anisotropy tensor components and phase-space portraits. The nonlinear model clearly falls within the scatter of the experimental data, while the LRR model prediction provides a less satisfactory description. The phase-space portrait is especially revealing, with the nonlinear model faithfully reflecting the nonlinear variation of $II^{1/2}$ with $III^{1/3}$.

Homogeneous turbulence experiments have also been performed that include irrotational plane strain [Townsend (1956) and Tucker and Reynolds (1968)] and uniform shear [Champagne, Harris and Corrsin (1970), Harris, Graham and Corrsin (1977), Tavoularis and Corrsin (1981), and Tavoularis and Karnik (1989)]. These flows can be used to establish closure coefficients such as C_2 in the LRR pressure-strain model. The velocity gradient tensor for these flows is

$$\frac{\partial U_i}{\partial x_j} = \begin{bmatrix} 0 & S & 0 \\ 0 & -a & 0 \\ 0 & 0 & a \end{bmatrix} \tag{6.96}$$

where a is the constant strain rate and S is the constant rate of mean shear.

While closed form solutions generally do not exist when mean strain rate and/or shear are present, analytical progress can be made for the asymptotic forms in the limit $t \to \infty$. In general, the specific dissipation rate, $\omega \sim \epsilon/k$, approaches a constant limiting value while k and the Reynolds stresses grow exponentially. Assuming solutions of this form yields closed-form expressions for the Reynolds stresses.

Using such analysis for uniform shear ($a = 0, S \neq 0$), Abid and Speziale (1993) have analyzed the LRR and SSG pressure-strain models and two nonlinear pressure-strain models developed by Shih and Lumley (1985) [SL model] and by Fu, Launder and Tselepidakis (1987) [FLT model]. Table 6.3 summarizes their results, along with results for the Stress-ω model and asymptotic values determined experimentally by Tavoularis and Karnik (1989). Inspection of the table shows that the SSG model most faithfully reproduces measured asymptotic values of the Reynolds stresses.

The parameter Sk/ϵ is the ratio of the turbulence time scale, ϵ/k, to the mean-flow time scale as represented by the reciprocal of S. Inspection of the table shows that the Stress-ω model predicts a value for Sk/ϵ that is within less

than 2% of the measured value, closest of the models tested. While the LRR model is also very close with the predicted and measured values differing by 3.4%, the SL, FLT and SSG models all differ by at least 10% and by as much as 49%. This is important because all of the other models use the ϵ equation, which plays a role in determining the time scale of the various physical processes represented in the Reynolds-stress equation. Errors associated with the ϵ equation clearly have an adverse impact on the balance of these physical processes.

Table 6.3: *Anisotropy-Tensor Limiting Values for Uniform Shear.*

Property	Stress-ω	LRR	SL	FLT	SSG	Measured
b_{xx}	0.142	0.152	0.120	0.196	0.218	0.210
b_{xy}	-0.156	-0.186	-0.121	-0.151	-0.164	-0.160
b_{yy}	-0.137	-0.119	-0.122	-0.136	-0.145	-0.140
b_{zz}	-0.005	-0.033	0.002	-0.060	-0.073	-0.070
Sk/ϵ	4.861	4.830	7.440	5.950	5.500	5.000

Note that the anisotropy tensor is proportional to the difference between the Reynolds-stress tensor and $\frac{2}{3}k$. Hence, percentage differences between computed and measured values of b_{ij} present an exaggerated estimate of the differences between computed and measured Reynolds stresses. For example, the SL model-predicted value of b_{xx} is 43% smaller than the measured value. However, this corresponds to a difference between computed and measured $\overline{u'^2}$ of only 17%.

Figure 6.13 compares Stress-ω model Reynolds stresses and corresponding measured values for the Tavoularis and Karnik (1989) uniform-shear experiments with $S = 29.0$ sec^{-1}, 39.9 sec^{-1} and 84.0 sec^{-1}. The initial values used for ω

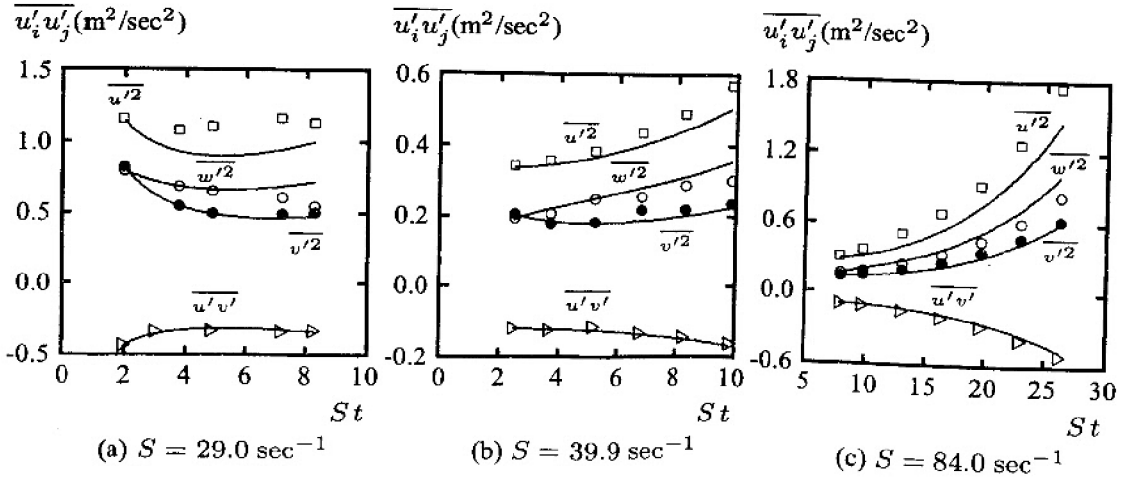

(a) $S = 29.0$ sec^{-1} (b) $S = 39.9$ sec^{-1} (c) $S = 84.0$ sec^{-1}

Figure 6.13: *Computed and measured Reynolds stresses for homogeneous, plane shear: —— Wilcox (2006) Stress-ω model; □, ●, ○, ▷ Tavoularis and Karnik ($\overline{u'^2}$, $\overline{v'^2}$, $\overline{w'^2}$, $\overline{u'v'}$).*

correspond to having $Sk_o/\epsilon_o = S/(\beta^*\omega_o)$ equal to 1.86, 3.10 and 3.81, respectively. Consistent with the asymptotic results summarized in Table 6.3, computed values of $\overline{uv}$ and $\overline{v'^2}$ are very close to measurements, while computed $\overline{u'^2}$ and $\overline{w'^2}$ values are generally 10% below and above measurements, respectively.

Turning to flows with irrotational strain rate ($a \neq 0, S = 0$), Figures 6.14(a) and (b) compare Stress-ω model and measured [Townsend (1956) and Tucker and Reynolds (1968), respectively] Reynolds stresses. The strain rate for the Townsend case is $a = 9.44$ sec^{-1} (with $ak_o/\epsilon_o = 0.57$), while that of the Tucker-Reynolds case is $a = 4.45$ sec^{-1} (with $ak_o/\epsilon_o = 0.49$). Launder, Reece and Rodi (1975) report very similar results for the Tucker-Reynolds case.

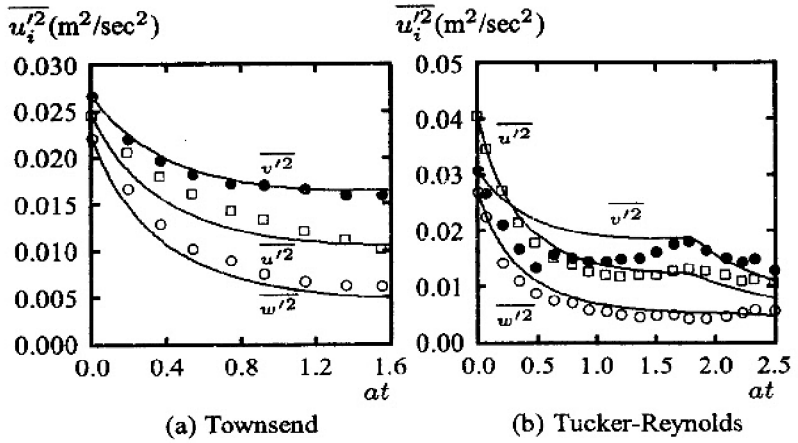

Figure 6.14: *Computed and measured Reynolds stresses for homogeneous, plane strain:* — *Wilcox (2006) Stress-ω model;* □, •, ○ *Experiment ($\overline{u'^2}$, $\overline{v'^2}$, $\overline{w'^2}$).*

To illustrate how much of an improvement stress-transport models make for flows with sudden changes in mean strain rate, Figure 6.15 compares measured distortion parameter, K, for the Tucker-Reynolds experiment with computed results obtained using the Stress-ω model and the Wilcox-Rubesin (1980) k-ω^2 model. As shown, the Stress-ω model predicts a gradual approach to isotropy and the computed K more closely matches the experimental data.

6.5 Application to Free Shear Flows

While stress-transport models eliminate many of the shortcomings of the Boussinesq eddy-viscosity approximation, they are not necessarily more accurate than two-equation models for free shear flows. This is true because the scale determining equation (ω, ϵ, ℓ, etc.) used by a stress-transport model plays a key role. For example, the Wilcox (1988b) multiscale model uses the ω equation of the Wilcox (1988a) k-ω model. Just as the spreading rates of this k-ω model are

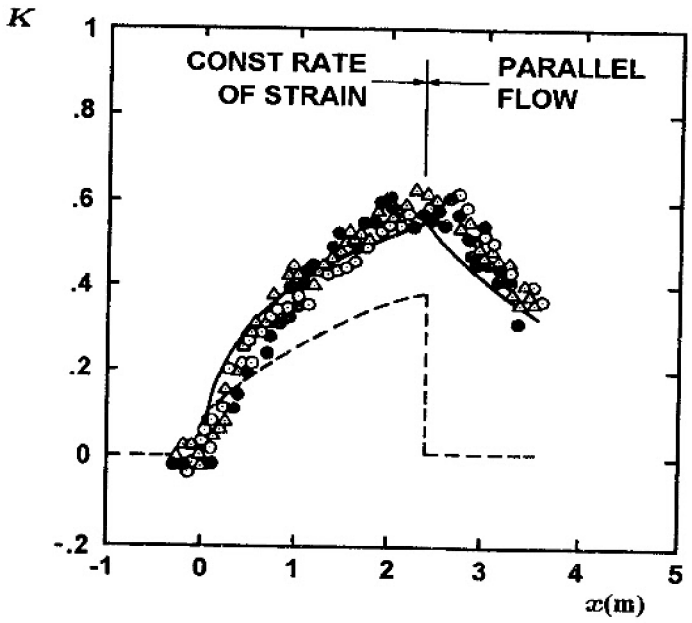

Figure 6.15: *Computed and measured distortion parameter for the Tucker-Reynolds plane-strain flow:* — *Wilcox (2006) Stress-ω model;* - - - *Wilcox-Rubesin (1980) k-ω^2 model;* ○ ● △ *Tucker-Reynolds.*

significantly larger than measured (see Table 4.5), so are those predicted by the multiscale model. Other shortcomings, such as the round-jet/plane-jet anomaly, also carry through from two-equation models to stress-transport models.

Table 6.4 summarizes computed and measured spreading rates for the LRR model and the Stress-ω model. Comparison with Table 4.4 shows that the Stress-ω model predicts spreading rates similar to those of the Wilcox (2006) k-ω model. The average difference between computed and measured spreading rates is 4%. Thus, the Stress-ω model provides credible solutions for plane, round and radial jets. The LRR model's spreading rates are roughly 10% larger than those of the Standard k-ϵ model [cf. Table 4.4]. As noted by Launder

Table 6.4: *Free Shear Flow Spreading Rates for the Stress-ω and LRR Models.*

Flow	Stress-ω Model	LRR Model	Measured
Far Wake	0.331	—	0.320-0.400
Mixing Layer	0.096	0.104	0.103-0.120
Plane Jet	0.110	0.123	0.100-0.110
Round Jet	0.091	0.135	0.086-0.096
Radial Jet	0.097	—	0.096-0.110

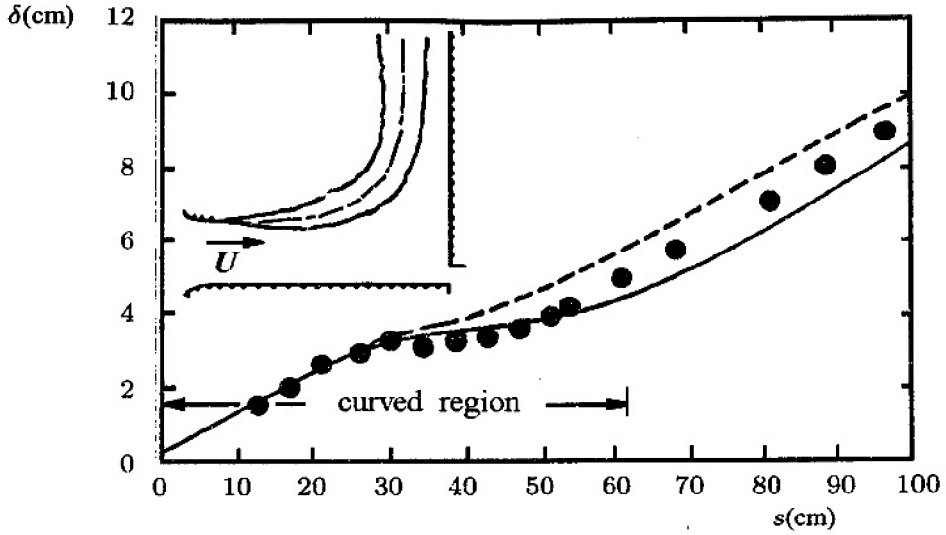

Figure 6.16: *Comparison of computed and measured width for a curved mixing layer: —— LRR model; - - - Standard k-ϵ model; • Castro and Bradshaw. [From Rodi (1981) — Copyright © AIAA 1981 — Used with permission.]*

and Morse (1979), because the predicted round-jet spreading rate exceeds the predicted plane-jet spreading rate, the LRR model fails to resolve the round-jet/plane-jet anomaly.

Figure 6.16 compares computed and measured width of a curved mixing layer. The computation was done using the LRR model [Rodi (1981)], and the measurements correspond to an experiment of Castro and Bradshaw (1976) with stabilizing curvature. The LRR model predicts a greater reduction in width than the Standard k-ϵ model. However, the LRR model's predicted width lies as far below the measured width as the k-ϵ model's prediction lies above. Although not shown in the figure, Rodi's (1976) Algebraic Stress Model predicts a width that is about midway between, and thus in close agreement with measured values.

As a final comment, with all of the additional new closure coefficients attending *nonlinear* pressure-strain models, it is very likely that such models can be fine tuned to correct the round-jet/plane-jet anomaly. However, we should keep in mind that the anomaly underscores a deficiency in our physical description and understanding of jets. Such fine tuning reveals nothing regarding the nature of these flows, and thus amounts to little more than a curve-fitting exercise.

By contrast, the physically-plausible argument presented by Pope (1978) regarding the role of vortex stretching (Subsection 4.5.5) offers a more credible solution. While the modification to the ϵ equation fails to rectify the k-ϵ model's deficiencies for jets, the modification to the coefficient β [Equation (6.87)] appearing in the Stress-ω model, which uses the *linear* LRR pressure-strain model, implements Pope's ideas quite effectively.

6.6 Application to Wall-Bounded Flows

This section focuses upon wall-bounded flows, including channel and pipe flow, and boundary layers with a variety of complicating effects. Before addressing such flows, however, we discuss surface boundary conditions. As with two-equation models, we have the option of using wall functions or integrating through the viscous sublayer.

6.6.1 Surface Boundary Conditions/Viscous Modifications

Wall-bounded flows require boundary conditions appropriate to a solid boundary for the mean velocity and the scale-determining parameter, e.g., ϵ or ω. Additionally, surface boundary conditions are needed for each component of the Reynolds-stress tensor (implying a boundary condition for k). The exact surface boundary conditions follow from the no-slip condition:

$$\tau_{ij} = 0 \qquad \text{at} \qquad y = 0 \tag{6.97}$$

Stress-transport models, like two-equation models, may or may not predict a satisfactory value of the constant C in the law of the wall when the equations are integrated through the viscous sublayer. If the model fails to predict a satisfactory value for C, we have the choice of either introducing viscous damping factors or using wall functions to obviate integration through the sublayer. The near-wall behavior of stress-transport models is strongly influenced by the scale-determining equation. Models based on the ϵ equation fail to predict an acceptable value of C unless damping factors are applied. When damping factors are used, the equations become very stiff and are very difficult to integrate through the sublayer [see Durbin (1991) and Laurence and Durbin (1994)]. By contrast, models based on the ω equation predict an acceptable value of C and are generally quite easy to integrate through the sublayer.

The most rational procedure for devising wall functions is to analyze the log layer with perturbation methods. As with the k-ϵ model, the velocity, k and either ϵ or ω are given by

$$U = u_\tau \left[\frac{1}{\kappa} \ell n \left(\frac{u_\tau y}{\nu} \right) + C \right] \tag{6.98}$$

$$k = \frac{u_\tau^2}{\sqrt{\beta^*}}, \qquad \omega = \frac{k^{1/2}}{(\beta^*)^{1/4} \kappa y}, \qquad \epsilon = (\beta^*)^{3/4} \frac{k^{3/2}}{\kappa y} \tag{6.99}$$

Similar relations are needed for the Reynolds stresses, and the precise forms depend upon the approximations used to close the Reynolds-stress equation. Regardless of the model, the general form of the Reynolds-stress tensor is

$$\tau_{ij} = W_{ij} k \qquad \text{as} \qquad y \to 0 \tag{6.100}$$

where W_{ij} is a constant tensor whose components depend upon the model's closure coefficients. The problems section examines log-layer structure for the LRR and Stress-ω models. The tensor W_{ij} for these two models is

$$W_{ij} = \begin{bmatrix} -0.908 & 0.304 & 0 \\ 0.304 & -0.435 & 0 \\ 0 & 0 & -0.658 \end{bmatrix} \qquad \text{(Stress-}\omega\text{ model)} \qquad (6.101)$$

$$W_{ij} = \begin{bmatrix} -0.852 & 0.301 & 0 \\ 0.301 & -0.469 & 0 \\ 0 & 0 & -0.679 \end{bmatrix} \qquad \text{(LRR model)} \qquad (6.102)$$

So, Lai, Zhang, and Hwang (1991) review low-Reynolds-number corrections for stress-transport models based on the ϵ equation. The damping functions generally introduced are similar to those proposed for the k-ϵ model (see Section 4.9). As with the k-ϵ model, many authors have postulated low-Reynolds-number damping functions, and the topic remains in a continuing state of development.

As with the k-ω model, the surface value of specific dissipation rate, ω_w, determines the value of the constant C in the law of the wall for the Stress-ω model. Perturbation analysis of the sublayer shows that the limit $\omega_w \to \infty$ corresponds to a perfectly-smooth wall and, without low-Reynolds-number corrections, the asymptotic behavior of ω approaching the surface for both the k-ω and Stress-ω models is

$$\omega \to \frac{6\nu_w}{\beta_o y^2} \qquad \text{as} \qquad y \to 0 \qquad \text{(Smooth Wall)} \qquad (6.103)$$

Using Program **SUBLAY** (see Appendix C), the Stress-ω model's sublayer behavior can be readily determined. Most importantly, the constant, C, in the law of the wall is predicted to be

$$C = 5.48 \qquad (6.104)$$

This is close enough to 5.0 to justify integrating the Stress-ω model equations through the sublayer without the aid of viscous damping functions. Figure 6.17 compares Stress-ω model smooth-wall velocity profiles with corresponding measurements of Laufer (1952), Andersen, Kays and Moffat (1972), and Wieghardt [as tabulated by Coles and Hirst (1969)]. Figure 6.18 compares computed turbulence production and dissipation terms with Laufer's (1952) near-wall pipe-flow measurements. Aside from the erroneous dissipation data for $y^+ < 10$, predictions are within experimental error bounds.

As with the k-ω model, the value of C is sensitive to the value of σ. Its value is also affected by the value chosen for C_2. For consistency with the k-ω model, the value of σ has been chosen to be $1/2$. Then, selecting $C_2 = 10/19 = 0.526$ gives the value quoted in Equation (6.104). To illustrate the sensitivity of C to C_2, note that choosing $C_2 = 0.500$ gives $C = 5.05$.

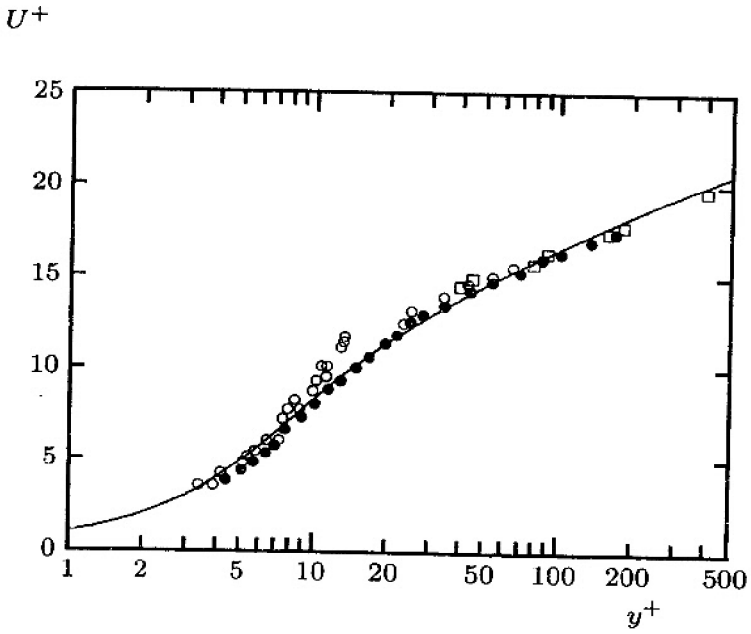

Figure 6.17: *Comparison of computed and measured sublayer velocity profiles:* —— *Wilcox (2006) Stress-ω model;* ○ *Laufer;* • *Andersen et al.;* □ *Wieghardt.*

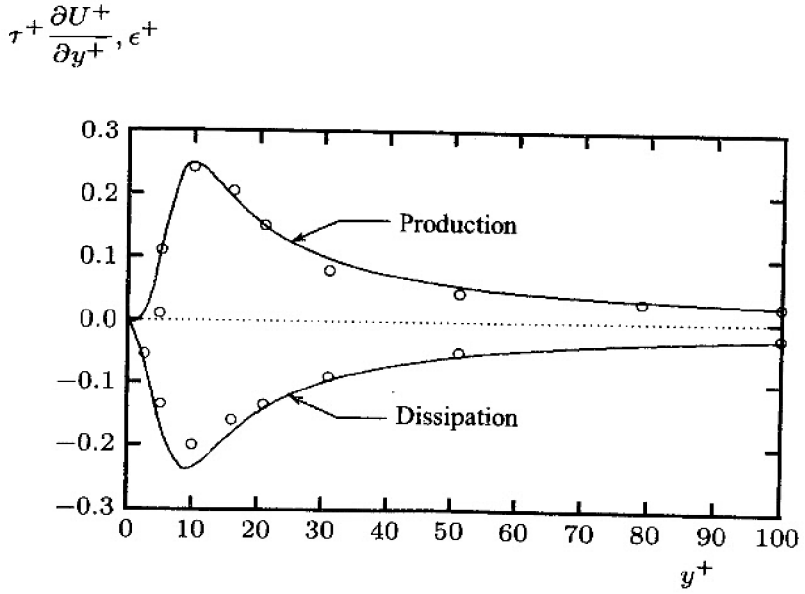

Figure 6.18: *Comparison of computed and measured production and dissipation:* —— *Stress-ω model;* ○ *Laufer.*

Since the Stress-ω model has the property that the constant C varies with the surface value of ω, we can correlate ω_w with surface roughness height, k_s, and surface mass-injection velocity, v_w. The resulting correlations are a little different from those appropriate for the k-ω model (see Subsections 4.7.2 and 4.7.3). The surface boundary conditions based on these correlations are as follows.

For rough surfaces:

$$\omega = \frac{u_\tau^2 S_R}{\nu_w} \qquad \text{at} \qquad y = 0 \qquad \text{(Rough Wall)} \tag{6.105}$$

where the dimensionless coefficient S_R is defined in terms of the dimensionless roughness height, $k_s^+ = u_\tau k_s/\nu_w$, by

$$S_R = \begin{cases} \left(\dfrac{200}{k_s^+}\right)^2, & k_s^+ \le 5 \\ \dfrac{70}{k_s^+} + \left[\left(\dfrac{200}{k_s^+}\right)^2 - \dfrac{70}{k_s^+}\right] e^{5-k_s^+}, & k_s^+ > 5 \end{cases} \tag{6.106}$$

For surfaces with mass injection:

$$\omega = \frac{u_\tau^2 S_B}{\nu_w} \qquad \text{at} \qquad y = 0 \qquad \text{(Mass Injection)} \tag{6.107}$$

where the dimensionless coefficient S_B is defined in terms of the dimensionless injection velocity, $v_w^+ = v_w/u_\tau$, by

$$S_B = \frac{24}{v_w^+(1 + 5v_w^+)} \tag{6.108}$$

As with the k-ω model, for flows with suction ($v_w < 0$), either the **smooth-surface** [Equation (6.103)] or **slightly-rough-surface** [Equation (4.203) with $k_s^+ < 5$] boundary condition for ω is appropriate.

While the Stress-ω model does not require viscous damping functions to achieve a satisfactory sublayer solution, introducing low-Reynolds-number corrections can improve model predictions for a variety of flows. Most importantly, with straightforward viscous damping functions very similar to those introduced for the k-ω model (see Subsection 4.9.2), the model's ability to predict transition can be greatly improved. As with the k-ω model, we let

$$\nu_T = \alpha^* \frac{k}{\omega} \qquad \text{and} \qquad Re_T = \frac{k}{\omega\nu} \tag{6.109}$$

and the closure coefficients in Equations (6.83) – (6.85) are replaced by:

$$\left.\begin{aligned}
\alpha^* &= \frac{\alpha_o^* + Re_T/R_k}{1 + Re_T/R_k}, \qquad \beta^* = \frac{9}{100} \cdot \frac{100\beta_o/27 + (Re_T/R_\beta)^4}{1 + (Re_T/R_\beta)^4} \\
\alpha &= \frac{13}{25} \cdot \frac{\alpha_o + Re_T/R_\omega}{1 + Re_T/R_\omega} \cdot \frac{3 + Re_T/R_\omega}{3\alpha_o^* + Re_T/R_\omega} \\
\hat{\alpha} &= \frac{1 + \hat{\alpha}_\infty (Re_T/R_\beta)^4}{1 + (Re_T/R_\beta)^4}, \qquad \hat{\beta} = \hat{\beta}_\infty \cdot \frac{(Re_T/R_\beta)^4}{1 + (Re_T/R_\beta)^4} \\
\hat{\gamma} &= \hat{\gamma}_\infty \cdot \frac{\hat{\gamma}_o + (Re_T/R_\beta)^4}{1 + (Re_T/R_\beta)^4}, \qquad C_1 = \frac{9}{5} \cdot \frac{5/3 + (Re_T/R_\beta)^4}{1 + (Re_T/R_\beta)^4}
\end{aligned}\right\} \tag{6.110}$$

$$\hat{\alpha}_\infty = (8 + C_2)/11, \quad \hat{\beta}_\infty = (8C_2 - 2)/11, \quad \hat{\gamma}_\infty = (60C_2 - 4)/55 \tag{6.111}$$

$$\beta = \beta_o f_\beta, \quad \sigma = \frac{1}{2}, \quad \sigma^* = \frac{3}{5}, \quad \sigma_{do} = \frac{1}{8}, \quad C_2 = \frac{10}{19} \tag{6.112}$$

$$\alpha_o^* = \frac{1}{3}\beta_o, \quad \alpha_o = \frac{1}{9}, \quad \hat{\gamma}_o = \frac{21}{2000} \tag{6.113}$$

$$R_\beta = 8, \qquad R_k = 6, \qquad R_\omega = \frac{22}{9} \tag{6.114}$$

With these viscous corrections, the Stress-ω model reproduces all of the low-Reynolds-number k-ω model transition-predictions discussed in Subsection 4.9.2, and other subtle features such as asymptotic consistency. The modification to the coefficient C_1 guarantees that the Reynolds shear stress goes to zero as y^3 for $y \to 0$. The values chosen for R_β, R_k and R_ω yield $C = 5.44$.

Finally, the rough-surface boundary condition for the low-Reynolds-number version of the Stress-ω model replaces Equation (6.106) with

$$S_R = \begin{cases} \left(\dfrac{200}{k_s^+}\right)^2, & k_s^+ \le 5 \\ \dfrac{50}{k_s^+} + \left[\left(\dfrac{200}{k_s^+}\right)^2 - \dfrac{50}{k_s^+}\right] e^{5-k_s^+}, & k_s^+ > 5 \end{cases} \tag{6.115}$$

For a surface with mass injection, Equation (6.108) is replaced by

$$S_B = \frac{11}{v_w^+(1 + 5v_w^+)} \tag{6.116}$$

6.6.2 Channel and Pipe Flow

Figure 6.19 compares computed and measured velocity and Reynolds-stress profiles for channel flow using the original Launder-Reece-Rodi model. The computation was done using wall functions. Velocity profile data shown are those of Laufer (1951) and Hanjalić (1970), while the Reynolds-stress data are those of Comte-Bellot (1965). As shown, with the exception of $\overline{u'^2}$, computed and measured profiles differ by less than 5%. The computed and measured $\overline{u'^2}$ profiles differ by no more than 20%. Although not shown, even closer agreement between computed and measured Reynolds stresses can be obtained with low-Reynolds-number versions of the LRR model [see So et al. (1991)].

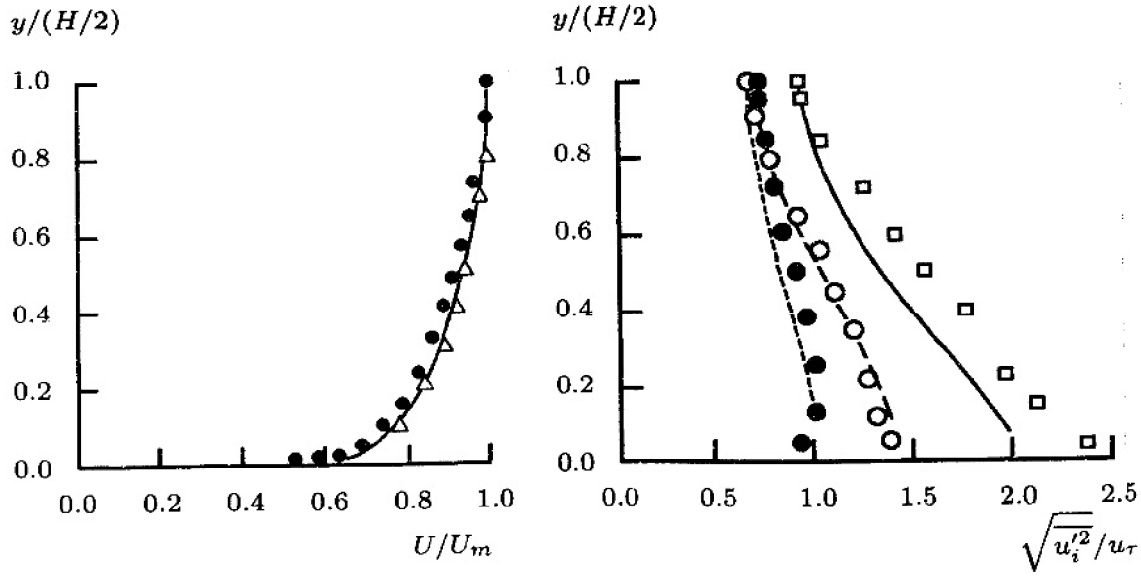

(a) Mean Velocity (b) Normal Reynolds stresses

Figure 6.19: *Computed and measured flow properties for channel flow: (a)* — *LRR model,* △ *Laufer,* • *Hanjalić; (b)* —, - - -, – – *LRR model* ($\sqrt{\overline{u'^2}}/u_\tau$, $\sqrt{\overline{v'^2}}/u_\tau$, $\sqrt{\overline{w'^2}}/u_\tau$), □, •, ○ *Comte-Bellot* ($\sqrt{\overline{u'^2}}/u_\tau$, $\sqrt{\overline{v'^2}}/u_\tau$, $\sqrt{\overline{w'^2}}/u_\tau$).

One of the most controversial features of the LRR-model solution for channel flow is the importance of the pressure-echo term throughout the flow. The pressure-echo contribution on the centerline is approximately 15% of its peak value. It is unclear that a supposed near-wall effect should have this large an impact at the channel centerline. On the one hand, some researchers argue that the echo effect scales with maximum eddy size which, for channel flow, would be about half the channel height. What matters is the ratio of eddy size to y. This is (nominally) constant through the log layer and doesn't fall much in the defect layer.

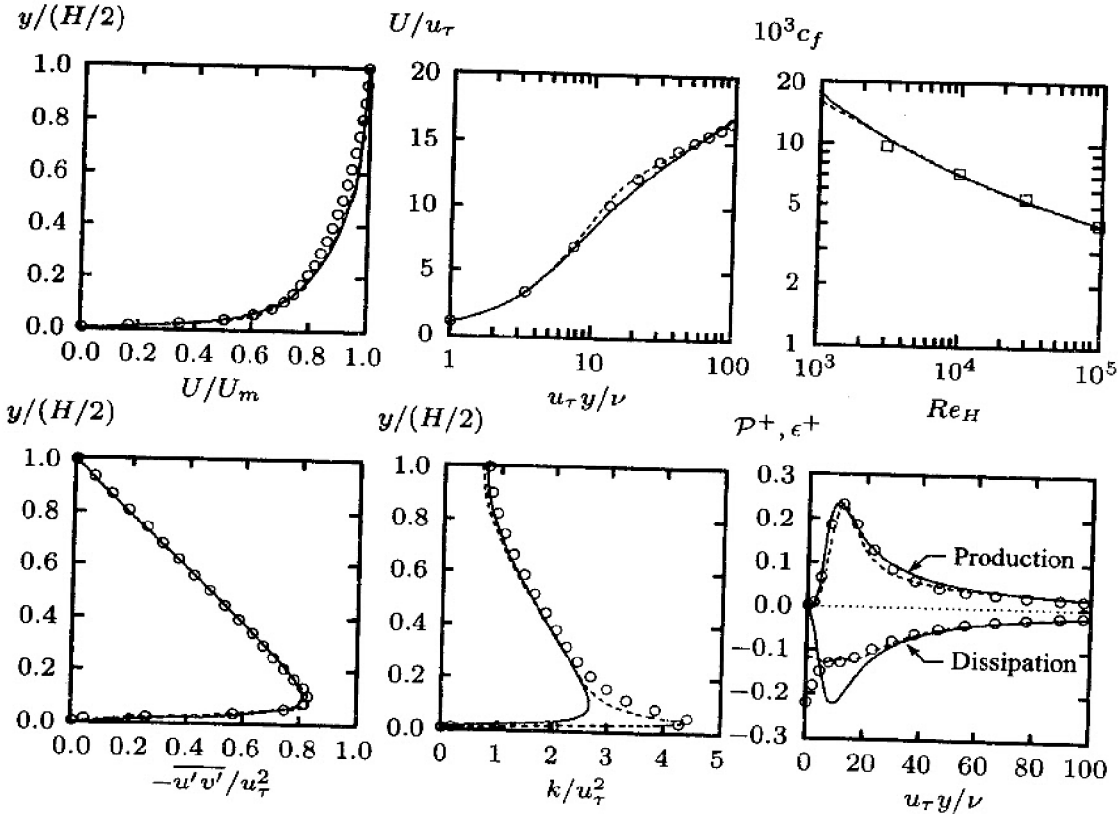

Figure 6.20: *Comparison of computed and measured channel-flow properties, $Re_H = 13750$. — High-Re Stress-ω model; - - - Low-Re Stress-ω model; ○ Mansour et al. (DNS); □ Halleen-Johnston correlation.*

On the other hand, the Stress-ω model — despite all its similarity to the LRR model aside from its use of the ω equation in place of the ϵ equation — does not require a pressure-echo contribution to achieve a satisfactory channel-flow solution. As noted earlier, this strongly suggests that the unreasonably-large pressure-echo term used in the LRR and other ϵ-equation-based stress-transport models is needed to accommodate a deficiency of the modeled ϵ equation, most likely its ill-conditioned near-wall behavior.

Figure 6.20 compares computed, measured and DNS channel-flow properties for the Stress-ω model with and without viscous corrections. Computed skin friction is generally within 6% of the Halleen and Johnston (1967) correlation [see Equation (3.139)]. Velocity, Reynolds shear stress, and turbulence kinetic energy profiles differ from DNS data by less than 6%. Most notably, the low-Reynolds-number model predicts the peak value of k near the wall to within 7% of the DNS value for channel flow. Turbulence-energy production, $\mathcal{P}^+ = \nu\tau_{xy}(\partial U/\partial y)/u_\tau^4$, is within 5% of the DNS results, and the dissipation rate, $\epsilon^+ = \nu\epsilon/u_\tau^4$, is within 10% of the DNS results except very close to the surface.

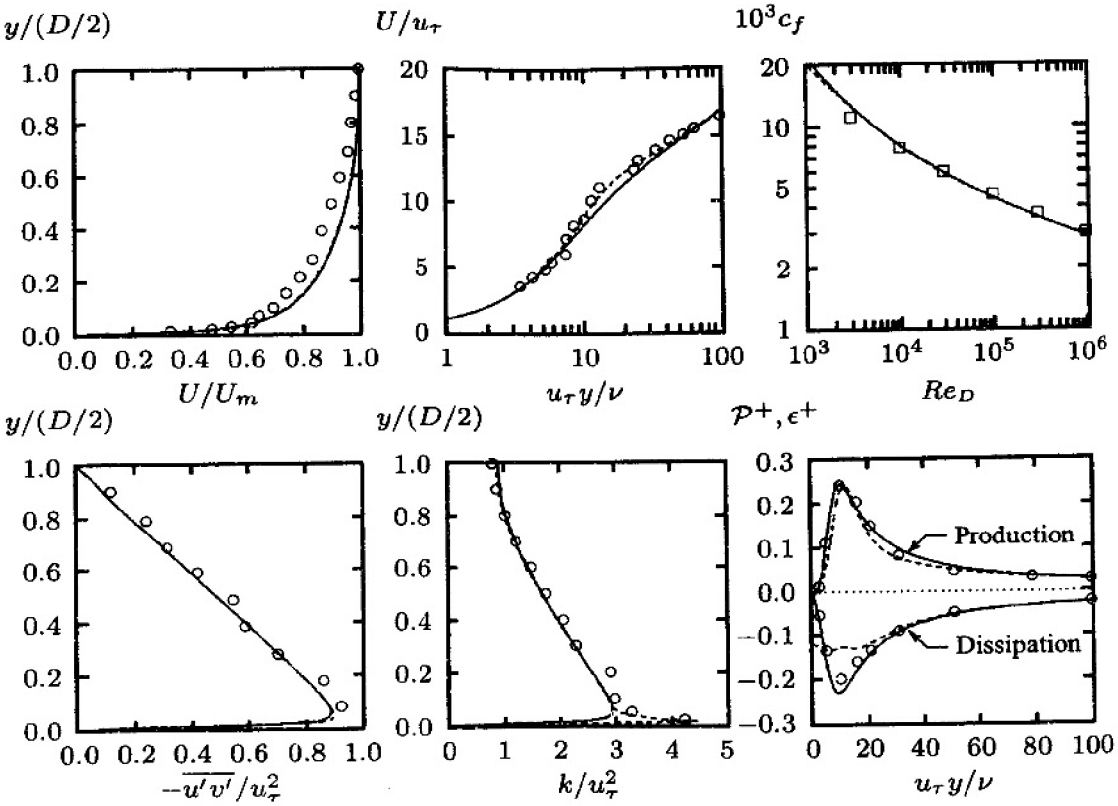

Figure 6.21: *Comparison of computed and measured pipe-flow properties,* $Re_D = 40000$. — *High Re Stress-ω model;* - - - *Low Re Stress-ω model;* ○ *Laufer;* □ *Prandtl correlation.*

Figure 6.21 compares computed and measured properties for pipe flow. Computed c_f differs from Prandtl's universal law of friction [see Equation (3.140)] by less than 7% except at the lowest Reynolds numbers, where the formula is known to be inaccurate. As with channel flow, velocity, Reynolds shear stress and turbulence kinetic energy profiles differ from measurements by less than 6%. The low-Reynolds-number Stress-ω model predicts a peak value of k near the wall within 5% of the measured value.

In both channel and pipe flow, the most noticeable difference between computed and measured flow properties occurs for the dissipation when $y^+ < 20$. The DNS channel-flow data show that dissipation achieves its maximum value at the surface, a feature that is not captured by the low-Reynolds-number version of the Stress-ω model. Several low-Reynolds-number versions of the LRR model have been developed that closely mimic the near-wall behavior of the dissipation. This is accomplished with viscous damping functions that are much more complicated than the simple bilinear forms used for the Stress-ω model [see Equations (6.110)]. The excellent overall agreement between theory and

experiment for all other features of the channel- and pipe-flow solutions casts doubt on the importance of duplicating this subtle feature of the solution, with the attendant complication (and the potential source of numerical mischief) that would be involved in forcing the model to duplicate the measured surface value of ϵ.

Capturing other subtle details such as the sharp peak in k near the surface, and achieving asymptotic consistency (e.g., $k \sim y^2$ and $\tau_{xy} \sim y^3$) has been done with virtually no change in skin friction and in mean-flow and turbulence-property profiles above $y^+ \approx 10$. Similarly, low-Reynolds-number versions of the LRR model have their most significant changes in turbulence-property profiles confined to the portion of the channel below $y^+ \approx 20$.

Unlike the Stress-ω model however, some low-Reynolds-number variants of the LRR model provide accurate descriptions of near-wall dissipation while simultaneously giving nontrivial discrepancies between computed and measured skin friction for typical wall-bounded flows. By contrast, the low-Reynolds-number corrections have virtually no effect on the Stress-ω model's predicted skin friction.

6.6.3 Rotating Channel Flow

Rotating channel flow is an interesting application of stress-transport models. As with flow over a curved surface, two-equation models require ad hoc corrections for rotating channel flow in order to make realistic predictions [e.g., Launder, Priddin and Sharma (1977) and Wilcox and Chambers (1977)]. To understand the problem, note that in a rotating coordinate frame, the Coriolis acceleration yields additional inertial terms in the Reynolds-stress equation. Specifically, in a coordinate system that is rotating with angular velocity, Ω, the Reynolds-stress equation is

$$\frac{\partial \tau_{ij}}{\partial t} + U_k \frac{\partial \tau_{ij}}{\partial x_k} + 2\left(\epsilon_{jkm}\Omega_k \tau_{im} + \epsilon_{ikm}\Omega_k \tau_{jm}\right)$$
$$= -\tau_{ik}\frac{\partial U_j}{\partial x_k} - \tau_{jk}\frac{\partial U_i}{\partial x_k} + \epsilon_{ij} - \Pi_{ij} + \frac{\partial}{\partial x_k}\left[\nu \frac{\partial \tau_{ij}}{\partial x_k} + C_{ijk}\right] \quad (6.117)$$

where ϵ_{jkm} is the permutation tensor. Note that if the rotation tensor, Ω_{ij}, appears in any of the closure approximations for ϵ_{ij}, Π_{ij} or C_{ijk}, it must be replaced by $\Omega_{ij} + \epsilon_{ikj}\Omega_k$.

Contracting Equation (6.117) yields the turbulence kinetic energy equation. Because the trace of the Coriolis term is zero, there is no explicit effect of rotation appearing in the equation for k. Since rotation has a strong effect on turbulence, this shows why ad hoc coordinate-frame-rotation modifications are needed for a two-equation model.

Figure 6.22 compares computed and measured velocity profiles for a channel with a constant angular velocity about the spanwise (z) direction. Computations have been done using the Gibson-Launder (1978) stress-transport model and the Standard k-ϵ model. Experimental data are those of Johnston et al. (1972), corresponding to an inverse Rossby number, $\Omega H/U_m = 0.21$, where H is channel height and U_m is average velocity. The k-ϵ model's velocity profile is symmetric about the center line. Consistent with measurements, the Gibson-Launder model predicts an asymmetric profile. However, as clearly shown in the figure, the velocity and shear stress on the "stable" side near $y = 0$ are underestimated.

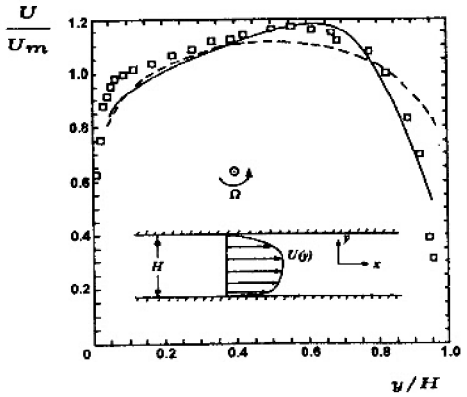

Figure 6.22: *Computed and measured velocity profiles for rotating channel flow with $\Omega H/U_m = 0.21$: —— Gibson-Launder model; - - - k-ϵ model; □ Johnston et al. [From Speziale (1991) — Published with the author's permission.]*

6.6.4 Boundary Layers

Table 6.5 and Figure 6.23 compare computed and measured skin friction for the 16 incompressible boundary layers considered in Chapters 3 and 4 (see Figures 3.17, 3.19, 4.4, 4.30 and 4.40). The figure includes numerical results for the Stress-ω model with and without low-Reynolds-number corrections. Both versions of the Stress-ω model provide acceptable predictions for all ranges of pressure gradients, from favorable to strong adverse.

Table 6.5: *Differences Between Computed and Measured Skin Friction.*

Pressure Gradient	Flows	Low Re Stress-ω	High Re Stress-ω
Favorable	1400, 1300, 2700, 6300	5%	5%
Mild Adverse	1100, 2100, 2500, 4800	5%	6%
Moderate Adverse	2400, 2600, 3300, 4500	12%	10%
Strong Adverse	0141, 1200, 4400, 5300	12%	13%
All	–	8%	8%

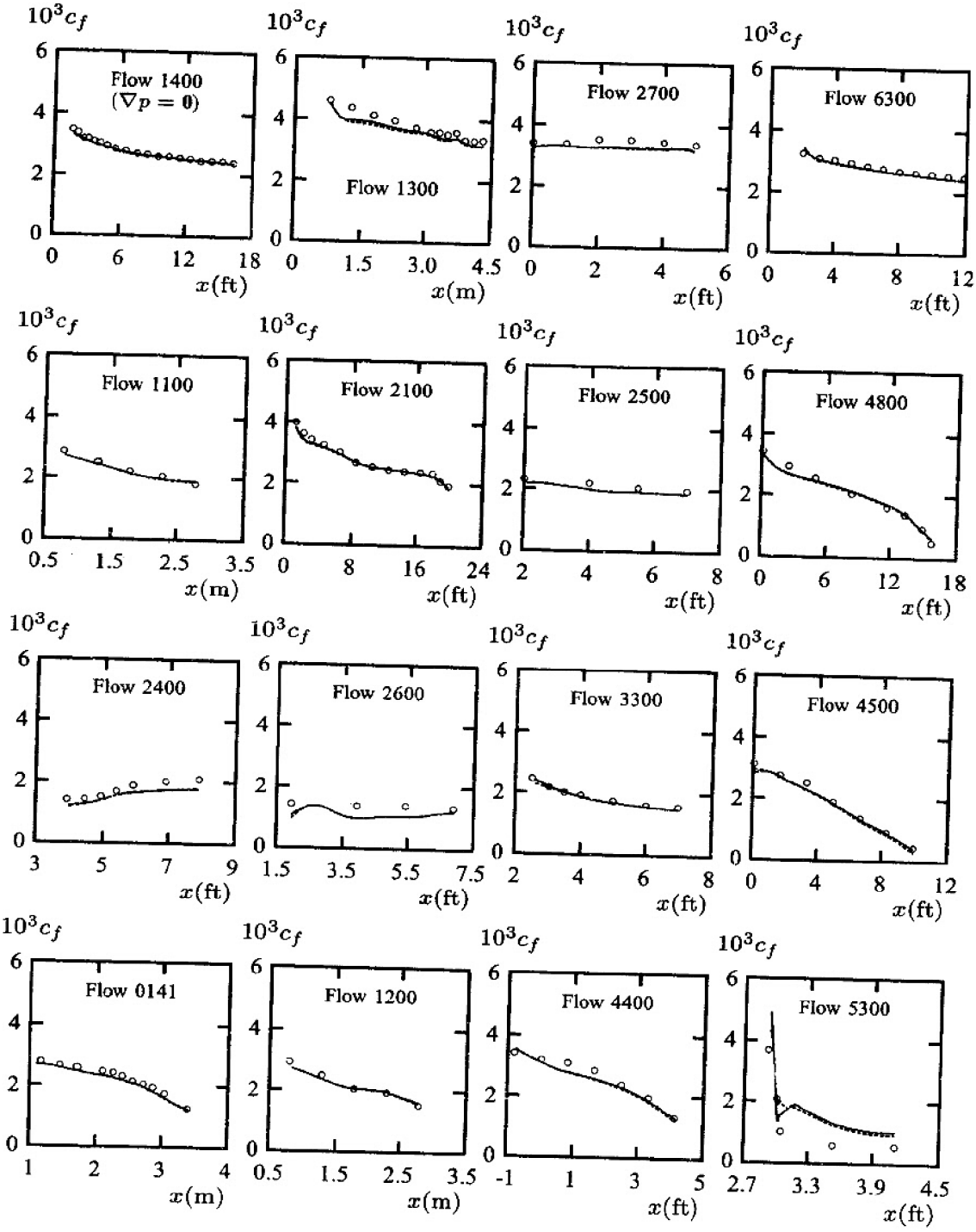

Figure 6.23: *Computed and measured skin friction for boundary layers subjected to a pressure gradient. Top row - favorable ∇p; next to top row - mild adverse ∇p; next to bottom row - moderate adverse ∇p; bottom row - strong adverse ∇p. — High Re Stress-ω model; - - - Low Re Stress-ω model; ○ measured.*

Although no results are included for ϵ-based stress-transport models, older versions are generally only a bit closer to measurements than the k-ϵ model (cf. Figure 4.4). By contrast, newer versions, especially those with nonlinear pressure-strain terms, appear to more faithfully reproduce experimental data. For example, Hanjalić et al. (1997) have developed an ϵ-based stress-transport model (with a linear pressure-strain term) that accurately predicts effects of adverse pressure gradient. Using perturbation methods, Henkes (1998a) has shown that this model is as close to measurements as the k-ω model for equilibrium boundary layers (i.e., for constant β_r – see Section 4.6), strongly suggesting that it will perform well in general boundary-layer applications.

Although the Hanjalić et al. model has a large number of empirical functions designed to permit the model to achieve asymptotic consistency and the ability to predict transition and relaminarization, the improved accuracy for effects of pressure gradient appears to result from a single modification to the ϵ equation. Specifically, Hanjalić et al. add a dissipation term of the form

$$S_\ell \propto \max\left[\left(\frac{1}{C_\ell^2}\frac{\partial \ell}{\partial x_j}\frac{\partial \ell}{\partial x_j} - 1\right)\frac{1}{C_\ell^2}\frac{\partial \ell}{\partial x_j}\frac{\partial \ell}{\partial x_j};\ 0\right]\frac{\epsilon^2}{k} \tag{6.118}$$

where $C_\ell = 2.5$ is a closure coefficient and $\ell = k^{3/2}/\epsilon$ is the turbulence length scale. This term limits the growth of ℓ in the log layer, and cancels the undesirable effects of cross diffusion (relative to the k-ω model) that plague the k-ϵ model [see the discussion at the end of Subsection 4.6.2].

Surface curvature, like system rotation, has a significant effect on structural features of the turbulent boundary layer. As discussed in Section 6.1, in the absence of ad hoc modifications, such effects cannot be accurately predicted with a two-equation model, as curvature has a trivial effect on the turbulence kinetic energy equation. In principle, stress-transport models display none of these shortcomings. Thus, computing curved-wall boundary layers poses an interesting test of stress-transport models.

Figure 6.24 presents results of two computations done with the Stress-ω model for flow over a convex surface. The two cases are the constant-pressure and adverse-pressure-gradient flows that So and Mellor (1972) have investigated experimentally. To insure accurate starting conditions, the measured momentum and displacement thickness at $x = 2$ ft. have been matched to within 1% for both cases, a point well upstream of the beginning of the curved-wall portion of the flow at $x = 4.375$ ft. For both cases, computed and measured flow properties differ by less than 8%.

The LRR model also offers important improvement in predictive accuracy relative to the k-ϵ model for flows with secondary motions. Lai et al. (1991), for example, have successfully applied three variants of the LRR model with wall functions to flow in a curved pipe. Consistent with measurements, their computations predict existence of secondary flows.

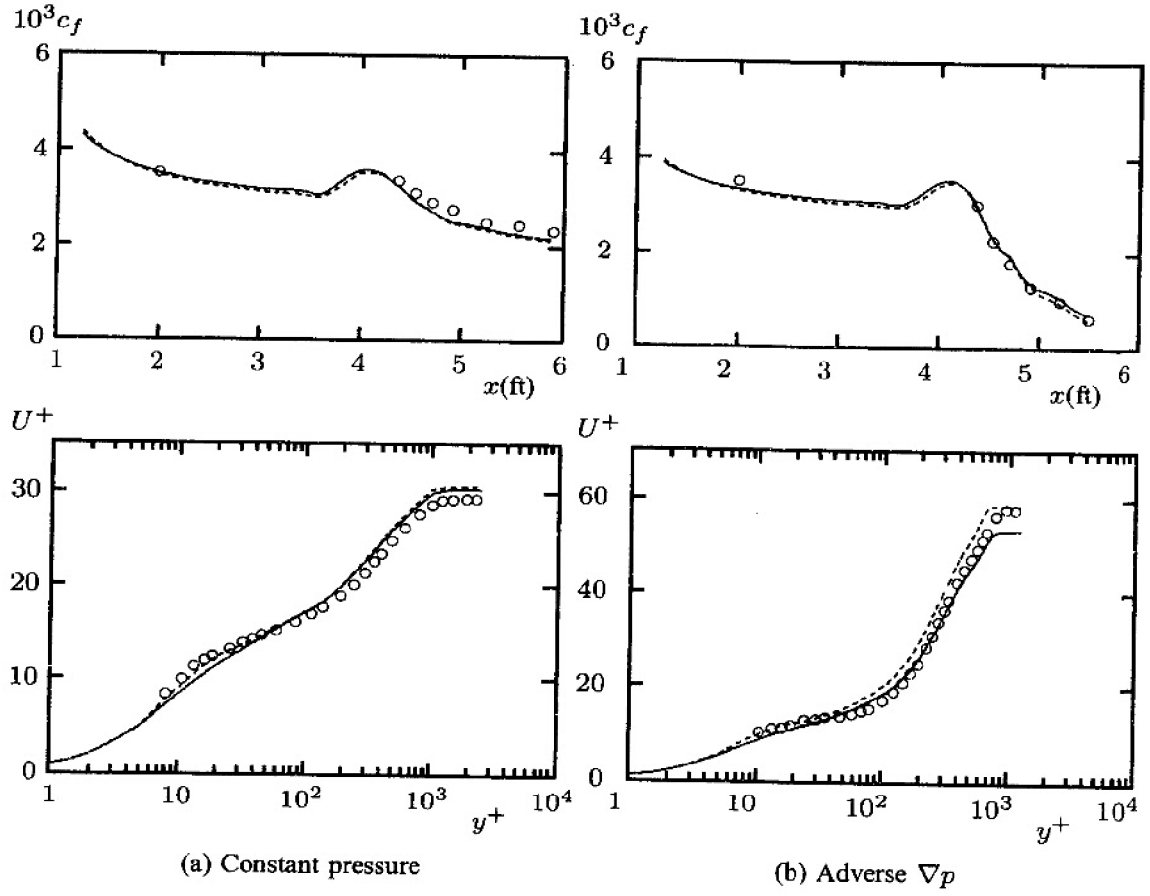

Figure 6.24: *Computed and measured skin friction for flow over a convex wall:* — *High Re Stress-ω model;* - - - *Low Re Stress-ω model;* ○ *So and Mellor.*

Turning to effects of compressibility, a stress-transport model's performance is intimately tied to the scale-determining equation. Models based on the ϵ equation will share the k-ϵ model's incorrect density scaling (see Section 5.6). By contrast, models based on the ω equation share the k-ω model's ability to accurately predict the compressible law of the wall.

Figure 6.25 confirms this point for the Stress-ω model. The figure compares computed effects of Mach number and surface cooling on flat-plate boundary layer skin friction. The turbulent heat-flux vector has been computed according to Equation (5.54) with constant turbulent Prandtl number. Figure 6.25(a) compares computed ratio of skin friction to the incompressible value, c_{f_o}, as a function of Mach number with the Van Driest correlation. Figure 6.25(b) focuses upon effects of surface temperature on flat-plate skin friction at Mach 5. In all computations, momentum-thickness Reynolds number, Re_θ, is 10^4 at the point where c_f/c_{fo} has been computed. Inspection of the figure shows that differences between the predicted values and the correlated values nowhere exceed 3%.

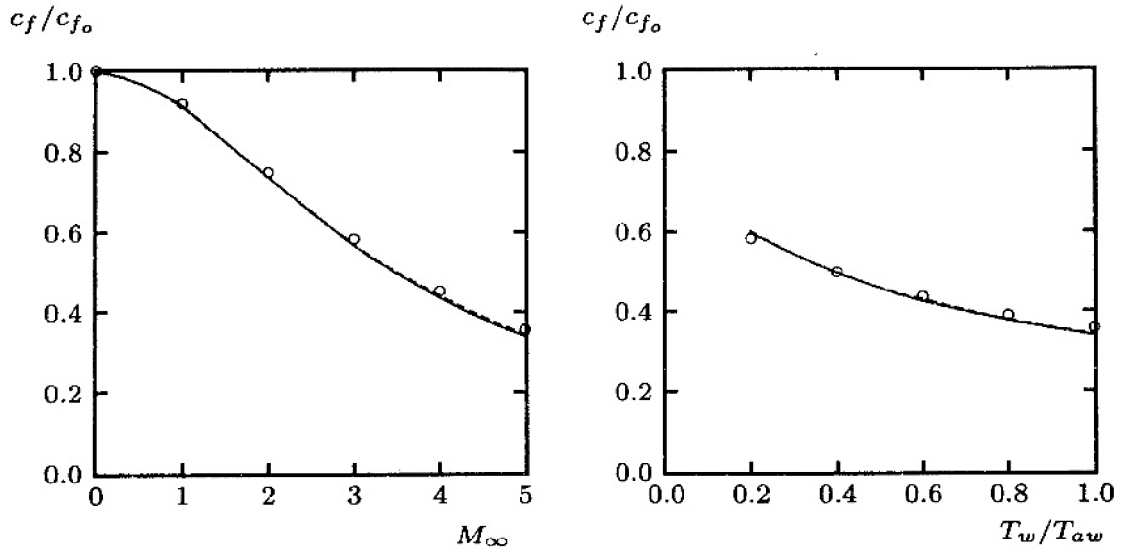

(a) Mach number (b) Surface cooling, $M_\infty = 5$

Figure 6.25: *Computed and measured effects of freestream Mach number and surface cooling on flat-plate boundary-layer skin friction:* — *Wilcox (2006) Stress-ω model;* - - - *Wilcox (2006) k-ω model;* ○ *Van Driest correlation.*

Stress-transport models hold promise of more accurate predictions for three-dimensional flows. The primary reason two-equation models are inaccurate for three-dimensional boundary layers, for example, lies in their use of an isotropic eddy viscosity. However, the eddy viscosities in the streamwise and crossflow directions of a typical three-dimensional boundary layer can differ significantly. Figure 6.26 compares computed and measured skin friction for such a flow, a boundary layer on a segmented cylinder, part of which rotates about its axis. The experiment was performed by Higuchi and Rubesin (1978). As shown, the Wilcox-Rubesin (1980) stress-transport model most accurately describes both the axial (c_{f_x}) and transverse (c_{f_z}) skin friction components in the relaxation zone, i.e., the region downstream of the spinning segment. The Cebeci-Smith algebraic model and the Wilcox-Rubesin (1980) two-equation model yield skin friction components that differ from measured values by as much as 20% and 10%, respectively.

The final round of applications is for incompressible, unsteady turbulent boundary layers. These flows pose a difficult challenge to a turbulence model because many complicated frequency-dependent phenomena are generally present, including periodic separation and reattachment.

Wilcox (1988b) has simulated the experiments performed by Jayaraman, Parikh and Reynolds (1982) with a simplified stress-transport model (viz. the multiscale model). In these experiments, a well developed steady turbulent

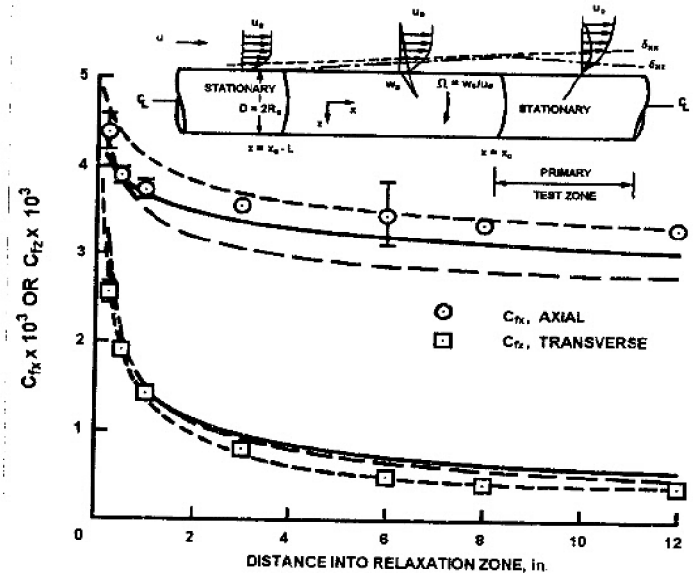

Figure 6.26: *Skin friction on a segmented spinning cylinder; —— Cebeci-Smith model; – – Wilcox-Rubesin k-ω^2 model; - - - Wilcox-Rubesin stress-transport model; ○□ Higuchi and Rubesin. [From Rubesin (1989) — Copyright ©AIAA — Used with permission.]*

boundary layer enters a test section which has been designed to have freestream velocity that varies according to:

$$U_e = U_o \{1 - ax'[1 - cos(2\pi ft)]\}, \qquad x' = (x - x_0)/(x_1 - x_0) \tag{6.119}$$

The quantity x' is fractional distance through the test section where x_0 and x_1 are the values of streamwise distance, x, at the beginning and end of the test section, respectively. Thus, an initially steady turbulent boundary layer is subjected to a sinusoidally varying adverse pressure gradient. The experiments were performed for low- and high-amplitude unsteadiness characterized by having $a \approx 0.05$ and 0.25, respectively. For both amplitudes, experiments were conducted for five frequencies, f, ranging from 0.1 Hz to 2.0 Hz. Wilcox simulates nine of the experiments, including all of the low-amplitude cases and four of the five high-amplitude cases.

In order to compare computed and measured flow properties, we must decompose any flow property $\lambda(\mathbf{x}, t)$ in terms of three components, viz.,

$$\lambda(\mathbf{x}, t) = \bar{\lambda}(\mathbf{x}) + \tilde{\lambda}(\mathbf{x}, t) + \lambda'(\mathbf{x}, t) \tag{6.120}$$

where $\bar{\lambda}(\mathbf{x})$ is the long-time averaged value of $\lambda(\mathbf{x}, t)$, $\tilde{\lambda}(\mathbf{x}, t)$ is the organized response component due to the imposed unsteadiness, and $\lambda'(\mathbf{x}, t)$ is the turbulent

fluctuation. Using an unsteady boundary-layer program, Wilcox computes the phase-averaged component, $< \lambda(\mathbf{x}, t) >$, defined by

$$< \lambda(\mathbf{x}, t) >= \bar{\lambda}(\mathbf{x}) + \tilde{\lambda}(\mathbf{x}, t) \tag{6.121}$$

Jayaraman et al. expand $< \lambda(\mathbf{x}, t) >$ in a Fourier series according to

$$< \lambda(\mathbf{x}, t) >= \bar{\lambda}(\mathbf{x}) + \sum_{n=1}^{\infty} A_{n,y}(\mathbf{x}) \cos\left[2n\pi f t + \phi_{n,y}(\mathbf{x})\right] \tag{6.122}$$

Velocity profile data, for example, are presented by Jayaraman et al. in terms of $\bar{u}(\mathbf{x})$, $A_{1,u}(\mathbf{x})$ and $\phi_{1,u}(\mathbf{x})$. These quantities can be extracted from the boundary-layer solution by the normal Fourier decomposition, viz., by computing the following integrals.

$$\bar{u}(\mathbf{x}) = f \int_0^{1/f} < u(\mathbf{x}, t) > \, dt \tag{6.123}$$

$$A_{1,u}(\mathbf{x}) \cos \phi_{1,u} = f \int_0^{1/f} < u(\mathbf{x}, t) > \cos(2\pi f t) \, dt \tag{6.124}$$

$$A_{1,u}(\mathbf{x}) \sin \phi_{1,u} = -f \int_0^{1/f} < u(\mathbf{x}, t) > \sin(2\pi f t) \, dt \tag{6.125}$$

Figure 6.27 compares computed and measured velocity profiles at $x' = 0.88$ for the five low-amplitude cases. As shown, computed mean velocity profiles differ from corresponding measured profiles by no more than 5% of scale. Comparison of computed and measured $A_{1,u}$ profiles shows that, consistent with measurements, unsteady effects are confined to the near-wall Stokes layer at the higher frequencies ($f > 0.5$ Hz). By contrast, at the two lowest frequencies, the entire boundary layer is affected, with significant amplification of the organized component occurring away from the surface. Differences between the numerical and experimental $A_{1,u}$ profiles are less than 10%. Computed and measured phase, $\phi_{1,u}$, profiles are very similar with differences nowhere in the flowfield exceeding 5^o.

Figure 6.28 compares computed and measured velocity profiles at $x' = 0.94$ for the high-amplitude cases. As for the low amplitude cases, computed and measured $\bar{u}(\mathbf{x})$ profiles lie within 5% of scale of each other. Similarly, computed $A_{1,u}$ and $\phi_{1,u}$ profiles differ from corresponding measurements by less than 10%. To provide a measure of how accurately temporal variations have been predicted, Figure 6.29 compares computed and measured shape factor through a complete cycle for all four frequencies. Differences between computed and measured shape factors are less than 5%.

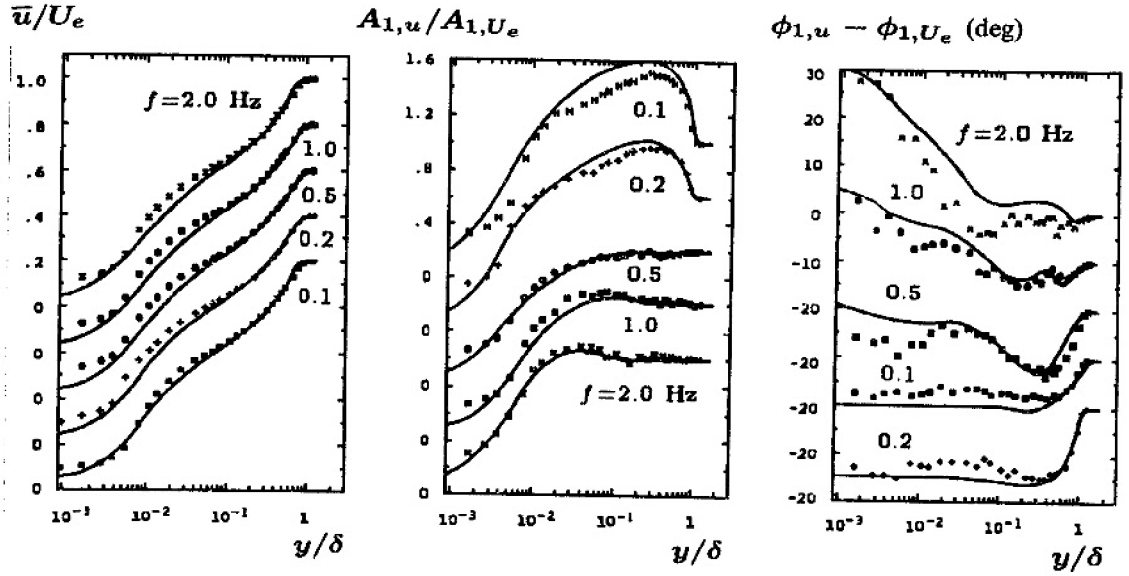

Figure 6.27: *Comparison of computed and measured mean velocity, $A_{1,u}$ and phase profiles at $x' = 0.88$ for low amplitude: — Wilcox (1988b) multiscale model; • Jayaraman et al. [From Wilcox (1988b) — Copyright © AIAA 1988 — Used with permission.]*

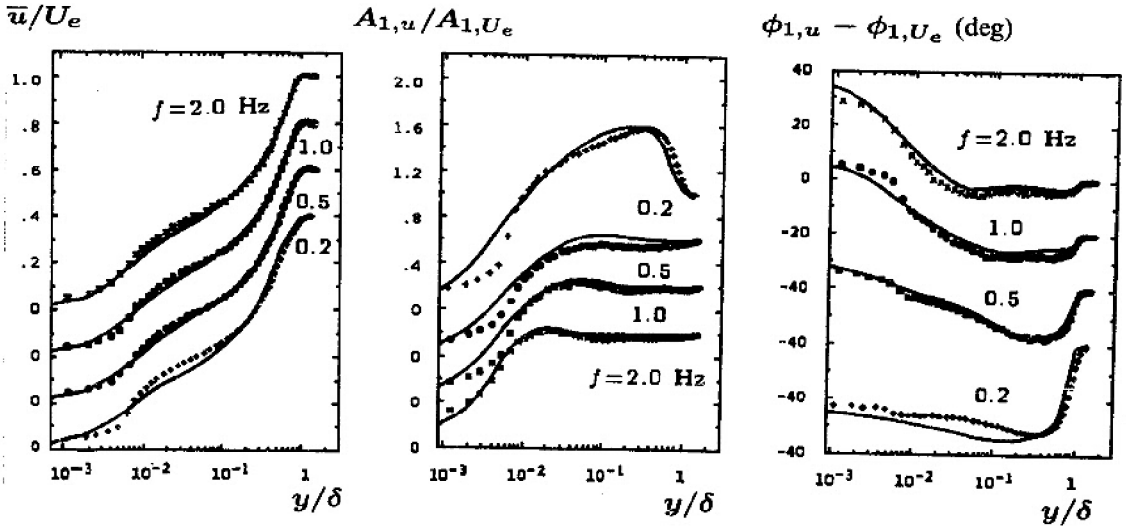

Figure 6.28: *Comparison of computed and measured mean velocity, $A_{1,u}$ and phase profiles at $x' = 0.94$ for high amplitude: — Wilcox (1988b) multiscale model; • Jayaraman et al. [From Wilcox (1988b) — Copyright © AIAA 1988 — Used with permission.]*

The four high-amplitude cases have also been computed using the Wilcox (1988a) k-ω model. Figure 6.29 shows that k-ω and multiscale-model predictions differ by only a few percent. Although it is possible the test cases are not as difficult as might be expected, this seems unlikely in view of the wide Strouhal number range and the fact that periodic separation and reattachment are present. More likely, the k-ω model fares well because all of the cases have attached boundary layers through most of each cycle and in the mean.

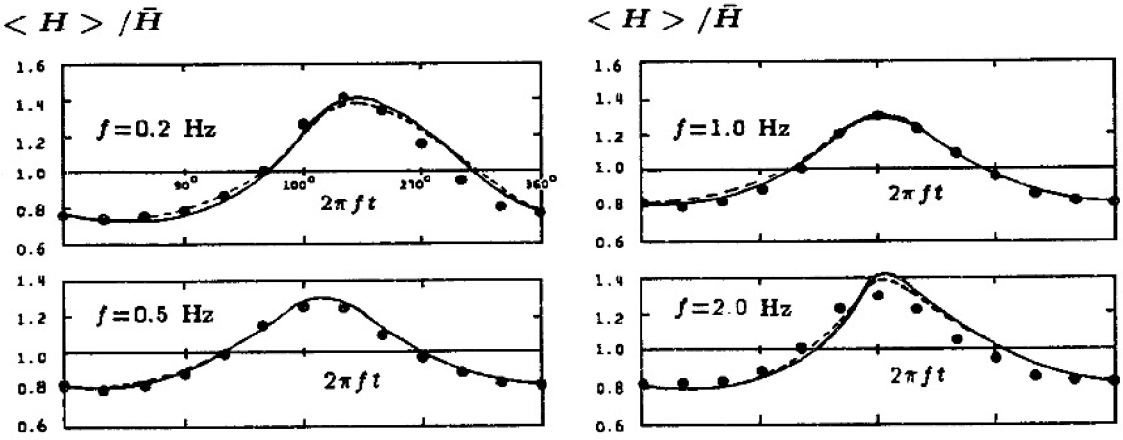

Figure 6.29: *Comparison of computed and measured temporal variation of shape factor for the high-amplitude cases: - - - Wilcox (1988a) k-ω model; —— Wilcox (1988b) multiscale model; • Jayaraman et al. [From Wilcox (1988b) — Copyright © AIAA 1988 — Used with permission.]*

As a closing comment, many recent turbulence modeling efforts focusing on unsteady boundary layers mistakenly credit their success (or lack of it) to achieving asymptotic consistency as $y \to 0$ with the k-ϵ model or with a stress-transport model based on the ϵ equation. Recall from Subsection 4.9.1 that asymptotic consistency is achieved when a turbulence model predicts

$$\overline{u'^2} \to y^2, \quad \overline{v'^2} \to y^4, \quad \overline{w'^2} \to y^2, \quad \overline{u'v'} \to y^3, \quad \epsilon \to \text{constant} \quad \text{as} \quad y \to 0 \tag{6.126}$$

The computations described above were done with the high-Reynolds-number versions of the Wilcox (1988a) k-ω and Wilcox (1988b) multiscale models, neither of which is asymptotically consistent. All that appears to be necessary is to achieve a satisfactory value for the constant C in the law of the wall. This makes sense physically as the dissipation time scale is so short in the sublayer that the sublayer responds to changes in the mean flow almost instantaneously and thus behaves as a quasi-steady region. Consequently, achieving asymptotically consistent behavior in the sublayer is neither more nor less important for unsteady flows than it is for steady flows.

6.7 Application to Separated Flows

As we have seen in preceding chapters, the k-ω model with a stress limiter yields reasonably accurate separated-flow solutions from incompressible to hypersonic flow regimes. Figures 5.16 underscore and 5.19 this point. By contrast, turbulence models that use the ϵ equation are generally unreliable for separated flows, especially shock-induced separation. Figure 5.10, for example, illustrates how poorly such models perform for Mach 3 flow into a compression corner. In this section, we will take a close look at how well stress-transport models perform for several separated flows.

Because stress-transport models require more computer resources than algebraic and two-equation models, applications to separated flows have been rare until recently. As we will see, results of recent applications tell a familiar story regarding the scale-determining equation. In this section, we will focus on incompressible flow past backward-facing steps and compressible-flow applications including compression corners and shock-wave/boundary-layer interactions for a range of Mach numbers.

As we proceed through this section, keep in mind that the Stress-ω model differs from the k-ω model only in the way the Reynolds-stress tensor is computed. All common closure coefficients assume precisely the same values. And, like the k-ω model, no special compressibility modifications to the model have been used. Similarly, the models involving the ϵ equation have only slight differences from the ϵ equation used in standard k-ϵ models.

6.7.1 Incompressible Backward-Facing Step

Focusing first on the incompressible backward-facing step, So et al. (1988) and So and Yuan (1998) have done interesting studies using a variety of turbulence models and closure approximations. The 1988 computations assess the effect of various models for the pressure-strain correlation, while the 1998 study focuses on low-Reynolds-number k-ϵ and ϵ-equation based stress-transport models.

The So et al. (1988) computations use Chien's (1982) low-Reynolds number version of the ϵ equation. Most importantly, they have used three different models for the pressure-strain correlation, viz., the models of Rotta (1951) [Model A1], Launder, Reece and Rodi (1975) [Model A2], and Gibson and Younis (1986) [Model A4]. Using the Rotta model, computations have been done with wall functions as well [Model H-A1]. For reference, their computations also include the Chien (1982) low-Reynolds-number k-ϵ model [Model Lk-ϵ]. These models differ mainly in their representation of the fast pressure-strain term, with the Rotta model ignoring it altogether. The computations simulate the experiments of Eaton and Johnston (1980) in a duct with a large expansion ratio, for which the measured reattachment length is 8 step heights.

As shown in Figure 6.30, computed reattachment length for all of the computations lies between 5 and 6 step heights, so that the result closest to measurements differs from the measured value by 25%. All of the models show large discrepancies between computed and measured wall pressure, while peak skin friction values are as much as 3 times measured values downstream of reattachment for the low-Reynolds-number models. In general, the stress-transport model skin friction results are as far from measurements as those of the low-Reynolds-number k-ϵ model. Only when wall functions are used with the stress-transport model does the computed skin friction lie reasonably close to measured values. So et al. note that the smallest discrepancies between computed and measured flow properties are obtained with the Rotta pressure-strain model, which omits the rapid pressure-strain correlation. That is, the LRR and Gibson-Younis models for the rapid pressure strain appear to yield larger discrepancies between computed and measured values.

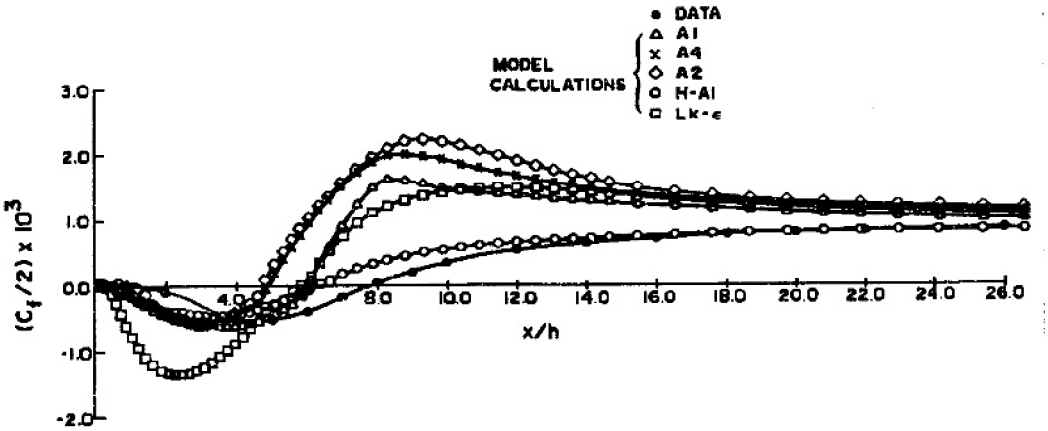

Figure 6.30: *Computed and measured skin friction for flow past a backward-facing step: A1=Rotta model; A2=LRR model; A4=Gibson-Younis model; H-A1=Rotta model with wall functions; Lk-ϵ=Chien k-ϵ model; •=Eaton and Johnston. [From So et al. (1988) — Published with permission.]*

Recalling how close to measurements k-ω model predictions are for flow past a backward-facing step (Section 4.10), the So et al. computations suggest that their poor predictions are caused by the ϵ equation. On the one hand, comparison of Figures 4.46 and 6.30 shows that for stress-transport model H-A1, c_f is very similar to k-ϵ model results when wall functions are used. Although the flows are a little different, the reattachment length is 25% smaller than measured for both cases. On the other hand, using the same low-Reynolds-number ϵ equation, c_f for stress-transport model A1 is very similar to the low-Reynolds-number k-ϵ model's skin friction, except in the reverse-flow region. Despite the latter difference, the reattachment length is the same in this case also. Thus, as with two-equation

models, a stress-transport model's performance for the backward-facing step is intimately linked to the scale-determining equation. This strongly suggests that much closer agreement between computed and measured flow properties would be obtained with a stress-transport model based on the ω equation, such as the Stress-ω model.

Figure 6.31 shows that the Stress-ω model does indeed provide a far more acceptable solution for the high-Reynolds-number backward-facing step of Driver and Seegmiller (1985). For reference, the Wilcox (2006) k-ω model solution is also shown. Both numerical solutions have been done on the same 301 x 163 finite-difference mesh.

Computed and measured flow properties are generally within a few percent. The Stress-ω model predicts a reattachment length of 6.74 step heights, which is 8% longer than the measured length of 6.26 step heights. By comparison, the Wilcox (2006) k-ω model predicts a reattachment length of 7.07 step heights

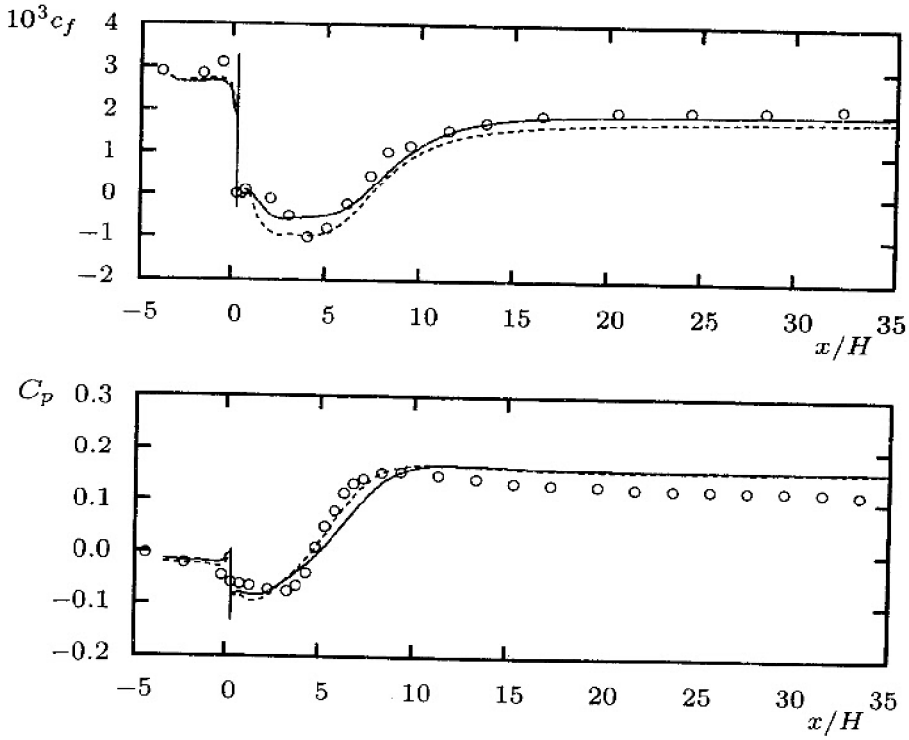

Figure 6.31: *Computed and measured skin friction and surface pressure for flow past a backward-facing step; $Re_H = 37500$; —— Wilcox (2006) Stress-ω model; - - - Wilcox (2006) k-ω model; ○ Driver-Seegmiller.*

In the more recent study, So and Yuan (1998) compute backstep flow with seven low-Reynolds-number k-ϵ models, the four-equation model of Durbin (1991) and three stress-transport models. The flow considered is a relatively low-Reynolds-number (5000 based on step height) case studied experimentally

by Jovic and Driver (1994) and computed with DNS by Le, Moin and Kim (1997). Overall, the computations are in closer agreement with measurements for this flow than those of the high-Reynolds-number Eaton and Johnston (1980) case discussed above. The So-Yuan computations show the following:

- The average difference between the predicted and measured reattachment length for the seven k-ϵ models is 9%. For Chien's (1982) model, the reattachment length is within 7% of the measured value. Note that this model's reattachment length is 25% shorter than measured for the high-Reynolds-number Eaton and Johnson (1980) flow.

- Durbin's four-equation model gives one of the best overall solutions, with a reattachment length within 4% of the measured value. As shown by Durbin (1995), this model also provides a credible solution for the high-Reynolds-number backstep experiment of Driver and Seegmiller (1985).

- The three stress-transport models considered predict reattachment lengths within 3%, 7% and 10% of the measured value.

It is difficult to draw any firm conclusions from the So-Yuan study as it concentrates on just one flow. Furthermore, the flow chosen is one that k-ϵ models predict reasonably well, and that doesn't reveal their inherent weakness for this type of application. Given their inaccurate predictions for backstep flows at higher Reynolds numbers, the close agreement is probably a lucky coincidence.

Figure 6.32 shows that the Stress-ω model yields a satisfactory solution for the Jovic-Driver low-Reynolds-number backstep flow. As with the Driver-Seegmiller case above, results obtained with the Wilcox (2006) k-ω model are included for reference. Based on reattachment length alone, these numerical results are not quite as close to measurements as those for the Driver-Seegmiller case. The Stress-ω model predicts a reattachment length of 7.10 step heights, which is 18% longer than measured. However, the overall differences between theory and experiment for most of the flowfield are generally less than 10%.

It is instructive to observe the close correlation between reattachment length, x_r, and the scale-determining equation.

- **High-Re Backstep:** ϵ-based stress-transport and two-equation models predict x_r appreciably shorter than measured;

- **High-Re Backstep:** ω-based stress-transport and two-equation models predict x_r slightly longer than measured;

- **Low-Re Backstep:** ϵ-based stress-transport and two-equation models predict x_r within a few percent of the measured length;

- **Low-Re Backstep:** ω-based stress-transport and two-equation models predict x_r somewhat longer than measured.

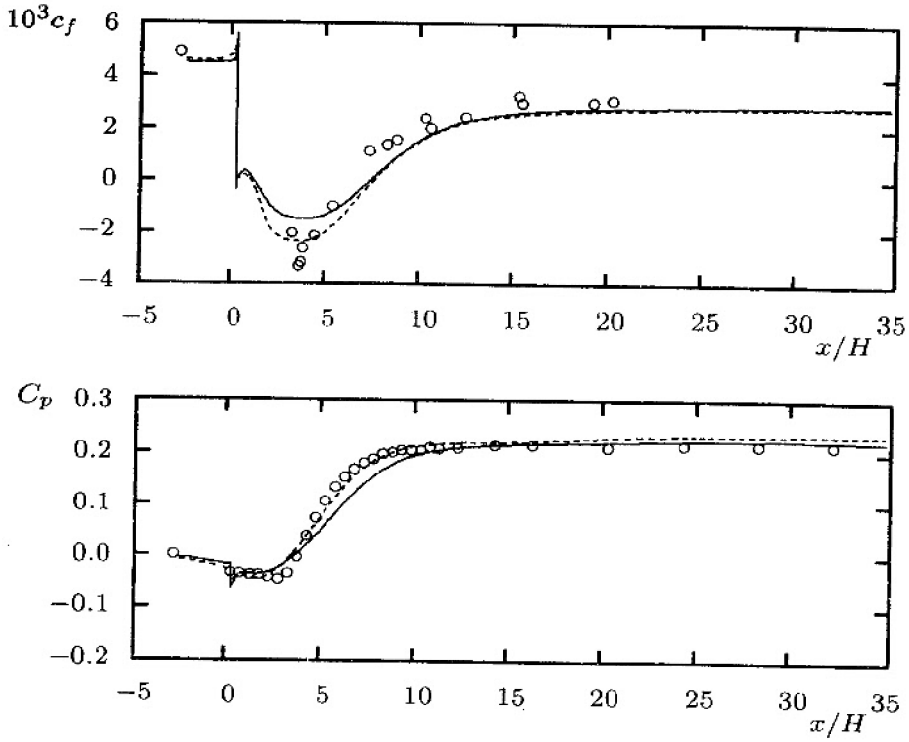

Figure 6.32: *Computed and measured skin friction and surface pressure for flow past a backward-facing step; $Re_H = 5000$; —- Wilcox (2006) Stress-ω model; - - - Wilcox (2006) k-ω model; ○ Jovic-Driver.*

One final observation regarding the performance of the Stress-ω model on incompressible backward-facing steps is of interest. For both of the cases discussed above, the reattachment length predicted by the Stress-ω model is closer to the measured length than that of the k-ω model. For the high-Re case, using the Stress-ω model reduces the difference from 13% for the Wilcox (2006) k-ω model to just 8%. For the low-Re case, the Stress-ω model's x_r is 18% longer than measured compared to 21% longer for the k-ω model.

6.7.2 Transonic Flow Over an Axisymmetric Bump

Subsection 5.8.5 includes computational results for the Bachalo-Johnson (1979) transonic-bump flow with three k-ω models and with the Spalart-Allmaras (1992) one-equation model. Although the Wilcox (2006) k-ω model and the Spalart-Allmaras model predict surface-pressure coefficient, C_p, values within 7% of measurements, the predicted shock location lies downstream of the shock in the experimental flowfield. While using a stress limiter with $C_{lim} = 1$ removes the k-ω model's discrepancy in shock location and brings C_p much closer to measured values, the same stress-limiter strength is much too strong for Mach

numbers of 3 and higher. An interesting question to pose is whether or not the Stress-ω model also misses the precise location of the shock for this flow. Figure 6.33 provides the answer to this question. Results shown are for an **EDDY2C** (see Appendix C) computation using the same 201 x 101 point mesh as for the k-ω model. As shown, the Stress-ω model's shock location and C_p distributions lie within 3% of corresponding measurements.

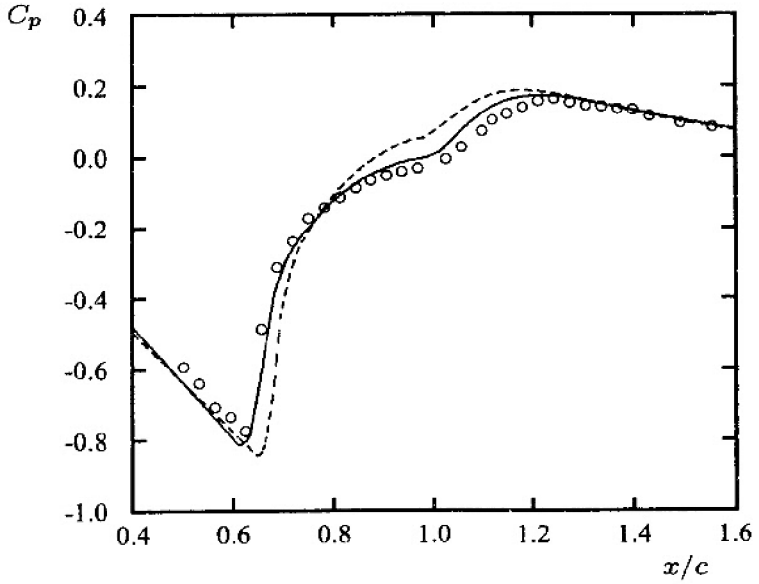

Figure 6.33: *Comparison of computed and measured surface-pressure coefficient for transonic flow past an axisymmetric bump:* — *Wilcox (2006) Stress-ω model;* - - - *Wilcox (2006) k-ω model;* o *Bachalo and Johnson.*

6.7.3 Mach 3 Compression Corners and Reflecting Shocks

We now consider the three shock-separated turbulent boundary-layer computations discussed in Subsection 5.8.7. The flows include two planar compression-corner flows and a reflecting-shock case. Figure 6.34 compares computed and measured surface pressure and skin friction using the high-Reynolds-number Stress-ω model. For reference, computed results for the Wilcox (2006) k-ω are included. In all cases, **EDDY2C** has been used with the same 401 x 201 finite-difference grids implemented for the k-ω model computations.

For all three cases, the Stress-ω model solution is quite close to the k-ω model solution, especially the surface pressure. The most noteworthy difference between the Stress-ω and k-ω solutions is in the skin friction downstream of reattachment. The values for the Stress-ω model are typically 15% higher than those for the k-ω model. This would correspond to a more rapid return to equilibrium, which more closely matches measurements.

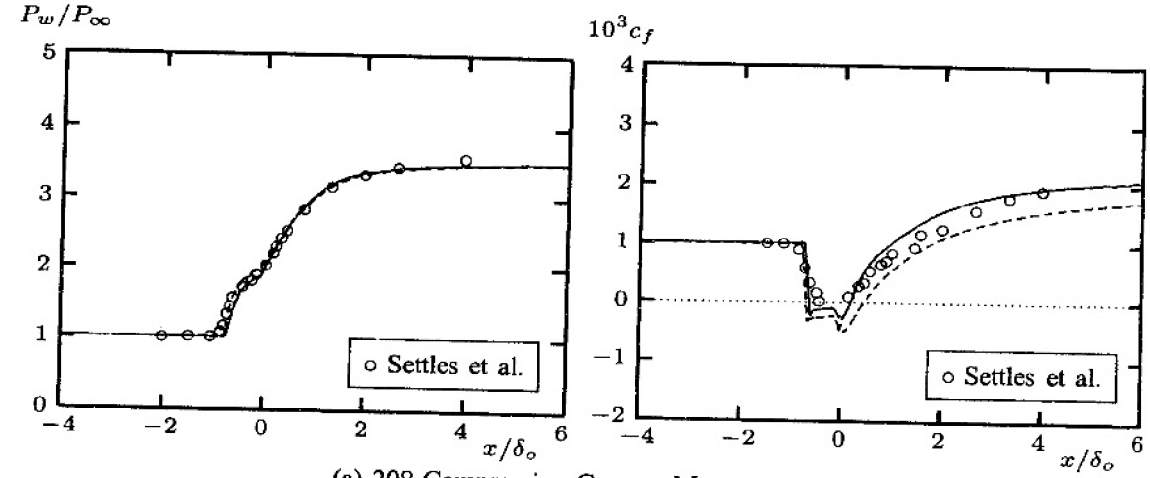

(a) 20° Compression Corner, $M_\infty = 2.79$

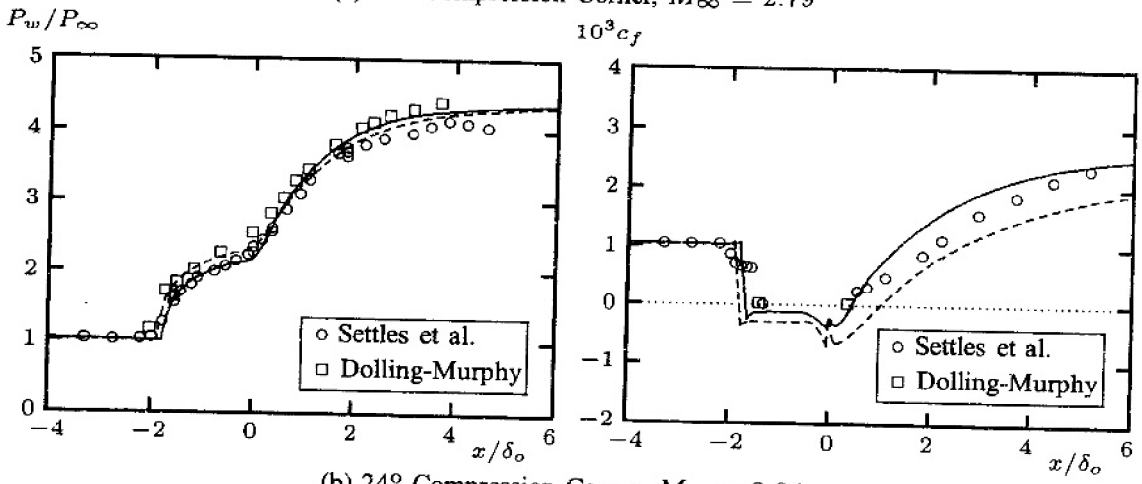

(b) 24° Compression Corner, $M_\infty = 2.84$

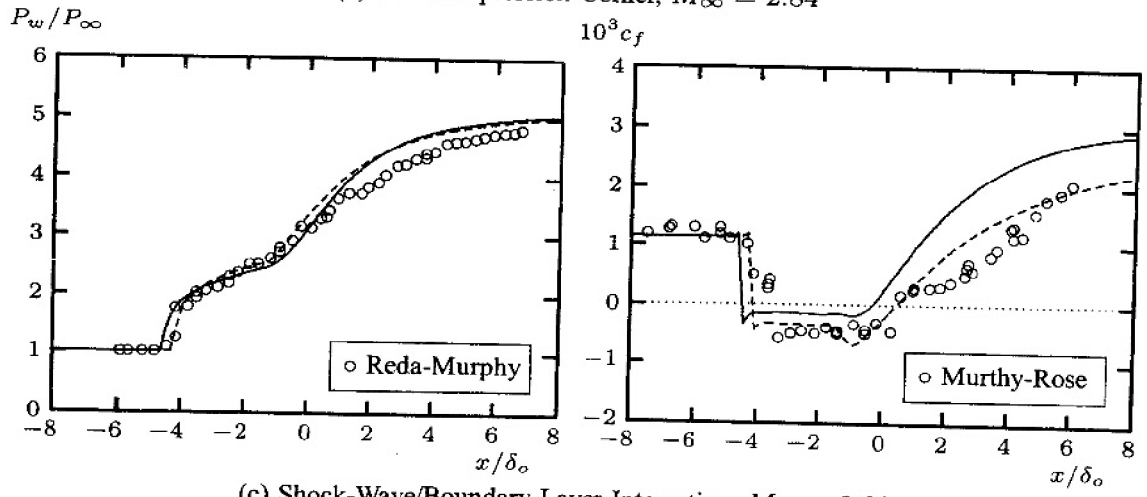

(c) Shock-Wave/Boundary-Layer Interaction, $M_\infty = 2.90$

Figure 6.34: *Comparison of computed and measured surface pressure and skin friction for Mach 3 shock-separated flows:* —— *Wilcox (2006) Stress-ω model;* - - - *Wilcox (2006) k-ω model.*

Gerolymos, Sauret and Vallet (2004) have computed these three flows using two ϵ-based stress-transport models. The first is the Gerolymos-Vallet (2001) stress-transport model and the second is a "wall-normal-free" version of the Launder-Shima (1989) stress-transport model. The terminology wall-normal-free (WNF) means free of any closure approximations that involve physical distance from a solid boundary. The primary differences between these two models is in the treatment of the pressure-strain correlation tensor, Π_{ij}, and the turbulent-transport tensor, C_{ijk} [see Equations (6.39) and (6.41)].

Figure 6.35 compares computed and measured surface pressure and skin friction for the Reda-Murphy shock-wave/boundary-layer interaction and Settles' 24° compression corner flow. As shown, the beginning of the pressure rise for the Gerolymos et al. (GV RSM) stress-transport model occurs a bit upstream of the measured rise for both cases. Computed skin friction downstream of reattachment is significantly larger than measured. The steep slope of the c_f curve indicates a much more rapid return to equilibrium than is present in the experimental flowfields.

For the Launder et al. (WNF-LSS RSM) stress-transport model, the beginning of the pressure rise occurs well downstream of the measured location, which would be consistent with a separation bubble about 2/3 the size of the bubble in the experiment. Although skin friction is not as large as with the Gerolymos et al. model, it still lies well above measured values. The steeper than measured slope of the c_f curve again indicates an approach to equilibrium that is significantly faster than that of the experimental flowfield.

As noted above, the main difference between these two stress-transport models based on the ϵ equation is in their treatment of the tensors Π_{ij} and C_{ijk}. The treatment of these two terms is far more complicated than that used for the Stress-ω model. By design, the Stress-ω model uses the *linear* Launder, Reece and Rodi (1975) closure model for Π_{ij} and an especially simple closure approximation for C_{ijk} based on standard gradient diffusion. The objective in developing the model has been to demonstrate how well an ω-based stress-transport model with an absolute minimum amount of complexity performs for complex turbulent flows. The Stress-ω model has just 8 closure coefficients, viz., C_1, C_2, α, β_o, β^*, σ, σ^* and σ_{do}, along with two very simple closure functions, f_β and σ_d/σ_{do} [see Equations (6.84) – (6.87)]. Note that all except C_1 and C_2 appear in the Wilcox (2006) k-ω model.

In distinct contrast, the Launder-Shima-Sharma model uses a *cubic* model for Π_{ij} and more than double the number of closure coefficients and closure functions used for the Stress-ω model. Although it is less complex, the Gerolymos model uses 4 closure coefficients and 4 closure functions just to model C_{ijk}.

Comparing the results shown in Figures 6.34 and 6.35 suggests an interesting question. How much of the complexity involved in these models is required to offset the deficiencies of the ϵ equation?

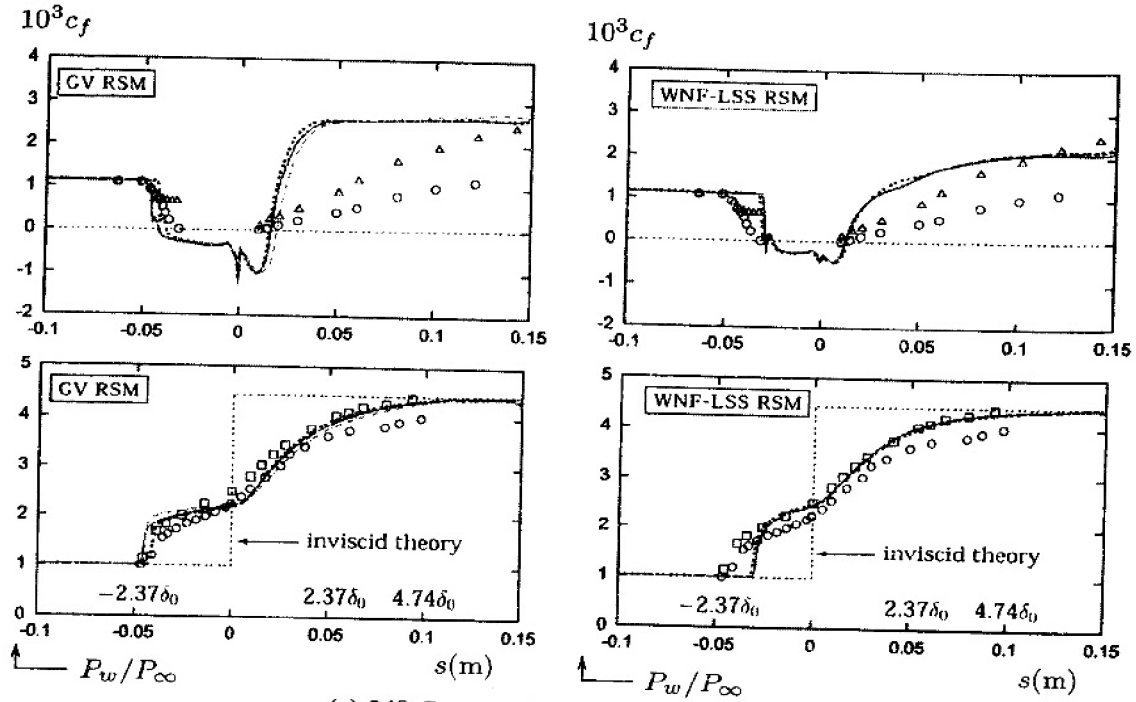

(a) 24° Compression Corner, $M_\infty = 2.84$

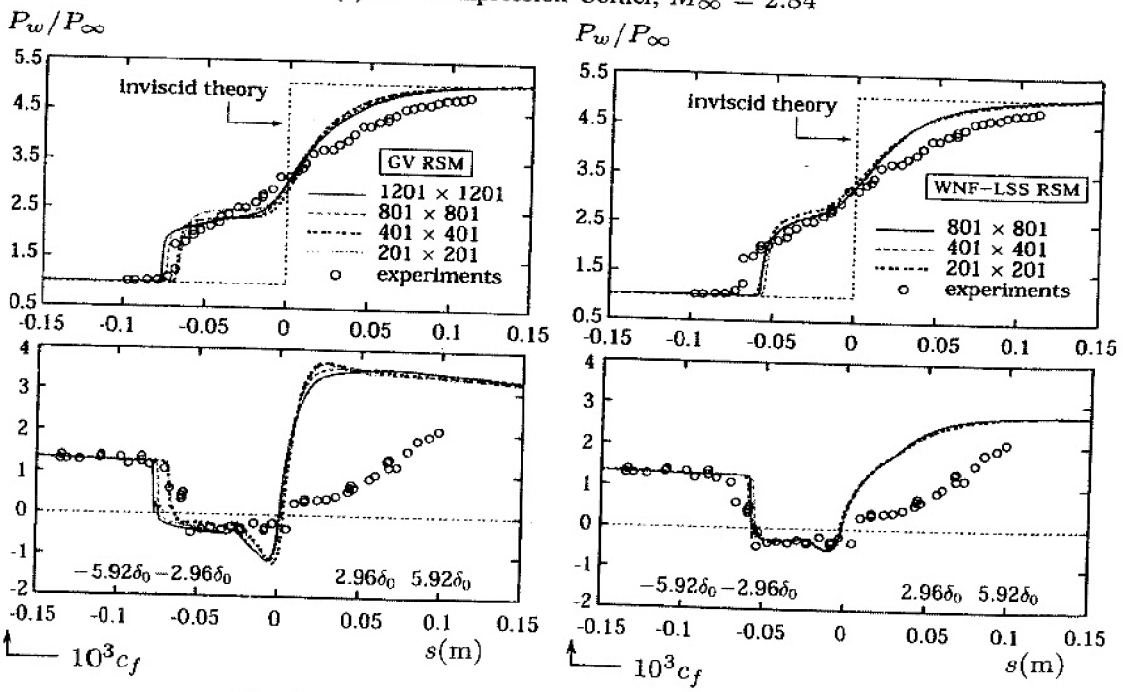

(b) Shock-Wave/Boundary-Layer Interaction, $M_\infty = 2.90$

Figure 6.35: *Comparison of computed and measured surface pressure and skin friction for Mach 3 shock-separated flows. [From Gerolymos et al. (2004) — Copyright © AIAA 2004 — Used with permission.]*

6.7.4 Hypersonic Shock-Separated Flows

Our final applications are for hypersonic flows. Figure 6.36 compares computed and measured surface pressure for the Mach 11 shock-wave/boundary-layer interaction experimentally documented by Holden (1978). The surface is highly cooled with a wall to adiabatic-wall temperature ratio of $T_w/T_{aw} = 0.2$. The **EDDY2C** computation employed the same 501 x 301 point finite-difference mesh that was used for the k-ω model computations of Subsection 5.8.8. Computed separation-bubble length for the Stress-ω model is $1.02\delta_o$, where δ_o is the incident boundary-layer thickness just upstream of the interaction. By comparison, the separation-bubble length is $1.53\delta_o$ for the k-ω model, so that the Stress-ω model solution shows larger differences between computed and measured surface pressure.

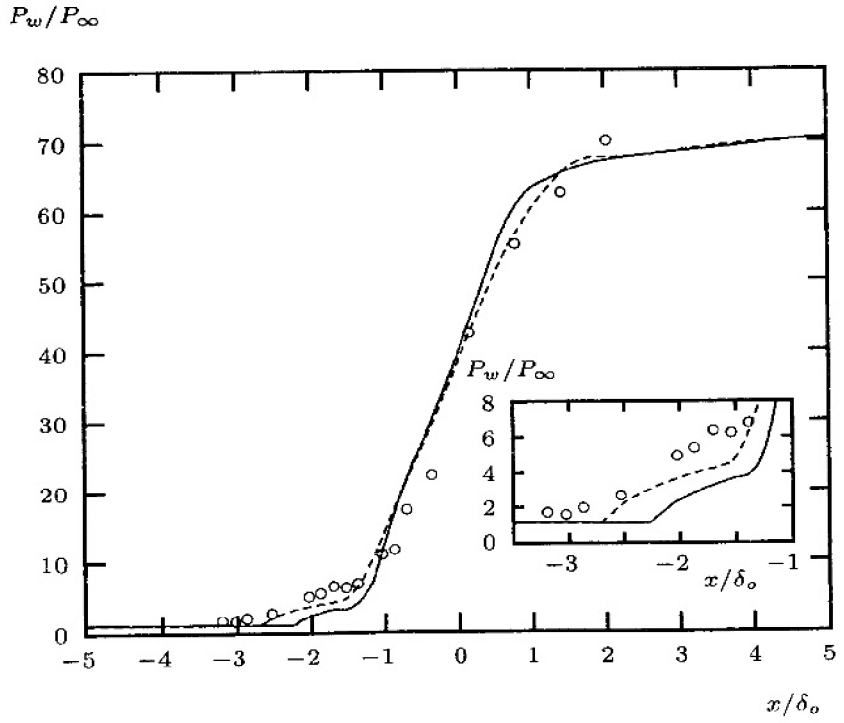

Figure 6.36: *Comparison of computed and measured surface pressure for a Mach 11 shock-wave/boundary-layer interaction:* —— *Wilcox (2006) Stress-ω model;* - - - *Wilcox (2006) k-ω model;* ○ *Holden (1978)*

We conclude with the Mach 7, 35 ° cylinder-flare configuration experimentally investigated by Kussoy and Horstman (1989). Like the Mach 11 flow above, this flow has a highly-cooled surface with $T_w/T_{aw} = 0.4$. Recall that analysis of this flow demonstrates the reattachment-point heat-transfer anomaly (see Subsection 5.8.9) that plagues two-equation turbulence models.

Figure 6.37 shows that, like the Wilcox (2006) k-ω model, the Stress-ω model gives a peak surface heat transfer rate, q_w, that is 50% higher than the measured rate. This is unsurprising for two reasons. First, both models use the Reynolds analogy in computing heat transfer. Second, the models differ in the way they compute the Reynolds stresses, which are determined from the larger energy-containing eddies. Since heat transfer occurs primarily in the smallest eddies, changes in the way the Reynolds stresses are computed should not be expected to make an appreciable difference. This is yet another example of how a stress-transport model reflects the strengths and weaknesses of the scale-determining equation.

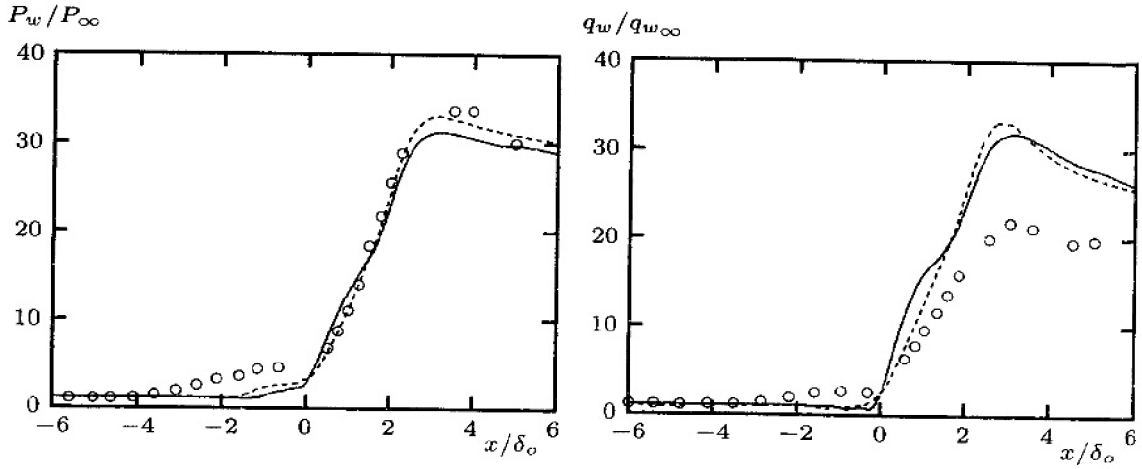

Figure 6.37: *Computed and measured surface pressure and heat transfer for Mach 7 flow into a 35° axisymmetric compression corner (cylinder-flare geometry):* —— *Wilcox (2006) Stress-ω model;* - - - *Wilcox (2006) k-ω model;* ○ *Kussoy-Horstman (1989)*

6.8 Range of Applicability

The two primary approaches to removing the limitations of the Boussinesq approximation are to use either a **nonlinear constitutive relation** or a **stress-transport model**. As discussed in Section 6.2, nonlinear constitutive relations offer some advantage over the Boussinesq approximation, most notably for flows in which anisotropy of the normal Reynolds stresses is important. **Algebraic Stress Models** provide a straightforward method for accurately predicting effects of streamline curvature and system rotation, although ad hoc corrections to standard two-equation models are just as effective. However, nonlinear constitutive relations offer no improvement over the Boussinesq approximation for flows with sudden changes in mean strain rate.

Despite their complexity, **stress-transport models** have great potential for removing shortcomings of the Boussinesq approximation in a natural way. Without ad hoc corrections, stress-transport models provide physically realistic predictions for flows with curved streamlines, system rotation, sudden changes in mean strain rate and secondary motions of the second kind. However, to be completely objective in our assessment, we must also note that in many such applications only qualitative agreement between theory and experiment has been obtained.

Just as older k-equation oriented, one-equation turbulence models share the shortcomings and successes of the mixing-length model, stress-transport models reflect the strengths and weaknesses of the scale-determining equation used with the model. There is an increasing pool of evidence that many of the shortcomings of stress-transport models are caused by the scale-determining equation. Results obtained for the backward-facing step and shock-separated flows (Section 6.7), for example, strongly suggest that predictions of standard stress-transport models can be improved by using the ω equation in place of the ϵ equation. This is not to say all of the ills of stress-transport models are caused by their use of the ϵ equation. Based on DNS results for backstep flows, Parneix et al. (1998) show that even when the dissipation rate is accurately predicted, current models are capable of predicting large discrepancies from measurements. We can reasonably infer that this points to deficiencies in modeling of the pressure-strain correlation tensor, Π_{ij}.

From a numerical point of view, stress-transport models are at least as difficult to solve as the corresponding two-equation model. Models based on the ϵ equation fail to predict a satisfactory law of the wall and require complicated viscous damping functions. Correspondingly, such models are generally very difficult to integrate. By contrast, models based on the ω equation require no special viscous corrections, and are much easier to integrate. In particular, the Stress-ω model usually requires only about 25% to 40% more computing time relative to the k-ω model.[7] Hence, the scale-determining equation may be even more important for stress-transport models than for two-equation models.

[7]Reflection of an oblique from a flat surface is an exception for the model. Much smaller timesteps are needed with Program **EDDY2C** to counter realizability violations mainly across the reflected shock. For such flows, required computing time can be 2-3 times longer than the time needed for the k-ω model.

Problems

6.1 The objective of this problem is to derive the modified law of the wall for flow over a curved wall according to the k-ω model.

(a) Verify that the dimensionless form of Equations (6.5) to (6.7) in the log layer is [with $\epsilon \equiv \nu/(u_\tau \mathcal{R})$ and assuming $\sigma_d = 0$ and $\beta = \beta_o$]:

$$\nu_T^+ \left(\frac{dU^+}{dy^+} - \epsilon U^+ \right) = 1, \qquad \nu_T^+ = \frac{k^+}{\omega^+}$$

$$\sigma^* \nu_T^+ \frac{d}{dy^+} \left[\nu_T^+ \frac{dk^+}{dy^+} \right] = \beta^* (k^+)^2 - 1 + \frac{9}{2} \epsilon (\nu_T^+)^2 U^+ \frac{dU^+}{dy^+}$$

$$\sigma \nu_T^+ \frac{d}{dy^+} \left[\nu_T^+ \frac{d\omega^+}{dy^+} \right] = \beta_o k^+ \omega^+ - \alpha \frac{\omega^+}{k^+}$$

(b) Assume a solution of the form

$$\begin{aligned} \frac{dU^+}{dy^+} &\sim \frac{1}{\kappa y^+} \left[1 + \epsilon a y^+ \ell n y^+ + O(\epsilon^2) \right] \\ k^+ &\sim \frac{1}{\sqrt{\beta^*}} \left[1 + \epsilon b y^+ \ell n y^+ + O(\epsilon^2) \right] \\ \omega^+ &\sim \frac{1}{\sqrt{\beta^*} \kappa y^+} \left[1 + \epsilon c y^+ \ell n y^+ + O(\epsilon^2) \right] \end{aligned}$$

with $\epsilon \ll 1$. Substitute into the equations for k^+ and ω^+ and verify that the coefficients b and c are given by

$$b = -\frac{9/2}{2 - \sigma^* \kappa^2 / \sqrt{\beta^*}} \qquad \text{and} \qquad c = \frac{\alpha}{\alpha - \beta_o/\beta^*} \, b$$

NOTE: Use the fact that for the k-ω model $\sigma \kappa^2 = (\beta_o/\beta^* - \alpha)\sqrt{\beta^*}$, and ignore terms proportional to y^+ relative to terms proportional to $y^+ \ell n y^+$.

(c) Substitute into the momentum equation and verify that

$$a + b - c = 1$$

(d) Using $\alpha = 13/25$, $\beta_o = 0.0708$, $\beta^* = 9/100$, $\sigma = 1/2$ and $\sigma^* = 3/5$, determine the numerical values of a, b and c, and show that the modified law of the wall is of the form

$$\left[1 - \beta_R \frac{y}{\mathcal{R}} \right] \frac{U}{u_\tau} \sim \frac{1}{\kappa} \ell n \left(\frac{u_\tau y}{\nu} \right) + \ldots$$

where $\beta_R \approx 8.9$.

6.2 For incompressible flow, we wish to use Speziale's nonlinear constitutive relation with the k-ω model. In terms of k-ω model parameters, the relation can be written as

$$\tau_{ij} = -\frac{2}{3}k\delta_{ij} + 2\nu_T S_{ij} + C_D \frac{k}{\beta^* \omega^2}\left(S_{ik}S_{kj} - \frac{1}{3}S_{mn}S_{mn}\delta_{ij}\right) + C_E \frac{k}{\beta^* \omega^2}\left(\mathring{S}_{ij} - \frac{1}{3}\mathring{S}_{mm}\,\delta_{ij}\right)$$

where C_D and C_E are closure coefficients whose values are to be determined.

(a) Verify for incompressible boundary layers that

$$S_{xy} = S_{yx} \approx \frac{1}{2}\frac{\partial U}{\partial y}, \qquad \text{all other } S_{ij} \approx 0$$

$$\mathring{S}_{xx} \approx -\left(\frac{\partial U}{\partial y}\right)^2, \qquad \text{all other } \mathring{S}_{ij} \approx 0$$

(b) Express the Reynolds-stress components τ_{xy}, τ_{xx}, τ_{yy} and τ_{zz} in terms of k, ν_T, β^*, ω and $\partial U/\partial y$ for incompressible boundary layers.

(c) Using the stresses derived in part (b), write the log-layer form of the mean-momentum, k and ω equations. Assume that $\sigma_d = 0$ and $\beta = \beta_o$.

(d) Assuming a solution of the form $\partial U/\partial y = u_\tau/(\kappa y)$ and k = constant, verify that

$$\left(\frac{\partial U}{\partial y}\right)^2 = \beta^* \omega^2$$

(e) Verify that

$$\overline{u'^2}/k = (8 - C_D + 8C_E)/12$$
$$\overline{v'^2}/k = (8 - C_D - 4C_E)/12$$
$$\overline{w'^2}/k = (8 + 2C_D - 4C_E)/12$$

(f) Determine the values of C_D and C_E that are consistent with the normal Reynolds stresses standing in the ratio

$$\overline{u'^2} : \overline{v'^2} : \overline{w'^2} = 4 : 2 : 3$$

6.3 Verify that in the log layer of an incompressible flat-plate boundary layer, the Wilcox-Rubesin nonlinear constitutive relation [Equation (6.15)] predicts that the normal Reynolds stresses stand in the ratio

$$\overline{u'^2} : \overline{v'^2} : \overline{w'^2} = 4 : 2 : 3$$

HINT: Recall that in the log layer, $\partial U/\partial y \approx \sqrt{\beta^*}\,\omega$.

6.4 Check the accuracy of Speziale's regularization approximation as quoted in Equation (6.28). To do so, let η vary from 0 to 1 and compare the right- and left-hand sides of the equation for $\xi = \frac{1}{4}, \frac{1}{2}$ and 1.

6.5 For incompressible flow in a rectangular duct, the strain rate and rotation tensors are approximately

$$S_{ij} = \begin{bmatrix} 0 & \frac{1}{2}\frac{\partial U}{\partial y} & \frac{1}{2}\frac{\partial U}{\partial z} \\ \frac{1}{2}\frac{\partial U}{\partial y} & 0 & 0 \\ \frac{1}{2}\frac{\partial U}{\partial x} & 0 & 0 \end{bmatrix} \quad \text{and} \quad \Omega_{ij} = \begin{bmatrix} 0 & \frac{1}{2}\frac{\partial U}{\partial y} & \frac{1}{2}\frac{\partial U}{\partial z} \\ -\frac{1}{2}\frac{\partial U}{\partial y} & 0 & 0 \\ -\frac{1}{2}\frac{\partial U}{\partial x} & 0 & 0 \end{bmatrix}$$

Determine τ_{xy}, τ_{xz}, τ_{yz} and $(\tau_{zz} - \tau_{yy})$ according to the Wilcox-Rubesin nonlinear constitutive relation [Equation (6.15)].

6.6 Derive the Poisson equation [Equation (6.51)] for the fluctuating pressure.

6.7 Consider the Launder-Reece-Rodi (LRR) rapid-pressure-strain closure approximation, Equation (6.63).

(a) Verify that a_{ijkl} satisfies the symmetry constraints in Equation (6.61).

(b) Invoke the constraints of Equation (6.62) and verify that α, β, η and υ are given by Equation (6.64).

(c) Form the tensor product

$$M_{ijkl}\frac{\partial U_k}{\partial x_l} = (a_{ijkl} + a_{jikl})\frac{\partial U_k}{\partial x_l}$$

and verify Equations (6.65) through (6.67).

6.8 Consider Lumley's general representation for Π_{ij} in Equation (6.69). Show that the LRR pressure-strain model [including A_{ij} as defined in Equation (6.58)] is the limiting case where all coefficients other than a_0, a_2, a_7 and a_9 equal to zero. Also, assuming $C_1 = 1.8$, determine the values of a_0, a_2, a_7 and a_9 that correspond to $C_2 = 0.4$, 0.5 and 0.6. Assume the flow is incompressible.

6.9 Suppose we have flow in a coordinate frame rotating with angular velocity $\boldsymbol{\Omega} = \Omega\mathbf{k}$, where $\mathbf{k}$ is a unit vector in the z direction. The incompressible Navier-Stokes equation is

$$\rho\frac{d\mathbf{u}}{dt} + 2\rho\boldsymbol{\Omega} \times \mathbf{u} = -\nabla p - \rho\boldsymbol{\Omega} \times \boldsymbol{\Omega} \times \mathbf{x} + \mu\nabla^2\mathbf{u}$$

where $\mathbf{x}$ is position vector and d/dt is the Eulerian derivative. Verify that the Reynolds-stress equation's inertial terms in a two-dimensional flow are as follows:

$$\frac{d}{dt}\begin{bmatrix} \tau_{xx} & \tau_{xy} & 0 \\ \tau_{xy} & \tau_{yy} & 0 \\ 0 & 0 & \tau_{zz} \end{bmatrix} + \begin{bmatrix} -4\Omega\tau_{xy} & 2\Omega(\tau_{xx} - \tau_{yy}) & 0 \\ 2\Omega(\tau_{xx} - \tau_{yy}) & 4\Omega\tau_{xy} & 0 \\ 0 & 0 & 0 \end{bmatrix} = \cdots$$

6.10 Consider the Launder, Reece and Rodi stress-transport model, Equations (6.73) through (6.77). This problem analyzes the model's predicted asymptotic solution for homogeneous plane shear, in which

$$\frac{\partial U_i}{\partial x_j} = \begin{bmatrix} 0 & S & 0 \\ 0 & 0 & 0 \\ 0 & 0 & 0 \end{bmatrix}$$

(a) Assuming that $\epsilon/k \longrightarrow$ constant as $t \longrightarrow \infty$, verify that

$$\frac{P}{\epsilon} \longrightarrow \frac{C_{\epsilon 2} - 1}{C_{\epsilon 1} - 1}$$

where $P = S\tau_{xy}$.

(b) Neglecting the pressure-echo effect, verify that

$$P_{ij} = \begin{bmatrix} 2S\tau_{xy} & S\tau_{yy} & S\tau_{yz} \\ S\tau_{yy} & 0 & 0 \\ S\tau_{yz} & 0 & 0 \end{bmatrix}, \quad D_{ij} = \begin{bmatrix} 0 & S\tau_{xx} & 0 \\ S\tau_{xx} & 2S\tau_{xy} & S\tau_{xz} \\ 0 & S\tau_{xz} & 0 \end{bmatrix}$$

(c) Assuming a solution of the form $\tau_{ij} = C_{ij}e^{\lambda t}$ where C_{ij} is independent of time and λ is a constant, verify that if τ_{xz} and τ_{yz} are initially zero, they are always zero, provided $\hat{\beta}(1 - \hat{\alpha}) > 0$.

(d) Determine ϵ/k and P/k as functions of $C_{\epsilon 1}$, $C_{\epsilon 2}$ and λ under the assumption that $\tau_{ij} = C_{ij}e^{\lambda t}$.

(e) Using results of Parts (a) – (d), determine $\overline{u'^2}/k$, $\overline{v'^2}/k$ and $\overline{w'^2}/k$ as algebraic functions of the closure coefficients. **HINT:** You can simplify your computations somewhat by first writing the equation for τ_{ij} as an equation for $\tau_{ij} + \frac{2}{3}k\delta_{ij}$.

(f) Using the following two sets of closure coefficient values, compute the numerical values of $\overline{u'^2}/k$, $\overline{v'^2}/k$ and $\overline{w'^2}/k$.

1. Original LRR: $C_1 = 1.5$, $C_2 = 0.4$, $C_{\epsilon 1} = 1.44$, $C_{\epsilon 2} = 1.90$
2. Revised LRR: $C_1 = 1.8$, $C_2 = 0.6$, $C_{\epsilon 1} = 1.44$, $C_{\epsilon 2} = 1.92$

6.11 Consider the Stress-ω model, Equations (6.78) through (6.87). In the following computations, you can assume $\sigma_d = 0$ and $\beta = \beta_o$.

(a) State the limiting form of the equations for the incompressible, two-dimensional log layer.

(b) Assuming a solution of the form

$$\frac{dU}{dy} \sim \frac{u_\tau}{\kappa y}, \qquad k \sim \frac{u_\tau^2}{\sqrt{\beta^*}}, \qquad \omega \sim \frac{u_\tau}{\sqrt{\beta^*}\kappa y}$$

determine κ, $-\overline{u'v'}/k$, $\overline{u'^2}/k$, $\overline{v'^2}/k$ and $\overline{w'^2}/k$ as algebraic functions of the closure coefficients. **HINT:** All are constant.

(c) Using the closure coefficient values in Equations (6.83) through (6.87), verify that $\kappa \approx 0.40$, $-\overline{u'v'}/k \approx 0.30$ and $\overline{u'^2} : \overline{v'^2} : \overline{w'^2} \approx 4.0 : 1.9 : 2.9$.

6.12 Consider the Launder, Reece and Rodi stress-transport model, Equations (6.73) through (6.77).

(a) State the limiting form of the equations for the incompressible, two-dimensional log layer.

(b) Assuming a solution of the form

$$\frac{dU}{dy} \sim \frac{u_\tau}{\kappa y}, \qquad k \sim \frac{u_\tau^2}{\sqrt{C_\mu}}, \qquad \epsilon \sim \frac{u_\tau^3}{\kappa y}$$

determine κ, $-\overline{u'v'}/k$, $\overline{u'^2}/k$, $\overline{v'^2}/k$ and $\overline{w'^2}/k$ as algebraic functions of the closure coefficients. **HINTS:** All are constant. Also, the ϵ equation yields κ as a function of the closure coefficients and $\overline{v'^2}/k$. You needn't simplify further.

(c) Using the closure coefficient values in Equation (6.77), verify that $\kappa \approx 0.39$, $-\overline{u'v'}/k \approx 0.30$, and $\overline{u'^2} : \overline{v'^2} : \overline{w'^2} \approx 4 : 2.2 : 3.2$. **HINT:** Combining the simplified ϵ and τ_{yy} equations yields a cubic equation for κ. It can be solved in closed form by assuming $\kappa = 0.4(1 + \delta)$, linearizing and solving for δ.

6.13 Consider the Stress-ω model, Equations (6.78) through (6.87). In the following computations, you can assume $\sigma_d = 0$ and $\beta = \beta_o$.

(a) State the limiting form of the equations for the incompressible, two-dimensional log layer.

(b) Assuming a solution of the form

$$\frac{dU}{dy} \sim \frac{u_\tau}{\kappa y}, \qquad k \sim \frac{u_\tau^2}{\sqrt{\beta^*}}, \qquad \omega \sim \frac{u_\tau}{\sqrt{\beta^*}\kappa y}$$

determine κ and verify that the Reynolds stress components according to the Stress-ω model are:

$$\begin{aligned}
\frac{\tau_{xx}}{k} &\sim \frac{1}{C_1}\left[\frac{2}{3}(1 - C_1) - \left(2 - \frac{4}{3}\hat{\alpha} + \frac{2}{3}\hat{\beta}\right)\right] \\
\frac{\tau_{yy}}{k} &\sim \frac{1}{C_1}\left[\frac{2}{3}(1 - C_1) - \left(\frac{2}{3}\hat{\alpha} - \frac{4}{3}\hat{\beta}\right)\right] \\
\frac{\tau_{zz}}{k} &\sim \frac{1}{C_1}\left[\frac{2}{3}(1 - C_1) - \left(\frac{2}{3}\hat{\alpha} + \frac{2}{3}\hat{\beta}\right)\right] \\
\frac{\tau_{xy}}{k} &\sim \frac{1}{C_1}\left[(\hat{\alpha} - 1)\frac{\tau_{yy}}{\tau_{xy}} + \hat{\beta}\frac{\tau_{xx}}{\tau_{xy}} + \frac{1}{2}\hat{\gamma}\frac{k}{\tau_{xy}}\right]
\end{aligned}$$

(c) Substituting for $\hat{\alpha}$, $\hat{\beta}$ and $\hat{\gamma}$ in terms of C_1 and C_2 from Equation (6.83), show that the normal stresses are

$$\begin{aligned}
\frac{\tau_{xx}}{k} &\sim -\frac{22C_1 + 12C_2 + 8}{33C_1} \\
\frac{\tau_{yy}}{k} &\sim -\frac{22C_1 - 30C_2 + 2}{33C_1} \\
\frac{\tau_{zz}}{k} &\sim -\frac{22C_1 + 18C_2 - 10}{33C_1}
\end{aligned}$$

(d) Substituting the results of Part (c) into the last of the equations developed in Part (b), show that the shear stress satisfies the following equation.

$$\left(\frac{\tau_{xy}}{k}\right)^2 = \frac{2}{15(11C_1)^2}\left(55 + 242C_1 - 330C_2 - 165C_2^2\right) \tag{6.127}$$

(e) Verify that if we insist upon τ_{xy}/k being equal to Bradshaw's constant so that $\sqrt{\beta^*} = \beta_r = 0.3$, necessarily C_1 and C_2 are related by a simple quadratic. Make a table of values of C_2 as a function for C_1 for the range of physically-realistic values based on measurements [cf. Equation (6.59)].

6.14 Consider the low-Reynolds-number version of the Stress-ω model, Equations (6.78) through (6.80), (6.82) and (6.109) through (6.114). Modify Program **SUBLAY** (see Appendix C) as needed to permit specifying the values of C_2 and R_ω (see Subroutine *START*).

(a) With $R_\omega = 22/9$, compute the value of the constant in the law of the wall, C, for $C_2 = 0.40, 0.45, 0.50$ and 0.55.

(b) Leaving all other values unchanged, determine the value of R_ω that gives $C = 5.50$ for $C_2 = 0.40, 0.45, 0.50$ and 0.55.

6.15 Using Program **MIXER** (see Appendix C), compute δ'/δ'_o at Mach 0, 0.5, 1, 2, 3, 4 and 5 for the Stress-ω model. Do your computations using 101 grid points, and exercise the program for the Sarkar, Zeman and Wilcox compressibility corrections defined in Equations (5.81) through (5.83). Plot your results for δ'/δ'_o and compare to the following experimental data compiled by Barone et al. (2006).

M_c	δ'/δ'_o	M_c	δ'/δ'_o	M_c	δ'/δ'_o	M_c	δ'/δ'_o
0.059	1.000	0.535	0.810	0.691	0.565	0.945	0.489
0.206	0.985	0.580	0.927	0.720	0.633	0.985	0.400
0.411	0.973	0.589	0.812	0.795	0.502	0.992	0.464
0.455	0.817	0.640	0.762	0.825	0.535	1.040	0.518
0.455	0.965	0.640	0.841	0.838	0.570	1.122	0.474
0.510	0.971	0.668	0.733	0.860	0.575	1.312	0.436
0.519	0.957	0.677	0.698	0.862	0.457	1.449	0.442

6.16 The object of this problem is to compare predictions of the Stress-ω model with measured properties of a turbulent boundary layer with surface mass injection. The experiment to be simulated was conducted by Andersen et al. (1972). Use Program **EDDYBL**, its menu-driven setup utility, Program **EDDYBL_DATA** and the input data provided on the companion CD (see Appendix C). Do computations using the high-Re and low-Re versions of the Stress-ω model. Compare computed skin friction with the following measured values.

s (ft)	c_f	s (ft)	c_f	s (ft)	c_f
0.8462	$1.92{\cdot}10^{-3}$	3.8376	$1.16{\cdot}10^{-3}$	6.8224	$9.00{\cdot}10^{-4}$
1.8368	$1.55{\cdot}10^{-3}$	4.8216	$1.04{\cdot}10^{-3}$	7.5112	$8.50{\cdot}10^{-4}$
2.8208	$1.31{\cdot}10^{-3}$	5.8384	$9.70{\cdot}10^{-4}$		

6.17 The object of this problem is to compare predictions of the Stress-ω model with measured properties of a turbulent boundary layer with adverse pressure gradient. The experiment to be simulated was conducted by Bradshaw [see Coles and Hirst (1969) – Flow 3300]. Use Program **EDDYBL**, its menu-driven setup utility, Program **EDDYBL_DATA** and the input data provided on the companion CD (see Appendix C). Do computations using the high-Re and low-Re versions of the Stress-ω model. Compare computed skin friction with the following measured values.

s (ft)	c_f	s (ft)	c_f
2.5	$2.45 \cdot 10^{-3}$	5.0	$1.74 \cdot 10^{-3}$
3.0	$2.17 \cdot 10^{-3}$	6.0	$1.61 \cdot 10^{-3}$
3.5	$2.00 \cdot 10^{-3}$	7.0	$1.56 \cdot 10^{-3}$
4.0	$1.91 \cdot 10^{-3}$		

6.18 The object of this problem is to compare predictions of the Stress-ω model with measured properties of a Mach 2.65 turbulent boundary layer with adverse pressure gradient and surface heat transfer. The experiment to be simulated was conducted by Fernando and Smits [see Fernholz and Finley (1981)]. Use Program **EDDYBL**, its menu-driven setup utility, Program **EDDYBL_DATA** and the input data provided on the companion CD (see Appendix C). Do computations using the high-Re and low-Re versions of the Stress-ω model. Compare computed skin friction with the following measured values.

s (m)	c_f	s (m)	c_f
1.151	$9.92 \cdot 10^{-4}$	1.273	$9.41 \cdot 10^{-4}$
1.172	$9.96 \cdot 10^{-4}$	1.299	$1.01 \cdot 10^{-3}$
1.197	$9.67 \cdot 10^{-4}$	1.324	$1.07 \cdot 10^{-3}$
1.222	$9.43 \cdot 10^{-4}$	1.349	$1.08 \cdot 10^{-3}$
1.248	$9.46 \cdot 10^{-4}$	1.361	$1.04 \cdot 10^{-3}$

6.19 Compute the Bachalo-Johnson transonic bump flow using the Stress-ω model with viscous modifications. Use Program **EDDY2C**, its menu-driven setup utility, Program **EDDY2C_DATA**, and the input data provided on the companion CD (see Appendix C).

(a) You must first run Program **EDDYBL** to establish flow properties at the upstream boundary. To avoid having to adjust the transition point, select the Stress-ω model "w/o viscous mods." Verify that the Reynolds number based on momentum thickness is 2390.

(b) Run **EDDY2C** for the Stress-ω model "with viscous mods" and make graphs of the "residual" and the separation-point location, x_s/c, as functions of timestep number.

(c) Compare the value of x_s/c predicted by the low-Re Stress-ω model relative to the value predicted without viscous modifications, viz., $x_s/c = 0.66$.

NOTE: This computation will take about a half hour of CPU time on a 3-GHz Pentium-D microcomputer.

6.20 Compute Settles' Mach 2.84 flow into a 24° compression corner using the Stress-ω model with viscous modifications. Use Program **EDDY2C**, its menu-driven setup utility, Program **EDDY2C_DATA**, and the input data provided on the companion CD (see Appendix C).

(a) You must first run Program **EDDYBL** to establish flow properties at the upstream boundary. After selecting the Stress-ω model "with viscous mods," modify the supplied input-data file *eddybl.dat*, using trial and error to adjust the "Maximum Arclength" (SSTOP) so that the Reynolds number based on momentum thickness is $9.38 \cdot 10^4$.

(b) Run **EDDY2C** for the Stress-ω model "with viscous mods" and make graphs of the "residual" and the length of the separation bubble, $(x_r - x_s)/\delta_o$, as functions of timestep number.

(c) Compare the value of $(x_r - x_s)/\delta_o$ predicted by the low-Re Stress-ω model relative to the value predicted without viscous modifications, viz., $(x_r - x_s)/\delta_o = 2.13$.

NOTE: This computation will take a little less than an hour of CPU time on a 3-GHz Pentium-D microcomputer.

Chapter 7

Numerical Considerations

Modern turbulence model equations pose special numerical difficulties that must be understood in order to obtain reliable numerical solutions, even for boundary-layer flows where the equations are parabolic. For one-equation, two-equation and stress-transport models, these difficulties can include stiffness caused by the presence of an additional time scale, singular behavior near solid boundaries, non-analytical behavior at sharp turbulent/nonturbulent interfaces and sensitivity to freestream boundary conditions. This chapter focuses on these difficulties and on the solution methods for turbulence-model equations that have evolved.

7.1 Multiple Time Scales and Stiffness

One key issue that must be addressed in developing a numerical algorithm for fluid-flow problems is that of the physically relevant time scales. Taking proper account of these time scales is a necessary condition for numerical accuracy. For example, when we deal with non-chemically-reacting laminar flow, there are two distinct time scales corresponding to different physical processes. If L and U denote characteristic length and velocity for the flowfield, a is sound speed and ν is kinematic viscosity, the time scales are:

- Wave propagation, $t_{wave} \sim L/|U \pm a|$
- Molecular diffusion, $t_{diff} \sim L^2/\nu$

When we use turbulence-transport equations, we have yet another time scale corresponding to the rate of decay of turbulence properties. In terms of the specific dissipation rate, $\omega \sim \epsilon/k$, this time scale is:

- Dissipation, $t_{diss} \sim 1/\omega \sim k/\epsilon$

Any numerical algorithm designed for use with turbulence-transport equations should take account of all three of these time scales.

In terms of the Reynolds number, $Re_L = UL/\nu$, and the Mach number, $M = U/a$, the ratio of t_{diff} to t_{wave} is given by

$$\frac{t_{diff}}{t_{wave}} \sim \frac{|M \pm 1| Re_L}{M} \tag{7.1}$$

Clearly, for high Reynolds number flows the diffusion time scale is much longer than the wave-propagation time scale regardless of Mach number. Diffusion will generally be important over very short distances such as the thickness of a boundary layer, δ, i.e., when $L \sim \delta$. For specified freestream Mach and Reynolds numbers, the relative magnitudes of the diffusion and wave-propagation time scales are more-or-less confined to a limited range. This is not the case for the dissipation time scale.

The specific dissipation rate, ω, can vary by many orders of magnitude across a turbulent boundary layer. Consequently, in the same flow, t_{diss} can range from values much smaller than the other time scales to much larger. This is a crude reminder of the physical nature of turbulence, which consists of a wide range of frequencies. Thus, regardless of the flow speed, we should expect the dissipation time to have a nontrivial impact on numerical algorithms.

Because of the multiplicity of time scales attending use of turbulence-transport equations, especially two-equation models and stress-transport models, we must contend with an unpleasant feature known as **stiffness**. An equation, or system of equations, is said to be stiff when there are two or more very different scales of the independent variable on which the dependent variables are changing. For example, consider the equation

$$\frac{d^2y}{dt^2} = 100y \tag{7.2}$$

The general solution to this equation is

$$y(t) = Ae^{-10t} + Be^{10t} \tag{7.3}$$

If we impose the initial conditions

$$y(0) = 1 \qquad \text{and} \qquad \dot{y}(0) = -10 \tag{7.4}$$

the exact solution becomes

$$y_{exact}(t) = e^{-10t} \tag{7.5}$$

Unfortunately, any roundoff or truncation error in a numerical solution can excite the e^{10t} factor, viz., we can inadvertently wind up with

$$y_{numerical}(t) = e^{-10t} + \epsilon e^{10t}, \qquad |\epsilon| \ll 1 \tag{7.6}$$

No matter how small ϵ is, the second term will eventually dominate the solution. The equivalent situation for a system of equations is to have eigenvalues of the characteristic equation of very different magnitudes.

It is easy to see that most turbulence-transport equations hold potential for being stiff. The k-ϵ model is notoriously stiff when some of the commonly used viscous damping functions are introduced. Stress-transport models that use the ϵ equation are often so stiff as to almost preclude stable numerical solution. Some of the difficulty with the ϵ equation occurs because the dissipation time scale is a function of both k and ϵ. Transient solution errors in both parameters can yield large variations in k/ϵ, so that the dissipation time scale can assume an unrealistic range of values. By contrast, near-wall solutions to models based on the ω equation have well-defined algebraic solutions approaching a solid boundary, and are thus much easier to integrate.

7.2 Numerical Accuracy Near Boundaries

Proper treatment of boundary conditions is necessary for all numerical solutions, regardless of the equations being solved. Because of the special nature of turbulence-transport equations, there are two types of boundary behavior that require careful treatment. Specifically, quantities such as dissipation rate, ϵ, and specific dissipation rate, ω, grow so rapidly approaching a solid boundary that they appear to be singular. In fact, ω is singular for a perfectly-smooth wall. Also, at interfaces between turbulent and nonturbulent regions, velocity and other properties have nearly discontinuous slopes approaching the interface. Because wall-bounded flows typically involve both types of boundaries, accurate numerical solutions must account for the special problems presented by this unusual solution behavior.

7.2.1 Solid Surfaces

We know that for a perfectly-smooth wall, the specific dissipation rate varies in the sublayer as y^{-2} approaching the surface (see Subsection 4.6.3). Even if we choose to use wall functions to obviate integration through the viscous sublayer, analysis of the log layer (see Subsection 4.6.1) shows that both ϵ and ω are inversely proportional to distance from the surface. In either case, care must be taken to accurately compute derivatives of such functions.

To illustrate the difficulty imposed by singular behavior approaching a solid boundary, consider the function ϕ defined by

$$\phi = \frac{1}{y^n}, \qquad n = 1 \text{ or } 2 \tag{7.7}$$

The exact first and second derivatives are

$$\frac{d\phi}{dy} = -\frac{n}{y^{n+1}} \quad \text{and} \quad \frac{d^2\phi}{dy^2} = \frac{n(n+1)}{y^{n+2}} \tag{7.8}$$

Using central differences on a uniform grid with $y_j = j\Delta y$, a straightforward calculation shows that

$$\left(\frac{d\phi}{dy}\right)_j \approx \frac{\phi_{j+1} - \phi_{j-1}}{2\Delta y} = \left[\frac{j^2}{j^2-1}\right]^n \left(\frac{d\phi}{dy}\right)_{exact} \tag{7.9}$$

and

$$\left(\frac{d^2\phi}{dy^2}\right)_j \approx \frac{\phi_{j+1} - 2\phi_j + \phi_{j-1}}{(\Delta y)^2} \approx \left[\frac{j^2}{j^2-1}\right]^n \left(\frac{d^2\phi}{dy^2}\right)_{exact} \tag{7.10}$$

where subscript j denotes the value at $y = y_j$. Table 7.1 lists the errors attending use of central differences as a function of $\Delta y/y_j$ for $n = 1$ and $n = 2$.

Table 7.1: *Central-Difference Errors for* $\phi = y^{-n}$.

j	$\Delta y/y_j$	(% Error)$_{n=1}$	(% Error)$_{n=2}$
2	0.50	33	78
3	0.33	13	27
5	0.20	4	9
7	0.14	2	4
10	0.10	1	2

Clearly, significant numerical errors are introduced if the ratio $\Delta y/y_j$ is not small. If wall functions are used (corresponding to $n = 1$), regardless of how close the grid point nearest the surface lies, nontrivial numerical errors in derivatives result for $j < 5$. Consequently, simply using wall functions as effective boundary conditions applied at the first grid point above the surface is unsatisfactory. Rather, the value for ω or ϵ should be specified for all points below $j = 4$ (at a minimum) to insure numerical accuracy. This is undoubtedly the primary reason why most researchers find their numerical solutions to be sensitive to near-wall grid-point spacing when they use wall functions. As an alternative, a relatively large cell can be used next to the surface, so that for example, $y_1 = 0$, $y_2 = \Delta y$, $y_3 = 1.2\Delta y$, etc. By using the Rubel-Melnik (1984) transformation, Program **DEFECT** (see Appendix C) automatically generates such a grid.

When the k-ω or Stress-ω model is integrated through the viscous sublayer for a perfectly-smooth surface (corresponding to $n = 2$), there is no practical

way to avoid having $\Delta y/y_2 \sim 1$. The exact solution to the ω equation in the viscous sublayer is

$$\omega \sim \frac{6\nu_w}{\beta_o y^2}, \qquad y^+ < 2.5 \tag{7.11}$$

If we simply use the value of ω according to Equation (7.11) at the first grid point above the surface, Table 7.1 shows that the molecular diffusion term will be in error by 78%. This, in turn, will increase values of ω at larger values of y. Recall that the surface value of ω has a strong effect on the additive constant, C, in the law of the wall (see Subsection 4.7.2). Thus, computing too large a value of ω near the surface will distort the velocity profile throughout the sublayer and into the log layer. That is, numerically inaccurate near-wall ω values can distort the entire boundary-layer solution.

The remedy that has proven very effective for eliminating this numerical error is to use Equation (7.11) for the first 7 to 10 grid points above the surface. Of course, these grid points must lie below $y^+ = 2.5$ since Equation (7.11) is not valid above this point. This procedure has been used in Programs **PIPE**, **SUBLAY** and **EDDYBL** (see Appendix C). This procedure is easy to implement for boundary-layer programs and simple one-dimensional time-marching applications. However, it is very inconvenient for general flow solvers, especially when unstructured grids are used.

An alternative procedure for accurately computing near-surface behavior of ω is to use the rough-wall boundary condition. As shown in Subsection 4.7.2 for the k-ω model and Subsection 6.6.1 for the Stress-ω model,

$$\omega = \frac{u_\tau^2}{\nu_w} S_R \qquad \text{at} \qquad y = 0 \tag{7.12}$$

where

$$S_R = (200/k_s^+)^2, \qquad k_s^+ < 5 \tag{7.13}$$

The quantity $k_s^+ = u_\tau k_s/\nu_w$ is the scaled surface-roughness height.

In order to simulate a smooth surface, we simply require that k_s^+ be smaller than 5. Then, combining Equations (7.12) and (7.13), we arrive at the **slightly-rough-surface boundary condition** on ω, viz.,

$$\omega = \frac{40000\nu_w}{k_s^2} \qquad \text{at} \qquad y = 0 \tag{7.14}$$

It is important to select a small enough value of k_s to insure that $k_s^+ < 5$. If too large a value is selected, the skin friction values will be larger than smooth-wall values.

As a final comment, the near-wall solution to the ω equation for a rough wall is given by

$$\omega = \frac{\omega_w}{\left(1 + \sqrt{\frac{\beta_o \omega_w}{6\nu_w}}\, y\right)^2}, \qquad y^+ < 2.5 \tag{7.15}$$

where ω_w is the surface value of ω. An important test for numerical accuracy of any finite-difference program implementing the ω equation is to verify that solutions match either Equation (7.11) or (7.15). If the program fails to accurately reproduce the near-wall ω variation, the program is unlikely to yield accurate results.

For smooth-surface applications, Menter (1992c) proposes an alternative to the slightly-rough-surface boundary condition. In Menter's approach, the surface value of ω depends upon the distance of the first grid point above the surface, Δy_2, according to

$$\omega = \frac{N\nu_w}{(\Delta y_2)^2} \qquad \text{at} \qquad y = 0 \tag{7.16}$$

where N is a constant. Comparison with Equation (7.14) shows that this corresponds to setting the surface-roughness height according to

$$\frac{40000\nu_w}{k_s^2} = \frac{N\nu_w}{(\Delta y_2)^2} \quad \Longrightarrow \quad k_s^+ = \frac{200\Delta y_2^+}{\sqrt{N}} \tag{7.17}$$

Choosing $N = 1600$, for example, means that whenever the grid is such that $\Delta y_2 < 1$, the effective surface-roughness height will be less than 5. This, of course, corresponds to a hydraulically-smooth surface.

The advantage of Menter's method for smooth surfaces is simple. The solution is guaranteed to have sufficiently small k_s to achieve hydraulic smoothness. The only disadvantage is that the boundary condition for ω is grid dependent, which complicates the task of determining grid independence of the solution. However, since the turbulence-model solution is more-or-less unaffected by decreasing k_s^+ below 5, the problem is minor.

Rapid variation of the dependent variable is not the only potential source of numerical error near solid boundaries. Another serious consideration is round-off error resulting from the relatively small difference between two numbers of comparable magnitude. This problem is frequently encountered with low-Reynolds-number k-ϵ models. For example, damping functions such as

$$f_2 = 1 - e^{-Re_T^2} \qquad \text{and} \qquad f_\mu = 1 - e^{-0.0115y^+} \tag{7.18}$$

appear in the Lam-Bremhorst (1981) and Chien (1982) models. Approaching the surface, desired asymptotic behavior depends upon accurate values of these damping functions. If single-precision accuracy is used, it is advisable to use Taylor-series expansions for the damping functions close to the surface. For example, Chien's f_μ can be computed according to

$$f_\mu = \begin{cases} 1 - e^{-0.0115y^+}, & y^+ > 0.01 \\ 0.0115y^+, & y^+ \le 0.01 \end{cases} \tag{7.19}$$

This procedure is used in Program **EDDYBL** (see Appendix C) to insure numerically accurate solutions.

7.2.2 Turbulent/Nonturbulent Interfaces

More often than not, turbulence-model equations that are in general usage appear to predict sharp interfaces between turbulent and nonturbulent regions, i.e., interfaces where discontinuities in derivatives of flow properties occur at the edge of the shear layer. As noted in earlier chapters, these interfaces bear no relation to the physical turbulent/nonturbulent interfaces that actually fluctuate in time and have smooth Reynolds-averaged properties. The mixing-length model, for example, exhibits a sharp interface for the far wake (see Subsection 3.3.1). That is, the predicted velocity profile is

$$U(x,y) = \begin{cases} U_\infty - 1.38\sqrt{\dfrac{D}{\rho x}}\left[1-(y/\delta)^{3/2}\right]^2, & y < \delta \\ U_\infty, & y \geq \delta \end{cases} \tag{7.20}$$

where U_∞ is freestream velocity, D is drag per unit width, ρ is density, y is distance from the centerline and δ is the half-width of the wake. Clearly, all derivatives of U above $\partial^2 U/\partial y^2$ are discontinuous at $y = \delta$. Such a solution is called a **weak solution** to the differential equation.

By definition [see Courant and Hilbert (1966)], a weak solution to a partial differential equation

$$\mathcal{L}[u] = \frac{\partial}{\partial x}P(x,y,u) + \frac{\partial}{\partial y}Q(x,y,u) + S(x,y,u) = 0 \tag{7.21}$$

satisfies the following conditions.

1. $u(x,y)$ is piecewise continuous and has piecewise continuous first derivatives in two adjacent domains, R_1 and R_2.

2. $\mathcal{L}[u] = 0$ in R_1 and R_2.

3. For any test function $\phi(x,y)$ that is differentiable to all orders and that is identically zero outside of R_1 and R_2, the following integral over the combined region $R = R_1 \cup R_2$ must be satisfied.

$$\int\int_R \left[P\frac{\partial\phi}{\partial x} + Q\frac{\partial\phi}{\partial y} - S\phi\right] dxdy = 0 \tag{7.22}$$

A similar result holds for a system of equations. Clearly, Equation (7.22) can be rewritten as

$$\int\int_R \left[\frac{\partial(\phi P)}{\partial x} + \frac{\partial(\phi Q)}{\partial y}\right] dxdy - \int\int_R \phi\left[\frac{\partial P}{\partial x} + \frac{\partial Q}{\partial y} + S\right] dxdy = 0 \tag{7.23}$$

The second integral vanishes since P, Q and S satisfy the differential equation in both R_1 and R_2. Then, using Gauss' theorem, if Γ is the curve of discontinuity that divides R_1 and R_2 and $\mathbf{n} = (n_x, n_y)$ is the unit normal to Γ, there follows:

$$\int_\Gamma \phi \left([P]n_x + [Q]n_y\right) ds = 0 \tag{7.24}$$

The symbols $[P]$ and $[Q]$ denote the jumps in P and Q across Γ. Since the function ϕ is arbitrary, we can thus conclude that the **jump condition** across the surface of discontinuity is given by

$$[P]n_x + [Q]n_y = 0 \tag{7.25}$$

For example, in the case of the far-wake solution given by the mixing-length model, we have $P = U_\infty U$, $Q = -(\alpha\delta\partial U/\partial y)^2$ and $S = 0$. Inspection of Equation (7.20) shows that the jumps in P and Q are both zero, corresponding to the fact that the discontinuity appears in the second derivative rather than the first.

The occurrence of weak solutions causes problems on at least two counts. First, the jump condition is not unique. For example, if Q can be written as a function of P, we can always multiply Equation (7.21) by an arbitrary function $\psi(P)$, and rearrange as follows:

$$\frac{\partial F}{\partial x} + \frac{\partial G}{\partial y} + S\psi = 0 \tag{7.26}$$

where

$$F = \int \psi(P)\, dP \quad \text{and} \quad G = \int \psi(P)Q'(P)\, dP \tag{7.27}$$

The jump condition then becomes

$$[F]n_x + [G]n_y = 0 \tag{7.28}$$

In other words, we can have any jump condition we want (and don't want!). This means we have no guarantee that our solution is unique.

The second difficulty posed by the presence of weak solutions has an adverse effect on accuracy and convergence of numerical-solution methods. For example, a central-difference approximation for a first derivative is second-order accurate provided the function of interest is twice differentiable. However, if the function has discontinuous first or second derivative, the accuracy of the central-difference approximation becomes indeterminate. Maintaining second-order accuracy is then possible only if we know the location of the curve of discontinuity in advance. For a hyperbolic equation, this curve is a characteristic curve so that the method of characteristics, for example, can provide a high degree of accuracy

in the vicinity of such discontinuities. Since we don't know the location of the characteristics a priori in standard finite-difference computations, accuracy is suspect when the equations have weak solutions.

One-equation models have problems similar to the mixing-length model near turbulent/nonturbulent interfaces. Spalart and Allmaras (1992), for example, demonstrate existence of weak solutions to their one-equation model at such interfaces. Saffman (1970) was the first to illustrate weak solutions for a two-equation model. He discusses the nature of solutions to his k-ω^2 model approaching a turbulent/nonturbulent interface. In fact, he builds in weak-solution behavior by choosing his closure coefficients to insure that approaching the interface from within the turbulent region, the streamwise velocity and turbulence length scale vary as

$$U_e - U \propto (\delta - y) \quad \text{and} \quad \ell = k^{1/2}/\omega \propto \text{constant} \qquad \text{as} \quad y \to \delta \tag{7.29}$$

where the interface lies at $y = \delta$. Vollmers and Rotta (1977) discuss solution behavior near a turbulent/nonturbulent interface for their k-$k\ell$ model, while Rubel and Melnik (1984) perform a similar analysis for the k-ϵ model. Cazalbou, Spalart and Bradshaw (1994) confirm existence of weak solutions for most k-ϵ, k-$k\ell$ and k-ω models (while demonstrating that there are parametric ranges of the closure coefficients where regular solutions exist). Finally, inspection of the k-ϵ model free shear flow velocity profiles [Figures 4.8 – 4.12] illustrates the nonanalytic behavior at the edge of the shear layer.

Rubel and Melnik (1984) offer an interesting solution for thin shear layers that effectively maps the turbulent/nonturbulent interface to infinity and implicitly clusters grid points near the interface. Their transformation consists of introducing a new independent variable, ξ, defined in terms of the normal distance, y, by

$$d\xi = \frac{dy}{\nu_T} \qquad \text{or} \qquad \frac{d}{d\xi} = \nu_T \frac{d}{dy} \tag{7.30}$$

where ν_T is kinematic eddy viscosity. The Rubel-Melnik transformation, which is useful primarily for self-similar flows, improves numerical accuracy because the edge of the shear layer that occurs at a finite value of y moves to infinity in terms of the transformed independent variable ξ (provided $\nu_T = 0$ in the freestream). Since $\nu_T \to 0$, the transformation produces fine resolution near the interface. For example, if the freestream velocity, U_e, is constant, close to the shear-layer edge, convection balances turbulent diffusion in the streamwise momentum equation. Hence,

$$V \frac{dU}{dy} = \frac{d}{dy}\left(\nu_T \frac{dU}{dy}\right) \tag{7.31}$$

where V is the entrainment velocity, which must also be constant in order to satisfy continuity. Since shear layers grow in thickness, necessarily $V < 0$.

Multiplying both sides of Equation (7.31) by ν_T and using Equation (7.30), we arrive at

$$V\frac{dU}{d\xi} = \frac{d^2U}{d\xi^2} \tag{7.32}$$

for which the solution is

$$U = U_e - \mathcal{U}e^{V\xi} \tag{7.33}$$

where $\mathcal{U}$ is a constant of integration.

Using the Rubel-Melnik transformation, it is a straightforward matter to determine the nature of solutions to turbulence-model equations approaching a turbulent/nonturbulent interface. Applying the transformation to the k-ϵ model, for example, we find

$$V\frac{dk}{d\xi} = \left(\frac{dU}{d\xi}\right)^2 - C_\mu k^2 + \frac{1}{\sigma_k}\frac{d^2k}{d\xi^2} \tag{7.34}$$

$$V\frac{d\epsilon}{d\xi} = C_{\epsilon 1}\frac{\epsilon}{k}\left(\frac{dU}{d\xi}\right)^2 - C_{\epsilon 2}C_\mu k\epsilon + \frac{1}{\sigma_\epsilon}\frac{d^2\epsilon}{d\xi^2} \tag{7.35}$$

Provided the closure coefficients σ_k and σ_ϵ are both less than 2, the production and dissipation terms are negligible in both equations. The solution approaching the interface is

$$k \sim \mathcal{K}e^{\sigma_k V\xi}, \qquad \epsilon \sim \mathcal{E}e^{\sigma_\epsilon V\xi} \qquad (\sigma_k < 2, \quad \sigma_\epsilon < 2) \tag{7.36}$$

where $\mathcal{K}$ and $\mathcal{E}$ are integration constants. Thus, the eddy viscosity is

$$\nu_T \sim C_\mu \frac{\mathcal{K}^2}{\mathcal{E}} e^{(2\sigma_k - \sigma_\epsilon)V\xi} \tag{7.37}$$

Finally, substituting Equation (7.37) into Equation (7.30) and integrating yields

$$e^{V\xi} \propto (1 - y/\delta)^{(2\sigma_k - \sigma_\epsilon)^{-1}} \tag{7.38}$$

So, the solution to the k-ϵ model equations approaching a turbulent/nonturbulent interface from the turbulent side behaves according to

$$\left.\begin{aligned} U_e - U &\sim \mathcal{U}(1 - y/\delta)^{(2\sigma_k - \sigma_\epsilon)^{-1}} \\ k &\sim \mathcal{K}(1 - y/\delta)^{\sigma_k(2\sigma_k - \sigma_\epsilon)^{-1}} \\ \epsilon &\sim \mathcal{E}(1 - y/\delta)^{\sigma_\epsilon(2\sigma_k - \sigma_\epsilon)^{-1}} \end{aligned}\right\} \quad \text{as} \quad y \to \delta \tag{7.39}$$

Using the standard values $\sigma_k = 1.0$ and $\sigma_\epsilon = 1.3$, the k-ϵ model predicts

$$\left.\begin{aligned} U_e - U &\sim \mathcal{U}(1 - y/\delta)^{10/7} \\ k &\sim \mathcal{K}(1 - y/\delta)^{10/7} \\ \epsilon &\sim \mathcal{E}(1 - y/\delta)^{13/7} \end{aligned}\right\} \quad \text{as} \quad y \to \delta \tag{7.40}$$

A similar analysis for the k-ω model with cross diffusion included (but no stress limiter) shows that the asymptotic behavior of U, k and ω is given by

$$\left.\begin{aligned} U_e - U &\sim \mathcal{U}(1-y/\delta)^{n_u} \\ k &\sim \mathcal{K}(1-y/\delta)^{n_k} \\ \omega &\sim \mathcal{W}(1-y/\delta)^{n_\omega} \end{aligned}\right\} \quad \text{as} \quad y \to \delta \tag{7.41}$$

where $\mathcal{U}$, $\mathcal{K}$ and $\mathcal{W}$ are integration constants and the three exponents are[1]

$$n_u = \frac{\sigma\sigma^*}{\sigma - \sigma^* + \sigma_{do}}, \qquad n_k = \frac{\sigma}{\sigma - \sigma^* + \sigma_{do}}, \qquad n_\omega = \frac{\sigma^* - \sigma_{do}}{\sigma - \sigma^* + \sigma_{do}} \tag{7.42}$$

In order for the solution to give $U \to U_e$, $k \to 0$ and $\omega \to 0$ as we approach the turbulent/nonturbulent interface from the turbulent side, all three exponents in Equations (7.42) must be positive. This is true provided the closure coefficients σ, σ^* and σ_{do} satisfy the following constraints.

$$\sigma_{do} > \sigma^* - \sigma \qquad \text{and} \qquad \sigma^* > \sigma_{do} \tag{7.43}$$

These are identical to the constraints deduced by Lele (1985) in analyzing a turbulent front (see Subsections 4.5.3 and 4.5.4). Table 7.2 lists the values of the exponents for several k-ω models, each having unique behavior.

Table 7.2: *Turbulent/Nonturbulent Interface Exponents for k-ω Models.*

Model	σ	σ^*	σ_{do}	$\sigma-\sigma^*+\sigma_{do}$	n_u	n_k	n_ω
Hellsten (2005)	1.000	1.100	0.400	0.300	3.333	3.333	2.333
Kok (2000)	0.500	0.667	0.500	0.333	1.000	1.500	0.500
Menter (1992c)	0.856	1.000	1.712	1.568	0.546	0.546	-0.454
Wilcox (2006)	0.500	0.600	0.125	0.025	20	20	19

1. Hellsten's model features continuous second derivatives for U, k and ω, so that its weak-solution behavior should be of no consequence in a second-order accurate numerical solution.

2. Kok's model has classic weak-solution behavior with discontinuities in the slope of U and ω.

3. Because Menter's model fails to satisfy the second condition of Equation (7.43), the solution for ω approaches ∞ as $y \to \delta$.

4. Wilcox's model is analytic approaching the interface so that it does not have nonphysical weak-solution behavior.

[1] With a stress limiter included (see problems section), n_k and n_ω are unchanged, but the solution for the velocity is such that $n_u = n_k$.

Hellsten makes the case for choosing the values of the model's closure coefficients based on achieving smooth solution behavior at a turbulent/nonturbulent interface. Part of Hellsten's arguments include a claim that in order to achieve such behavior it is necessary to have $\sigma^* > 1$. Since the Wilcox (2006) k-ω model has a completely analytical solution at such an interface while having $\sigma^* < 1$, a closer look is in order.

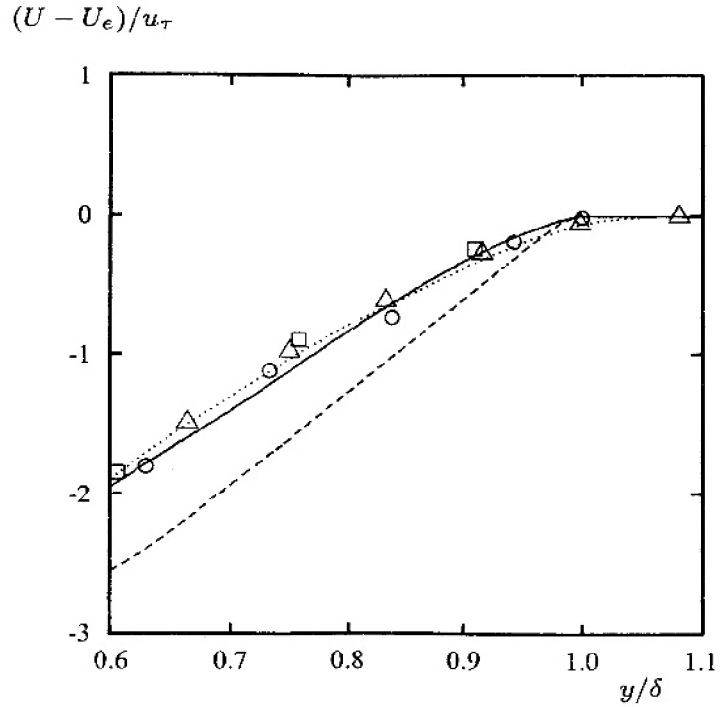

Figure 7.1: *Computed and measured velocity defect near the boundary-layer edge for a flat-plate boundary layer using three k-ω models:* —— *Wilcox (2006);* - - - *Kok (2000);* · · · *Hellsten (2005);* ○ *Klebanoff (1955);* □ *Wieghardt and Tillman (1951);* △ *Winter and Gaudet (1973).*

Figure 7.1 compares computed and measured [Klebanoff (1955), Wieghardt and Tillman (1951) and Winter and Gaudet (1973)] velocity profiles in the immediate vicinity of the boundary-layer edge for a constant-pressure boundary layer. Results for the Wilcox model and the Kok model were obtained from Program **DEFECT** (see Appendix C), which is extremely accurate at the turbulent/nonturbulent interface. The Hellsten-model profile is from Hellsten (2005). Hellsten presents a similar graph showing the linear approach of Kok's velocity profile and the discontinuity in slope at the interface. By contrast, both the Hellsten and Wilcox models exhibit a smooth approach to freestream values, with both curves falling within experimental-data scatter.

The apparent contradiction in Hellsten's claim regarding the minimum value of σ^* needed to achieve smooth solutions near a turbulent/nonturbulent interface

is easily resolved. Inspection of Figure 7.1 shows that below $y/\delta \approx 0.95$ all three velocity profiles are very nearly linear functions of y/δ. The region in which the asymptotic solution given in Equations (7.41) and (7.42) is valid lies well within the upper 1%-5% of the boundary layer, depending on the precise values of n_u, n_k and n_ω. Consequently, on the scale shown in the graph, it is difficult to discern much difference between the solutions for the Hellsten (2005) model and the Wilcox (2006) model. As noted above, both models have continuous second derivatives (and higher) approaching the interface and should be expected to cause no troublesome numerical issues to arise.

The solution for the Wilcox (1988a) k-ω model is a quite a bit more complicated. This model has $\sigma = \sigma^* = 1/2$ and there is no cross-diffusion term so that $\sigma_{do} = 0$. For this model, only the dissipation terms are negligible. The production term in the transformed k equation yields a secular term, which complicates the solution. That is, the approximate transformed equations for k and ω assume the following form.

$$\frac{d^2k}{d\xi^2} - 2V\frac{dk}{d\xi} = 2V^2\mathcal{U}^2e^{2V\xi} \tag{7.44}$$

$$\frac{d^2\omega}{d\xi^2} - 2V\frac{d\omega}{d\xi} = 2\alpha V^2\mathcal{U}^2\frac{\omega}{k}e^{2V\xi} \tag{7.45}$$

The solution for k and ω is

$$k \sim \mathcal{U}^2V\xi\, e^{2V\xi}, \qquad \omega \sim \mathcal{W}\xi^{-\alpha} \tag{7.46}$$

where $\mathcal{W}$ is an integration constant. Computing the eddy viscosity and substituting into Equation (7.30), we arrive at

$$y \sim \delta + \frac{\mathcal{U}^2V}{\mathcal{W}}\int_\xi^\infty \xi^{1+\alpha}e^{2V\xi}d\xi \tag{7.47}$$

Integrating by parts, we can approximate the limiting form of the integral for $\xi \to \infty$ as follows.

$$\delta - y \sim \frac{\mathcal{U}^2}{2\mathcal{W}}\xi^{1+\alpha}e^{2V\xi} \tag{7.48}$$

Now, we must solve this equation for ξ as a function of $\delta - y$. To do this, let

$$\eta = \frac{2\mathcal{W}}{\mathcal{U}^2}(\delta - y) \tag{7.49}$$

Then, Equation (7.48) simplifies to

$$\eta \sim \xi^{1+\alpha}e^{2V\xi} \tag{7.50}$$

This equation can be solved for ξ as a function of η by assuming

$$2V\xi \sim \ell n\eta + \phi(\eta) \tag{7.51}$$

where $\phi(\eta)$ is a function to be determined. In the limit $\xi \rightarrow \infty$, which corresponds to $\eta \rightarrow 0$, the approximate solution for $\phi(\eta)$ is

$$\phi(\eta) \sim -(1+\alpha)\ell n\left(\frac{\ell n\eta}{2V}\right) \tag{7.52}$$

With a bit more algebra, there follows

$$e^{V\xi} \propto \eta^{1/2}\left(\frac{2V}{\ell n\eta}\right)^{(1+\alpha)/2} \tag{7.53}$$

Thus, for the Wilcox (1988a) k-ω model approaching a turbulent/nonturbulent interface from within the turbulent region, we have

$$\left.\begin{aligned} U_e - U &\sim \mathcal{U}\sqrt{\lambda} \\ k &\sim -\mathcal{K}\lambda\ell n\lambda \\ \omega &\sim \mathcal{W}(-\ell n\lambda)^{-\alpha} \\ \lambda &\sim \frac{(1-y/\delta)}{[-\ell n(1-y/\delta)]^{1+\alpha}} \end{aligned}\right\} \quad \text{as} \quad y \rightarrow \delta \tag{7.54}$$

Clearly, ω approaches zero very slowly from the turbulent side as compared to the variation of $\epsilon/k \sim (\delta - y)^{3/7}$ predicted by the k-ϵ model. Also, the velocity profile has discontinuous first derivative at the shear-layer edge, or more generally, at any turbulent/nonturbulent interface.

Wilcox (1998) has verified that the asymptotic behavior predicted in Equations (7.54) is consistent with results of numerical computations. Figure 7.2 compares numerical solutions with Equation (7.54). The computations are for an incompressible flat-plate boundary layer, and have been done using Program **EDDYBL** (see Appendix C) with two finite-difference grids. The first grid has 140 points normal to the surface, while the second grid has 289 points. As shown, the 289-point solution matches the closed-form solution to within 3% of scale for U, k and ω. The largest discrepancies are present for points very close to the interface. This is true because the computation has a nonzero value for ω in the freestream, while the closed-form solution is strictly valid for $\omega = 0$ in the freestream. Because of the coarser resolution, the 140-point solution shows slightly larger differences, again mainly for points closest to the interface. Results shown clearly indicate that the numerical solution is consistent with the weak-solution.

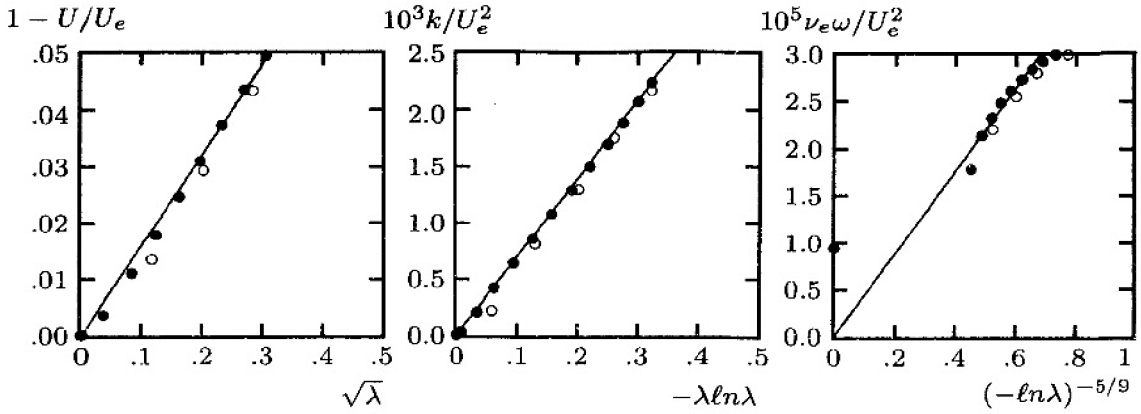

Figure 7.2: *Velocity, k and ω profiles near a turbulent/nonturbulent interface, Wilcox (1988a) k-ω model: ○ 140 points; • 289 points; —— Equation (7.54).*

7.2.3 Sensitivity to Freestream Boundary Conditions

Usually it is more convenient to assign small nonzero values to k and other turbulence parameters in the freestream, especially when the parameter appears in the denominator of the eddy viscosity. Cazalbou, Spalart and Bradshaw (1994) show that when this is done in boundary-layer computations with the k-ϵ model, the weak solution prevails below the interface. Small gradients in k and ϵ appear above the interface that yield an asymptotic approach to the prescribed freestream values. There is "no significant influence on the predicted flow."

By contrast, Menter (1992a) shows that for the far wake, in which the entrainment velocity increases in magnitude linearly with distance from the centerline, the Wilcox (1988a) k-ω model predicts that k and ω decay exponentially with distance squared. However, they decay at the same rate so that the eddy viscosity remains constant. As a consequence, consistent with results presented in Section 4.5, the freestream value of ω has a nontrivial effect on the solution. Menter indicates a smaller effect on boundary layers, primarily because of the large values of ω prevailing near the surface. The behavior of ω in Equation (7.54) is consistent with Menter's observation that the Wilcox (1988a) k-ω model solutions have discontinuous derivatives at the shear layer edge. However, the discontinuity in $d\omega/dy$ would probably be difficult to detect.

The Wilcox (2006) k-ω model is far less sensitive to the freestream value of ω than its predecessors. There is nevertheless some sensitivity [cf. Figure 4.13]. However, as long as the freestream value of ω is less than 1% of the maximum value in a turbulent shear layer, the sensitivity is of little consequence.

Studies have been published [cf. Bardina et al. (1997)] where the freestream value of ω has been set to very large values. With an extremely large freestream ω, any k-ω model solution for many flows, especially free shear flows, will

be grossly distorted. This type of analysis is very misleading because having freestream values of ω more than a percent or so of the maximum value in the turbulent region is physically incorrect. What ω quantifies is the vorticity of the energy containing eddies. Assigning huge values of ω in the freestream would imply that there is significant fluctuating vorticity above the turbulent region, which is absurd.

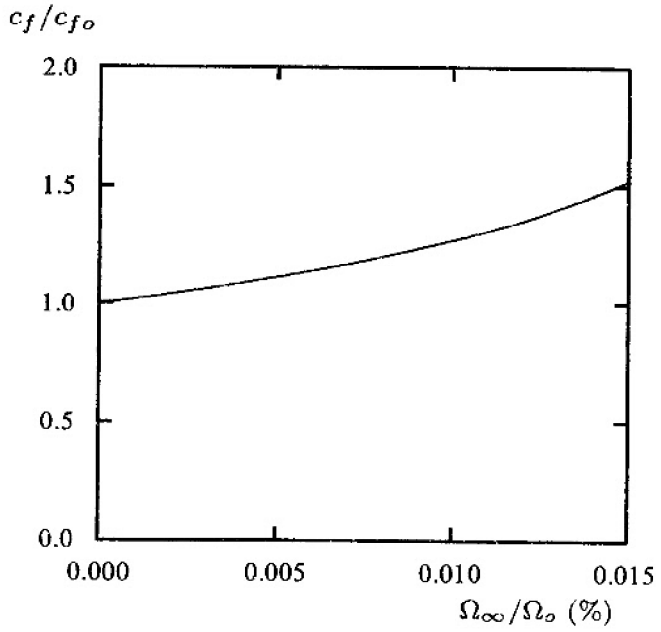

Figure 7.3: *Effect of freestream vorticity on an incompressible, laminar flat-plate boundary later.*

As an analogy, consider the laminar boundary layer with zero pressure gradient. The boundary-layer equations admit a similarity solution, viz., the Blasius solution. Imagine that, rather than imposing the freestream boundary condition on the velocity, we choose to specify the freestream value of the vorticity. For zero freestream vorticity, the solution is identical to the Blasius solution. Figure 7.3 shows how the skin friction varies with the freestream vorticity, Ω_∞. There is significant distortion when Ω_∞ exceeds one thousandth of a percent (0.001%) of the peak vorticity, Ω_o, in the boundary layer. How different is this from selecting a physically unrealistic freestream boundary condition on the vorticity of the energy-containing eddies with the k-ω model? We can reasonably conclude the following.

The same logic that would cite the sensitivity to a freestream value of ω that exceeds 1% of the peak value in the turbulent region as a flaw in the turbulence model would conclude that Prandtl's boundary-layer equations are fundamentally flawed for the same reason!

7.2.4 Viscous-Interface Layer

In principle, solutions with discontinuous derivatives will not occur if molecular viscosity is included in the diffusion terms of the equations of motion. As shown by Saffman (1970), there is a thin **viscous-interface layer** of thickness

$$\delta_{vi} \sim \nu/|V| \tag{7.55}$$

in which the discontinuities are resolved. This is a singular-perturbation problem in the limit $|V|\delta_{vi}/\nu \to \infty$, and the weak solution discussed above is the outer solution. The inner solution holds in the viscous-interface layer. For example, in the interface layer, Saffman's equations simplify to

$$\left.\begin{aligned} V\frac{dU}{dy} &= \frac{d}{dy}\left[\left(\nu+\frac{k}{\omega}\right)\frac{dU}{dy}\right] \\ V\frac{dk}{dy} &= \frac{d}{dy}\left[\left(\nu+\sigma^*\frac{k}{\omega}\right)\frac{dk}{dy}\right] \\ V\frac{d\omega^2}{dy} &= \frac{d}{dy}\left[\left(\nu+\sigma\frac{k}{\omega}\right)\frac{d\omega^2}{dy}\right] \end{aligned}\right\} \tag{7.56}$$

These equations must be solved subject to the following boundary conditions, which correspond to formal matching of the solutions that hold on each side of the turbulent/nonturbulent interface:

$$U_e - U \to \mathcal{U}(\delta-y),\quad k \to \mathcal{K}(\delta-y)^2,\quad \omega \to \frac{\mathcal{K}}{|V|}(\delta-y)\quad \text{as}\quad \frac{|V|(\delta-y)}{\nu} \to \infty \tag{7.57}$$

and

$$U_e - U \to 0,\quad k \to 0,\quad \omega \to 0\quad \text{as}\quad \frac{|V|(\delta-y)}{\nu} \to -\infty \tag{7.58}$$

As can be easily verified, for $\sigma = \sigma^* = 1/2$, the solution is given by

$$\left.\begin{aligned} U_e - U &= \frac{\mathcal{U}|V|^3}{\mathcal{K}^2\nu}\left(\frac{\omega^2}{1+V^2\omega/\mathcal{K}\nu}\right) \\ k &= \frac{V^2\omega^2}{\mathcal{K}} \\ \delta - y &= \frac{|V|\omega}{\mathcal{K}} + \frac{2\nu}{|V|}\ell n\left(\frac{V^2\omega}{\mathcal{K}\nu}\right) \end{aligned}\right\} \tag{7.59}$$

In practice, finite-difference grids are never sufficiently fine to resolve the viscous-interface layer. Generally, grid points are packed close to the surface to

permit accurate resolution of the sublayer. Hence, even when molecular viscosity is included in a typical finite-difference computation, turbulent/nonturbulent interfaces are not sufficiently resolved. As a consequence, the interfaces are sharp, and the weak solutions generally prevail. However, truncation error, numerical diffusion and dissipation will generally yield diffused solutions close to the interfaces. The most significant numerical problem typically encountered is the appearance of nonphysical negative values of k and/or other normally positive turbulence parameters such as ω, ϵ and ℓ.

For self-similar flows such as the far wake, mixing layer, jet and defect layer, the Rubel-Melnik transformation cures the problem by mapping the interface to ∞. Programs **WAKE**, **MIXER**, **JET** and **DEFECT** (see Appendix C) all use this transformation. In addition to eliminating difficulties associated with the turbulent/nonturbulent interface, the transformation linearizes the first and second derivative terms in the equations. This linearization tends to improve the rate of convergence of most numerical methods. The only shortcoming of the method is its sensitivity to the location of "∞." Using too large or too small a value of ξ_{max} (the farfield value of ξ) can impede convergence of the numerical solution.

In general finite-difference computations, for which the Rubel-Melnik transformation is impractical, the correct jump condition will be obtained provided the diffusion terms in all equations are differenced in a conservative manner. For the same reasons, we use conservative differencing for the Navier-Stokes equation to guarantee that the exact shock relations are satisfied across a shock wave in a finite-difference computation. Program **EDDYBL** (see Appendix C), for example, uses conservative differencing for diffusion terms and rarely ever encounters numerical difficulties attending the presence of sharp turbulent/nonturbulent interfaces.

For nonzero freestream values of k, etc., some researchers prefer zero-gradient boundary conditions at a boundary-layer edge. While such conditions are clean from a theoretical point of view, they are undesirable from a numerical point of view. Almost universally, convergence of iterative schemes is much slower with zero-gradient (Neumann-type) conditions than with directly-specified (Dirichlet-type) conditions.

In order to resolve this apparent dilemma, we can appeal directly to the equations of motion. Beyond the boundary-layer edge, we expect to have vanishing normal gradients so that the equations for k and ω simplify to the following:

$$U_e \frac{dk_e}{dx} = -\beta^* \omega_e k_e \tag{7.60}$$

$$U_e \frac{d\omega_e}{dx} = -\beta_o \omega_e^2 \tag{7.61}$$

where subscript e denotes the value at the boundary-layer edge. The solution to Equations (7.60) and (7.61) can be obtained by simple quadrature, independent

of integrating the equations of motion through the boundary layer. Once k_e and ω_e are determined from Equations (7.60) and (7.61), it is then possible to specify Dirichlet-type boundary conditions that guarantee zero normal gradients. Clearly, the same procedure can be used for any turbulence model. Program **EDDYBL** (see Appendix C) uses this procedure.

7.3 Parabolic Marching Methods

In general, numerical methods for solving parabolic systems of equations such as the boundary-layer equations are unconditionally stable. A second-order accurate scheme like the Blottner (1974) variable-grid method, for example, involves inversion of a tridiagonal matrix. If the matrix is diagonally dominant, the scheme will run stably with arbitrarily large streamwise stepsize, Δx. Turbulent boundary layer computations using algebraic models often run with $\Delta x/\delta$ between 1 and 10, where δ is boundary-layer thickness. By contrast, early experience with two-equation models indicated that much smaller steps must be taken. Rastogi and Rodi (1978) found that their three-dimensional boundary-layer program based on the Jones-Launder (1972) k-ϵ model required initial steps of about $\delta/100$, and that ultimately Δx could not exceed $\delta/2$. Similar results hold for models based on the ω equation.

Wilcox (1981b) found that the problem stems from a loss of diagonal dominance caused by the production terms in the turbulence-model equations. To illustrate the problem's essence, consider the k-ω model's turbulence kinetic energy equation for an incompressible two-dimensional boundary layer, viz.,

$$U\frac{\partial k}{\partial x} + V\frac{\partial k}{\partial y} = \left[\frac{(\partial U/\partial y)^2}{\omega} - \beta^*\omega\right]k + \frac{\partial}{\partial y}\left[(\nu + \sigma^*\nu_T)\frac{\partial k}{\partial y}\right] \tag{7.62}$$

The following analysis is based on the Blottner variable-grid method, which is the scheme implemented in Program **EDDYBL** (see Appendix C). This algorithm uses a three-point forward difference formula [Adams-Bashforth — see Roache (1998a)] in the streamwise direction, central differencing for the normal convection term, and conservative differencing for the diffusion terms. Hence, discretization approximations for all except the source terms are as follows:

$$U\frac{\partial k}{\partial x} \doteq \frac{U}{\Delta x}\left(3k_{m+1,n} - 4k_{m,n} + k_{m-1,n}\right) \tag{7.63}$$

$$V\frac{\partial k}{\partial y} \doteq \frac{V}{2\Delta y}\left(k_{m+1,n+1} - k_{m+1,n-1}\right) \tag{7.64}$$

$$\frac{\partial}{\partial y}\left[(\nu + \sigma^*\nu_T)\frac{\partial k}{\partial y}\right] \doteq \frac{\nu^+(k_{m+1,n+1} - k_{m+1,n}) - \nu^-(k_{m+1,n} - k_{m+1,n-1})}{(\Delta y)^2} \tag{7.65}$$

where $k_{m,n}$ denotes the value of k at $x = x_m$ and $y = y_n$, and Δy denotes the vertical distance between grid points. Unsubscripted quantities are assumed known during the typically iterative solution procedure. Also, the quantity ν^- denotes the value of $(\nu+\sigma^*\nu_T)$ midway between y_{n-1} and y_n, while ν^+ denotes the value midway between y_n and y_{n+1}. For simplicity, we assume points are equally spaced in both the x and y directions, so that the grid consists of rectangular cells. Figure 7.4 shows the finite-difference molecule.

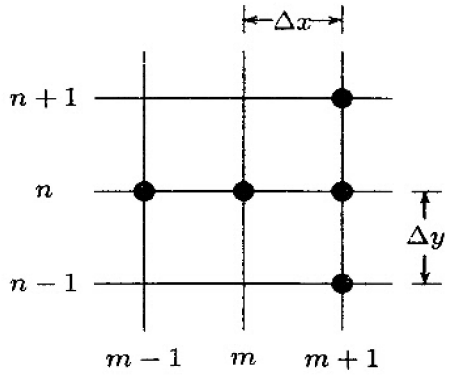

Figure 7.4: *Finite-difference molecule for Blottner's variable-grid method.*

Turning to the source terms, the simplest second-order accurate discretization approximation is

$$\left[\frac{(\partial U/\partial y)^2}{\omega} - \beta^*\omega\right] k \doteq \left[\frac{(\partial U/\partial y)^2}{\omega} - \beta^*\omega\right] k_{m+1,n} \tag{7.66}$$

where the quantity in brackets is also evaluated at $(m+1, n)$ using values extrapolated from (m, n) and $(m-1, n)$. Substituting Equations (7.63) – (7.66) into Equation (7.62) and regrouping terms leads to a tridiagonal matrix system as follows:

$$A_n k_{m+1,n-1} + B_n k_{m+1,n} + C_n k_{m+1,n+1} = D_n \tag{7.67}$$

where A_n, B_n, C_n and D_n are defined by

$$A_n = -\left[\frac{V}{2\Delta y} + \frac{\nu^-}{(\Delta y)^2}\right], \qquad B_n = 3\frac{U}{\Delta x} + \frac{\nu^- + \nu^+}{(\Delta y)^2} - \frac{(\partial U/\partial y)^2}{\omega} + \beta^*\omega \tag{7.68}$$

$$C_n = \left[\frac{V}{2\Delta y} - \frac{\nu^+}{(\Delta y)^2}\right], \qquad D_n = \frac{U}{\Delta x}\left[4k_{m,n} - k_{m-1,n}\right] \tag{7.69}$$

Now, in order to have a diagonally dominant system, the condition

$$B_n \geq -(A_n + C_n) \tag{7.70}$$

must be satisfied. Substituting Equations (7.68) – (7.69) into Equation (7.70) yields the following condition.

$$3\frac{U}{\Delta x} - \frac{(\partial U/\partial y)^2}{\omega} + \beta^*\omega \geq 0 \tag{7.71}$$

If dissipation exceeds production, so that $\beta^*\omega > (\partial U/\partial y)^2/\omega$, Equation (7.71) is satisfied so long as we march in the direction of flow (i.e., so long as U and Δx are of the same sign). The system is then said to be **unconditionally stable**. When production exceeds dissipation, we have the following limit on stepsize.

$$\Delta x \leq (\Delta x)_{theory} \equiv \frac{3\omega U}{(\partial U/\partial y)^2 - \beta^*\omega^2} \tag{7.72}$$

Hence, the scheme is **conditionally stable**, subject to Equation (7.72).

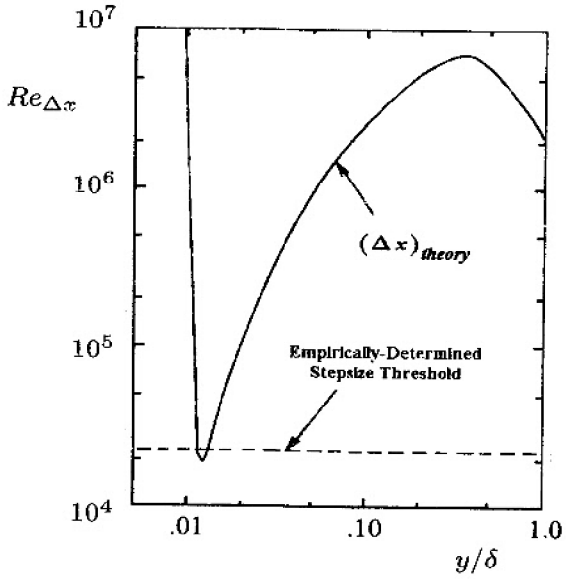

Figure 7.5: *Theoretical and empirically determined stepsize threshold for a flat-plate boundary layer. [From Wilcox (1981b) — Copyright © AIAA 1981 — Used with permission.]*

To demonstrate the validity of Equation (7.72), Wilcox (1981b) presents computed results for an incompressible flat-plate boundary layer using the Wilcox-Rubesin (1980) k-ω^2 model. At a plate-length Reynolds number, Re_x, of $1.2 \cdot 10^6$, stable computation is found empirically to be possible provided the Reynolds number based on Δx satisfies $Re_{\Delta x} < 2.2 \cdot 10^4$, which corresponds to $\Delta x/\delta = 1.15$. Figure 7.5 shows $Re_{\Delta x}$ as predicted by Equation (7.72) throughout the boundary layer. The minimum value of $Re_{\Delta x}$ according to Equation (7.72) is $1.9 \cdot 10^4$ and occurs at $y/\delta \doteq 0.012$. This close agreement verifies

that the source of instability is lack of diagonal dominance in the tridiagonal matrix system defined in Equations (7.67) – (7.69).

To remedy this situation, note that because of nonlinearity, Equation (7.67) always requires an iterative solution. Letting superscript i denote iteration number, we replace B_n and D_n by the following revised discretization approximations:

$$B_n = 3\frac{U}{\Delta x} + \frac{\nu^- + \nu^+}{(\Delta y)^2} - \frac{(\partial U/\partial y)^2}{\omega} + (1+\psi_k)\,\beta^*\omega \tag{7.73}$$

$$D_n = \frac{U}{\Delta x}\left[4k_{m,n} - k_{m-1,n}\right] + \psi_k \beta^* \omega k^{i-1}_{m+1,n} \tag{7.74}$$

where ψ_k will be defined below. Then, Equation (7.67) is replaced by

$$A_n k^i_{m+1,n-1} + B_n k^i_{m+1,n} + C_n k^i_{m+1,n+1} = D_n \tag{7.75}$$

Inspection of Equations (7.73) – (7.75) shows that when convergence has been achieved (i.e., when $k^i_{m+1,n}$ and $k^{i-1}_{m+1,n}$ differ by a negligible amount), terms on the right- and left-hand sides of Equation (7.75) proportional to ψ_k cancel identically. Hence, $k^{i}_{m+1,n}$ satisfies the correct equation. The advantage of this procedure becomes obvious upon inspection of the stability condition, which now becomes

$$3\frac{U}{\Delta x} - \frac{(\partial U/\partial y)^2}{\omega} + (1+\psi_k)\,\beta^*\omega \geq 0 \tag{7.76}$$

Clearly, ψ_k can be chosen to insure that this inequality is always satisfied, regardless of the value of Δx. This corresponds to unconditional stability.

Numerical experimentation shows that the best results are obtained when $(1+\psi_k)\beta^*\omega$ exceeds $(\partial U/\partial y)^2/\omega$ by about 30%, a condition that is insured by defining ψ_k as follows.

$$\psi_k = \begin{cases} \dfrac{3}{10}, & (\partial U/\partial y)^2 \leq \beta^*\omega^2 \\ \dfrac{(\partial U/\partial y)^2}{\beta^*\omega^2} - \dfrac{7}{10}, & (\partial U/\partial y)^2 > \beta^*\omega^2 \end{cases} \tag{7.77}$$

A similar factor, ψ_ω, must be introduced for the ω equation, and experience has shown that selecting

$$\psi_\omega = \psi_k \tag{7.78}$$

is satisfactory to achieve both unconditional stability and rapid convergence.

The prescription for ψ_k and ψ_ω given in Equations (7.77) and (7.78) permits stepsizes comparable to those used with algebraic models. While the numerical procedure is unconditionally stable for other values of ψ_k, using these values for ψ_k and ψ_ω optimizes k-ω^2 and k-ω model computations with respect to the

Table 7.3: *Values of ψ_ϵ for Low-Reynolds-Number k-ϵ Models.*

Model	ψ_ϵ
Jones-Launder (1972)	0.50
Launder-Sharma (1974)	0.50
Lam-Bremhorst (1981)	0.50
Chien (1982)	-0.25
Yang-Shih (1993)	-0.25
Fan-Lakshminarayana-Barnett (1993)	-0.25

number of iterations required for the solution to converge. Interestingly, if ψ_k is too large, say $\psi_k = 2$, stable integration is inhibited. The value of ψ_ω cannot be too large either, although the upper bound appears to be dependent upon details of the specific model.

The same analysis applies to the k-ϵ model. For the k equation, writing Equation (7.77) in terms of the model's variables leads to the following entirely equivalent form.

$$\psi_k = \begin{cases} \dfrac{3}{10}, & \nu_T(\partial U/\partial y)^2 \leq \epsilon \\ \dfrac{\nu_T(\partial U/\partial y)^2}{\epsilon} - \dfrac{7}{10}, & \nu_T(\partial U/\partial y)^2 > \epsilon \end{cases} \tag{7.79}$$

By contrast, the value of the corresponding factor for the ϵ equation, ψ_ϵ, is very much dependent upon details of the model. Low-Reynolds-number viscous damping functions have a pronounced effect on the most appropriate value. Table 7.3 lists the values of ψ_ϵ used in Program **EDDYBL** (see Appendix C) for six different low-Reynolds-number k-ϵ models. The values listed have been found empirically to yield optimum convergence rates for incompressible boundary layers.

7.4 Elementary Time-Marching Methods

One of the most effective procedures for solving complex flowfields is the use of time-marching methods. If the desired solution is unsteady, time-marching solutions yield a true time history. Time-marching methods can also be used for steady-flow problems by letting the solution evolve in time until temporal variations become negligibly small. That is, we begin with an initial approximation and update the solution at each timestep until the solution differs between timesteps by less than a prescribed tolerance level. Prior to discussing the impact

of turbulence-model source terms on explicit and implicit methods, this section presents a brief overview of these methods. For more complete details see a general text on Computational Fluid Dynamics such as Peyret and Taylor (1983), Anderson et al. (1984), Minkowycz et al. (1988), Ferziger and Perić (1996) or Roache (1998a).

The simplest time-marching schemes are **explicit methods**, such as the DuFort-Frankel (1953), Godunov (1959), Lax-Wendroff (1960) and MacCormack (1969) methods. Most explicit schemes were developed prior to 1970. In an explicit scheme, the solution at time t^{n+1} depends only on past history, i.e., the solution at time t^n. For example, consider the one-dimensional wave equation:

$$\frac{\partial k}{\partial t} + U\frac{\partial k}{\partial x} = 0, \qquad U > 0 \tag{7.80}$$

where k is a flow property, U is velocity, t is time and x is streamwise direction. Letting k_j^n denote $k(x_j, t^n)$, we approximate $\partial k/\partial t$ with a **forward-difference approximation** so that

$$\frac{\partial k}{\partial t} \doteq \frac{k_j^{n+1} - k_j^n}{\Delta t} + O(\Delta t) \tag{7.81}$$

where $\Delta t = t^{n+1} - t^n$. For simplicity, consider simple **upwind differencing** in which we approximate $\partial k/\partial x$ according to

$$\frac{\partial k}{\partial x} \doteq \frac{k_j^n - k_{j-1}^n}{\Delta x} + O(\Delta x) \tag{7.82}$$

Using these discretization approximations, we arrive at the following first-order accurate difference equation that approximates Equation (7.80).

$$k_j^{n+1} = k_j^n - \frac{U\Delta t}{\Delta x}\left(k_j^n - k_{j-1}^n\right) \tag{7.83}$$

This is not a particularly accurate method, but nevertheless illustrates the general nature of explicit schemes. Note that all terms on the right-hand side of Equation (7.83) are known from time t^n. Hence, k_j^{n+1} is obtained from simple algebraic operations. Because only algebraic operations are needed (as opposed to inversion of a large matrix), explicit methods are easy to implement.

The primary shortcoming of explicit schemes is a limit on the timestep that can be used. For too large a timestep, solution errors will grow with increasing iterations and the computation becomes unstable. The most commonly used method for determining the stability properties of a time-marching finite-difference scheme is von Neumann stability analysis [see Roache (1998a) or Anderson et al. (1984)]. In this method, we introduce a discrete Fourier series solution to the finite-difference equation under study, and determine the growth

rate of each mode. If all Fourier modes decay as we march in time, the scheme is stable. However, if even a single mode grows, the scheme is unstable. We write each Fourier component as

$$k_j^n = G^n e^{i(j\kappa\Delta x)} \tag{7.84}$$

where G is called the **amplitude factor**, $i = \sqrt{-1}$ and κ is wavenumber. The stability of a scheme is determined as follows:

$$\left.\begin{array}{ll} |G| < 1, & \text{Stable} \\ |G| = 1, & \text{Neutrally Stable} \\ |G| > 1, & \text{Unstable} \end{array}\right\} \tag{7.85}$$

In general, G is complex, and the notation G^n means G raised to the power n. The amplitude factor for Equation (7.83) is

$$G = 1 - \frac{U\Delta t}{\Delta x}\left(1 - e^{-i\theta}\right), \qquad \text{where} \qquad \theta = \kappa\Delta x \tag{7.86}$$

Thus,

$$|G|^2 = 1 + 2(1 - \cos\theta)\frac{U\Delta t}{\Delta x}\left(\frac{U\Delta t}{\Delta x} - 1\right) \tag{7.87}$$

In order to have a stable scheme, $|G|$ must be less than or equal to 1 for all possible values of θ. Clearly, for the upwind-difference scheme, errors will not grow provided the condition

$$\Delta t < \frac{\Delta x}{U} \qquad \text{or} \qquad N_{CFL} = \frac{U\Delta t}{\Delta x} < 1 \tag{7.88}$$

is satisfied. This is the famous Courant-Friedrichs-Lewy (1967), or CFL condition. It arises because a disturbance traveling at speed U cannot propagate a distance exceeding Δx in a time equal to Δt. N_{CFL} is known as the **CFL Number**.

Explicit methods are of interest in modern CFD applications mainly for time-dependent flows. Their algebraic simplicity makes them especially easy to implement on any computer. Their primary drawback is their conditional stability, and thousands of timesteps are often needed to achieve steady-flow conditions. There has been renewed interest in these methods because of their suitability for massively-parallel computers, where they may actually be more efficient than implicit schemes which can run with larger timesteps but are trickier to program.

Implicit methods date back to 1947 when the Crank-Nicolson (1947) method first appeared. Other methods such as the Euler [Lilly (1965)] and Alternating Direction Implicit (ADI) schemes [Peaceman and Rachford (1955)] are implicit. The solution at time t^{n+1} and location x_j in this type of scheme depends not only

upon the solution at the earlier timestep, but upon the solution at other spatial locations at time t^{n+1} as well. For example, the Crank-Nicolson method uses

$$\frac{\partial k}{\partial x} \doteq \frac{1}{2}\left(\frac{k_{j+1}^{n} - k_{j-1}^{n}}{2\Delta x} + \frac{k_{j+1}^{n+1} - k_{j-1}^{n+1}}{2\Delta x}\right) + O\left[(\Delta x)^2\right] \tag{7.89}$$

Thus, Equation (7.80) is approximated by the following second-order accurate difference equation:

$$-\lambda k_{j-1}^{n+1} + k_j^{n+1} + \lambda k_{j+1}^{n+1} = k_j^n - \lambda\left(k_{j+1}^n - k_{j-1}^n\right) \tag{7.90}$$

where

$$\lambda = \frac{U\Delta t}{4\Delta x} \tag{7.91}$$

Hence, as with the Blottner method discussed in the preceding section, a tridiagonal matrix system of equations must be solved. Although inverting any matrix is more time consuming than solving a simple algebraic equation, the increased complexity is attended by a significant increase in the maximum permissible timestep. That is, stability analysis shows that the scheme defined in Equation (7.90) is unconditionally stable.

Implicit schemes have proven to be especially useful for steady-flow computations where the CFL limit can be exceeded by factors as large as 5. While these schemes will run at a larger CFL number, using larger values of Δt sometimes introduces significant truncation errors if convective effects have a significant effect on the physics of the flow. The number of timesteps required, relative to explicit methods, to achieve steady-flow conditions typically is reduced, although the factor is N_{CFL}^{-n} where $n < 1$.

Recall from Section 7.1 that there are three physically relevant time scales when turbulence-model equations are used. If we use an explicit finite-difference scheme to approximate the Favre-averaged Navier-Stokes equation, stability analysis shows that the wave speed is $|\tilde{u}| + a$, where $\tilde{u}$ is mass averaged velocity and a is sound speed. If ν denotes kinematic viscosity, the wave-propagation and diffusion timestep limitations are as follows.

$$\Delta t \leq \frac{\Delta x}{|\tilde{u}| + a} \quad \text{and} \quad \Delta t \leq \frac{(\Delta x)^2}{2\nu} \tag{7.92}$$

We might also anticipate that including source terms in the stability analysis would lead to an additional timestep constraint such as $\Delta t \leq t_{diss}$. This is indeed the case, and this timestep limitation is sometimes more restrictive than either condition in Equation (7.92).

To illustrate the problem, we add a source term, Sk, to Equation (7.80), giving

$$\frac{\partial k}{\partial t} + U\frac{\partial k}{\partial x} = Sk \tag{7.93}$$

If we suppose that k denotes turbulence kinetic energy, the condition $S > 0$ corresponds to production exceeding dissipation, and vice versa for $S < 0$. To cast this equation in discretized form, we use Crank-Nicolson differencing and we approximate the source term as follows:

$$Sk \doteq S\left[\psi k_j^n + (1-\psi)k_j^{n+1})\right] + O\left[(\psi - \tfrac{1}{2})\Delta t, (\Delta t)^2\right] \tag{7.94}$$

where ψ lies between 0 and 1. Hence, our finite-difference approximation to Equation (7.93) is

$$k_j^{n+1} = k_j^n - \lambda\left(k_{j+1}^{n+1} + k_{j+1}^n - k_{j-1}^{n+1} - k_{j-1}^n\right) + S\Delta t\left[\psi k_j^n + (1-\psi)k_j^{n+1})\right] \tag{7.95}$$

The complex amplification factor for this scheme is

$$G = \frac{1 + \psi S\Delta t - 2i\lambda\sin\theta}{1 - (1-\psi)S\Delta t + 2i\lambda\sin\theta} \tag{7.96}$$

Hence, in order for this scheme to be stable, we must require

$$|G|^2 = \frac{[1+\psi S\Delta t]^2 + 4\lambda^2\sin^2\theta}{[1-(1-\psi)S\Delta t]^2 + 4\lambda^2\sin^2\theta} \leq 1 \tag{7.97}$$

After a little algebra, the stability condition simplifies to

$$S\Delta t\left[1 + (\psi - \tfrac{1}{2})S\Delta t\right] \leq 0 \tag{7.98}$$

When $S < 0$, we find

$$\begin{cases} \Delta t \leq \dfrac{1}{(\psi - \frac{1}{2})|S|}; & \psi > \tfrac{1}{2}, \quad S < 0 \\ \\ \text{Unconditionally Stable;} & \psi \leq \tfrac{1}{2}, \quad S < 0 \end{cases} \tag{7.99}$$

When $S > 0$, upon first inspection, von Neumann stability analysis indicates this scheme is unstable when $\psi \geq \frac{1}{2}$ and that Δt must have a lower bound (as opposed to an upper bound) to insure stable computation when $\psi < \frac{1}{2}$. However, these results are irrelevant. This is true because the exact solution to Equation (7.93) is proportional to e^{St}, and is thus unbounded as $t \to \infty$. When this occurs, even if the error is a small fraction of the exact solution, it will also be unbounded. The requirement $|G| \leq 1$ is thus too stringent for an unbounded function. According to von Neumann, the condition for stability when the exact solution is unbounded is:

$$|G| \leq 1 + O(\Delta t) \tag{7.100}$$

With a little rearrangement of terms, Equation (7.97) can be written as

$$|G|^2 = 1 + \left(\frac{2[1 + (\psi - \frac{1}{2})S\Delta t]}{[1-(1-\psi)S\Delta t]^2 + 4\lambda^2\sin^2\theta}\right)S\Delta t \tag{7.101}$$

Since the factor proportional to $\sin^2\theta$ serves only to increase the denominator, we can omit it and say that

$$|G|^2 \leq 1 + \left(\frac{2[1 + (\psi - \frac{1}{2})S\Delta t]}{[1 - (1 - \psi)S\Delta t]^2} \right) S\Delta t \tag{7.102}$$

Clearly, the function in parentheses is bounded as $\Delta t \rightarrow 0$ as long as the denominator doesn't vanish, so that Equation (7.100) is satisfied provided:

$$\Delta t \leq \frac{1}{(1 - \psi)S}, \qquad S > 0 \tag{7.103}$$

Although this analysis has been done for implicit Crank-Nicolson differencing of the convective term, the same result holds for explicit methods. While Equation (7.94) involves k_j^{n+1}, the terms in an explicit scheme can be rearranged to preserve its explicit nature. For example, if we use upwind differencing for the convective term in Equation (7.93), the discretized equation becomes

$$k_j^{n+1} = \frac{\left[1 + \psi S\Delta t - \frac{U\Delta t}{\Delta x}\right] k_j^n + \frac{U\Delta t}{\Delta x} k_{j-1}^n}{1 - (1 - \psi)S\Delta t} \tag{7.104}$$

We now have sufficient information to discuss the most suitable discretization approximations for source terms in both explicit and implicit methods. If second-order accuracy is required, as it would be for numerical simulation of an unsteady flow, ψ must be 1/2. On the other hand, if only steady-state solutions are needed, we can take advantage of the fact that using $\psi = 0$ when $S < 0$ and $\psi = 1$ when $S > 0$ yields an unconditionally stable (albeit first-order accurate in time) scheme. In summary, the following has proven satisfactory for turbulence-model equations.

Second-Order Time Accuracy — Conditional Stability

$$Sk \doteq \frac{1}{2} S \left(k_j^n + k_j^{n+1} \right), \qquad \Delta t \leq \frac{2}{|S|} \tag{7.105}$$

First-Order Time Accuracy — Unconditional Stability

$$Sk \doteq \begin{cases} Sk_j^{n+1} & \text{for} \quad S < 0 \\ Sk_j^n & \text{for} \quad S > 0 \end{cases} \tag{7.106}$$

All of the one-dimensional time-marching programs discussed in Appendix C use Equation (7.106).

7.5 Block-Implicit Methods

The most efficient numerical methods currently available for complex flowfields are **block-implicit** methods. They differ from elementary implicit methods in one very important respect. Specifically, when an elementary implicit scheme is applied to a coupled set of equations, each equation is solved in sequence. In the context of a system of equations, this is usually referred to as a **sequentially-implicit** method. By contrast, a block-implicit scheme solves all of the equations simultaneously at each grid point. The block-implicit formulation, generally requiring inversion of block-tridiagonal matrices, entails more computational effort than a sequentially-implicit method. The additional computation at each grid point and timestep is usually compensated for by a dramatically improved convergence rate. Block-implicit solvers can achieve CFL numbers in excess of 100, and often converge in fewer than 500 timesteps for flows including boundary-layer separation. For example, using a block-implicit method, a supersonic two-dimensional shock-separated turbulent flow can be simulated with 80000 grid points and a k-ω model on a 3-GHz Pentium-D microcomputer in about 45 minutes of CPU time. On the same computer, a similar computation would take about 6 hours using a sequentially-implicit method [Wilcox (1990)] and 18 hours using an explicit method [Wilcox (1974)].

As in the preceding section, we begin with a brief overview of block-implicit methods. For simplicity, we focus on a well-known one-dimensional system. The primary concern in this section is, of course, upon how turbulence-model source terms impact such methods.

Consider the one-dimensional conservation equations for flow of a viscous, perfect gas, written in vector form, viz.,

$$\frac{\partial \mathbf{Q}}{\partial t} + \frac{\partial}{\partial x}\left(\mathbf{F} - \mathbf{F}_v\right) = \mathbf{0} \tag{7.107}$$

where

$$\mathbf{Q} = \left\{ \begin{array}{c} \bar{\rho} \\ \bar{\rho}\tilde{u} \\ \bar{\rho}E \end{array} \right\}, \quad \mathbf{F} = \left\{ \begin{array}{c} \bar{\rho}\tilde{u} \\ \bar{\rho}\tilde{u}^2 + P \\ (\bar{\rho}E + P)\tilde{u} \end{array} \right\}, \quad \mathbf{F}_v = \left\{ \begin{array}{c} 0 \\ \hat{\tau}_{xx} \\ \tilde{u}\hat{\tau}_{xx} - \hat{q}_x \end{array} \right\} \tag{7.108}$$

The quantities $\hat{\tau}_{xx}$ and $\hat{q}_x$ denote total stress and heat flux, respectively. Also, the total energy for one-dimensional flow is $E = \tilde{e} + \frac{1}{2}\tilde{u}^2$ and the pressure is given by $P = (\gamma - 1)\bar{\rho}\tilde{e}$.

The first step often taken in establishing a block-implicit scheme for this system of equations is to introduce a first-order backward-difference (implicit backward-Euler) scheme, which can be written symbolically as follows.

$$\frac{\mathbf{Q}^{n+1} - \mathbf{Q}^n}{\Delta t} + \left[\frac{\partial}{\partial x}\left(\mathbf{F} - \mathbf{F}_v\right)\right]^{n+1} = \mathbf{0} \tag{7.109}$$

Now, we expand the flux vectors $\mathbf{F}$ and $\mathbf{F}_v$ in a Taylor series about time level n, wherefore

$$\mathbf{F}^{n+1} \doteq \mathbf{F}^n + \frac{\partial \mathbf{F}}{\partial t}\Delta t + O\left[(\Delta t)^2\right] \tag{7.110}$$

and similarly for $\mathbf{F}_v$. Then, using the chain rule of calculus, we have

$$\frac{\partial \mathbf{F}}{\partial t} = \frac{\partial \mathbf{F}}{\partial \mathbf{Q}}\frac{\partial \mathbf{Q}}{\partial t} \tag{7.111}$$

where $\partial \mathbf{F}/\partial \mathbf{Q}$ is the **inviscid-flux Jacobian matrix**. The incremental change in the dependent-variable vector, $\Delta \mathbf{Q}$, is defined by

$$\Delta \mathbf{Q} = \mathbf{Q}^{n+1} - \mathbf{Q}^n \tag{7.112}$$

Since we approximate the unsteady term according to $\partial \mathbf{Q}/\partial t \doteq \Delta \mathbf{Q}/\Delta t$, we can rewrite Equation (7.110) as

$$\mathbf{F}^{n+1} \doteq \mathbf{F}^n + \frac{\partial \mathbf{F}}{\partial \mathbf{Q}}\Delta \mathbf{Q} + O\left[(\Delta t)^2\right] \tag{7.113}$$

Because of the prominent role played by $\Delta \mathbf{Q}$, this approach is usually referred to as the **delta formulation**.

Finally, we must introduce a discretization approximation for the spatial derivatives of the vectors $\mathbf{F}$ and $\mathbf{F}_v$. In general, this means forming a matrix that multiplies $(\mathbf{F} - \mathbf{F}_v)$, and yields a desired degree of accuracy. Details of this matrix are unimportant for our discussion, and it is sufficient to introduce symbolic notation with the understanding that an approximation to spatial differentiation is implied. Thus, we introduce a finite-difference matrix operator, δ_x, so that

$$\left[\frac{\partial}{\partial x}\left(\mathbf{F} - \mathbf{F}_v\right)\right]^{n+1} \doteq \delta_x\left(\mathbf{F}^n - \mathbf{F}_v^n\right) + \delta_x\left(\frac{\partial \mathbf{F}}{\partial \mathbf{Q}} - \frac{\partial \mathbf{F}_v}{\partial \mathbf{Q}}\right)\Delta \mathbf{Q} \tag{7.114}$$

where $\partial \mathbf{F}_v/\partial \mathbf{Q}$ is the **viscous-flux Jacobian matrix**. Collecting all of this, we arrive at the symbolic form of a typical block-implicit method:

$$\left[\frac{I}{\Delta t} + \delta_x\left(\frac{\partial \mathbf{F}}{\partial \mathbf{Q}} - \frac{\partial \mathbf{F}_v}{\partial \mathbf{Q}}\right)\right]\Delta \mathbf{Q} = -\delta_x\left(\mathbf{F}^n - \mathbf{F}_v^n\right) \tag{7.115}$$

where I is the unit (identity) matrix. The matrix multiplying $\Delta \mathbf{Q}$ in Equation (7.115) is of block-tridiagonal form. In the present example, the blocks are 3 by 3, corresponding to the three equations being solved simultaneously at each mesh point.

Now, suppose we choose to use a two-equation turbulence model to determine the Reynolds stress, still considering one-dimensional flow for simplicity. The following three points must be considered in modifying a block-implicit solution scheme.

1. Decide whether to solve all equations simultaneously or to solve the model equations and mean-flow equations sequentially.
2. If the preferred option is to solve all equations simultaneously, determine the changes to the flux-Jacobian matrices.
3. Make provision for handling source terms.

In principle, solving all equations simultaneously will yield the most rapidly convergent scheme in the number of iterations, but not necessarily in CPU time. However, the coupling between the turbulence-model equations and the mean-flow equations appears to be relatively weak. The primary coupling from the turbulence-model equations to the mean-flow equations is through the diffusion terms in the mean-momentum and mean-energy equations, and the eddy viscosity is usually treated as a constant in forming the viscous-flux Jacobian matrix. Limited experience to date seems to indicate there is little advantage to solving all equations simultaneously as opposed to solving the model equations and mean-flow equations sequentially.

If all equations are solved simultaneously, the basic system of equations for the k-ω model would be as follows:

$$\frac{\partial \mathbf{Q}}{\partial t} + \frac{\partial}{\partial x}\left(\mathbf{F} - \mathbf{F}_v\right) = \mathbf{S} \tag{7.116}$$

where the dependent-variable and inviscid-flux vectors are

$$\mathbf{Q} = \begin{Bmatrix} \bar{\rho} \\ \bar{\rho}\tilde{u} \\ \bar{\rho}E \\ \bar{\rho}k \\ \bar{\rho}\omega \end{Bmatrix}, \qquad \mathbf{F} = \begin{Bmatrix} \bar{\rho}\tilde{u} \\ \bar{\rho}\tilde{u}^2 + P \\ (\bar{\rho}E + P)\tilde{u} \\ \bar{\rho}\tilde{u}k \\ \bar{\rho}\tilde{u}\omega \end{Bmatrix} \tag{7.117}$$

The viscous-flux and source-term vectors are given by

$$\mathbf{F}_v = \begin{Bmatrix} 0 \\ \frac{4}{3}\mu\frac{\partial \tilde{u}}{\partial x} + \bar{\rho}\tau_{xx} \\ \tilde{u}\left(\frac{4}{3}\mu\frac{\partial \tilde{u}}{\partial x} + \bar{\rho}\tau_{xx}\right) - \hat{q}_x \\ (\mu + \sigma^*\mu_T)\frac{\partial k}{\partial x} \\ (\mu + \sigma\mu_T)\frac{\partial \omega}{\partial x} \end{Bmatrix}, \quad \mathbf{S} = \begin{Bmatrix} 0 \\ 0 \\ 0 \\ \bar{\rho}\tau_{xx}\frac{\partial \tilde{u}}{\partial x} - \beta^*\bar{\rho}\omega k \\ \alpha\left(\frac{\omega}{k}\right)\bar{\rho}\tau_{xx}\frac{\partial \tilde{u}}{\partial x} - \beta\bar{\rho}\omega^2 \end{Bmatrix} \tag{7.118}$$

There are two places where the turbulence kinetic energy appears that have an impact on the flux-Jacobian matrices. Specifically, the specific total energy, E, should be written as

$$E = \tilde{e} + \frac{1}{2}\tilde{u}^2 + k \tag{7.119}$$

and the Reynolds-stress tensor is

$$\bar{\rho}\tau_{xx} = \frac{4}{3}\mu_T\frac{\partial\tilde{u}}{\partial x} - \frac{2}{3}\bar{\rho}k \tag{7.120}$$

Hence, since the vector $\mathbf{Q}$ contains $\bar{\rho}k$ as one of its elements, the inviscid- and viscous-flux Jacobian matrices must be evaluated from scratch. Some of the original 9 elements appropriate for laminar flow or an algebraic model will be affected by the appearance of k in E and $\hat{\tau}_{xx}$. For this system, the inviscid-flux Jacobian matrix assumes the following form:

$$\frac{\partial\mathbf{F}}{\partial\mathbf{Q}} = \begin{bmatrix} 0 & 1 & 0 & 0 & 0 \\ \left(\frac{\gamma-3}{2}\right)\tilde{u}^2 & (3-\gamma)\tilde{u} & (\gamma-1) & -(\gamma-1) & 0 \\ -\left[H - \frac{\gamma-1}{2}\tilde{u}^2\right]\tilde{u} & \left[H-(\gamma-1)\tilde{u}^2\right] & \gamma\tilde{u} & -(\gamma-1)\tilde{u} & 0 \\ -\tilde{u}k & k & 0 & \tilde{u} & 0 \\ -\tilde{u}\omega & \omega & 0 & 0 & \tilde{u} \end{bmatrix} \tag{7.121}$$

where H is the specific total enthalpy defined by

$$H = \tilde{h} + \frac{1}{2}\tilde{u}^2 + k \tag{7.122}$$

As shown in Equation (7.121), the first two components on row 3 involve H, and are thus affected by k. In modifying an existing computer program based on this block-implicit scheme, all that would be required to modify the inviscid-flux Jacobian matrix components would be to have H appear as indicated, and to include k in the computation of H.

By contrast, if we solve the mean-flow and turbulence-model equations sequentially, we retain the original conservation equations [Equation (7.107)]. All of the flux-Jacobian matrices and, in fact, the entire algorithm remain the same. To determine k and ω, we then consider the following vector equation:

$$\frac{\partial\mathbf{q}}{\partial t} + \frac{\partial}{\partial x}(\mathbf{f} - \mathbf{f}_v) = \mathbf{s} \tag{7.123}$$

where

$$\mathbf{q} = \begin{Bmatrix} \bar{\rho}k \\ \bar{\rho}\omega \end{Bmatrix}, \quad \mathbf{f} = \begin{Bmatrix} \bar{\rho}\tilde{u}k \\ \bar{\rho}\tilde{u}\omega \end{Bmatrix}, \quad \mathbf{f}_v = \begin{Bmatrix} (\mu+\sigma^*\mu_T)\frac{\partial k}{\partial x} \\ (\mu+\sigma\mu_T)\frac{\partial\omega}{\partial x} \end{Bmatrix} \tag{7.124}$$

$$\mathbf{s} = \begin{Bmatrix} \bar{\rho}\tau_{xx}\frac{\partial\tilde{u}}{\partial x} - \beta^*\bar{\rho}\omega k \\ \alpha\left(\frac{\omega}{k}\right)\bar{\rho}\tau_{xx}\frac{\partial\tilde{u}}{\partial x} - \beta\bar{\rho}\omega^2 \end{Bmatrix} \tag{7.125}$$

Consistent with the block-implicit approach, we linearize the flux and source vectors according to

$$(\mathbf{f} - \mathbf{f}_v)^{n+1} \doteq (\mathbf{f} - \mathbf{f}_v)^n + \left(\frac{\partial\mathbf{f}}{\partial\mathbf{q}} - \frac{\partial\mathbf{f}_v}{\partial\mathbf{q}}\right)\Delta\mathbf{q} \tag{7.126}$$

$$\mathbf{s} \doteq \mathbf{s}^n + \frac{\partial \mathbf{s}}{\partial \mathbf{q}} \Delta \mathbf{q} \tag{7.127}$$

where $\partial \mathbf{s}/\partial \mathbf{q}$ is the **source-Jacobian matrix**. The flux-Jacobian matrices are generally much simpler than their counterparts in the mean-flow equations. For example, the inviscid-flux Jacobian matrix is

$$\frac{\partial \mathbf{f}}{\partial \mathbf{q}} = \begin{bmatrix} \tilde{u} & 0 \\ 0 & \tilde{u} \end{bmatrix} \tag{7.128}$$

This brings us to the all important question of how to handle the source-term vector $\mathbf{s}$. Several prescriptions are possible, and the primary considerations are to: maintain numerical stability; achieve rapid convergence rate; and guarantee that k and ω are positive definite. Wilcox (1991) has found the following linearization of the source terms to be quite satisfactory for the k-ω model, within the framework of MacCormack's (1985) block-implicit method. Specifically, the source-term vector is rearranged as follows.

$$\mathbf{s} = \begin{Bmatrix} \bar{\rho}\tau_{xx}\frac{\partial \tilde{u}}{\partial x} - \beta^* \left(\frac{\omega}{k}\right) \frac{(\bar{\rho}k)^2}{\bar{\rho}} \\ \alpha \left(\frac{\omega}{k}\right) \bar{\rho}\tau_{xx}\frac{\partial \tilde{u}}{\partial x} - \beta \frac{(\bar{\rho}\omega)^2}{\bar{\rho}} \end{Bmatrix} \tag{7.129}$$

Then, treating both $\bar{\rho}\tau_{xx}\partial\tilde{u}/\partial x$ and ω/k as constants in computing the source-Jacobian matrix, we arrive at

$$\mathbf{s}^n = \begin{Bmatrix} \bar{\rho}\tau_{xx}\frac{\partial \tilde{u}}{\partial x} - \beta^* \bar{\rho}\omega k \\ \alpha \left(\frac{\omega}{k}\right) \bar{\rho}\tau_{xx}\frac{\partial \tilde{u}}{\partial x} - \beta \bar{\rho}\omega^2 \end{Bmatrix}, \qquad \frac{\partial \mathbf{s}}{\partial \mathbf{q}} = \begin{bmatrix} -2\beta^*\omega & 0 \\ 0 & -2\beta\omega \end{bmatrix} \tag{7.130}$$

In this treatment of the source-term vector the production terms are evaluated explicitly (i.e., computed at time level n), and the dissipation terms are treated implicitly (computed at time level $n+1$). The block-tridiagonal scheme for the turbulence-model equations becomes

$$\left[\frac{I}{\Delta t} + \delta_x \left(\frac{\partial \mathbf{f}}{\partial \mathbf{q}} - \frac{\partial \mathbf{f}_v}{\partial \mathbf{q}}\right) - \frac{\partial \mathbf{s}}{\partial \mathbf{q}}\right] \Delta \mathbf{q} = -\delta_x \left(\mathbf{f}^n - \mathbf{f}_v^n\right) + \mathbf{s}^n \tag{7.131}$$

Since $\partial \mathbf{s}/\partial \mathbf{q}$ is a diagonal matrix and its diagonal elements are always negative, its contribution is guaranteed to enhance diagonal dominance of the matrix multiplying $\Delta \mathbf{q}$. Additionally, Spalart and Allmaras (1992) show that this form guarantees that k and ω (or ϵ for a k-ϵ model) will always be positive.

However, Spalart and Allmaras also point out that in regions where production and dissipation are both large and dominate the overall balance of terms in the equation, this form can result in slow convergence. This appears to be a more serious problem for the k-ϵ model than it is for the k-ω model. Wilcox

(1991), for example, has shown that the scheme described above yields very rapid convergence in flows with attached equilibrium boundary layers and in flows with large regions of separation. The procedure recommended by Spalart and Allmaras is similar to the procedure recommended for elementary implicit methods in Equation (7.106). That is, they recommend linearizing the source term according to

$$\mathbf{s} \doteq \mathbf{s}^n + \text{neg}\left(\frac{\partial \mathbf{s}}{\partial \mathbf{q}}\right)\Delta\mathbf{q} \tag{7.132}$$

where the function $\text{neg}(x)$ is defined as

$$\text{neg}(x) = \begin{cases} x, & x < 0 \\ 0, & x \geq 0 \end{cases} \tag{7.133}$$

The production terms are then included in computing the source-Jacobian matrix. The neg operator is understood to apply to each element of the resulting (diagonal) matrix. Thus, as long as dissipation exceeds production, both production and dissipation are treated implicitly, and explicitly when production exceeds dissipation. Huang and Coakley (1992) have successfully applied a linearization similar to that recommended by Spalart and Allmaras. Gerolymos (1990), Shih et al. (1993) and Merci et al. (2000) also offer interesting information regarding stiffness and numerical issues resulting from source terms in turbulence-model equations.

7.6 Solution Convergence and Grid Sensitivity

Regardless of the application, there is a need for control of numerical accuracy in CFD [Roache (1990, 1998b)]. This need is just as critical in CFD work as it is in experiments where the experimenter is expected to provide estimates for the accuracy of his or her measurements. All CFD texts of any value stress this need.

7.6.1 Iteration Convergence and Grid Convergence

One key issue determining numerical accuracy is **iteration convergence**. Most numerical methods used in CFD applications require many iterations to converge. The iteration convergence error is defined as the difference between the current iterate and the exact solution to the difference equations. Often, the difference between successive iterates is used as a measure of the error in the converged solution, although this in itself is inadequate. A small relaxation factor can always give a false indication of convergence [Anderson et al. (1984)]. Whatever the algorithm is, you should always be careful to check that a converged

solution has been obtained. This can be done by trying a stricter than usual convergence criterion, and demonstrating that there is a negligible effect on the solution. Most reputable engineering journals require demonstration of iteration convergence and grid independence as a condition for publication. This is not specific to turbulence-model applications — all of the usual criteria for standard CFD applications apply.

Specific to turbulence-model computations, the approach to iteration convergence often is more erratic, and typically much slower, than for laminar-flow computations. A variety of factors including stiffness and nonlinearity of the equations, as well as the severely stretched finite-difference grids needed to resolve thin viscous layers, yield less rapid and less monotone convergence. Ferziger (1989) explains the slow convergence often observed in terms of the eigenvalues of the matrix system corresponding to the discretized equations. He notes that any iteration scheme for a linear system can be written as

$$\phi^{n+1} = A\phi^n + S \tag{7.134}$$

where ϕ^n is the solution after the n^{th} iteration, A is a matrix, and S is a source term. He then shows that the actual solution error is given by

$$\phi_{exact} - \phi^n \approx \frac{\phi^{n+1} - \phi^n}{1 - \lambda_{max}} \tag{7.135}$$

where ϕ_{exact} denotes the **exact solution to the discretized equations** and λ_{max} is the largest eigenvalue of the matrix A. Of course, all eigenvalues of A must be less than 1 for the solution to converge. This result shows that the solution error is larger than the difference between iterates. Furthermore, the closer λ_{max} is to 1, the larger the ratio of solution error to the difference between iterates. In other words, the slower the rate of convergence of the method, the smaller the difference between iterates must be to guarantee iteration convergence.

A second key issue is **grid convergence** or **grid independence**. Because of the finite size of finite-difference cells, discretization errors exist that represent the difference between the solution to the difference equations and the **exact (continuum) solution to the differential equations**. It is important to know the magnitude of these discretization errors and to insure that a fine enough grid has been used to reduce the error to an acceptable level.

As with iteration convergence, all CFD work should demonstrate grid convergence, regardless of what equations are being solved. In most engineering journals, it is no longer sufficient to publish results performed on a single fixed grid. While grid sensitivity studies should be done for all CFD work, they are even more crucial for turbulence-model computations because of the need to separate numerical error from turbulence-model error. This issue came into sharp focus at the 1980-81 AFOSR-HTTM-Stanford Conference on Complex

Turbulent Flows [see Kline, Cantwell, and Lilley (1981)]. Clearly, no objective evaluation of the merits of different turbulence models can be made unless the discretization error of the numerical algorithm is known.

7.6.2 Richardson Extrapolation

The best known way to demonstrate grid convergence is to repeat a computation on a grid with twice as many grid points, and compare the two solutions. If computer resources are unavailable to facilitate a grid doubling, a grid halving is also appropriate, although the error bounds will not be as sharp. Using results for two different grids, techniques such as **Richardson extrapolation** [see Roache (1998b)] can be used to determine discretization error. This method is very simple to implement, and should be used whenever possible.

For a second-order accurate method with central differences, Richardson extrapolation assumes the error, $E_h \equiv \phi_{exact} - \phi_h$, where ϕ_h denotes the solution when the grid-point spacing is h, can be expanded as a Taylor series in h, wherefore

$$E_h = e_2 h^2 + e_4 h^4 + e_6 h^6 + \cdots \tag{7.136}$$

Note that for three-point upwind differences the leading term is still $e_2 h^2$, but the next term is $e_3 h^2$, and Richardson extrapolation is only $O(h^3)$ rather than $O(h^4)$. By hypothesis, the e_i are, at worst, functions of the coordinates, but are nevertheless independent of h. Now, if we halve the number of grid points so that h is doubled, the error is given by

$$E_{2h} = 4e_2 h^2 + 16e_4 h^4 + 64e_6 h^6 + \cdots \tag{7.137}$$

For small values of h, we can drop all but the leading terms, whence the discretization error is given by

$$E_h \approx \frac{1}{3}(\phi_h - \phi_{2h}) \tag{7.138}$$

Equation (7.138) provides an excellent estimate of the difference between the exact continuum solution and ϕ_h. The terminology "extrapolation" simply reflects the fact that we can use our pair of solutions to extrapolate to the continuum solution by writing

$$\phi_{exact} = \phi_h + E_h \approx \frac{4}{3}\phi_h - \frac{1}{3}\phi_{2h} \tag{7.139}$$

As a final comment, Richardson extrapolation has limitations. First, if it is applied to primitive variables such as velocity and internal energy, its implications regarding momentum and energy conservation may be inaccurate. Second, the method implicitly assumes the solution has continuous derivatives to all orders. Hence, its results are not meaningful near shock waves or turbulent/nonturbulent interfaces of the type discussed in Subsection 7.2.2.

7.6.3 Grid Convergence Index

As noted by Roache (1998b), Richardson extrapolation is not limited to doubling or halving the grid-point spacing. For the **generalized theory of Richardson extrapolation**, we write

$$\phi_{exact} \approx \phi_h + \frac{\phi_h - \phi_{rh}}{r^p - 1} \tag{7.140}$$

where p is the order of the finite-difference scheme and r is the grid-refinement ratio. By definition, if we halve the size of the grid-point spacing, then $r = 1/2$ and doubling the size corresponds to $r = 2$.

It is a straightforward matter to use Richardson extrapolation on two grids that differ in cell size by a factor of 2 because the grid-point locations on the coarse grid are identical to those on the fine grid at every other point. Nevertheless, the method applies to any value of r. Since the solutions have to be compared at the same physical point, interpolation is needed on one of the grids to establish solution values at the same points for comparison.

Building on Richardson extrapolation, Roache (1998b) has developed the **Grid Convergence Index** (GCI) to help establish a uniform method for reporting the estimated error in a computation. By definition,

$$GCI \equiv F_s \frac{|\epsilon_h|}{r^p - 1}, \qquad \epsilon_h = \frac{\phi_h - \phi_{rh}}{\phi_h} \tag{7.141}$$

The quantity ϵ_h is the **fractional error** for the grid with spacing h. If two grids are used, Roache recommends using $F_s = 3$. This will provide a conservative estimate of solution error for virtually all fluid-flow problems. If three different grids are used, $F_s = 1.25$ is appropriate. In the latter case, the three-grid sequence of computations can be used to first establish the actual order of the method, p. Then, the index can be computed to provide a measure of how accurate the solutions on the finest grids are.

The GCI is especially useful as a measure of how accurately key quantities such as lift and drag coefficients, skin friction and surface-pressure coefficients have been computed. That is, its use is not confined to an overall measure of solution errors at specific grid points. It can be applied to any key feature of the solution that is of particular interest.

To determine the order of a finite-difference method, we observe that if it is p^{th}-order accurate, then the solution error will change according to

$$E_h \approx Ch^p, \qquad C = \text{constant} \tag{7.142}$$

The value of p is the slope of E_h as a function of h on a log-log plot. At least three grids are needed to accurately determine p. It is simplest if the three grids

have been done with constant r. That is, if the finest grid has spacing h, the next to finest would have rh and the coarsest would have r^2h. In this case, the value of p can be determined as follows.

$$p = \frac{\ell n \left| (\phi_{rh} - \phi_{r^2h})/(\phi_{rh} - \phi_h) \right|}{\ell n r} \tag{7.143}$$

If r is not constant, computing p is a bit more complicated and typically requires an iterative solution [see Roache (1998b)].

As an example, consider the results from a grid-convergence study shown in Table 7.4. The computation was done on a uniformly spaced mesh with N points that has been doubled from one grid to the next so that $r = 2$. Since the table includes information for four grids, we can apply Equation (7.143) twice, first to the 32-64-128 trio and then to the 64-128-256 results.

Table 7.4: *Grid Convergence Study Results.*

N	h	ϕ_h	p	ϵ_h	GCI
32	0.03125000	1.08359	—	—	—
64	0.01562500	1.00539	—	$-7.7780 \cdot 10^{-2}$	0.648%
128	0.00781250	1.00034	3.95	$-5.0482 \cdot 10^{-3}$	0.042%
256	0.00390625	1.00002	3.98	$-3.1999 \cdot 10^{-4}$	0.003%

Clearly, p is very close to 4 and we conclude that the method used in this computation is 4^{th}-order accurate. Hence, in applying the GCI, Equation (7.141) becomes

$$GCI = 1.25 \frac{|\epsilon_h|}{r^4 - 1} \tag{7.144}$$

Normally expressed as a percent, the GCI provides an excellent estimate of the error band that can be placed on a fine-grid solution.

7.6.4 Near-Wall Grid-Point Spacing

There is another grid-related factor affecting solution accuracy. In order to resolve thin viscous layers, for example, highly stretched grids are normally used. Conventional central-difference approximations are only first-order accurate on such a grid, and care must be taken to account for this. Also, the location of the grid point nearest the surface has a nontrivial effect on the accuracy of skin friction and surface heat flux. Wilcox (1989), for example, has found that grid-insensitive computations using wall functions that account for pressure gradient [e.g., Equation (5.126)] can be obtained with block-implicit methods provided

$$10 < y_2^+ < 100, \qquad \text{(wall functions)} \tag{7.145}$$

where y_2^+ is the sublayer-scaled value of the first grid point above the surface. This range appears to hold for boundary-layer computations as well [Chambers and Wilcox (1977)], again provided pressure gradient is accounted for. When turbulence-model equations are integrated through the viscous sublayer, many researchers have shown that it is imperative to require

$$y_2^+ < 1, \qquad \text{(integration through the sublayer)} \tag{7.146}$$

For shock separated flows, particularly at hypersonic speeds, Marvin and Huang (1996) recommend the more-stringent condition $y_2^+ < 0.3$. When these limits are not adhered to, consistent with the discussion in Subsection 7.2.1, solution errors throughout the boundary layer generally are large.

Problems

7.1 For a Mach 3 turbulent flat-plate boundary layer, it is a fact that $Mc_f Re_L \approx Re_{\delta^*}$.

(a) In the viscous sublayer, the appropriate scaling for the specific dissipation rate is $\omega \sim u_\tau^2/\nu$. Noting that $u_\tau \approx U\sqrt{c_f}$, express the ratio of t_{diss} to t_{wave} as a function of Re_{δ^*} in the sublayer.

(b) In the defect layer, the appropriate scaling for the specific dissipation rate is given by $\omega \sim u_\tau/\Delta$ where $\Delta = U\delta^*/u_\tau$. Express the ratio of t_{diss} to t_{wave} as a function of Re_{δ^*} in the defect layer.

(c) Comment on the implications of your estimates in Parts (a) and (b).

7.2 Determine whether or not the following systems of equations are stiff with regard to the specified initial conditions.

(a)

$$\frac{d}{dt}\begin{Bmatrix} x \\ y \end{Bmatrix} = \begin{bmatrix} -3 & 4 \\ 4 & 3 \end{bmatrix}\begin{Bmatrix} x \\ y \end{Bmatrix}, \qquad \begin{Bmatrix} \dot{x}(0) \\ \dot{y}(0) \end{Bmatrix} = -5\begin{Bmatrix} x(0) \\ y(0) \end{Bmatrix}$$

(b)

$$\frac{d}{dt}\begin{Bmatrix} x \\ y \end{Bmatrix} = \begin{bmatrix} -3 & 1 \\ 4 & -3 \end{bmatrix}\begin{Bmatrix} x \\ y \end{Bmatrix}, \qquad \begin{Bmatrix} \dot{x}(0) \\ \dot{y}(0) \end{Bmatrix} = -\begin{Bmatrix} x(0) \\ y(0) \end{Bmatrix}$$

7.3 Consider the high-Reynolds-number k-ω model's near-wall variation of specific dissipation rate, ω, for a rough wall, i.e.,

$$\omega = \frac{\omega_w}{[1 + Ay]^2}, \qquad A = \sqrt{\frac{\beta_o \omega_w}{6\nu_w}}$$

(a) Assuming equally-spaced grid points, show that the central-difference approximation to $d^2\omega/dy^2$ at the first grid point above the surface (i.e., at $y = \Delta y$) is given by

$$\left(\frac{d^2\omega}{dy^2}\right)_2 \approx \Phi(\Delta y)\left(\frac{d^2\omega}{dy^2}\right)_{exact}$$

where

$$\Phi(\Delta y) = \frac{[1 + A\Delta y]^2[1 + 2A\Delta y + \frac{2}{3}(A\Delta y)^2]}{[1 + 2A\Delta y]^2}$$

(b) Assuming a slightly-rough wall so that $\omega_w = 40000\nu_w/k_s^2$ and using $\beta_o = 0.0708$, show that

$$A\Delta y = 21.7\frac{\Delta y^+}{k_s^+}$$

(c) Determine the percentage error introduced by the central-difference approximation in computing $d^2\omega/dy^2$ when we assume a hydraulically-smooth wall with $k_s^+ = 5$, and set $\Delta y^+ = 1/8$.

7.4 This problem shows that while trapezoidal-rule integration is second-order accurate for a piecewise continuous function with a discontinuous first derivative, the truncation error depends upon placement of the nodes. Using the trapezoidal rule, the integral of a function $f(x)$ is

$$\int_a^b f(x)\,dx \approx \sum_{k=1}^{N} f(x_k)\Delta x + \frac{1}{2}[f(a) - f(b)]\Delta x$$

where

$$x_k = k\Delta x \qquad \text{and} \qquad \Delta x = \frac{b-a}{N}$$

Consider the following piecewise continuous function $f(x)$:

$$f(x) = \begin{cases} x^2, & 0 \le x \le 1 \\ 1, & 1 < x \le 2 \end{cases}$$

Note that a node lies at $x = 1$ only for even values of N.

(a) Verify that the exact integral of $f(x)$ for x ranging from 0 to 2 is

$$I \equiv \int_0^2 f(x)\,dx = \frac{4}{3}$$

(b) Assuming N is odd show that the trapezoidal rule yields

$$I \approx \frac{4}{3}\left[1 - \frac{1}{16}(\Delta x)^2\right]$$

(c) Assuming N is even show that the trapezoidal rule yields

$$I \approx \frac{4}{3}\left[1 + \frac{1}{8}(\Delta x)^2\right]$$

HINT: Use the fact that $\displaystyle\sum_{k=1}^{M} k^2 = \frac{1}{6}M(M+1)(2M+1)$.

7.5 Consider the mixing-length model with $\ell_{mix} = \alpha\delta$, where α is a constant and δ is shear-layer thickness.

(a) Assuming that $dU/dy > 0$, verify that according to the Rubel-Melnik transformation,

$$\nu_T = \ell_{mix}\sqrt{\frac{dU}{d\xi}}$$

(b) For flow near a turbulent/nonturbulent interface with constant entrainment velocity, $V < 0$, determine the velocity difference, $U_e - U$, as $y \to \delta$. Express your answer as a function of $|V|$, α and y/δ.

7.6 Verify that, *with the stress limiter excluded*, the solution for the Wilcox (2006) k-ω model at a turbulent/nonturbulent interface is given by Equations (7.41). To do this, begin with the interface equations, which (with $\nu_T = k/\omega$) are as follows.

$$V\frac{dU}{dy} = \frac{d}{dy}\left(\nu_T \frac{dU}{dy}\right), \qquad V\frac{dk}{dy} = \nu_T\left(\frac{dU}{dy}\right)^2 - \beta^*\omega k + \sigma^*\frac{d}{dy}\left[\nu_T\frac{dk}{dy}\right]$$

$$V\frac{d\omega}{dy} = \alpha\left(\frac{dU}{dy}\right)^2 - \beta_o\omega^2 + \frac{\sigma_{do}}{\omega}\frac{dk}{dy}\frac{d\omega}{dy} + \sigma\frac{d}{dy}\left[\nu_T\frac{d\omega}{dy}\right]$$

(a) Introduce the Rubel-Melnik transformation and show that these equations transform to

$$V\frac{dU}{d\xi} = \frac{d^2U}{d\xi^2}, \qquad V\frac{dk}{d\xi} = \left(\frac{dU}{d\xi}\right)^2 - \beta^*k^2 + \sigma^*\frac{d^2k}{d\xi^2}$$

$$V\frac{d\omega}{d\xi} = \alpha\frac{\omega}{k}\left(\frac{dU}{d\xi}\right)^2 - \beta_o k\omega + \frac{\sigma_{do}}{k}\frac{dk}{d\xi}\frac{d\omega}{d\xi} + \sigma\frac{d^2\omega}{d\xi^2}$$

(b) Assume a solution of the form $U_e - U \sim \mathcal{U}e^{\lambda_u V\xi}$, $k \sim \mathcal{K}e^{\lambda_k V\xi}$ and $\omega \sim \mathcal{W}e^{\lambda_\omega V\xi}$ and determine the constants λ_u, λ_k and λ_ω. **NOTE:** Use the fact that $V < 0$ in deriving your solution.

(c) Using your solution from Part (b), solve for n_u, n_k and n_ω.

7.7 Verify that, *with the stress limiter included*, the solution for the Wilcox (2006) k-ω model at a turbulent/nonturbulent interface is given by Equations (7.41) with the exception that now $n_u = n_k$. To do this, begin by noting that the interface equations are:

$$V\frac{dU}{dy} = \frac{d}{dy}\left(\frac{\sqrt{\beta^*}}{C_{lim}}k\right), \qquad V\frac{dk}{dy} = \frac{\sqrt{\beta^*}}{C_{lim}}k\left|\frac{dU}{dy}\right| - \beta^*\omega k + \sigma^*\frac{d}{dy}\left[\frac{k}{\omega}\frac{dk}{dy}\right]$$

$$V\frac{d\omega}{dy} = \alpha\frac{\sqrt{\beta^*}}{C_{lim}}\omega\left|\frac{dU}{dy}\right| - \beta_o\omega^2 + \frac{\sigma_{do}}{\omega}\frac{dk}{dy}\frac{d\omega}{dy} + \sigma\frac{d}{dy}\left[\frac{k}{\omega}\frac{d\omega}{dy}\right]$$

(a) Introduce the Rubel-Melnik transformation with $\nu_T = k/\omega$ and show that these equations transform to

$$V\frac{dU}{d\xi} = \frac{\sqrt{\beta^*}}{C_{lim}}\frac{dk}{d\xi}, \qquad V\frac{dk}{d\xi} = \frac{\sqrt{\beta^*}}{C_{lim}}k\left|\frac{dU}{d\xi}\right| - \beta^*k^2 + \sigma^*\frac{d^2k}{d\xi^2}$$

$$V\frac{d\omega}{d\xi} = \alpha\frac{\sqrt{\beta^*}}{C_{lim}}\omega\left|\frac{dU}{d\xi}\right| - \beta_o k\omega + \frac{\sigma_{do}}{k}\frac{dk}{d\xi}\frac{d\omega}{d\xi} + \sigma\frac{d^2\omega}{d\xi^2}$$

(b) Assume a solution of the form $U_e - U \sim \mathcal{U}e^{\lambda_u V\xi}$, $k \sim \mathcal{K}e^{\lambda_k V\xi}$ and $\omega \sim \mathcal{W}e^{\lambda_\omega V\xi}$ and determine the constants λ_u, λ_k and λ_ω. **NOTE:** Use the fact that $V < 0$ in deriving your solution.

(c) Using your solution from Part (b), solve for n_u, n_k and n_ω.